Measurement of the azimuthal anisotropy for charged particle production in Pb+Pb collisions at $\sqrt{s_{\mathrm{NN}}}$=2.76 TeV and in p+Pb collisions at $\sqrt{s_{\mathrm{NN}}}$=5.02 TeV with the ATLAS detector at the LHC

A Dissertation Presented

by

Soumya Mohapatra

to

The Graduate School

in Partial Fulfillment of the Requirements

for the Degree of

Doctor of Philosophy

in

Physics

Stony Brook University

August 2013

Stony Brook University

The Graduate School

Soumya Mohapatra

We, the dissertation committee for the above candidate for the Doctor of Philosophy degree, hereby recommend acceptance of this dissertation.

Jiangyong Jia – Dissertation Advisor
Associate Professor, Department of Chemistry

Derek Teaney – Chairperson of Defense
Associate Professor, Department of Physics and Astronomy

Roy A. Lacey
Professor, Department of Chemistry

Robert McCarthy
Professor, Department of Physics and Astronomy

Maria Victoria Fernandez-Serra
Assistant Professor, Department of Physics and Astronomy

David Morrison
Physicist, Physics Department
Brookhaven National Lab

This dissertation is accepted by the Graduate School.

Charles Taber
Interim Dean of the Graduate
School

Abstract of the Dissertation

Measurement of the azimuthal anisotropy for charged particle production in Pb+Pb collisions at $\sqrt{s_{\mathrm{NN}}}$=2.76 TeV and in p+Pb collisions at $\sqrt{s_{\mathrm{NN}}}$=5.02 TeV with the ATLAS detector at the LHC

by

Soumya Mohapatra

Doctor of Philosophy

in

Physics

Stony Brook University

2013

In this work, detailed measurements of the p_{T}, η and centrality dependence of the flow harmonics v_n in Pb+Pb collisions at $\sqrt{s_{\mathrm{NN}}} =$ 2.76 TeV with the ATLAS detector at the LHC are presented. Consistent values of harmonics v_2-v_6 are measured the via event-plane and two-particle correlation methods. Dipolar flow v_1 associated with initial dipole asymmetry is measured via two-particle correlations. The long-range correlations in the two-particle correlations such as *ridge* and the *cone* are shown to be accounted for by collective flow. Sizable values of the odd harmonics especially v_3 are measured that indicate significant event-by-event (EbyE) fluctuations in the initial geometry.

The nature of the initial collision geometry and the hydrodynamic response to it are investigated by measuring the EbyE distributions for harmonics v_2-v_4 , as well as correlations between two and three event-planes Φ_n of different orders. These measurements show the presense of considerable EbyE fluctuations in the initial geometry as well as the importance of non-linear hydrodynamic response of the medium to these fluctuations. By measuring the EbyE v_n distributions separately for particles with $p_{\mathrm{T}} > 1$ GeV and with $p_{\mathrm{T}} \in (0.5, 1.0)$ GeV, the hydrodynamic response is shown to factorize into a function of p_{T} and a function of the initial geometry. The EbyE v_n distributions are shown to contain additional information than the multi-particle cumulants.

Two-particle correlations in p+Pb collisions at $\sqrt{s_{\mathrm{NN}}} = 5.02$ TeV are measured. Long range correlations are observed along $\Delta\eta$ at $\Delta\phi \sim 0$ that increase with increasing event-activity. A symmetric long range correlation is also shown to exist at $\Delta\phi \sim \pi$ which is obtained by subtracting out the expected contribution from recoiling dijets. These correlations are shown to be similar to those seen in Pb+Pb collisions suggesting similar physics in both systems.

To my parents, my sister and my wife.

Contents

List of Figures

List of Tables

Acknowledgements

First and foremost I would like to thank my advisor Prof. Jiangyong Jia for guiding me through out my PhD years. He was always patient with me despite my making mistakes. His dedication to his work always motivated me and watching him work relentlessly made me push myself as well. I hope that I too will one day be as good a researcher and an advisor as he is.

I would also like to thank my ATLAS colleagues, without whom the data used in my research work never have been recorded. The way the whole collaboration works is simply astounding. The smooth functioning of ATLAS, could not have been possible without the dedicated hard work of every single ATLAS member, and for that every one of them has my gratitude.

My thanks also goes to my friends at the Nuclear Chemistry group at Stony Brook. To my friend Arkadiy for always helping me out with advice, analyses and also with my thesis. To my fellow graduate students Alex, Damian, Sooraj, Xiaoyang and Yi. It was a real pleasure working with you guys. I would also like to thank Roy and Ajit for their support and help during my time with the group.

I would also like to thank my nuclear physics buddies Prasad and Deepali for the good times that I had because of them. Hopefully I will be able to collaborate with them in the future. To my friends Abhijit, Manas, Mithun, Prerit, Rik, Ritwik, Somnath and Sheng without whom the years at Stony Brook would not have been enjoyable.

Also many thanks to my committee members for taking time out of their busy schedules and coming to my defence, and also for going carefully through my thesis and suggesting improvements.

Last but not the least I would like to thank my family. I thank my parents for giving me life and inspiring me to pursue a path of knowledge and learning, and for always standing by me. I thank my sister for bringing humor into my life. Her positive attitude taught me no matter how tough it gets there is always light at the end of the tunnel. I thank my wife for bearing with me during my graduate work, and never complaining. She has always been supportive of me. Her presence in my life has made it complete.

Chapter 1

Introduction

The goal of the thesis work presented here is to study the properties of strongly interacting matter (QCD[1] matter) under conditions of extreme temperature and pressure that is produced in ultra-relativistic heavy-ion collisions. Figure 1.1 shows a schematic diagram of the expected phases of QCD matter as a function of temperature (T) and baryochemical potential[2] (μ_{B}). On this plot, the vacuum is at the origin $T = 0, \mu_{\mathrm{B}} = 0$ and ordinary nuclear matter at[3] $T \approx 0$ MeV and $\mu_{\mathrm{B}} \approx 900$ MeV (the mass of a nucleon). The lower left region corresponds to matter at low temperatures and μ_{B}. In this phase the quarks and gluons are confined within color neutral hadrons. Since the hadrons are color neutral, the interactions are relatively weak and this phase behaves like a gas, and is thus called the "hadron-gas phase". On the other hand if the temperature is increased keeping μ_{B} constant then a different phase of matter commonly called the Quark Gluon Plasma (QGP) [1–3] is expected to be reached. In this phase the quarks and gluons are not confined within colorless hadrons, but instead form the degrees of freedom. The temperature at which this de-localization takes place can currently be estimated via numerical lattice QCD calculations [4–6]. Such computations show that there is a large increase in the energy density $\epsilon(T)$ over a temperature range of $T \sim$160–190 MeV as shown in Fig. 1.2. This large change in energy density indicates a change in the number of degrees of freedom from the three light pions which dominate the thermodynamics at low temperature to quarks and gluons (having much more degrees of freedom) at high temperature [5].

The lattice calculations shown here are done at $\mu_b = 0$, and show that while the transition is sharp, it is not discontinuous, and thus is a cross-over rather than a phase transition. However at some finite value of μ_b, the crossover

---

[1] QCD stands for Quantum Chromodynamics, the theory of strong interactions.

[2] Baryochemical potential is the amount of energy needed to add a baryon to the system.

[3] A temperature of 273K is equivalent to 23.5 meV.

is conjectured to change into a first order phase transition, with the energy density exhibiting discontinuity at the phase boundary, implying the presence of a critical point in the QCD phase diagram [7].

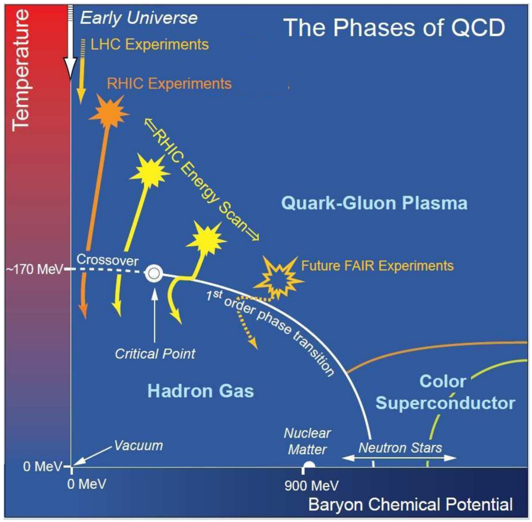

Figure 1.1: Schematic phase-diagram of QCD matter. Solid lines indicate phase boundaries between the different phases. The solid circle indicates the critical point for the hadron-gas to QGP phase transition. Note that the existence of a critical point is conjectured, its existence has not been established. Figure taken from [8].

1.1 Recreating QGP in the laboratory via relativistic heavy-ion collisions

The QGP phase is believed to be the state of the universe a few micro-seconds after the Big-Bang, when the energy density and temperatures were high enough for this phase to exist, after which the universe cooled down sufficiently for nuclei to form. However, it is possible to recreate QGP in the laboratory by colliding heavy nuclei at relativistic energies. The heavy-ion collisions are thus often nicknamed “little-bangs”. Such collisions have been done with ever increasing energies at various accelerator facilities such at the Alternating Gradient Synchrotron (AGS), the Super Proton Synchrotron (SPS) and the Relativistic Heavy Ion Collider (RHIC).

At RHIC several different types of colliding systems such as Au+Au, Cu+Cu, U+U as well as asymmetric large-small systems such as d+Au and p+Au,

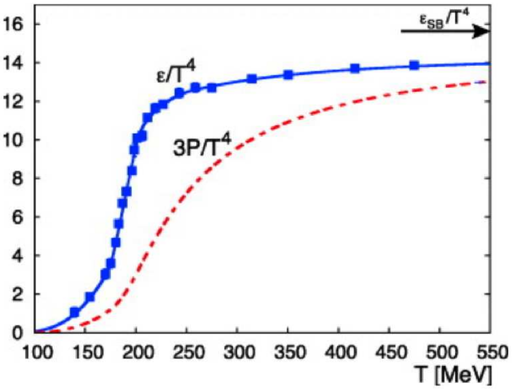

Figure 1.2: Energy density and pressure scaled by the fourth power of temperature as a function of temperature from Lattice-QCD calculations (at baryochemical potential $\mu_b = 0$). The arrow on the right indicates the value in the ideal gas limit. The large increase in the energy dencity in the T ~160–190 MeV range is indicative of a crossover from a hadron-gas phase to QGP phase. Figure taken from [6].

which serve as baseline measurements for the heavy-ion collisions, were studied at varying collision energies per nucleon pair[4] ($\sqrt{s_{\rm NN}}$=7–200 GeV). These measurements gave compelling evidence of the existence of the QGP phase and greatly pushed forward our understanding of its properties.

Finally with the recent arrival of the Large Hadron Collider (LHC) into the picture, TeV scale collision energies have been reached. This coupled with the next generation detectors at the LHC have made possible several precise measurements that can further improve the understanding of the properties of the QGP. At the LHC the colliding systems include Pb+Pb at $\sqrt{s_{\rm NN}} = 2.76$ TeV and p+Pb at $\sqrt{s_{\rm NN}} = 5.02$ TeV, the analysis of which is presented in this work.

1.1.1 A simple picture of heavy-ion collisions

In this section and the next, a simplistic view of heavy-ion collisions is presented. This was the picture at the beginning of RHIC experiments and has evolved considerably since then. However a chronological approach that shows how the understanding of heavy-ion collisions developed in the last decade sets the stage more appropriately for the measurements presented here.

---

[4] $\sqrt{s_{\rm NN}}$ is the sum of energy per nucleon of the first nucleus and energy per nucleon of the second nucleus, in the center of mass frame of the colliding nuclei.

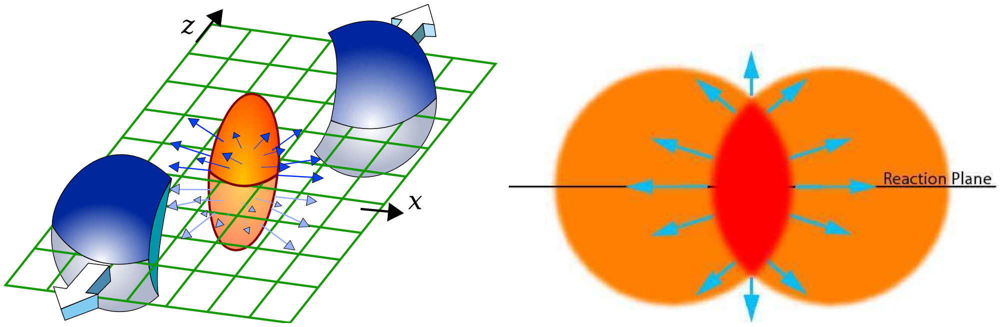

Figure 1.3: Simplified description of the geometry for a heavy-ion collision.

Figure 1.3 shows a schematic description of the geometry in a heavy-ion collision. The beam-axis i.e. the initial direction of motion of the nuclei is taken to be the z-direction. The plane formed by the beam axis and the vector connecting the centers of the two nuclei is called the **reaction plane**. The impact parameter b_{imp} is defined as the distance between the centres of the two colliding nuclei in the transverse (i.e. x-y) plane. Not all the nucleons participate in a collision, the number of "participating nucleons" is called as N_{part} while the number of non-participating "spectator nucleons" is called as N_{spec}. The total number of binary nucleon-nucleon collisions is called N_{coll}. Events with smaller b_{imp} i.e. more overlap between colliding nuclei, and thus having larger N_{part} are called central collisions and with larger b_{imp} (and correspondingly smaller N_{part}) are called peripheral collisions. Experimentally centrality is measured by the multiplicity or transverse energy in a particular sub-detector and then defined in percentile classes. For example events in "(0-5)% centrality class" consists of the 5% of all events having the highest multiplicity (or E_{T}) while "(90-100)% centrality class" consists of 10% of all events with the lowest multiplicity. The experimentally measured centrality values are then related to theoretical quantities such as the N_{part} and b_{imp} by some model dependent parameterizations. Typically the sub-detector used to determine the centrality classes is different than those used in the physics analysis, this minimizes artificial auto-correlations.

The initial overlap geometry between the colliding nuclei has an elliptical shape (Fig. 1.3) and can be characterized by its eccentricity given by [9, 10]:

$$\epsilon = \frac{\langle y^2 \rangle - \langle x^2 \rangle}{\langle y^2 \rangle + \langle x^2 \rangle} \tag{1.1}$$

where, x and y are the transverse positions of the participating nucleons about the center of mass, with the x-axis along the reaction plane, and the averaging is done over all participating nucleons.

1.1.2 Time evolution of ultra-relativistic heavy-ion collisions

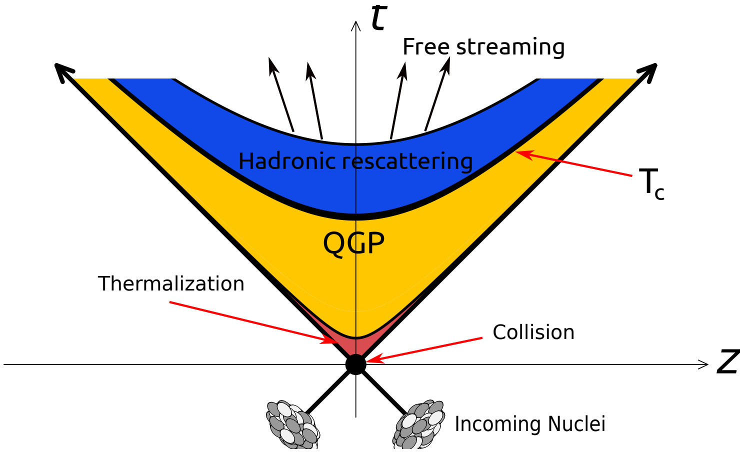

Figure 1.4: Schematic diagram representing the different stages of a heavy-ion collision. The horizontal axis represents the beam-axis (z-axis), while the vertical axis represents time. Figure adapted from [11].

The ultra-relativistic heavy-ion collisions (henceforth called heavy-ion collisions) go through several successive stages before the final produced particles are measured. The various expected stages are shown schematically in Fig. 1.4 and can be roughly categorized as the following:

1. Incoming nuclei: these are Lorentz contracted by large factors in the lab frame. For example, in the Pb+Pb collisions at $\sqrt{s_{\mathrm{NN}}}$=2.76 TeV at the LHC, the energy per nucleon is $\sqrt{s_{\mathrm{NN}}}/2 = 1.38$ TeV which corresponds to a Lorentz factor $\gamma \sim 1400$. In other words, the nuclei are contracted by a factor of ~ 1400 along the beam direction. Thus they look like pancakes rather than spheres.

2. Collision : the time-scales of collisions are related to the momentum transfer Q as[5] $t \sim 1/Q$. Thus all the hard scatterings that produce high p_{T} jets, heavy quarks and vector bosons takes place at the initial

---

[5] This follows from the uncertainty principle.

stages of the collision ($t \lesssim 0.2$ fm). This is followed by the production of softer particles with $p_{\mathrm{T}} \sim \mathcal{O}(1)$ GeV. This is when most of the entropy (multiplicity) is produced in the collision.

3. Thermalization : The produced matter is initially not in thermal equilibrium. However the produced partons interact among themselves and reach local thermal equilibrium fairly quickly. The data suggests that the thermalization is reached by $t \sim 1$ fm [12, 13].

4. QGP: The thermalized QGP is produced which expands outward due to the large pressure difference inside the matter and the vacuum outside. These pressure gradients are anisotropic, due to the elliptic nature of the average overlap geometry between the colliding nuclei as well as because of fluctuations in the initial energy distribution, resulting in the expansion being asymmetric. This stage of the collision has been shown to be very well described by relativistic hydrodynamics with a very small shear-viscosity to entropy-density ratio[6] η/s [14–16]. While the bulk medium expands, the hard scattered partons produced in the very initial stages of the collision traverse through it, exhibiting strong energy loss and getting "quenched". This phenomena discovered at RHIC is commonly termed as "jet-quenching" [17–22].

5. Hadronic rescattering: As the QGP expands and cools down, the transition (or crossover) to a hadron-gas phase takes place. In this stage, the temperatures are low enough to fix the relative chemical abundances of the various species, however the densities are still large enough for the produced particles to continue scattering among themselves, i.e. chemical equilibrium is not maintained but kinetic equilibrium is. Throughout this stage the matter continues to expand and cool down.

6. Free streaming: Finally the particles are sufficiently separated to be treated as free particles. They stream freely to the detector.

1.1.3 Properties of QGP measured at RHIC

As explained in the last section, the asymmetry in the initial geometry gets mapped into anisotropies in the final distributions of the particles. The average initial geometry is elliptic with the strongest pressure gradients along the reaction-plane (minor axis in Fig 1.3). Thus the expansion is strongest along this direction and the final azimuthal distributions of the particles have

---

[6] The symbol η is used to describe both shear-viscosity as well as pseudorapidity.

the largest density along this "in-plane" direction and lowest density perpendicular to it. Starting from this elliptic overlap geometry, it is reasonable to parameterize the final distributions of particles as:

$$\frac{dN}{d\phi} \propto 1 + 2v_2 \cos 2(\phi - \Phi) + 2v_4 \cos 4(\phi - \Phi) + \ldots \tag{1.2}$$

where, $v_n = \langle \cos n(\phi - \Phi) \rangle$ and Φ is the azimuthal direction with the maximum particle yield. The v_n are commonly called flow harmonics to signify that they develop due to hydrodynamic expansion, in particular v_2 is called elliptic flow harmonic. Since the overlap region is elliptical and the final distribution of particles must have the symmetries of the initial geometry, only even harmonics of the form v_{2n} are present in the final distribution. Furthermore in this situation, Φ coincides with the minor axis of the elliptic overlap region (i.e. the reaction-plane). However, as will be shown later, this simple picture is not the actual case. The parameter v_2 is called the "elliptic flow" parameter and is expected to be largest among the v_{2n} due to the elliptic shape of the overlap geometry.

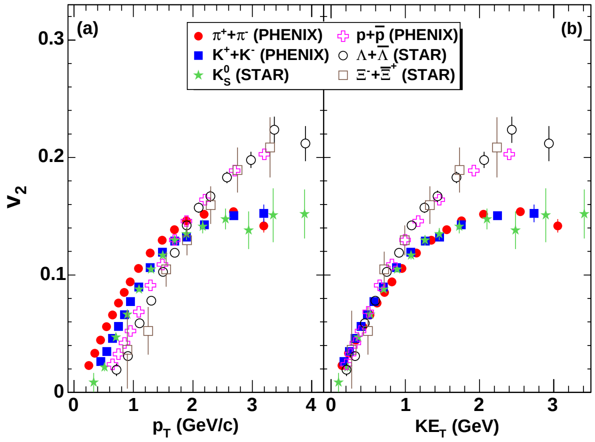

Figure 1.5: Elliptic flow as a function of p_T and KE_T measured at RHIC for three meson and three baryon species. Figure taken from [23].

The presence of large elliptic flow in Au+Au and Cu+Cu collisions was one of the major discoveries at RHIC [24–27]. Figure 1.5 shows the v_2 as a function of transverse momentum $p_\mathrm{T} = \sqrt{p_x^2 + p_y^2}$ and transverse kinetic energy $KE_\mathrm{T} = \sqrt{m^2 + p_\mathrm{T}^2}$ for several particle species measured at RHIC [23]. The v_2 values values become as large as 0.2 at intermediate p_T of ~ 3 GeV. Note that a v_2 of 0.2 implies the particle yield in the in-plane direction is larger than in the out of plane direction by a factor of $(1+2\times0.2)/(1-2\times0.2)\sim2.3$, and indicates a large modulation in the particle yields.

The large v_2 values measured at RHIC were supportive of using hydrodynamics in describing the expansion, as the p_{T} and KE_{T} dependence of the v_2 and its ordering for the various species was well reproduced by hydrodynamic calculations [28]. Further the hydrodynamic calculations indicated a very low η/s values of the QGP. The larger the shear-viscosity, the more the initial anisotropy get dissipated as the system expands and consequently smaller the v_2. Theoretical calculations that relate the eccentricities in the initial state to the anisotropies in the final state [15, 16, 29] indicate that the η/s in the QGP produced at RHIC could be as small as the quantum lower bound of $\hbar/4\pi k_{\mathrm{B}}$ [30, 31][7]. Figure 1.6 shows such comparisons [29] of viscous hydrodynamics calculations to minimum-bias STAR data for $v_2(p_{\mathrm{T}})$ of charged hadrons [32]. The left plot shows the hydrodynamic calculations done starting from a Glauber model initial conditions [33], which best describe the data for η/s=0.08, while the right plot shows similar calculations starting from a CGC initial conditions [34] which best describe the data for η/s=0.16. While there is a factor of two difference from the two initial geometry models on the "best" value of η/s, however both of them indicate that η/s is very small. Thus while the precise value of η/s cannot be determined from the v_2 measurements, but it is fairly certain that it cannot be more than an order of magnitude larger than the conjectured lower bound of $1/4\pi$. The applicability of hydrodynamics in describing the v_2 data was also indicative of early thermalization times of the medium [12, 13].

Large v_2 values for a variety of hadron species, having large and small cross-sections, indicated that flow developed at a partonic stage. For example, the ϕ meson is expected to have a small hadronic cross-section, as compared to other hadrons [35]. Thus if flow originated in a hadronic phase, the ϕ meson would have a much smaller v_2 than the other hadrons (p,π). Large v_2 for the ϕ meson measured at RHIC [36] thus provided compelling evidence of flow developing in a partonic phase.

The second important property of the QGP discovered at RHIC was its opaqueness to high p_{T} particles passing thought it. Figure 1.7 shows the ratio of spectra of several particle species observed in Au+Au collisions at RHIC to those expected from elementary superimposition of proton-proton collisions at the same $\sqrt{s_{\mathrm{NN}}}$. This quantity is called the nuclear modification-factor or R_{AA}[8]. It is seen that the high-p_{T} spectra for baryons and mesons is strongly suppressed in heavy-ion collisions w.r.t. to the p-p reference, however

---

[7] In natural units where $\hbar$=1 and k_{B}=1 this becomes $1/4\pi\approx0.08$.

[8] The subscript 'AA' in R_{AA} signifies that this is the modification in Au+Au collisions.

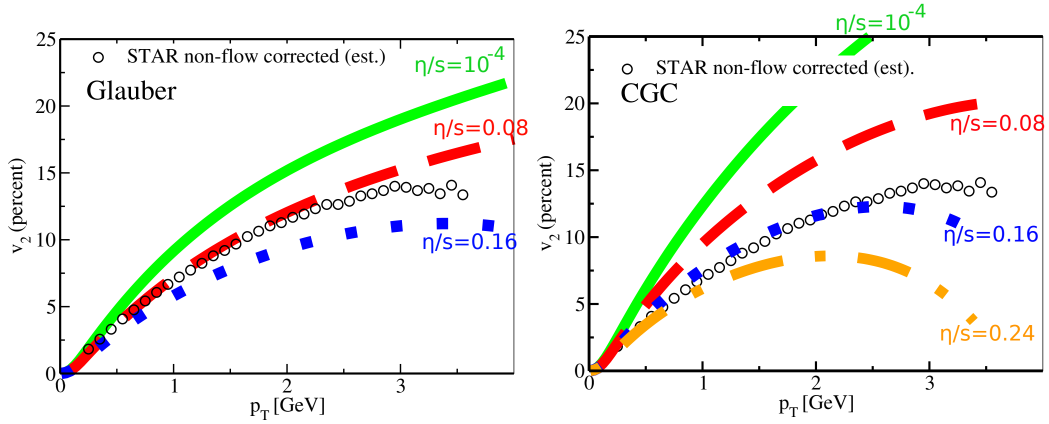

Figure 1.6: Comparison of hydrodynamic models to experimental data on charged hadron minimum bias elliptic flow by STAR [32]. Figure taken from [29].

no such suppression is seen for direct photons which do not interact with the QGP (being color neutral). These measurements gave further support for the production of QGP at RHIC.

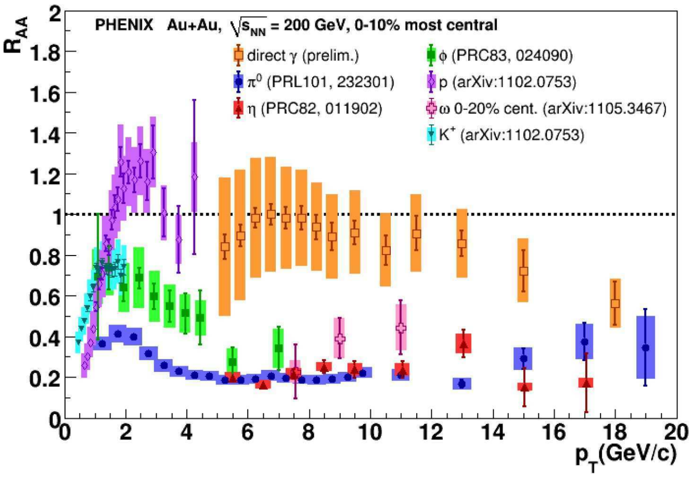

Figure 1.7: Left Plot: R_{AA} for several identified particle species in (0-10)% central 200 GeV Au+Au collisions [37–41].

1.2 Role of fluctuations in the initial geometry

If the nuclear overlap region were smooth as shown in the left plot of Fig. 1.9, it would imply that only even order flow harmonics would be present in the final particle distributions. However, the initial geometry is made up from a finite number of participating nucleons whose positions can fluctuate considerably event-by-event [42] leading to fluctuations in the collision geometry.

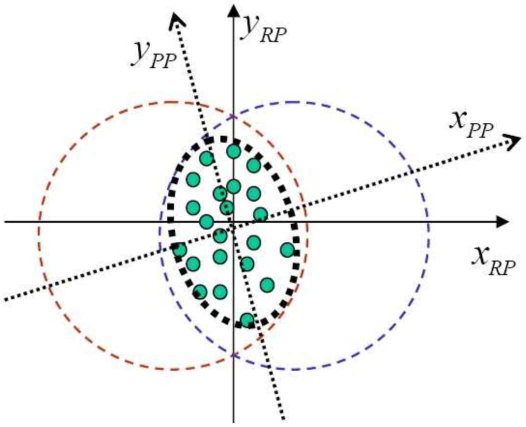

Figure 1.8: Schematic diagram showing fluctuations in the initial geometry lead to a "participant eccentricity" that is not necessarily oriented along the reaction plane. Figure taken from [43].

The idea of the presence of such fluctuations came after elliptic flow measurements in Cu+Cu collisions at RHIC in 2005 showed the presence of a fairly large v_2 even in most central collisions [9]. Prior to these measurements it was expected that the v_2 in Cu+Cu collisions would be much smaller due to a smaller system size. These measurements could only be explained after accounting for the presence of sizable fluctuations in the configuration of participating nucleons. This resulted in the concept of "participant eccentricity" where the eccentricity ϵ_{part} was defined using the configuration of the participating nucleons as shown in Fig. 1.8 rather than along the impact parameter as [44]:

$$\begin{aligned} \epsilon_{\text{part}} &= \frac{\sqrt{(\langle y^2\rangle - \langle x^2\rangle)^2 + \langle 2xy\rangle^2}}{\langle y^2\rangle + \langle x^2\rangle} = \frac{\sqrt{\langle r^2\cos 2\phi\rangle^2 + \langle r^2 \sin 2\phi\rangle^2}}{\langle r^2\rangle} \\ \tan(2\Phi^*_{\text{part}}) &= \frac{\langle 2xy\rangle}{\langle y^2\rangle - \langle x^2\rangle} = \frac{\langle r^2\sin 2\phi\rangle}{\langle r^2\cos 2\phi\rangle} \qquad (1.3) \end{aligned}$$

where r and ϕ refer to the transverse positions of the participating nucleons in radial coordinates (about the center of mass) and x and y have the same meaning as in Eq. 1.1. Φ^*_{part} gives the orientation of the participant-eccentricity plane (x_{pp} in Fig. 1.8) which could in general be different than the reaction plane. The idea behind the participant eccentricity was that while the mean eccentricity, given by Eq. 1.1 can be relatively small, but the participant eccentricity Eq. 1.3 which drives the flow can be large due to fluctuations in the positions of the participating nucleons.

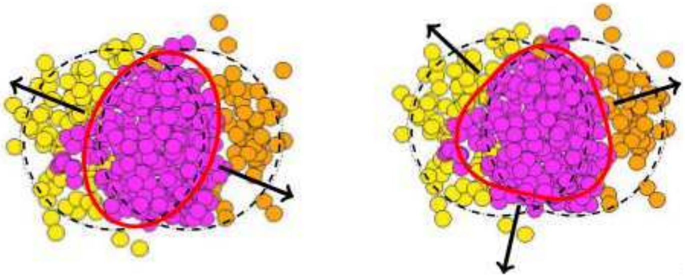

Figure 1.9: Schematic diagram showing fluctuations in the initial geometry due to finite number of participating nucleons. The fluctuations lead to Φ'_2 being different than the impact parameter and also a triangular asymmetry. Figure taken from [11].

Another breakthrough idea came in 2010, when it was realized that these fluctuations could result in the production of odd order eccentricities in the initial geometry [42, 45] each with its own orientation as shown schematically in Fig. 1.9. The moments of n^{th} order are a generalization of Eq. 1.3, their magnitude and orientation are given by [46, 47]:

$$\begin{aligned} \epsilon_n &= \frac{\sqrt{\langle r^n \cos n\phi\rangle^2 + \langle r^n \sin n\phi\rangle^2}}{\langle r^n\rangle} \\ \tan(n\Phi^*_n) &= \frac{\langle r^n \sin n\phi\rangle}{\langle r^n \cos n\phi\rangle} \qquad (1.4) \\ \Phi'_n &= \Phi^*_n + \pi/n \end{aligned}$$

The Φ^*_n (Φ'_n) point along the major (minor) axes of the n^{th} order eccentricity and have a n-fold degeneracy[9]. The presence of multiple orders of eccentricities ϵ_n in the initial geometry, as well as that each moment can have an independent orientation implies that Eq. 1.2 must be generalized to [45]:

---

[9] Denoting the major and minor axes by Φ^*_n and Φ'_n is not universally used notation.

$$\frac{dN}{d\phi} \propto 1 + 2\sum_{n=1}^{\infty} v_n \cos n(\phi - \Phi_n) \tag{1.5}$$

where the possibility of all harmonics v_n each with a different phase Φ_n, commonly called the n^{th}-order **event-planes**, is allowed.

This realization of the presence of fluctuations and their influence on the v_n caused a paradigm shift in the theoretical and experimental flow analyses. Firstly they implied that v_3 and higher order flow harmonics should be present in the final particle yields and thus measurable, providing additional constraints on η/s.

The fluctuations also imply that no two heavy-ion collisions, even if they have the same N_{part} or b_{imp}, are identical, as the fluctuations produce event-by event variations in the initial density. Since then a variety of experimental methods that are sensitive to fluctuations, such as multi-particle cumulants [48] and Lee-Yang Zeroes [49], have come to the forefront of flow measurements[10]. Similarly on the theoretical side event-by-event hydrodynamical simulations have replaced the older method of using single-shot hydrodynamics over averaged initial conditions. These event-by-event hydro simulations have been shown to have different spectra and v_n values as compared to the single-shot calculations [50–52], and thus point out the importance of measuring the flow fluctuations.

1.3 Motivation and outline of this work

It was against in the backdrop of these developments, i.e. the realization of the important role of fluctuations, that the first Pb+Pb run at the LHC took place and consequently the work presented in this thesis began. This work involves investigation of the properties of the initial geometry produced in heavy-ion collisions – with an emphasis on the fluctuations – and equally importantly, the study of nature of the hydrodynamic response to the initial geometry. This is achieved by detailed measurements of the anisotropies v_n as well as their fluctuations using a variety of experimental techniques.

In Chapters 3 and 4 measurements of the p_{T}, η and centrality dependence of the harmonics $v_2 - v_6$ using two different methods: the event-plane method and the two-particle correlation method are presented. The v_n values can

---

[10] These methods were initially developed to study effects of non-flow correlations on the v_n measurements, but they are also sensitive to flow fluctuations, and consequently are being used for these studies.

constrain η/s. As shown in Fig. 1.6, the main reason why η/s could not be constrained precisely from v_2 measurements alone was due to the large uncertainty in the initial geometry. However the measurements of multiple orders of flow harmonics, which have to be reproduced for the same η/s can not only constrain η/s, but also the initial geometry. In fact it has been shown that the higher the order of a harmonic, the easier it is for it to be damped out by viscous effects during the hydrodynamic expansion [53]. This is demonstrated in Fig. 1.10, where the final energy density distributions starting from the same initial state but evolved with ideal and viscous hydrodynamics are compared. It is seen that the viscous evolution leads to a smoother distribution with the finer structures (i.e. higher order moments) getting washed out. Thus the higher order harmonics are more sensitive to η/s and can strongly constrain it. The measurements of v_n for $n \geq 3$ presented here are among the first measurements of odd order harmonics in heavy-ion collisions.

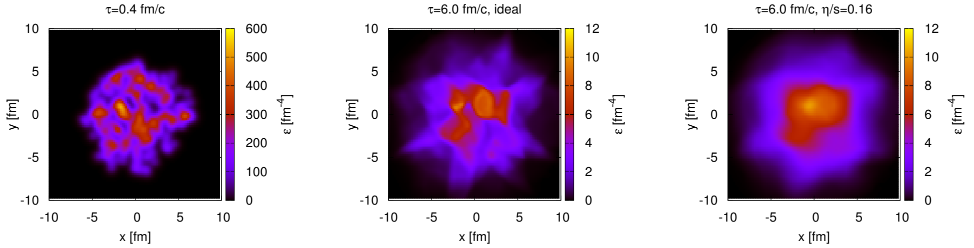

Figure 1.10: Effect of finite shear-viscosity in smoothing out initial anisotropies. The left panel shows the initial energy density in the transverse plane for an event with $b_{\text{imp}} = 2.4$ fm. The middle panel and right panels show this initial condition evolved via ideal and viscous hydrodynamics (η/s=0.16) respectively. Figure taken from [50].

The event-by-event fluctuations in the initial geometry, apart from generating odd harmonics, also lead to event-by-event fluctuations in the v_n values themselves. In Chapter 5, these fluctuations are studied by measuring the event-by-event distributions of the harmonics v_2–v_4. For the lower order harmonics (n=2,3) hydrodynamic calculations have shown that the v_n are strongly correlated to the ϵ_n in the initial geometry [47, 52]. Thus measurements of the event-by-event distributions of the v_n give a clear insight into the nature of the fluctuations. The measurements will be shown to not only be able to test models used to describe initial geometry, but at the same time get an understanding of the hydrodynamic response of the medium.

In Chapter 6, the correlations between event-planes Φ_n of different orders are studied. These correlations can arise from correlations between the eccentricities in the initial geometry. For example, in the limit of linear hydrodynamic response (i.e. $v_n \propto \epsilon_n$) correlations between the magnitude and orientation of ϵ_2 and ϵ_4 in the initial geometry can produce correlations between Φ_2 and Φ_4 in the final state. An alternative mechanism that can produce correlations between the Φ_n is non-linear hydrodynamic response to the eccentricities in the initial geometry [47]. For example v_4 can be generated from non-linear hydrodynamic response to ϵ_2. To leading order the non-linear response is [47]:

$$v_4 \propto \epsilon_2^2 \tag{1.6}$$

Such non-linear response can also lead to correlations between Φ_4 and Φ_2. It will be shown that from the correlations themselves it is possible to determine the mechanism–i.e. initial-state correlations between ϵ_n or non-linear response to the ϵ_n–that leads to the correlations. The linear and non-linear responses are affected differently by viscous effects, and thus these measurements can provide additional constraints on η/s. The event-by-event v_n measurements and the event-plane correlation measurements are the first of their kind in heavy-ion physics.

Typically global anisotropies in the particle distributions are expected in heavy-ion collisions where collective behavior is expected due to the production of a bulk medium. The CMS collaboration recently showed that long range correlations exist in between particle-pairs in *p*-*p* collisions with sufficiently large multiplicities [54], suggesting the possibility of bulk dynamics or initial state nuclear effects similar to those seen in heavy-ion collisions in much smaller systems. In Chapter 7 such long range correlations in *p*+Pb collisions are investigated. Comparing the strength of these long-range correlations to the ones in Pb+Pb can shed light on how they switch on with increasing system-size and multiplicity.

In each chapter the experimental results are compared to theoretical calculations, demonstrating how these measurements can constrain the initial geometry and the properties of the hydrodynamic response.

Chapter 2

The ATLAS detector and trigger

2.0.1 The Large Hadron Collider

The Large Hadron Collider (LHC) [55] is the world's largest and highest energy particle accelerator. It is situated on the French-Swiss border and operated by the European Organization for Nuclear Research (CERN). It can accelerate and collide protons at a center of mass energy of up to 14 TeV and Pb ions at up to 5.5 TeV per nucleon pair. As of August 2013, the LHC has achieved collision energies of 8 TeV in p-p, 2.76 TeV per nucleon pair in Pb+Pb and 5.02 TeV per nucleon pair in p+Pb collisions.

The LHC beam-pipe is 27 km long and located approximately 100 m underground. It contains two counter-propagating beams containing bunches of protons or ions that cross each other at four points, called Interaction Points (IP), where the collisions take place. At these crossing points the four LHC detectors: ATLAS, CMS, ALICE and LHCb are located. The bending power for the beams is provided by 1232 superconducting dipole magnets, each 15m long and capable of generating 8.3 T magnetic fields. Furthermore, quadrupole magnets focus the beam, and accelerating cavities compensate for energy losses and keep the bunches at a constant energy.

Figure 2.1 shows the sequence that Pb ions go through before being injected into the LHC. Starting from the LINAC3, the Pb ions go through the following sequence LINAC3 → LEIR → PS → SPS → LHC, with the energy being ramped up at each stage as shown in Fig. 2.1.

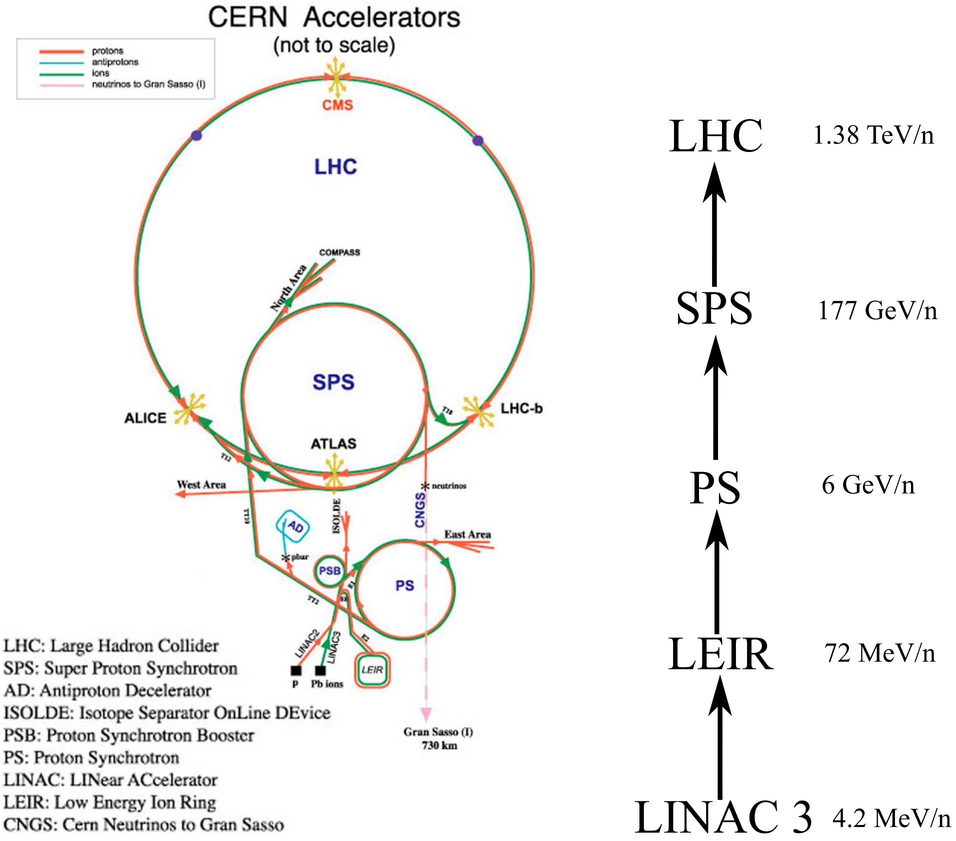

Figure 2.1: The CERN Accelerator complex. The energy/nucleon of the Pb ions at the end of each stage are shown.

2.1 The ATLAS detector and trigger

ATLAS (A Toroidal LHC ApparatuS) is a multi purpose detector located at Point-1 of the LHC cavern. While mainly designed to study *p*-*p* collisions, its fine granularity and large acceptance makes it an ideal detector for studying Pb+Pb and *p*+Pb collisions as well. Figure 2.2 shows the main subsystems of the ATLAS detector along with the solenoid and toroid magnets. The detector is nominally forward-backward symmetric, and covers 2π in azimuth. The ATLAS sub-systems and their design performance are comprehensively described in [56], here only the sub-systems that are use in this work are described. They include the Inner Detector (ID), the Electromagnetic Calorimeters and the Forward Calorimeter (FCal), as well as the following two detectors that are used for triggering on the events: Minimum-Bias Trigger Scintillators (MBTS) and the Zero-Degree Calorimeter (ZDC).

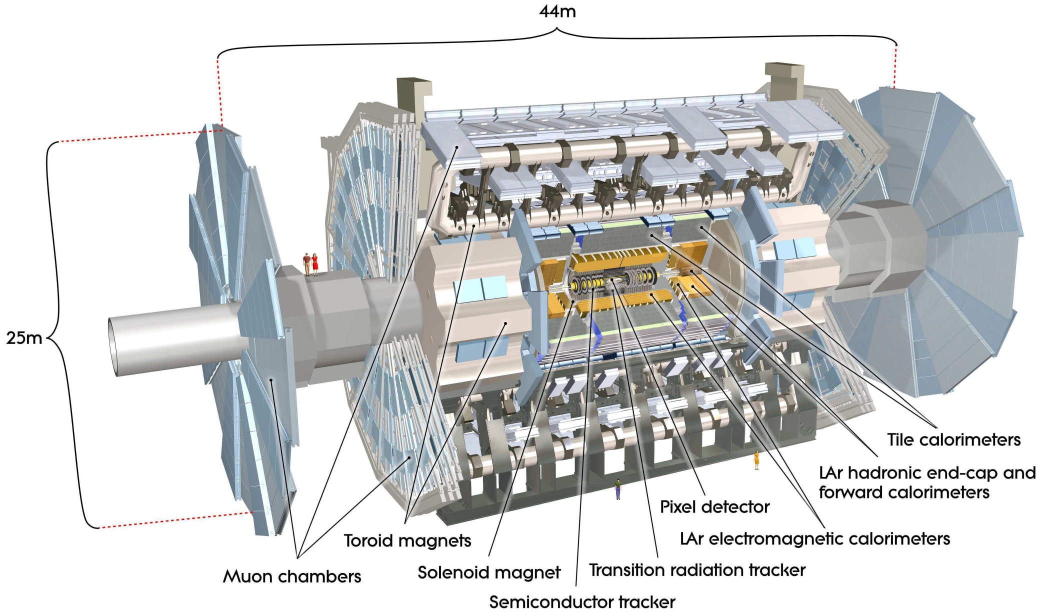

Figure 2.2: Main subsystems of the ATLAS detector.

2.1.1 Inner Detector

The ID occupies a cylindrical volume around the detector center spanning[1] $\pm 3512\,\text{mm}$ in the z direction and $1150\,\text{mm}$ in radius. It is immersed in a 2T magnetic field generated by the solenoid magnet and is used for reconstructing charged tracks and consequently for their momentum and vertex measurements. The ID consists of three independent sub-detectors, they are the pixel, silicon-microstrip (SCT) and the transition radiation tracker (TRT) which provide space-point measurements for charged-track reconstruction. Each of the three sub-detectors is divided into barrel (detector layers parallel to the beam pipe) and an end-cap modules (detector layers perpendicular to beam-pipe). The Pixel and SCT detectors are high-resolution, precision tracking detectors and cover the region $|\eta| < 2.5$, while the TRT covers $|\eta| < 2$. Figure 2.3 shows a cut-away view of the ID showing the three sub-detectors. Figure 2.4 shows the dimensions of the various sub-detectors and the typical detector layers that 10 tracks at various η traverse.

---

[1] ATLAS uses a right-handed coordinate system with its origin at the nominal IP in the center of the detector and the z-axis along the beam-pipe. The x-axis points from the IP to the center of the LHC ring, and the y-axis points upward. Cylindrical coordinates (r,ϕ) are used in the transverse plane, ϕ being the azimuthal angle around the beam-pipe. The

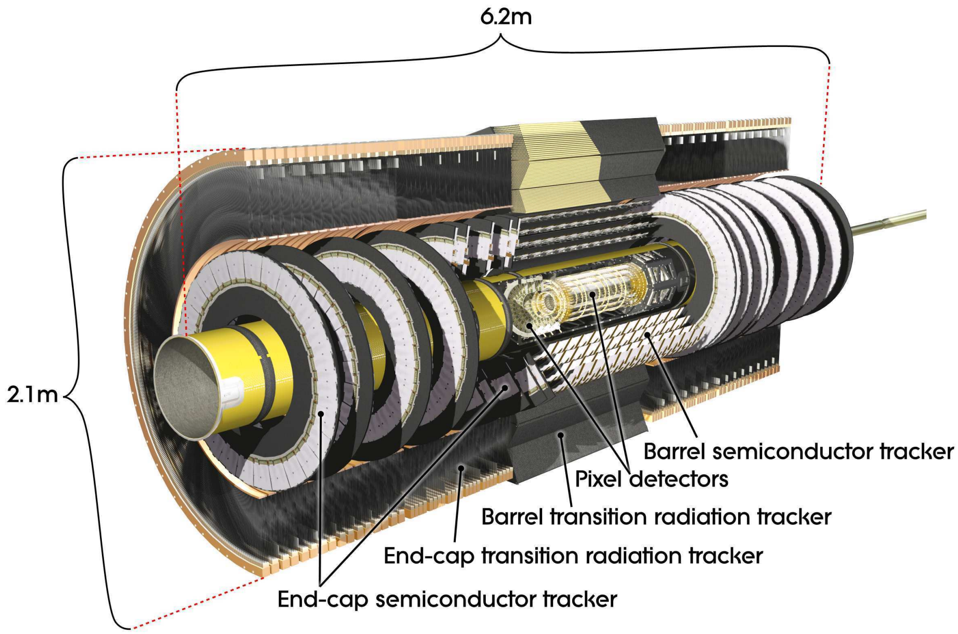

Figure 2.3: Cut-away view of the ATLAS inner detector.

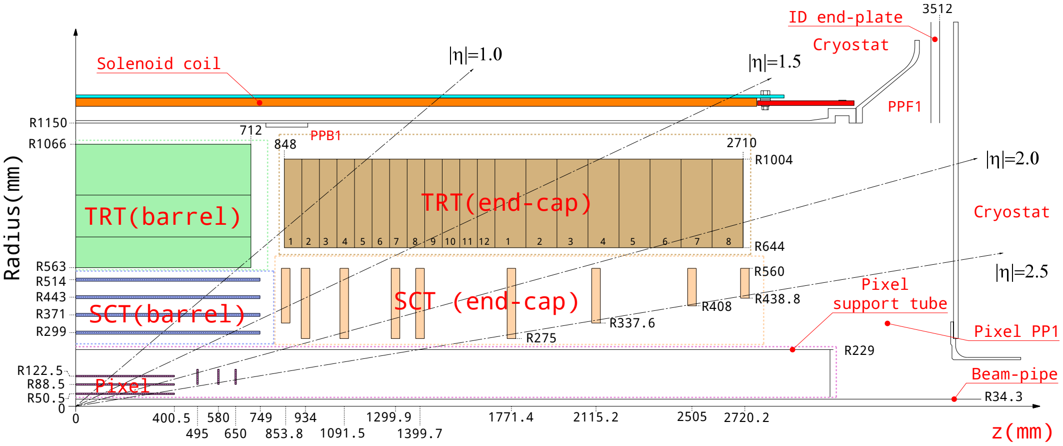

Figure 2.4: Quarter-section of the ATLAS inner detector showing the major detector elements along with their dimensions. Also shown are the typical number of detector elements that tracks at different η have to cross.

---

pseudorapidity is defined in terms of the polar angle θ as $\eta = \ln(\tan(\theta/2))$.

Pixel

The pixel detector has three layers in the barrel and three on either side in the end-cap region. It consists of 1744 identical modules, each having 47232 pixels of nominal[2] size $50 \times 400\,\mu\text{m}^2$ for a total of approximately 80.4 million readout channels. This extremely fine granularity is needed in the pixel detector due to its proximity to the interaction point. The first layer of pixels (called called B-layer) is only at a distance of 5 cm from the center of the beam pipe. The intrinsic accuracies for the pixel detector in the barrel are $10\,\mu$m in R-ϕ and $115\,\mu$m in z and in the end-cap are $10\,\mu$m in R-ϕ and $115\,\mu$m in R. A typical track crosses at least three pixel layers.

SCT

The SCT comprises of four cylindrical layers in the barrel region and nine discs on either side in the end-cap region. In the barrel region, this detector uses small-angle (40 mrad) stereo strips to measure both coordinates, with one set of strips in each layer parallel to the beam direction, measuring R-ϕ. They consist of two 6.4 cm long daisy-chained sensors with a strip pitch of $80\,\mu$m. In the end-cap region, the detectors have a set of strips running radially and a set of stereo strips at an angle of 40 mrad. The mean pitch of the strips is also approximately $80\,\mu$m. The total number of readout channels in the SCT is approximately 6.3 million. The intrinsic accuracy per module in the barrel is $17\,\mu$m in R-ϕ and $580\,\mu$m in z and in the end-cap is $17\,\mu$m in R-ϕ and $580\,\mu$m in R.

TRT

The TRT comprises of many layers of straw tube elements filled with a mixture of $\text{Xe}/\text{CO}_2/\text{O}_2$ gases, interleaved with transition radiation material. It is chiefly used for electron identification and provides only R-ϕ information for which it has an accuracy of $130\,\mu$m per straw. The TRT was not used in the heavy-ion running due to high occupancy in most central events which limited its use for tracking and electron identification. However it can be used for mid-central and peripheral events. The analyses presented here do not make use of the TRT hits information.

---

[2] About 10% of the pixels are $50 \times 600\,\mu\text{m}^2$ in size

2.1.2 Calorimeters

Figure 2.5 shows a schematic of the ATLAS calorimeters. The calorimeters have full azimuthal coverage over the range $|\eta| < 4.9$. They are sampling calorimeters with alternating layers of a dense absorber material to help initiate an electromagnetic or hadronic shower, and layers of an active material for detecting the shower. In the analyses done here, only the EM calorimeter and FCal are used.

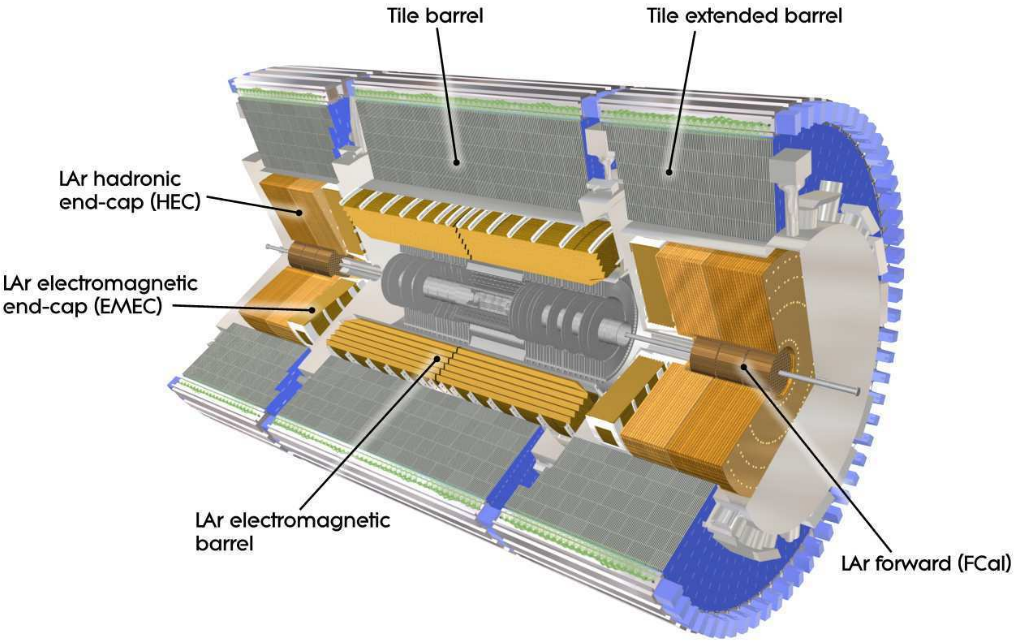

Figure 2.5: A schematic of the ATLAS calorimeters.

LAr electromagnetic calorimeter

The EM calorimeter in the innermost calorimeter. It is divided into a barrel (EMBr) for $\eta < 1.475$ and two end-cap components (EMEC) for $1.375 < |\eta| < 3.2$. It is a lead-LAr detector with accordion-shaped kapton electrodes immersed in LAr (which serves as the active material) and lead absorber plates. The accordion geometry provides complete ϕ symmetry without azimuthal cracks. In the barrel, the accordion waves are axial and run in ϕ, and the folding angles of the waves vary with radius to keep the liquid-argon gap constant. In the end-caps, the waves are parallel to the radial direction and run axially. Since the liquid-argon gap increases with radius in the end-caps, the wave amplitude and the folding angle of the absorbers and electrodes vary with radius. The calorimeter has two to three-longitudinal layers depending on the η, with varying degree of segmentations in $\Delta\eta \times \Delta\phi$ in the different layers. The EM calorimeters have finer granularity as compared to the other calorimeters especially over the region matched with the ID ($|\eta|$ <2.5) for precision measurements of electrons and photons. A pre-sampler is also present over the range $|\eta| < 1.8$ and is used to correct for the energy that electrons and photons lose upstream of the calorimeters. The EM calorimeters have finer granularity for precision measurements of electrons and photons, as compared to the other calorimeters. Figure 2.6 shows the $\Delta\eta \times \Delta\phi$ segmentation for the three layers of the EMBr at $\eta = 0$, as well as the accordion geometry of the calorimeter. The segmentations are projective in $\Delta\eta \times \Delta\phi$ throughout the EMBr and EMEC and is always smaller than or equal to 0.1×0.1.

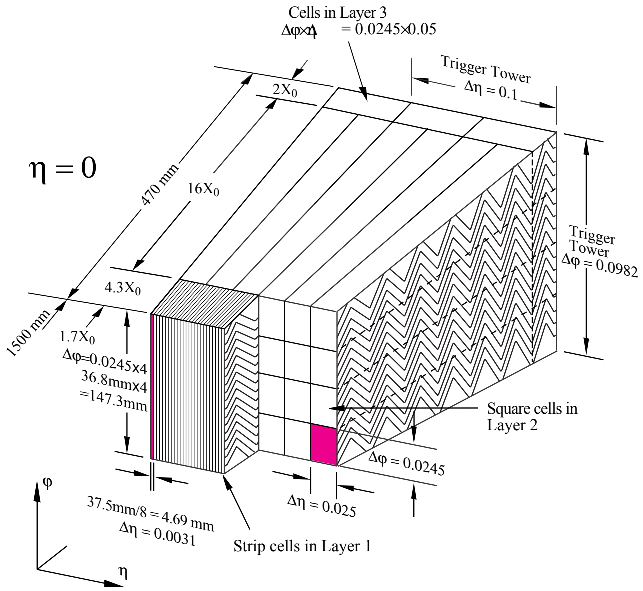

Figure 2.6: The $\Delta\eta\times\Delta\phi$ segmentation of the three layers of the EMBr at $\eta = 0$ (the presamler is not shown). The accordion structure of the EM calorimeters is also shown.

Forward calorimeters

The ATLAS FCal consists of three longitudinal modules (FCal1, fCal2 and FCal3) covering $3.2 < |\eta| < 4.9$ (Fig. 2.7). The first module is an electromagnetic-calorimeter while the last two are hadronic calorimeters. Copper is used as the

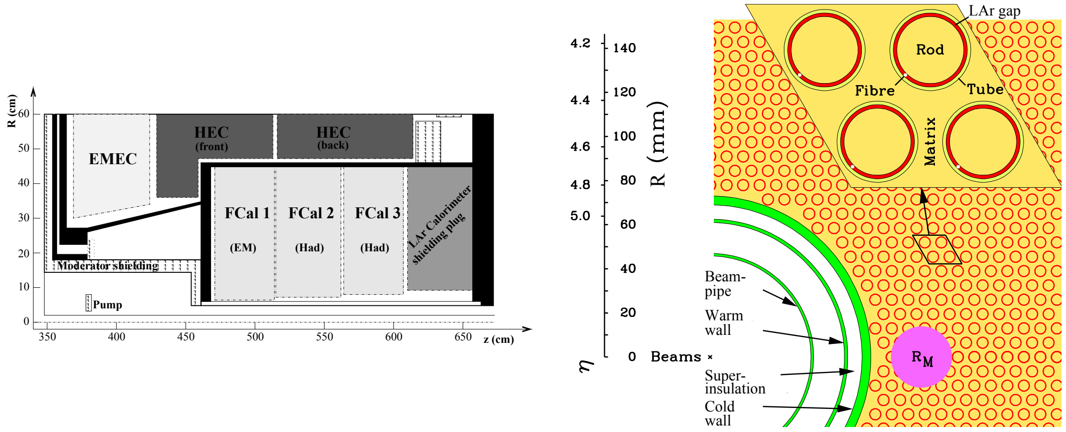

Figure 2.7: Left Plot: The positioning of the three layers of the FCal. Right Plot: A cross-section of the FCal1 (perpendiculat to beam-direction) showing the arrangement of the electrodes.

absorber for FCal1, while tungsten is used in FCal2 and FCal3. The FCal1 layer is made of copper plates stacked one behind the other with holes drilled in them through which the electrode structures are inserted. An electrode consists of a co-axial copper rod and copper tube separated by a precision, radiation-hard plastic fibre wound around the rod. The arrangement of electrodes and the effective Moliere radius for the modules can be seen in Fig. 2.7. The hadronic modules FCal2 and FCal3 consist of two copper end-plates, each 2.35 cm thick, which are spanned by electrode structures, similar to the ones used in FCal1, except for the use of tungsten rods instead of copper rods. The space between the end-plates and the tubes is filled with small tungsten slugs, maximizing the amount of tungsten in the modules and increasing the absorption length. Note that the FCal electrodes are placed parallel to the beam-pipe in a x-y grid as compared to the EMCal where the segmentations were projective in $\Delta\eta - \Delta\phi$.

In this work the fine $\Delta\eta - \Delta\phi$ segmentations of the calorimeters is not used. Instead, the smaller segmentations (cells) are combined to form towers having segmentation in $\Delta\eta \times \Delta\phi$ of 0.1×0.1. In regions were the segmentation of the calorimeter cells is larger than 0.1×0.1 (for example last layer of the tile barrel), the cell contributes to multiple towers with its energy divided between the towers. Similarly for the FCal where the segmentations are in x-y rather than in $\Delta\eta - \Delta\phi$, the x-y cells are combined to make towers of 0.1×0.1 in $\Delta\eta \times \Delta\phi$ with the energy of cells that span multiple towers divided between them. These calorimeter towers are used in the final analyses.

2.1.3 Trigger

The LHC can provide bunch-crossing rates of up to 40 MHz while ATLAS can record events at only a few 100 Hz. The ATLAS trigger system is designed to select interesting events worth recording while rejecting the rest to reduce the recording rate. The trigger system has three distinct levels: Level-1 (L1), Level-2 (L2), and the Event Filter (EF). L1 is purely hardware based, built using custom made electronics. L2 and EF are software based running on CPU farms and are together called the High Lever Triggers (HLT).

The L1 trigger typically searches for signatures such as high-p_{T} muons, electrons, photons, jets etc. It also selects more general events : so-called minimum-bias or zero-bias events, typically at very low rates. The L1 accept decision is made by the Central Trigger Processor (CTP). The L1 trigger also identifies Regions-of-Interest (ROI's) in $\eta - \phi$ that are then passed as seeds to the L2 algorithms if the event is accepted at L1. If accepted at L2, the event is then passed to the EF stage. The EF uses offline analysis procedures on fully-built events (i.e. it is not restricted to the L1 ROI's) to further reduce the event rates down to a few 100 Hz, which can be recorded for subsequent offline analysis. The latency times[3] for the L1, L2 and EF are $2.5\,\mu$s, 40 ms and 4 s respectively.

The event-rates for a particular trigger (at L1, L2 or EF) can be further reduced by applying prescales, which throw out a fraction of events that would otherwise be selected by that trigger. For example a prescale of 10 applied to a L2 trigger means at random 9 out of 10 events that pass this trigger are masked out at the L2 stage (and thus not passed to the EF).

In the Pb+Pb and p+Pb runs analyzed in this work, the luminosities were not high enough to require the HLT triggers to be run. Events were recorded based on a set of minimun-bias L1 triggers which were simply passed through the L2 and EF without prescales. The following two detectors were used in the Pb+Pb and p+Pb runs analyzed here:

2.1.4 Minimum bias trigger scintillators

The MBTS detector is one of the primary trigger detectors used in this analysis. It is positioned on the inner face of the end-cap calorimeter cryostat at $z = \pm 3560\,\mathrm{mm}$. Each side consists of 16 scintillator counters of 2 cm thickness each, organized into a disk perpendicular to the beam direction as shown in Fig. 2.8. Each disk is divided into an outer and an inner ring covering $2.09 < |\eta| < 2.82$ and $2.82 < |\eta| < 3.84$ respectively. Light emitted by each scintillator counter is collected by wavelength-shifting optical fibers and guided

---

[3] This is the time that it takes to make a decision on whether to keep the event or not.

to a photomultiplier tube (PMT). The PMT signals are read out by the Tile Calorimeter (TileCal) electronics. The MBTS signals, after being shaped and amplified by the TileCal electronics, are fed into leading edge discriminators and sent as 25 ns NIM pulses to the CTP. An MBTS hit is defined as a signal above a discriminator threshold. L1 trigger items are built from these hits of the form L1_MBTS_N, that indicate N hits in both sides combined, and L1_MBTS_N_N that indicate N hits on each side.

The MBTS detectors are also used for offline timing. For each of the 32 scintillators, the time difference between when the pulse is recorded in the detector and the time at which the bunches crosses the detector (obtained via the LHC clock) are measured. The mean time for each side of the MBTS is calculated as the average of the hit times of the scintillators on that side. For events occurring close to the center of the detector, the produced particles would reach the two sides of the MBTS almost simultaneously, and thus the MBTS timing on both sides should be roughly the same, whereas for non-collision backgrounds, collisions among satellite bunches, or beam-gas backgrounds, the timings are expected to be different. A cut on the time difference between the A and C sides : $|\Delta t_{\mathrm{MBTS}}|$ can thus be used to remove such events.

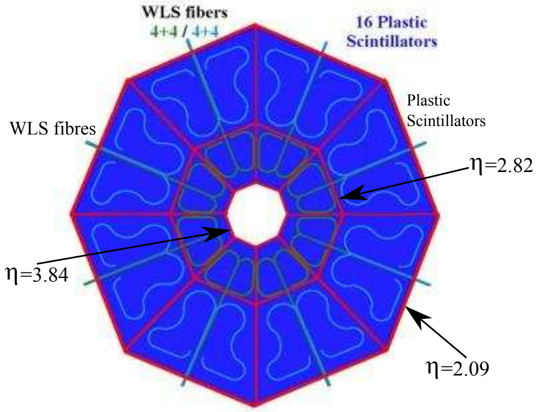

Figure 2.8: The ATLAS MBTS detector (one side only). The sixteen plastic scintillators are the trapezoidal regions (red boundary). The wave length shifting (WLS) fibres are also shown: green curves for inner disc and teal curves for outer disc.

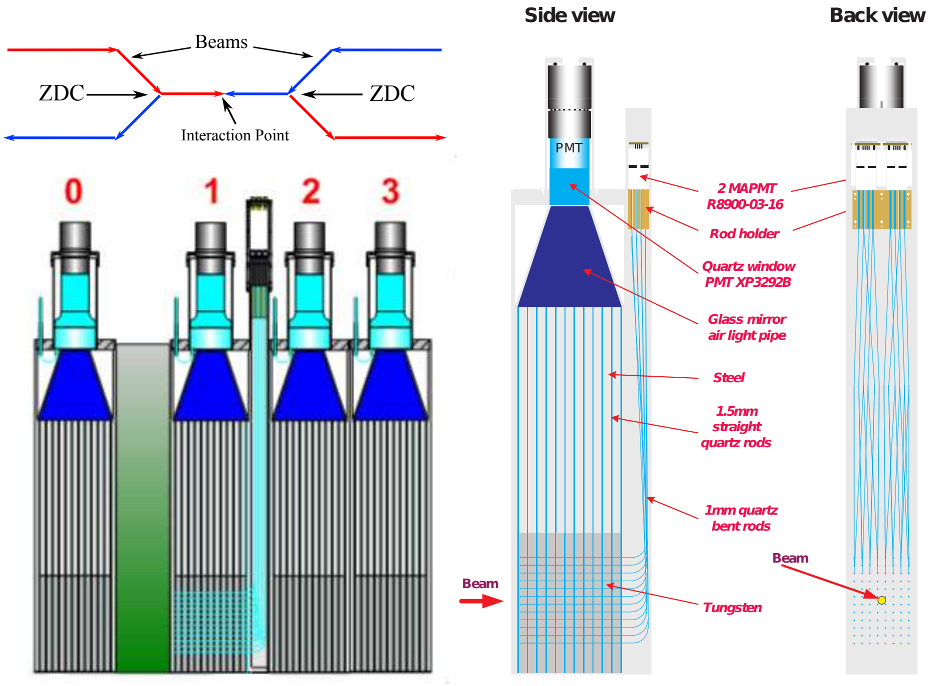

Figure 2.9: Left top: The location of the ZDC. Left Bottom: the four ZDC modules on the A-side. Right Plot: The details of a ZDC module.

2.1.5 Zero degree calorimeter

The zero degree calorimeter (ZDC) is located 140 m from the center of ATLAS on either side, after the beam-pipe splits into two, covering the region $|\eta| > 8.3$. It gets its name as it is located along the beam (i.e. at zero degrees). Only the neutral particles from the event manage to reach the ZDC as the charged particles are deflected away by the magnetic fields in the beam-pipe. Thus in Pb+Pb collisions the ZDC measures spectator neutrons. Each side of the ZDC consists of four modules as shown in the left bottom plot of Fig. 2.9. The detailed design of the modules is shown in the right panel of Fig. 2.9. Each module consists of 11 tungsten plates 10 mm thick in the beam direction and steel plates at the front and back (also 10 mm thick). Sandwiched between the plates are 1.5 mm diameter quartz rods that run vertically and are viewed by photomultiplier tubes (PMT) from above, via light-pipes. The quartz rods collect Cherenkov radiation from shower particles and guide them to the PMTs. Each PMT is read out by several channels of a Pre Processor Module (PPM). The PPMs are 64 channel, 40 MHz, 10 bit ADCs. The first two ZDC modules on the C side and the second module on the A side also have quartz rods arranged in an x-y grid along the beam-pipe. These can be used for position measurements of the showers. They were however not used in any of the analyses presented here.

The ZDC is primarily used in the Pb+Pb and in the p+Pb running as a minimum-bias trigger. The trigger decision for a side (A or C) is made based on whether or not the sum of the signals measured on all four modules on that side is above a certain threshold. These are defined as the L1_ZDC_A and L1_ZDC_C triggers, while the coincidence trigger L1_ZDC_AND requires both sides to be above a threshold. A software version of the coincidence trigger is also implemented by the CPT, called L1_ZDC_A_C, which is obtained by the logical AND of the L1_ZDC_A and L1_ZDC_C triggers.

2.2 Heavy-ion physics with the ATLAS detector

In this section the trigger requirements and the track selection cuts applied to the Pb+Pb and p+Pb data are described. Also the procedure for evaluating centrality and other event-parameters are diccussed.

2.2.1 Pb+Pb data taking

Event selections

The Pb+Pb analysis done in this work uses data taken during the 2010 Pb+Pb LHC run over the period Nov.6-Dec.6 and corresponds to an integrated luminosity of $7\,\mu\mathrm{b}^{-1}$. The ion beams were configured at an energy of 1.38 TeV per-nucleon, corresponding to a nucleonnucleon center-of-mass energy of $\sqrt{s_{\mathrm{NN}}}$=2.76 TeV for the Pb+Pb collisions. In order to select good events and reject non-collision backgrounds, the following trigger requirements and offline cuts are imposed on the events (these are the minimum bias cuts):

1. It must be from a running period with stable beams and detector conditions.

2. It must have a reconstructed vertex.

3. The event must pass at least one of the following triggers after prescale and veto:

    - L1_MBTS_N_N where N=1,2,3 or 4
    - L1_ZDC_AND

  - L1_ZDC_A_C

4. The event must pass L1_ZDC_AND or L1_ZDC_A_C triggers (before prescale). This was found to reject photo-nuclear events.

5. It must have good MBTS timing : $|\Delta t_{\mathrm{MBTS}}| < 3\,\mathrm{ns}$.

With the above selection criteria, approximately 50 Million events are obtained for the 2010 Pb+Pb run. An additional cut on the z position of the primary-vertex: z_{vtx} <150 mm is also applied. Events containing multiple collisions (pileup) are expected to be present at the 10^{-4} level and are negligible.

To determine the fraction of the total non-Coulomb inelastic cross section selected by the triggers, i.e. the trigger efficiency, a convolution of the FCal $\sum E_{\mathrm{T}}$ distributions[4] measured in proton-proton data at $\sqrt{s} = 2.76$ TeV is done with a Monte Carlo Glauber calculation [53] to reproduce the FCal $\sum E_{\mathrm{T}}$ distributions seen in the Pb+Pb events. The calculation assumes the number of effective proton-proton collisions per lead-lead event, N, scales according to the "two-component model" [57] with the number of participating nucleons (N_{part}) and the number of binary collisions (N_{coll}) as :

$$N = (1-x)N_{\mathrm{part}}/2 + xN_{\mathrm{coll}}. \tag{2.1}$$

where, the free parameter x controls the relative contribution of N_{part} and N_{coll}. The best description of the data is found to be for $x = 0.088$ (Fig. 2.10). The value of the trigger efficiency and its uncertainty is estimated by systematically varying the effect of trigger and event selection inefficiencies as well as backgrounds in the most peripheral FCal $\sum E_{\mathrm{T}}$ interval[5] to achieve the best agreement between the measured and simulated distributions. Using this analysis of the FCal E_{T} distribution, the trigger efficiency has been estimated to be $98 \pm 2\%$.

Centrality

The centrality classes[6] are then defined using the Fcal $\sum E_{\mathrm{T}}$ to categorize the event into percentiles. Figure 2.10 also shows the FCal $\sum E_{\mathrm{T}}$ thresholds corresponding to 10% wide centrality classes. The mean N_{part} values, are evaluated for the experimental centrality intervals by dividing the Glauber

---

[4] FCal $\sum E_{\mathrm{T}}$ is the sum of E_{T} measured in all cells of the FCal. The FCal E_{T} is stated at the electro-magnetic energy scale, which does not correct for the response of the calorimeter to hadrons.

[5] This was done by artificially injecting and removing counts in that interval.

[6] The trigger-efficiency and centrality determination are not part of this thesis work. The values are simply used in this analysis.

model $\sum E_{\mathrm{T}}$ distribution into the same percentile centralities, and evaluating the average number of participants in the Glauber MC events contributing to a given interval. These are listed in Table 2.1. The systematic errors on N_{part} are evaluated from the quoted uncertainty of the trigger efficiency and the known uncertainties in the Glauber model parameters.

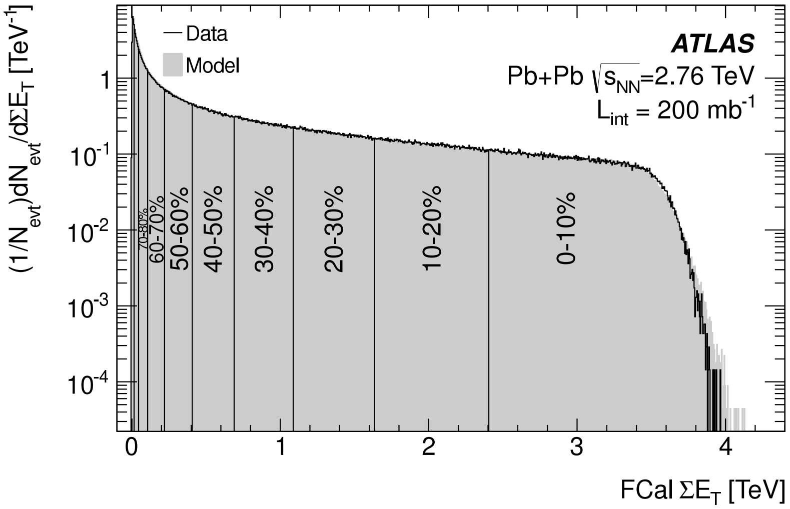

Figure 2.10: FCal $\sum E_{\mathrm{T}}$ distribution (black histogram) and the distribution obtained by convoluting the *p*-*p* data with Glauber MC (grey). The $\sum E_{\mathrm{T}}$ values corresponding to 10% wide centrality classes are also shown. This plot is made using a sub-set of the 2010 Pb+Pb data.

Centrality	0–1%	1–2%	2–3%	3–4%	4–5%
$\langle N_{\mathrm{part}} \rangle$	400.6 ± 1.3	392.6 ± 1.8	383.2 ± 2.1	372.6 ± 2.3	361.8 ± 2.5
Centrality	0–5%	5–10%	10–15%	15–20%	20–25%
$\langle N_{\mathrm{part}} \rangle$	382.2 ± 2.0	330.3 ± 3.0	281.9 ± 3.5	239.5 ± 3.8	202.6 ± 3.9
Centrality	25–30%	30–35%	35–40%	40–45%	45–50%
$\langle N_{\mathrm{part}} \rangle$	170.2 ± 4.0	141.7 ± 3.9	116.8 ± 3.8	95.0 ± 3.7	76.1 ± 3.5
Centrality	50–55%	55–60%	60–65%	65–70%	70–75%
$\langle N_{\mathrm{part}} \rangle$	59.9 ± 3.3	46.1 ± 3.0	34.7 ± 2.7	25.4 ± 2.3	18 ± 2

Table 2.1: $\langle N_{\mathrm{part}} \rangle$ for different centrality intervals, estimated from the Glauber model [58].

Track selections

To improve the reliability of the ID track reconstruction in the tracking environment in heavy ion collisions, the track quality requirements are more stringent than those used for proton-proton collisions [59]. Only tracks with $p_{\mathrm{T}} > 0.5$ GeV are used. The charged particle tracks are required to pass the following topological cuts :

1. It must have a hit in the B-layer if a hit is expected.
2. It must have at least one pixel hit and no pixel holes.
3. It must have at least 8 SCT hits and at most 1 SCT hole.

Apart from the above topological cuts, the following geometrical cuts are also applied on the reconstructed tracks:

1. $|d_0|$ w.r.t primary-vertex $< 1\,\mathrm{mm}$.
2. $|z_0 \times \sin(\theta)|$ w.r.t. primary-vertex $< 1\,\mathrm{mm}$.

where $d0$ w.r.t. primary-vertex and $z0\sin(\theta)$ w.r.t. to primary-vertex are the distance of the reconstructed track from the primary-vertex projected to the transverse plane (transverse to the beam axis) and along the beam axis respectively. The minimum bias p-p analysis applies 1.5 mm cuts on these variables. Due to the more stringent cuts, the tracking efficiency is lower than in p-p events. A detailed study of the tacking efficiency and fake rates for the heavy-ion data has been done in [60], although with slightly different cuts. Figure 2.11 shows the p_{T} η and centrality dependence of the tracking efficiency from that study. The efficiency drops with increasing $|\eta|$, largely due to loss from hadronic interactions with the detector material, which increases with $|\eta|$ [59]. The efficiency also decreases for more central events, due to the difficulty in track reconstruction in a high-multiplicity environment.

2.2.2 p+Pb data taking

In this work, analysis of proton-lead (p+Pb) data at $\sqrt{s_{\mathrm{NN}}} = 5.02$ TeV is also done. The data was recorded during a small 4 hour run on 13 September 2012 corresponding to an integrated luminosity of $1\,\mu\mathrm{b}^{-1}$. The LHC was configured with protons beams at 4 TeV and Pb ions at 1.57 TeV per-nucleon, corresponding to a nucleonnucleon center-of-mass energy of $\sqrt{s_{\mathrm{NN}}}$=5.02 TeV, and a rapidity shift of 0.47 relative to the ATLAS rest frame.

The following trigger and quality requirements are imposed on the events:

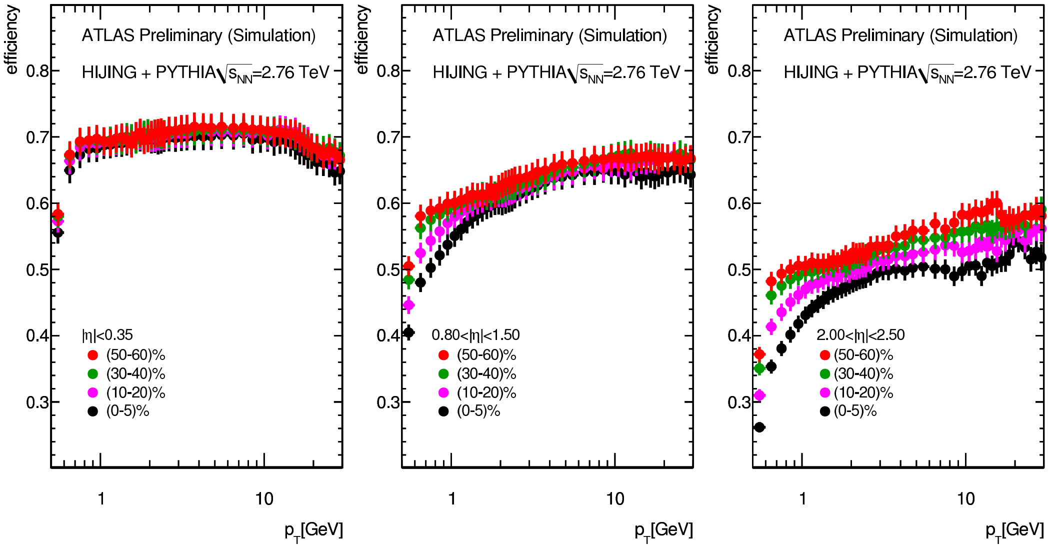

Figure 2.11: Tracking efficiency vs p_{T} for different centralities and η bins. These plots are taken from [60] and use slightly different cuts than the ones used here.

1. It must be from a running period with stable beams and detector conditions.
2. It must have a reconstructed vertex, containing at least two associated tracks, with its z position satisfying $|z_{\mathrm{vtx}}|$ <150 mm.
3. The event must pass the L1_MBTS_2 trigger
4. It must have good MBTS timing : $|\Delta t_{\mathrm{MBTS}}| < 10\,\mathrm{ns}$.

The pileup events are suppressed by rejecting events with more than one reconstructed vertex that are seperated in z by more than 15 mm. The residual plieup fraction is estimated to be $\leq 10^{-4}$.

The asymmetric nature of the p+Pb makes the estimation centrality percentiles tricky. Instead the events were categorized into event-activity classes, based on either the number of reconstructed charged-particle tracks with $p_{\mathrm{T}} >$ 0.4 GeV and $|\eta| < 2.5$ ($N_{\mathrm{ch}}^{\mathrm{rec}}$), or the FCal $\sum E_{\mathrm{T}}$ on the Pb going side ($\Sigma E_{\mathrm{T}}^{\mathrm{Pb}}$). Only the Pb going side FCal $\sum E_{\mathrm{T}}$ was used, as it was found to be correlated with the number of reconstructed tracks, while the p going side FCal $\sum E_{\mathrm{T}}$ showed such correlations only at low $N_{\mathrm{ch}}^{\mathrm{rec}}$. Tables 2.2-2.3 list the percentage of events in each event-activity class.

$N_{\mathrm{ch}}^{\mathrm{rec}}$ range	≥ 150	130-150	110-130	95-110	80-95	65-80
Percentage [%]	0.25	0.58	1.64	2.68	4.85	8.03
$\langle N_{\mathrm{ch}}^{\mathrm{rec}} \rangle$	165.6	137.8	118.0	101.3	86.3	71.4
$N_{\mathrm{ch}}^{\mathrm{rec}}$ range	50-65	40-50	30-40	20-30	10-20	< 10
Percentage [%]	12.08	10.45	12.33	14.07	16.10	16.93
$\langle N_{\mathrm{ch}}^{\mathrm{rec}} \rangle$	56.6	44.4	34.4	24.4	14.4	5.3
$N_{\mathrm{ch}}^{\mathrm{rec}}$ range	≥ 110	80-110	40-80	20-40	0-20	
Percentage [%]	2.478	7.53	30.56	26.40	33.03	
$\langle N_{\mathrm{ch}}^{\mathrm{rec}} \rangle$	128.2	91.7	56.4	29.1	9.7	

Table 2.2: A list of the $N_{\mathrm{ch}}^{\mathrm{rec}}$ based event activity classes, with the percentage of events, the average charged particle multiplicity $\langle N_{\mathrm{ch}}^{\mathrm{rec}} \rangle$ in each class.

$\Sigma E_{\mathrm{T}}^{\mathrm{Pb}}$ range [GeV]	> 110	95-110	80-95	65-80	55-65	45-55
Percentage [%]	0.21	0.45	1.24	3.11	3.99	6.37
$\langle \Sigma E_{\mathrm{T}}^{\mathrm{Pb}} \rangle$ [GeV]	122.4	101.2	86.4	71.4	59.6	49.7
$\Sigma E_{\mathrm{T}}^{\mathrm{Pb}}$ range [GeV]	35-45	25-35	20-25	15-20	10-15	< 10
Percentage [%]	9.71	13.80	8.67	10.11	11.98	30.36
$\langle \Sigma E_{\mathrm{T}}^{\mathrm{Pb}} \rangle$ [GeV]	39.7	29.7	22.4	17.4	12.4	4.9
$\Sigma E_{\mathrm{T}}^{\mathrm{Pb}}$ range [GeV]	> 80	55-80	25-55	< 20	< 25	
Percentage [%]	1.90	7.12	29.88	52.45	61.12	
$\langle \Sigma E_{\mathrm{T}}^{\mathrm{Pb}} \rangle$ [GeV]	94.4	64.8	37.3	9.0	11.0	

Table 2.3: A list of the $\Sigma E_{\mathrm{T}}^{\mathrm{Pb}}$ based event activity classes, with the percentage of events and the mean transverse energy, $\langle \Sigma E_{\mathrm{T}}^{\mathrm{Pb}} \rangle$ in each class.

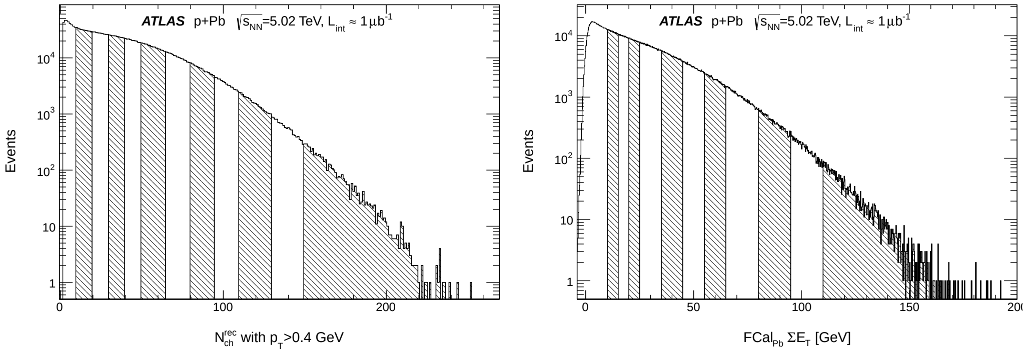

Figure 2.12: The distributions of $\mathrm{N}_{\mathrm{ch}}^{\mathrm{rec}}$ (left) and $\mathrm{FCal}_{\mathrm{Pb}} \sum E_{\mathrm{T}}$ (right), together with the 12 bins for event activity (Tables 2.2–2.3).

Track selections

Because the track multiplicity is much smaller than the heavy-ion runs, the tracking cuts are much weaker. In fact they are comparable to those used for proton-proton collisions [59]. The charged particle tracks are required to pass the following requirements:

1. It must have a hit in the B-layer if a hit is expected.
2. It must have at least one pixel hit.
3. It must have at least n SCT hits, where
    - $n = 2$ for $p_{\mathrm{T}} \in (100, 200)$ MeV
    - $n = 4$ for $p_{\mathrm{T}} \in (200, 300)$ MeV
    - $n = 6$ for $p_{\mathrm{T}} > 300$ MeV
4. $|d_0|$ w.r.t primary-vertex < 1 mm.
5. $|z_0 \times \sin(\theta)|$ w.r.t. primary-vertex $< 1\,\mathrm{mm}$.
6. The tracks are also required to pass the following significance cuts
    - $|d_0/\sigma_{d_0}| < 3$
    - $|z_0 \times \sin(\theta)/\sigma_{z_0 \times \sin(\theta)}| < 3$

    where, σ_{d_0} and $\sigma_{z_0 \times \sin(\theta)}$ are the significances of the d_0 w.r.t. primary-vertex and $z_0 \times \sin(\theta)$ w.r.t. primary-vertex measurements.

Chapter 3

Measurement of flow harmonics in Pb+Pb collisions via event-plane method

In this chapter, the measurements of flow harmonics v_2-v_6 using the event-plane (EP) method are presented. This method involves determining the orientation of the n^{th} order event-plane in an event using one detector and then measuring the distribution of particles (or E_{T}) about that plane using another detector to obtain the v_n. The measured event-planes denoted by Ψ_n, are in general different than the true event-planes Φ_n due to finite statistical precision. The distributions of particles about the Ψ_n, after being averaged over many events to increase statistical precision, are used to obtain the raw v_n values, which are then corrected by a factor termed **event-plane resolution** – which accounts for the difference between the Ψ_n and Φ_n [61, 62] – to obtain the true v_n values.

In section 3.1, the methodology of the EP method and how it is implemented in ATLAS is explained. In Sections 3.2 and 3.3 the two key steps in the EP method: the event-plane resolution and raw v_n measurements are described. In Section 3.4 the various sources of systematic errors and several cross-checks that were done in this analysis are discussed. Finally in Section 3.5 the results, which include the p_{T}, η and centrality dependence of the v_n are presented. The results are also compared to theoretical calculations that were published following these measurements. The theory comparisons demonstrate how these results can be used to constrain both η/s and to validate (or invalidate) initial geometry models. The measurements presented in this chapter have been published in [63].

3.1 Methodology

The n^{th} order event-plane of a event defines the global azimuthal anisotropy of particles in that event, thus, it can be estimated independently using detectors situated at different η. The large acceptance and fine segmentation of the ATLAS calorimeters allows for many independent ways to measure the EP. This analysis uses the FCal detector as the event-plane detector. As will be shown later, the FCal has good precision for determining harmonics planes for n=2-6, while minimizing any short-range correlations with the tracks from the ID, by virtue of the two being well separated in η.

Figure 3.1 illustrates the idea behind the EP method. The elongated blob represents the fireball, which is extended in the η direction. While the FCal and the ID are situated at different η, the azimuthal anisotropies that they observe, arise from the same collision geometry. Thus, the FCal $dE_{\mathrm{T}}/d\phi$ distribution in an event can be used to measure the orientation of the Ψ_n. Due to flow correlations the $dE_{\mathrm{T}}/d\phi$ distribution can be expressed as a Fourier series :

$$dE_{\mathrm{T}}/d\phi = Q_0 + 2\sum_{n=1}^{\text{inf}} |\overrightarrow{Q_n}| \cos n(\phi - \Psi_n) \tag{3.1}$$

where, the flow vector $\overrightarrow{Q_n}$ can be calculated by vectorially summing the E_{T} of the individual colorimeter towers.

$$\overrightarrow{Q_n} = (Q_{x,n}, Q_{y,n}) = (\sum_i E_{T,i} \cos n\phi_i, \sum_i E_{T,i} \sin n\phi_i) \tag{3.2}$$

The orientation of the Q vector gives the EP angle Ψ_n :

$$\Psi_n = \frac{1}{n}\tan^{-1}\left(\frac{Q_{y,n}}{Q_{x,n}}\right) = \frac{1}{n}\tan^{-1}\left(\frac{\Sigma\ E_T \sin(n\phi)}{\Sigma\ E_T \cos(n\phi)}\right) \tag{3.3}$$

Once the n^{th} order event-plane Ψ_n is determined, the raw harmonic coefficient v_n^{obs} is calculated by correlating with it the tracks from the ID:

$$v_n^{\text{obs}} = \langle \cos n(\phi_i - \Psi_n) \rangle. \tag{3.4}$$

where, $\langle ... \rangle$ implies averaging over tracks and events[1]. The v_n^{obs} is then corrected to account for the event-plane resolution Res$\{n\Psi_n\}$, given by [61](also see Appendix A.1.2):

---

[1] Thus by construction the EP method measures the v_n averaged over many events

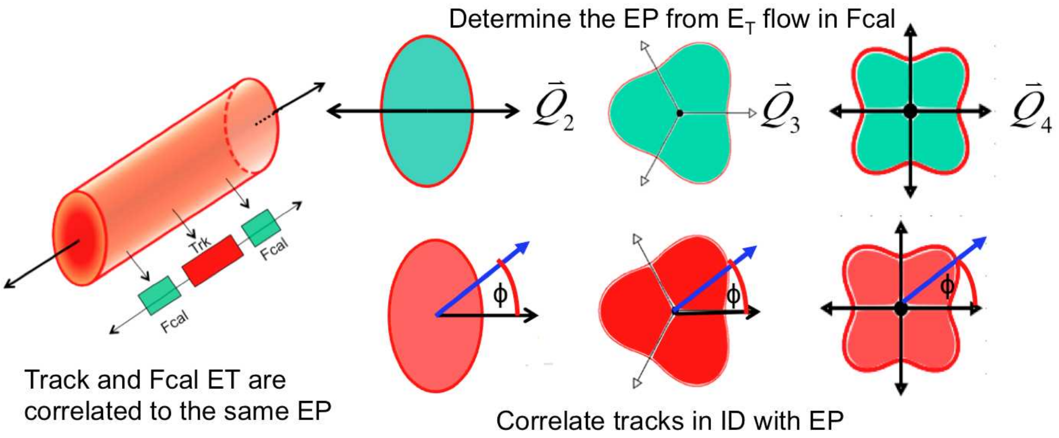

Figure 3.1: Schematic description of the event-plane method.

$$\mathrm{Res}\{n\Psi_n\} \quad = \quad \langle \cos\left(n(\Psi_n - \Phi_n)\right)\rangle. \tag{3.5}$$

which is determined using several independent methods (discussed later). The corrected v_n is obtained as:

$$v_n = \frac{v_n^{\mathrm{obs}}}{\mathrm{Res}\{n\Psi_n\}} = \frac{\langle \cos\left(n(\phi - \Psi_n)\right)\rangle}{\langle \cos\left(n(\Psi_n - \Phi_n)\right)\rangle}. \tag{3.6}$$

3.2 Event-plane resolution

3.2.1 Event-plane detector

The FCal detector was described in Section 2.1.2. For this analysis, only the first two layers are used, as the third layer contains little energy and is more susceptible to noise. Also the calorimeter towers are restricted to $|\eta| \in (3.3, 4.8)$, as the first η segment overlaps with the EM end-cap detector and thus has a considerably smaller signal, while the last η segment has significant non-uniformities.

Either of the two FCal sub-detectors, A-side and C-side (denoted as $\mathrm{FCal_P}$ and $\mathrm{FCal_N}$), as well as the full-FCal (A+C) can be used to determine the event-planes, albeit with different resolutions. In this analysis, two different, but complementary methods of measuring the v_n are employed. The first method calculates the raw harmonic flow v_n^{obs} by correlating tracks in $-2.5 <$

$\eta < 2.5$ with the EP measured by the combined FCal detector (**full-FCal** EP); followed by applying the correction for the full-FCal resolution. In the second method, tracks are correlated with the EP measured with the FCal in the opposite η side, i.e. tracks with $\eta > 0$ ($\eta < 0$) are correlated with the EP obtained from FCal_{N} (FCal_{P}), followed by applying the correction for the sub-FCal resolution. This method is denoted as **sub-FCal** EP and is illustrated in Fig. 3.2. In comparison with the full-FCal, the sub-FCal method considerably increases the η separation between the tracks and the EP detector ($\text{FCal}_{\text{P(N)}}$). The average gap is increased roughly from 3 units to 5 units in η. Thus the sub-FCal method is much less susceptible to non-flow correlations: correlations from jets, decays etc. that correlate a few particles but are typically localized in η. The sub-FCal method is especially useful for measuring the η dependence of the v_n. However, the disadvantage of the sub-FCal method is that the $\text{FCal}_{\text{P(N)}}$ have smaller EP resolutions as compared to the full-FCal, and can not measure the higher order harmonics with similar accuracy.

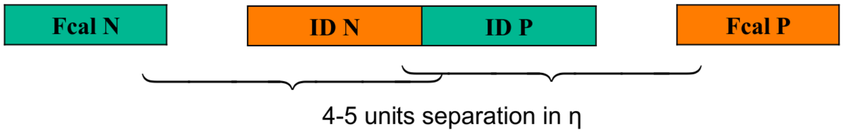

Figure 3.2: Illustration of the sub-FCal method. The tracks at positive η are correlated with FCal_{N} and those at negative η with FCal_{P}.

3.2.2 Detector calibration

The methodology discussed in Section 3.1 assumes an ideal event-plane detector, i.e. the azimuthal anisotropy in the FCal $dE_{\text{T}}/d\phi$ distribution is caused by the physical flow. In reality, detector effects such as dead areas, inefficiencies, mis-calibration etc., lead to false modulations of the $E_{\text{T}}(\phi)$ which affect the determination of the Ψ_n. Note that this is a detector effect and is different than the resolution $\text{Res}\{n\Psi_n\}$ which by definition, was statistical in origin. In order to account for detector effects a recentering-flattening technique [64, 65] is used, which is described in detail in Appendix A.1.4.

Figure 3.3 shows the normalized distributions for the orientation of the Ψ_n for n=2-4, both before and after the corrections are implemented. Since the orientation of the Φ_n (in the lab frame) changes randomly from one event to the next, the distributions for the Ψ_n are expected to be flat. However, it can be seen that the uncorrected Ψ_n distributions have modulations, signifying the presence detector effects. The recentering step corrects for most of the acceptance effects and the flattening step produces further minor improvements.

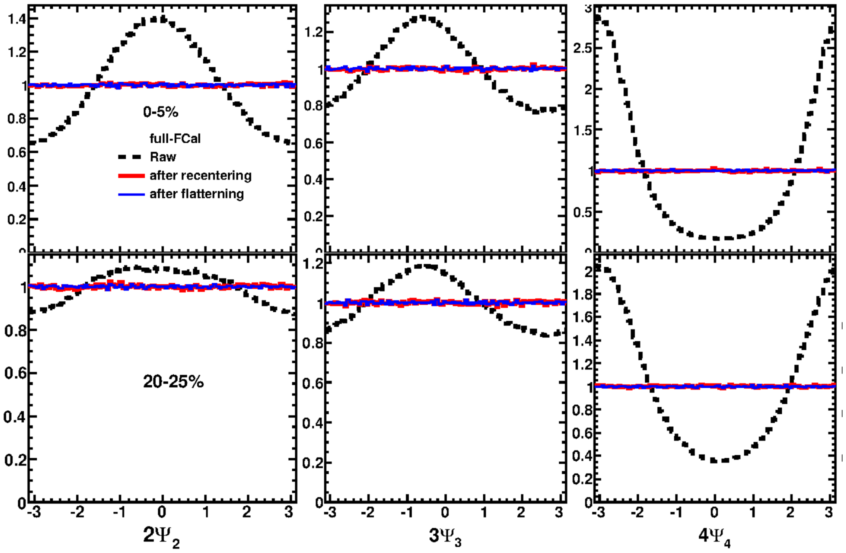

Figure 3.3: The effects of the calibration for Full-FCal detector from $n = 2$ to $n = 6$. A central bin (top) and mid-central bin (bottom) are used. It can be seen that most of the calibration arises from the re-centering step.

3.2.3 Methods for determining the event-plane resolution

In this section the methods used for determining the EP resolution are discussed. All the formulae used here are derived in Appendix A.1.3.

The resolution for a detector is related to the quality parameter χ [61] as[2] (Eq. A.14):

$$\mathrm{Res}\{n\Psi_n\} = \frac{\chi\sqrt{\pi}}{2} e^{-\frac{\chi^2}{2}} \left[I_0(\frac{\chi^2}{2}) + I_1(\frac{\chi^2}{2}) \right]. \tag{3.7}$$

The parameter χ is related to the multiplicity measured in the detector and the true v_n as

$$\chi \propto v_n \sqrt{N} \tag{3.8}$$

---

[2] This formula makes the assumption that the fluctuations that result in Ψ_n to be different than Φ_n are Gaussian fluctuations. See [62] (but with very different notation).

The χ can be obtained using the **two-subevent method** [61], where a detector is divided into two sub-detectors, such that the two sub-detectors have the same resolution. The $\mathrm{FCal_P}$ and $\mathrm{FCal_N}$ are such a division for the FCal. Since each sub-detector has half the acceptance as the full detector, the χ parameter of each detector is $\sqrt{2}$ times smaller than the χ of the full-detector (Eq. 3.8):

$$\chi_{\mathrm{sub}} = \chi_{\mathrm{full}}/\sqrt{2}. \tag{3.9}$$

Denoting the n^{th} order EP measured by the positive-side sub-detector as Ψ_n^{P} and by the negative-side sub-detector as Ψ_n^{N}, the distribution $\Delta\Psi_n = \Psi_n^{\mathrm{P}} - \Psi_n^{\mathrm{N}}$, is given in terms of χ_{sub} as [61] (Eq. A.16):

$$\frac{dN}{d(n\Delta\Psi_n)} = \frac{e^{-\chi_{\mathrm{sub}}^2}}{2}\left[\frac{2}{\pi}(1+\chi_{\mathrm{sub}}^2) + z(I_0(z)+L_0(z)) + \chi_{\mathrm{sub}}^2(I_1(z)+L_1(z))\right]. \tag{3.10}$$

Where, $z = \chi_{\mathrm{sub}}^2\cos(n\Delta\Psi_n)$, I_n is the modified Bessel function of the first kind and L_n is the modified Struve function. The χ_{sub} value can be obtained by fitting the measured $dN/d(n\Delta\Psi_n)$ distribution with Eq. 3.10. The sub-detector and full-detector resolutions can then be obtained by evaluating Eq. 3.7 at $\chi = \chi_{\mathrm{sub}}$ and $\chi = \chi_{\mathrm{full}}$ respectively.

The EP resolution for the sub-detector can also be directly calculated from the $dN/d(n\Delta\Psi_n)$ distribution as (Eq. A.20):

$$\mathrm{Res}\{n\Psi_n^{\mathrm{P(N)}}\} = \sqrt{\langle\cos(n[\Psi_n^{\mathrm{P}} - \Psi_n^{\mathrm{N}}])\rangle}, \tag{3.11}$$

This formula does not assume Eq. 3.7 (i.e. Gaussian fluctuations) to hold and can be directly used in the sub-FCal v_n analysis. However, for calculating the full-FCal resolution, starting from the resolution obtained via Eq. 3.11, the χ_{sub} value for the subevent is first calculated using Eq. 3.7. Then the full-FCal resolution is calculated evaluating into Eq. 3.7 at $\chi_{\mathrm{full}} = \sqrt{2}\chi_{\mathrm{sub}}$.

The two-subevent method has the disadvantage that it relies on the assumption that the two sub-detectors have the same resolution and also the validity of Eq. 3.7 (i.e. Gaussian fluctuations). A second method, known as **three-subevent method** [61] can be used to directly calculate $\mathrm{Res}\{n\Psi_n\}$ of a given detector A using the correlation of its estimated event-plane with those of two other reference detectors (B and C) sitting at different η windows,

$$\mathrm{Res}\{n\Psi_n^A\} = \sqrt{\frac{\langle\cos\left(n\left(\Psi_n^A - \Psi_n^B\right)\right)\rangle\langle\cos\left(n\left(\Psi_n^A - \Psi_n^C\right)\right)\rangle}{\langle\cos\left(n\left(\Psi_n^B - \Psi_n^C\right)\right)\rangle}} \tag{3.12}$$

The three-subevent method does not require the prior knowledge of χ, instead $\text{Res}\{n\Psi_n^A\}$ is obtained directly, which can then be used to calculate the χ (Eq. 3.7). A second advantage of the three-subevent method is that, for a given detector A, several different detectors B and C can be chosen, to get independent estimates of $\text{Res}\{n\Psi_n^A\}$. A drawback however, is that the precision with which $\text{Res}\{n\Psi_n^A\}$ can be determined depends on the reference detectors B and C. If the reference detectors have poor resolution, then the $\text{Res}\{n\Psi_n\}$ obtained will have large systematic errors.

The resolutions for the full-FCal and sub-FCal are measured using both the two-subevent and three-subevent methods. The two subevent method is used as the primary method for obtaining the FCal resolution, and a detailed study using the three-subevent method is done to estimate the systematic uncertainties.

3.2.4 Resolution from two-subevent method

Figure 3.4 shows the $n(\Psi_n^{\text{P}} - \Psi_n^{\text{N}})$ distributions for the FCal for n=2-6 for two different centralities. Also shown are the fits to the functional form in Eq. 3.10. The sub-FCal resolution can be calculated by using the χ_{sub} obtained from these fits in Eq. 3.7. It can also be calculated using Eq. 3.11, which can then be used to obtain χ_{sub} via Eq. 3.7. For the Full-FCal, starting with the χ_{sub} from either of the two methods, χ_{full} is calculated, and the resolution is obtained from Eq. 3.11.

Figure 3.5 and 3.6 show the ratio of the resolutions for n=2-4 obtained using these two slightly different approaches for the sub-FCal and full-FCal respectively. For n=2, a 0.5% (1%) systematic deviation is observed in mid-central collisions for the sub-FCal (full-FCal), with the fitting method giving a higher value, this can be attributed to the small deviations of the fit from the $2(\Psi_2^{\text{P}} - \Psi_2^{\text{N}})$ distributions that can be seen in Fig. 3.4. This difference is included in the final systematic errors for the resolution. For $n \geq 3$ the two methods give identical results.

3.2.5 Resolution from three-subevent methods

The large coverage of the ATLAS EMCal ($|\eta| < 3.2$) along with its fine segmentation, allows for a very flexible choice for the reference detectors for three-subevent measurements of the FCal EP resolution. Besides the EMCal, the tracking detectors can also be used as reference detectors. A large set of three-subevent measurements for measuring the FCal resolution are performed in this analysis. They are detailed in Appendix A.1.5. The resolutions are determined both for the full-FCal, as well as for the $\text{FCal}_{\text{P}}/\text{FCal}_{\text{N}}$ detectors.

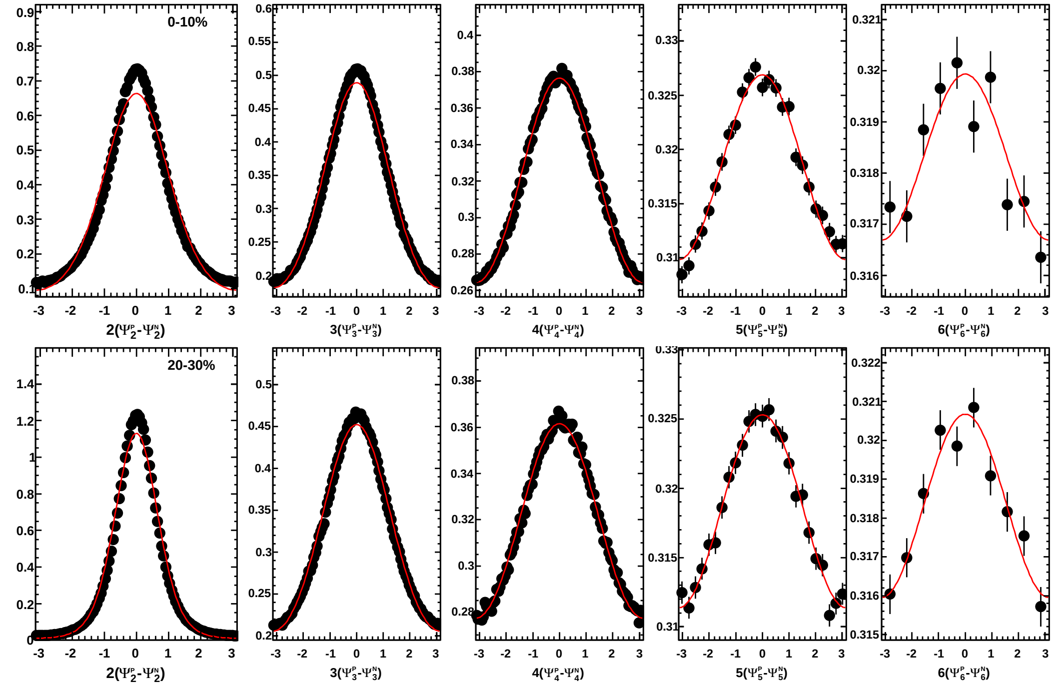

Figure 3.4: $(\Psi_n^{\mathrm{P}} - \Psi_n^{\mathrm{N}})$ distributions for FCal for the (0-10)% centrality interval (top rows) and the (20-30)% centrality interval (bottom rows) intervals. Also shown are the fits to the functional form in Eq. 3.10 used to obtain the value of χ_{sub}.

The variation in the resolutions from the two-subevent method are used as systematic errors on the resolutions and are listed in Table 3.1 as a fraction of the nominal resolution. The errors are chosen, such that they cover the systematics for both the full-FCal and sub-FCal. In general, the spread of these different estimates is less than 5% for n=2-4, 10% for n=5 and up to 30% for n=6. To account for the sizable systematic difference between the three and two-subevent methods for n=5 and 6, a 5% upward correction for n=5 and a 15% downward correction for n=6 are applied on the two-subevent resolutions. The size of the spread between the two and three-subevent methods is used to determine the centrality range over which the final results are presented. It is (0-80)% for v_2, (0-70)% for v_3 and v_4, and (0-50)% for v_5 and v_6, beyond which the systematic errors for the resolutions become too large to make reliable v_n measurements.

Figure 3.7 summarizes the Res$\{n\Psi_n\}$ and χ values together with the systematic errors for the full-FCal detector. Similar plots for the sub-FCal detector are shown in Fig. 3.8.

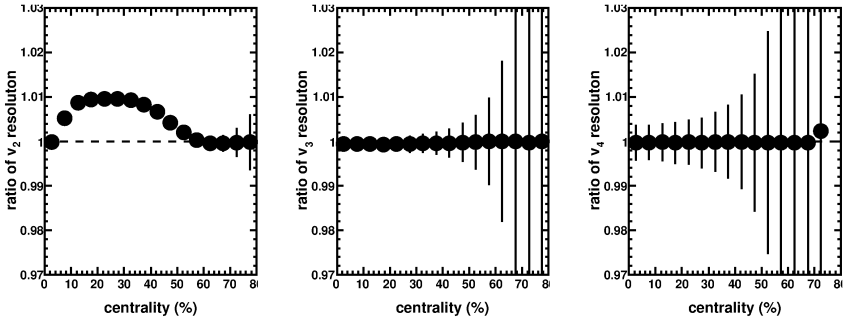

Figure 3.5: The ratio between the sub-FCal resolution obtained using two different methods: fitting the two subevent distribution, or calculating directly via Eq 3.11.

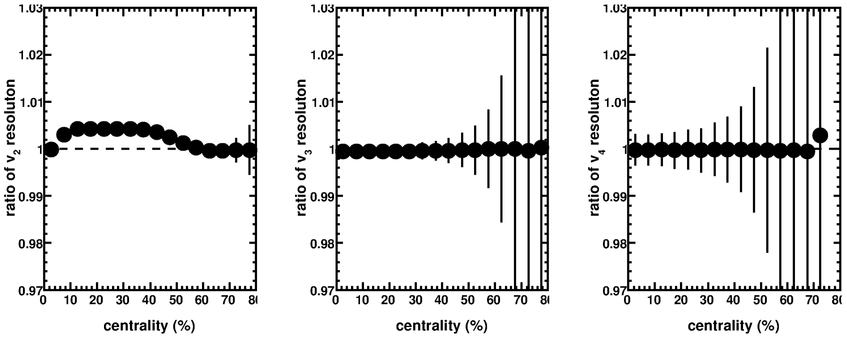

Figure 3.6: The ratio of the full-FCal resolution between the two methods used to obtain the full-FCal χ: fitting the two subevent distribution, or calculating via Eq 3.11.

One caveat of the EP method is that the same resolution correction is applied for all events in a centrality interval. In reality, the resolution is a function of χ (Eq. 3.7), which depends on both the true v_n and the multiplicity (i.e. the total E_{T} in the FCal). The multiplicity may or may not vary appreciably within a centrality interval, depending on the size of the interval. However, the v_n have large event-by-event fluctuations, as will be shown in Chapter 5. The EP results for the v_n are thus dependent of the value of the resolution. It has been shown that in the limit of large and small resolution the v_n^{EP} is [66, 67]:

$$v_n^{EP} = \begin{cases} \langle v_n \rangle & \mathrm{Res}\{n\Psi_n\} \to 1 \\ \langle \sqrt{v_n^2} \rangle & \mathrm{Res}\{n\Psi_n\} \to 0 \end{cases} \tag{3.13}$$

centrality	0-20%	20-40%	40-50%	50-70%	70-80%
n=2	0.05-0.02	0.015-0.01	0.015-0.02	0.03-0.04	0.04-0.06
n=3	0.03	0.03	0.03	0.03-0.05	
n=4	0.04	0.04	0.04	0.04-0.05	
n=5	0.1	0.1	0.1		
n=6	0.3	0.3	0.3		

Table 3.1: Summary of the systematic errors for the event-plane resolutions for both full-FCal and sub-FCal method. The values are expressed as a fraction of the nominal resolution.

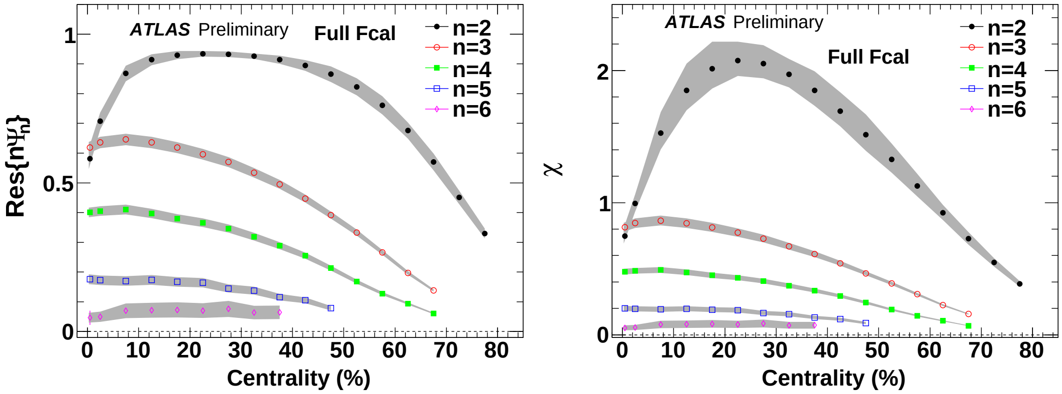

Figure 3.7: The final resolution (left) and χ (right) values for the full-FCal detector together with the systematic error band.

where, $\langle v_n \rangle$ and $\langle \sqrt{v_n^2} \rangle$ are the mean and r.m.s. of the v_n over all events in the centrality interval. Typically for $n \geq 3$ the low resolution limit is reached and the v_n^{EP} are close to the $\langle \sqrt{v_n^2} \rangle$ values. For v_2, this is true in central and peripheral events where the resolution is poor, while in mid-central events, an intermediate value between $\langle v_2 \rangle$ and $\langle \sqrt{v_2^2} \rangle$ is measured.

3.3 Determination of the raw v_n (v_n^{obs})

In this section, the measurements of the raw v_n (v_n^{obs}) are described. For each event, the estimated EP angle Ψ_n is determined using either $\mathrm{FCal}_{\mathrm{P(N)}}$ or the full-FCal. Then the tracks are binned in azimuthal angle relative to the Ψ_n: $\Delta\phi = \phi - \Psi_n$ to obtain the distribution $dN/d\,(n\Delta\phi)$. These distributions are then summed over all events in the desired centrality interval, but in intervals of track p_{T} and η. Note that the distribution is made in $n\Delta\phi$, rather than

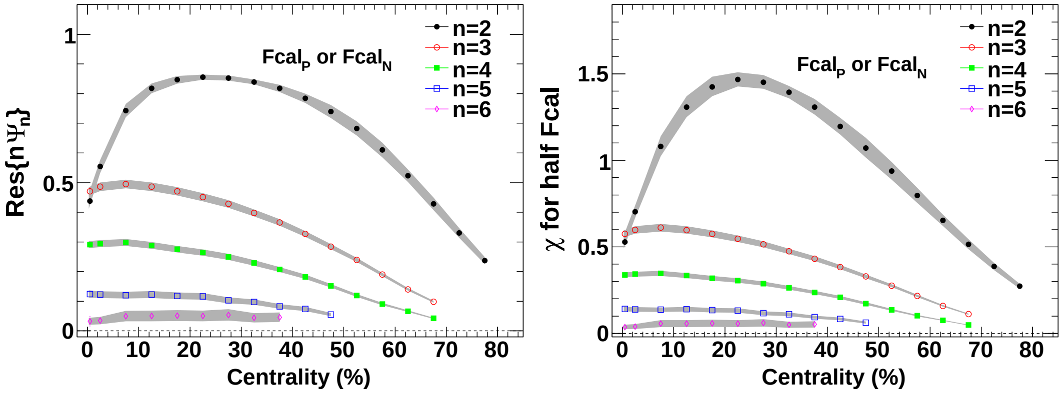

Figure 3.8: The final resolution (left) and χ (right) values for the sub-FCal detector together with the systematic error band.

in $\Delta\phi$ so that they are 2π periodic (rather than $2\pi/n$ periodic). Examples of such distributions for n=2-4 are shown in Fig. 3.9. The raw flow signals are the Fourier coefficients of these distributions:

$$dN/d(n\Delta\phi) = A(1 + 2v_n^{\mathrm{obs}} \cos n\Delta\phi + 2v_{2n}^{\mathrm{obs}} \cos 2n\Delta\phi + ..) \tag{3.14}$$

Note that higher order harmonic flow coefficients can appear at lower order event-planes due to physical correlations between planes of different orders. In general $(kn)^{\mathrm{th}}$ order flow can be measured in the n^{th} order plane, where $k = 1, 2, 3....$ The higher moments in a lower order plane are called mixed harmonics, and are not a topic of current study. They are directly related to the correlations between event-planes Φ_n and Φ_{kn} that are studied in Chapter 6, and their existence is worth pointing out.

The v_{kn} can be calculated directly from these distributions via a Discrete Fourier Transformation (DFT) as:

$$v_{kn}^{\mathrm{obs}} = \frac{\sum_{i=1}^{N} C_i \cos kn\Delta\phi_i}{\sum_{i=1}^{N} C_i}, k = 1, 2, 3.. \tag{3.15}$$

where, N is the number of $\Delta\phi$ bins, $\Delta\phi_i$ is the center of the i^{th} bin and C_i is the number of counts in the i^{th} bin. In this analysis $k = 1$ as only the n^{th} order harmonic in the n^{th} order plane is studied. The statistical error of v_n^{obs} can be calculated via a simple error propagation of Eq. 3.15 with k=1.

To see the contribution of the mixed harmonics to the $n\Delta\phi$ distributions, the expected distributions using the v_{kn} values obtained from the DFT are

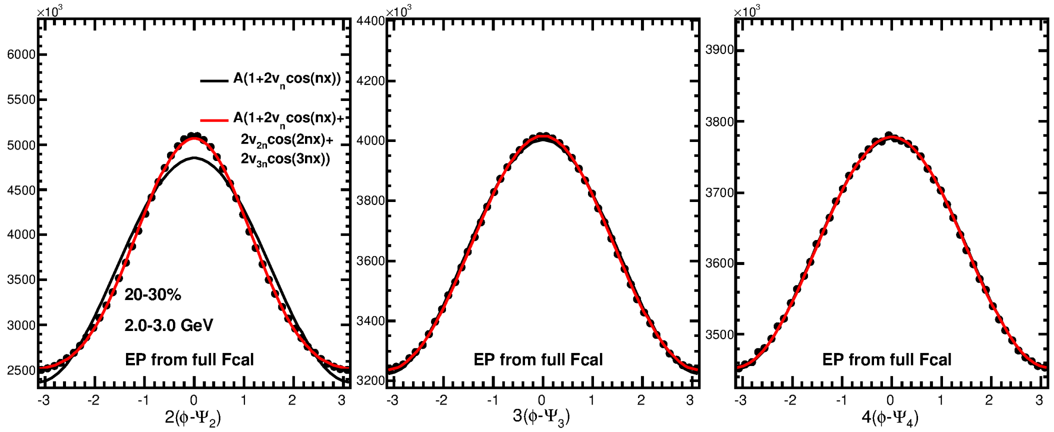

Figure 3.9: The azimuthal distribution of charged particles in 2-3 GeV relative to the Ψ_n determined by the full-FCal for events in the (20-30)% centrality interval.

calculated, but truncated to include only the first three harmonics. This is shown by the red line in Fig. 3.9, while the black line shows contribution of only the lowest order (k=1) term, i.e. only the v_n term in n^{th} harmonic plane. The presence of mixed harmonics in the 2^{nd} order EP is clearly seen. However, for the other planes, the mixed harmonics are not visible at the raw level.

3.3.1 Residual $\langle\sin\left(n(\phi-\Psi_n)\right)\rangle$ values in Ψ_n plane

The magnitude of residual detector effects that survive the recentering-flattening calibration procedure, and can lead to artificial correlations between the tracks and the measured EP, are estimated by calculating the sine component of the track distributions with respect to the EP:

$$s_n^{\text{obs}} = \langle\sin n(\phi - \Psi_n)\rangle. \tag{3.16}$$

In an ideal case, the track distributions about the event planes should be symmetric, and thus these s_n^{obs} terms should be zero. This residual sine term is quantified by taking its ratio to the observed cosine term (i.e. v_n^{obs}). The results of this check for the full-FCal are shown in Figs. 3.10 and 3.11 for (0-5)% and (20-30)% centrality intervals respectively. For the sub-FCal these ratios are almost identical. A small but significant sine signal for is seen whose strength relative to the v_n^{obs} is roughly independent of p_{T}, indicating that this is a residual effect of the EP determination that affects all particles identically. No obvious centrality dependence is seen for these terms. Conservatively estimating, the magnitudes of these terms are within 0.5%, 1%, 2% and 4% for n=2, 3, 4, and 5 respectively, and are always negative. For n=6, the shift is significantly larger and positive with an average value of about 10% of v_n^{obs}. These sine terms are considered as systematic errors for the v_n^{obs}.

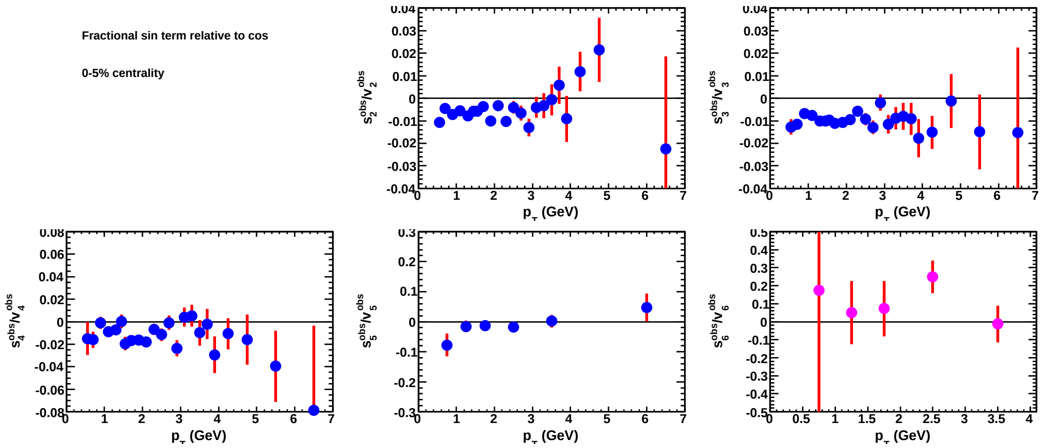

Figure 3.10: The ratio of raw observed sine term (s_n^{obs}) to the cosine term (v_n^{obs}) as function of p_{T} for the (0-5)% centrality interval.

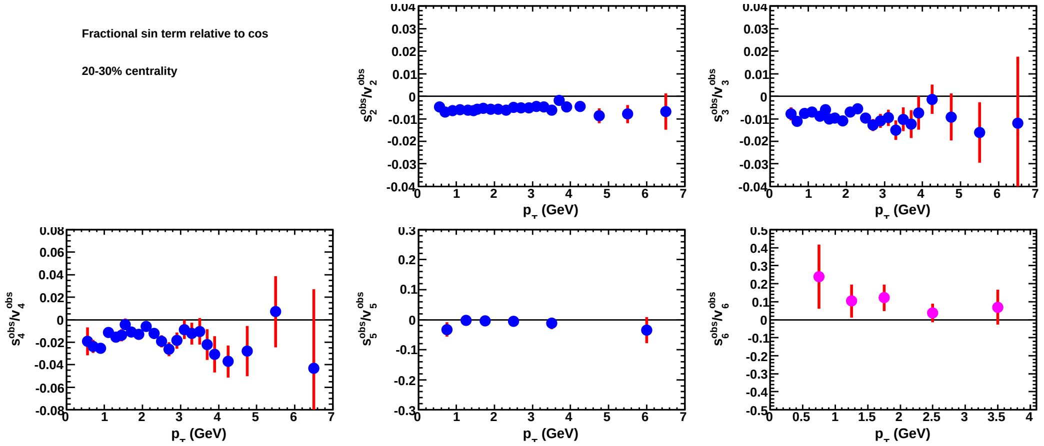

Figure 3.11: The ratio of raw observed sine term (s_n^{obs}) to the cosine term (v_n^{obs}) as function of p_{T} for (20-30)% centrality interval.

3.4 Systematic errors

3.4.1 Resolution correction and v_n^{obs}

Since the v_n is calculated as the ratio of the v_n^{obs} to the EP resolution $\mathrm{Res}\{n\Psi_n\}$, all the systematic uncertainties come from these two factors. The systematic error on the resolution correction are evaluated using the three subevent method, while those for the v_n^{obs} are evaluated by measuring the sine terms in the distribution of tracks relative to the EP. Both of these two sources of error have been discussed.

In addition to these studies, the stability of the results against the track and event selection used in this analysis are also studied. This includes the tracking cuts, centrality selection, and run by run variation of the v_n. Only the full-FCal measurements are used for these checks, since the results are essentially the same for the sub-FCal.

3.4.2 Effect of tracking cuts on v_n

In this analysis, a standard set of cuts on tracks have been applied to select high quality tracks. The set of cuts are listed in Section 2.2.1. Despite the high multiplicity environment in heavy-ion collisions, the number of fake tracks due to random combinations of hits in Pixel and SCT detectors are expected to be small. The effect of the contamination on the v_n if any, can be estimated by applying various degrees of cuts on the geometric parameters $d0$ w.r.t. primary-vertex and $z0\sin(\theta)$ w.r.t. to primary-vertex, of the reconstructed tracks. The following sets of cuts are imposed on the $d0$ and $z0\sin(\theta)$ track parameters[3]:

1. The standard "tight cuts" : $|d0|$ and $|z0\sin(\theta)|$ less than 1 mm. These are the default cuts used in the analysis.
2. 3.5σ cuts : $|d0| < 3.5\sigma_{d0}$ and $|z0\sin(\theta)| < 3.5\sigma_{z0\sin(\theta)}$, used on top of the tight cuts.
3. 1.0σ cuts : $|d0| < \sigma_{d0}$ and $|z0\sin(\theta)| < \sigma_{z0\sin(\theta)}$, used on top of the tight cuts.

where, σ_{d0} and $\sigma_{z0\sin(\theta)}$ are given by:

---

[3] The "w.r.t. primary-vertex" suffix on these parameters is dropped for clarity

$$
\begin{aligned}
\sigma_{d0} &= \sqrt{(0.0211)^2 + \left(\frac{0.182\,\mathrm{GeV}}{p_\mathrm{T}}\right)^2}\ \mathrm{mm} \\
\sigma_{z0\sin(\theta)} &= \sqrt{(0.0542)^2 + \left(\frac{0.252\,\mathrm{GeV}}{p_\mathrm{T}}\right)^2}\ \mathrm{mm}
\end{aligned} \tag{3.17}
$$

The σ_{d0} and $\sigma_{z0\sin(\theta)}$ are momentum dependent one standard deviation values of the $d0$ and $z0\sin(\theta)$ distributions. They are obtained by fitting the $d0$ and $z0\sin(\theta)$ distributions in narrow p_T slices with Gaussian functions. The fit results for obtaining σ_{d0} and $\sigma_{z0\sin(\theta)}$ are shown in Fig. 3.12.

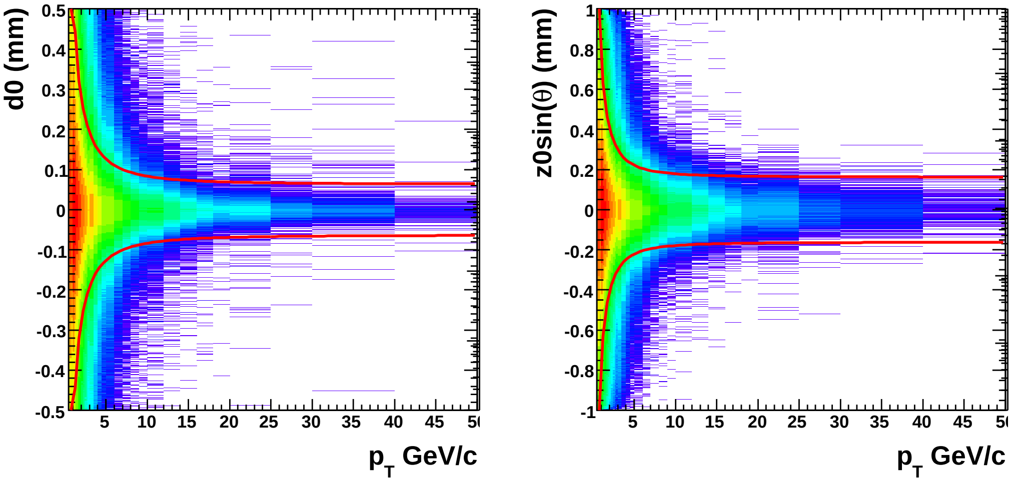

Figure 3.12: $d0$ and $z0\sin(\theta)$ distributions for tracks as a function of p_T. The curves indicate the p_T dependent 3.5σ cuts.

The whole analysis is repeated with these three sets of cuts (keeping other cuts fixed) and the v_n values are re-evaluated. Figure 3.13 and 3.14 summarize the variation of the v_n as a function of p_T for the (0-5)% and (20-30)% centrality intervals upon applying the additional cuts. The fraction of the default tight-cut tracks removed by the 3.5σ and 1.0σ cuts is approximately 2% and 40% for $p_\mathrm{T} \in (1,2)$ GeV, 4% and 50% for $p_\mathrm{T} \in (2,3)$ GeV. These cuts thus cover a considerable variation in the number of tracks.

The variation is quantified in terms of the ratios between the v_n with and without the additional matching cuts. In general the variations are small for all p_T and centrality selections for n=2,3 and 4, but are somewhat larger for $n = 5$ and 6. However, the statistical errors associated with v_5 and v_6

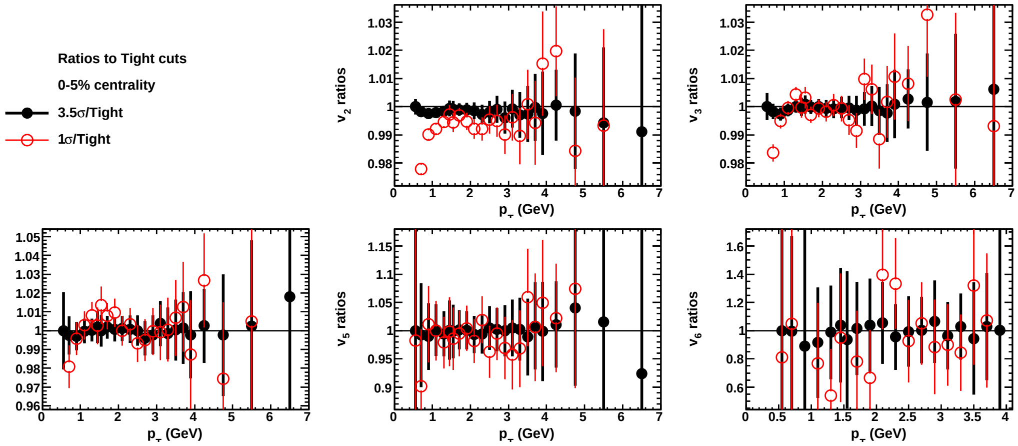

Figure 3.13: Ratios of the Full-FCal v_n for tracks with matching cuts to those without matching cut to d_0 and $z_0 \sin\theta$. This is for (0-5)% most central events.

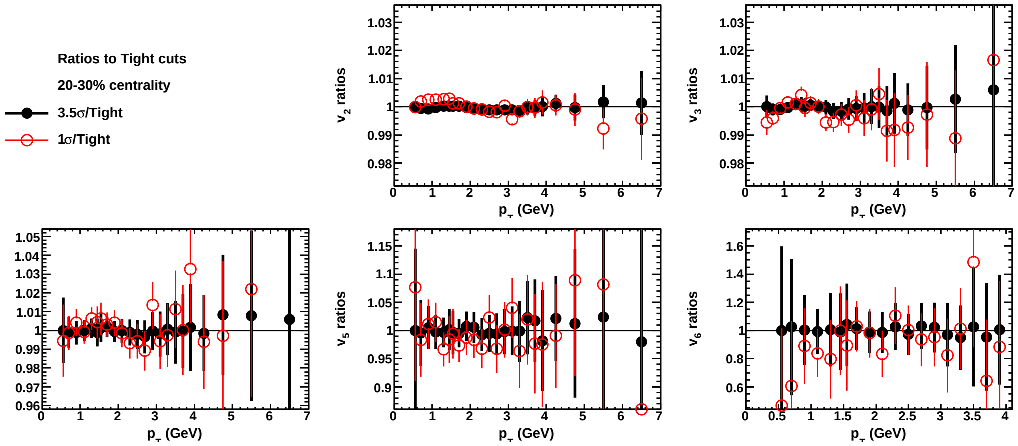

Figure 3.14: Same as previous plot but for (20-30)% centrality.

make the three values compatible with each other. A small but significant p_{T} dependence is seen for $p_{\mathrm{T}} < 2$ GeV in most central collisions. The variation is up to 2% at $p_{\mathrm{T}} \sim 0.5$ GeV, indicating that the v_n are slightly smaller when a tighter vertex-matching cut is used. This can be understood from the changing of the particle mixture when a tight matching is used. Namely, the protons and kaons tend to have larger multiple scattering than charged pions, so they have broader matching distribution and wold be preferentially removed when a tighter cut is used. In addition, the feed-down contribution from particle decays also tends to have larger matching distribution as well. If these particles have a larger v_n, then the tighter matching cuts which tends to throw them away, lead to a smaller v_n. However this p_{T} dependence is only significant for the (0-5)% most central collisions.

In other centrality bins the variations are always less than 0.5% for v_2 and v_3, 2% for v_4, 3% for v_5 and 10% for v_6. Table 3.2 lists the final systematic errors quoted based on the tracking cuts. While the differences in many cases are covered by statistical errors, they are conservatively quoted as the systematic errors.

The systematic errors associated with tracking cuts				
	Centrality	$p_{\mathrm{T}} < 1$ GeV	$1 < p_{\mathrm{T}} < 2$ GeV	$2 < p_{\mathrm{T}}$ GeV
v_2	0-10%	2%	0.5%	0.2%
	>10%	0.5%	0.5%	0.2%
v_3	0-10%	2%	0.5%	0.2%
	>10%	0.5%	0.5%	1%
v_4	0-40%	2%	1%	1%
	>40%	2%	2%	2%
v_5	0-50%	3%	3%	3%
v_6	0-50%	10%	10%	10%

Table 3.2: Summary of systematic errors for the v_n associated with tracking cuts.

3.4.3 Dependence of v_n on running periods

The ATLAS detector performance may vary from run to run. For example certain calorimeter towers might be disabled for some runs while enabled for others. These variations are typically small and are not expected to affect the results. Furthermore, the calibration of the FCal and other detectors used in determining the Ψ_n is done run-by-run, which reduces the effect of such variations in the detector. Nevertheless, a check of the stability of detector over the heavy-ion data taking period, and its effects on the measured v_n is done. Since such checks severely lower the statistics, it is not possible to do it on a run-by-run basis. Instead the runs are grouped into four different run-groups with approximately the same statistics and the analysis is repeated for each group. The variation is studied by taking the ratio of the v_n obtained in each run group with that for the full statistics.

Figure 3.15 shows the variation in the p_{T} dependence of the v_n for the (20-30)% centrality interval for the four run-groups. Additional centralities are shown in Appendix A.2.1). Overall no clear variations are seen for the

p_{T} or centrality dependence of v_n, although the ratios show larger spreads due to increasing statistical errors. The level of p_{T} and centrality dependent deviations beyond statistical fluctuations are about 0.5%, 1%, 2%, 3% and 10% for v_2-v_6, respectively and are quoted as additional systematic errors for the v_n.

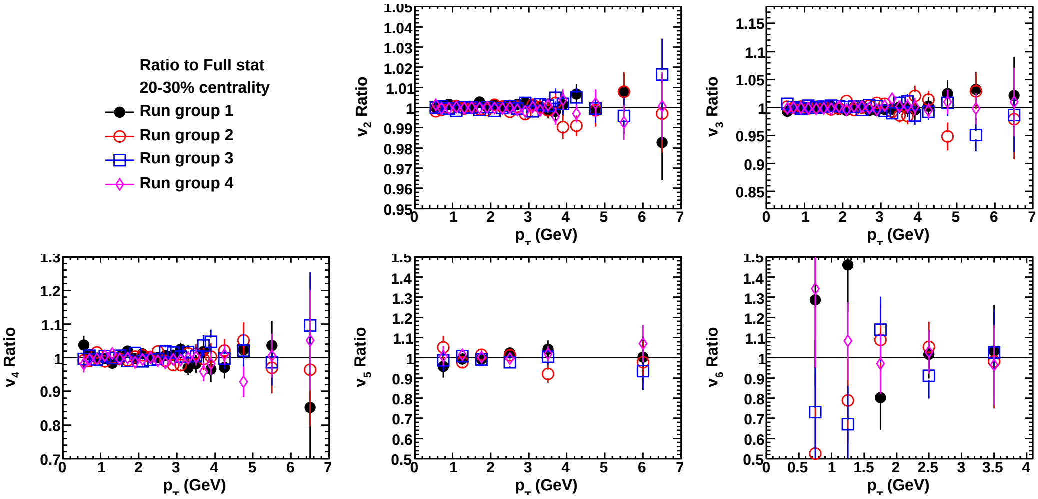

Figure 3.15: variation in the p_{T} dependence of v_n for four different run groups for (20-30)% centrality.

3.4.4 Sensitivity on trigger efficiency

The centrality binning was done using a trigger efficiency of 98 ± 2% (Section 2.2.1). A trigger efficiency of 98% means that 2% of the events fail to pass the triggers and were not recorded. These 2% are assumed to be the most peripheral 2% events. Thus while determining the centrality percentile, the recorded minimum-bias events are chopped into 98 bins according to FCal $\sum E_{\mathrm{T}}$ i.e. the events have a centrality between 0 and 98.

Since the trigger efficiency has a ±2% uncertainty, this automatically translates into an uncertainty in the centrality definition. For example if the trigger efficiency is taken to be 100% then the events are divided into into 100 bins based on the FCal $\sum E_{\mathrm{T}}$ and if it is taken to be 96% then they are divided into 96 bins. Thus the categorization of the events into different centrality intervals has errors associated with the uncertainty in the trigger efficiency (though only by a small amount).

To account for this uncertainty, the analysis is repeated assuming the trigger efficiency to be 96% and 100% and the change in the v_n is considered as a systematic error due to trigger condition and centrality selection.

3.4.5 Summary of the systematic uncertainties

Tables 3.3-3.7 summarize the systematic errors for v_2-v_6 measurements for full-FCal and sub-FCal methods for various centrality ranges. They are quoted nominally for 5% centrality bins. For example (0-20)% refers to (0-5)%, (5-10)%, (10-15)%, and (15-20)% bins, the corresponding errors refer to the range of errors for those four bins. For example an 5-2% error means that the error for (0-5)% centrality bin is 5% and that for (15-20)% centrality bin is 2%. The error for a special (0-1)% centrality interval is also quoted in some cases. For the others, this bin has same uncertainty as the (0-5)% centrality interval. These errors are quoted independent of p_{T}, by taking the larger error when there is any variation of the error with p_{T}.

Centrality	0–20%	20–50%	50–70%	70–80%
Resolution[%]	5.0–2.0	1.0–2.0	3.0–4.0	4.0–6.0
Track selection[%]	2.0	0.5	0.5	1.0
Residual sine term[%]	0.8	0.6	0.5	0.2
Running periods[%]	0.2	0.2	0.5	1.0
Trigger & event sel.[%]	1.0	1.0–0.5	1.0	1.5
Total[%]	5.6–3.2	1.4–2.3	3.4–4.2	4.6–6.4

Table 3.3: Summary of relative systematic uncertainties, in percentage, for v_2 for both full-FCal and $\mathrm{FCal}_{\mathrm{P(N)}}$. See text for explanation of the arrangement of the uncertainties.

Centrality[%]	0–20%	20–50%	50–70%
Resolution[%]	3.0	3.0	3.0–5.6
Track selection[%]	2.0	0.5	0.5–2.0
Residual sine term[%]	1.0	1.0	1.5
Running periods[%]	0.5	0.5–1.5	2.0
Trigger & event sel.[%]	0.4	0.5–1.0	1.5–3.5
Total[%]	3.8	3.5–3.9	4.6–7.4

Table 3.4: Summary of relative systematic uncertainties, in percentage, for v_3 for both full-FCal and $\mathrm{FCal}_{\mathrm{P(N)}}$.

Centrality	0–20%	20–50%	50–70%
Resolution[%]	4.0	4.0	4.4–16.0
Track selection[%]	1.0	1.0–2.0	4.0
Residual sine term[%]	2.0	2.0	3.0–5.0
Running periods[%]	1.0	1.5–2.0	4.0
Trigger & event sel.[%]	0.6	0.7	1.0–2.0
Total[%]	4.9	4.9–5.4	7.9–17.5

Table 3.5: Summary of relative systematic uncertainties, in percentage, for v_4 for both full-FCal and $\mathrm{FCal}_{\mathrm{P(N)}}$.

Centrality	0–1%	0–20%	20–40%	40–50%
Resolution[%]	10.8	10.2	10.2–10.4	11.2–22.4
Track selection[%]	1.0	1.0	1.0	2.0
Residual sine term[%]	5.0			
Running periods[%]	2.0	2.0	2.0	4.0
Trigger & event sel.[%]	1.0			
Total[%]	12.1	11.6	11.6–12.1	13.0–23.0

Table 3.6: Summary of relative systematic uncertainties, in percentage, for v_5 for both full-FCal and $\mathrm{FCal}_{\mathrm{P(N)}}$.

Centrality	(0–1)%	(0–20)%	(20–40)%	(40–50)%
Resolution[%]	58	34–31	31	32–38
Track selection[%]	10			
Residual sine term[%]	10			
Running periods[%]	10			
Trigger & event sel.[%]	1			
Total[%]	61	38–35	36	37–42

Table 3.7: Summary of relative systematic uncertainties, in percentage, for v_6 for both full-FCal and $\mathrm{FCal}_{\mathrm{P(N)}}$.

3.5 Results

3.5.1 η dependence

The η dependence of v_n is more sensitive to short-range correlations, especially at large η, where the track is close to the FCal. Hence a reasonable η gap is

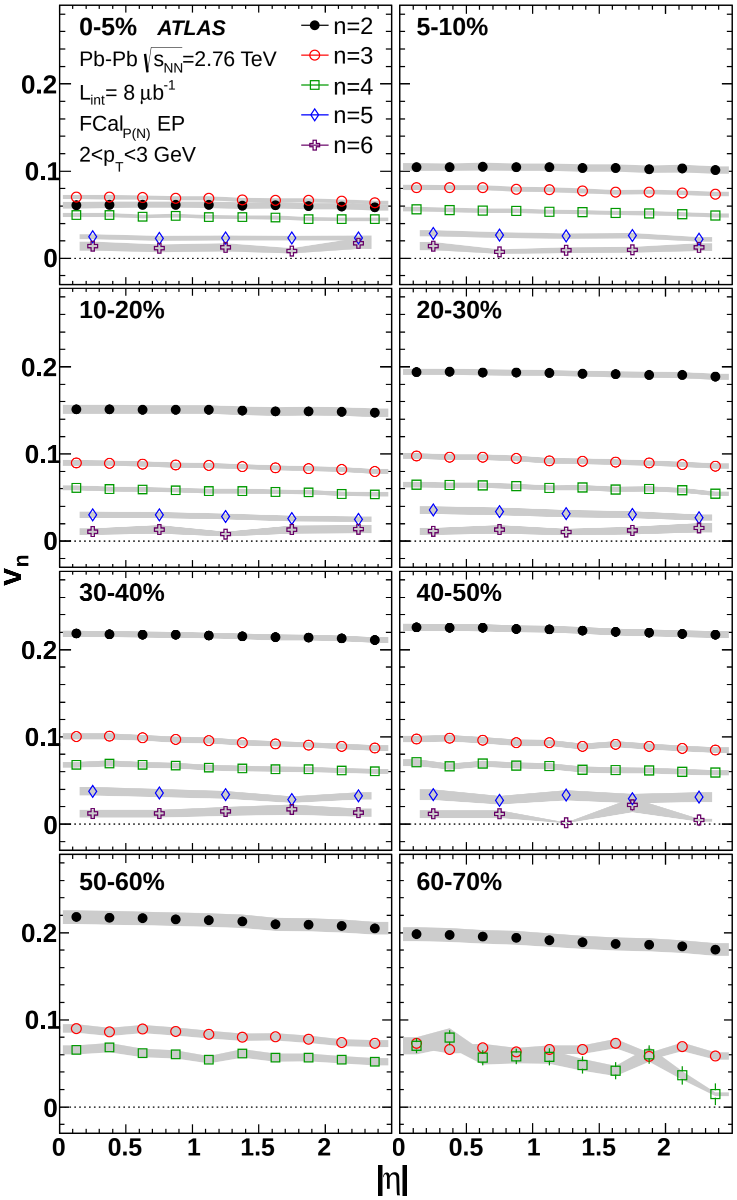

Figure 3.16: η dependence of v_n for $p_\mathrm{T} \in (2, 3)$ GeV. Each panel corresponds to a different centrality interval. The values are obtained using sub-FCal EP measurements.

necessary between the tracks and the detector used to determine the event-plane. The full-FCal has a minimum η separation from the tracks of 0.8 units, while the minimum separation for the sub-FCal is 3.3 units. Based on this, the sub-FCal measurements are used to study the η dependence, while the full-FCal results are used to study the p_{T} and centrality dependence. The reason for this is that the full-FCal has a better resolution than the sub-FCal. This is especially important for v_5 and v_6 measurements where the resolution is very low (in which case the full-FCal has $\sim\sqrt{2}$ times higher resolution). The difference between full-FCal and sub-FCal for η integrated v_n results differ by about 2.5% on average. A detailed set of comparisons of the v_n from full-FCal and sub-FCal are presented in Appendix A.4.

Figure 3.16 shows the $v_n(\eta)$ obtained using the $\mathrm{FCal}_{\mathrm{P(N)}}$ for $p_{\mathrm{T}} \in (2,3)$ GeV and for several centrality selections. In general a weak η dependence is seen across all centralities and p_{T}. For central and mid-central collisions the decrease in v_2 is less than 5% from η=0 to η =2.5. The decrease is larger for the higher order harmonics and also increases for the peripheral events. Results for additional p_{T} bins are given in Appendix A.3.1.

3.5.2 p_{T} dependence

Figure 3.17 shows the p_{T} dependence of v_2-v_6 for several centrality selections. All harmonics show a similar p_{T} dependence trend, namely, they first increase with p_{T} to about 3-4 GeV, then decrease, but remain positive at the highest measured p_{T} values (within statistical fluctuations). A similar trend was also observed at RHIC [68, 69]. This characteristic p_{T} dependence is interpreted as the mechanism driving the v_n changing from hydrodynamic expansion at low p_{T} to path-length dependent energy-loss [70, 71] at high p_{T}. The magnitude of the v_n decrease for larger n, except in most central bins where the v_3 and v_4 become larger than v_2 at sufficiently high p_{T}.

Previous RHIC measurements have shown that $v_4^{1/4}/v_2^{1/2}$ is approximately independent of p_{T} [72, 73]. Figure 3.18 shows a generalized version of this scaling : $v_n^{1/n}/v_2^{1/2}$ vs. p_{T} for several centrality intervals. The ratios vary weakly with p_{T} except in the 5% most central events, indicating that such a scaling relation largely describes the p_{T} dependence (within 10%).

3.5.3 Centrality dependence

Figure 3.19 shows the centrality dependence of the v_n for several p_{T} bins. The centrality bins are 5% in width, with a special bin for the top 1% most central events. This bin is important, as it mainly consists of events with full head-on collision between the nuclei. Going from central to peripheral collisions, v_2 first increases, reaches maximum at around the (30-40)% centrality interval, and then decreases; v_3 shows a similar but much weaker centrality dependence; while v_4-v_6 almost show no clear centrality dependence trend. For

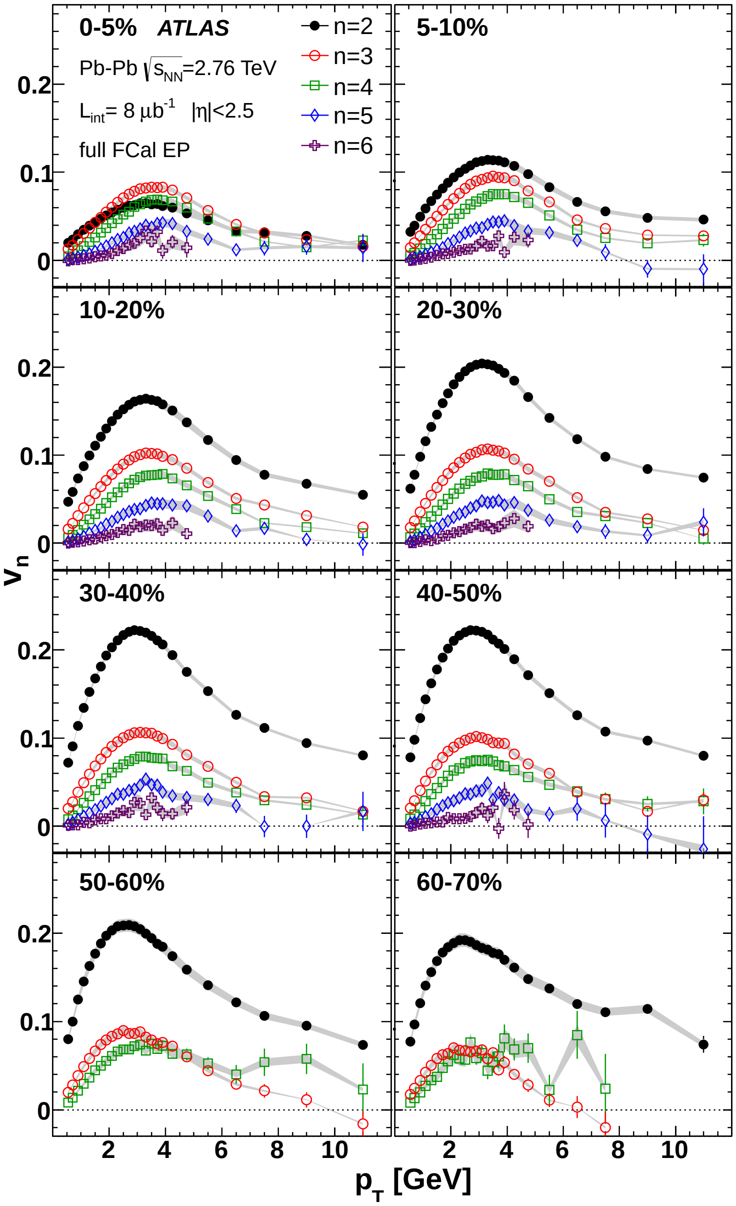

Figure 3.17: p_{T} dependence of v_n. Each panel corresponds to a different centrality interval.

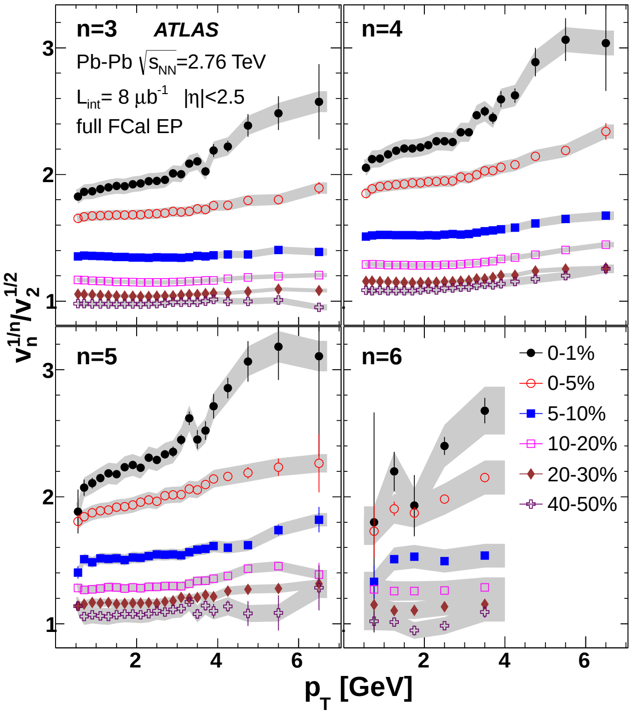

Figure 3.18: v_n scaling with p_{T}. The plotted quantity is $v_n^{1/n}/v_2^{1/2}$. Each panel is a different harmonic.

nature), but does not have v_3, v_4 etc.

In general v_2 is much larger than the other harmonics. This is because the fireball produced in the collision has a natural ϵ_2 which translates into large v_2. For the same reason v_2 has a strong centrality dependence as the average geometry changes dramatically over the different centrality ranges. In the most central events (in the top 5% and more so in the top 1%) which correspond to (almost) complete overlap between the colliding nuclei, there is no natural ϵ_2 present in the fireball. In these events, all eccentricities come from fluctuations in the initial geometry of the fireball. In such central events, the v_3 values are larger than the v_2, and in some p_T bins, even v_4 and v_5 are larger than v_2.

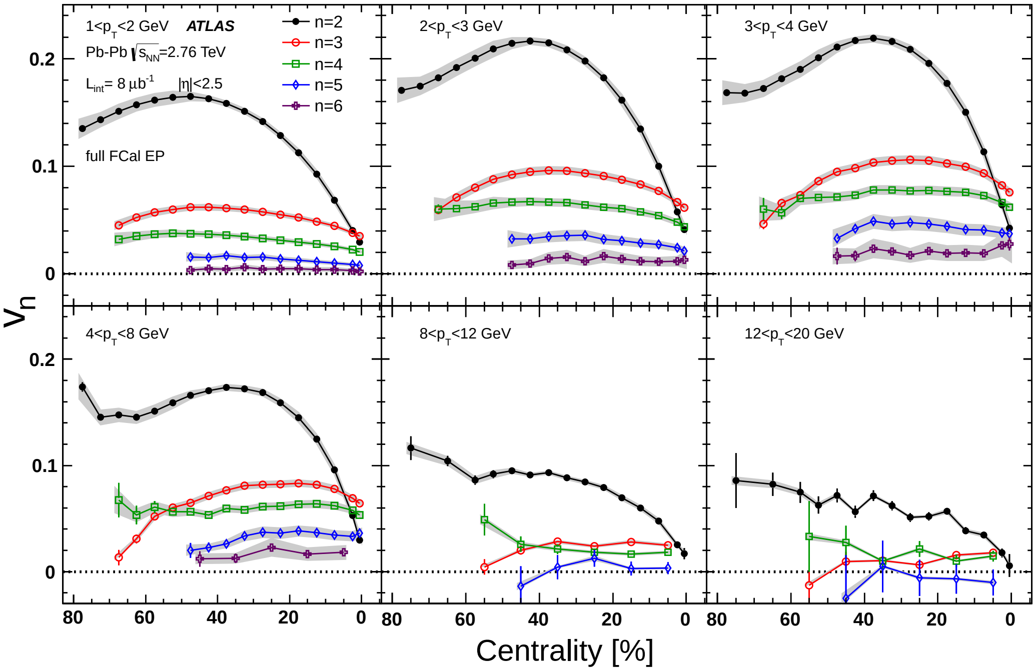

Figure 3.19: v_n as a function of centrality for different p_T bins in 5% centrality steps plus a 0-1% most central bin. The right end of the X-axis corresponds to most central events.

3.5.4 Comparison to theory

The v_n measurements presented here are among the first measurements of the v_n that were made at the LHC. They are an exhaustive set of four-dimensional measurements in: n, p_T, η and centrality, and can strongly constrain η/s of the medium as well as theoretical initial geometry models. Any model must reproduce the p_{T}, η and centrality dependence of all harmonics for the same η/s value.

Figure 3.20 shows comparison of the centrality dependence of the v_n^{EP} measured in this work to theoretical calculations starting with the IP-Glasma initial conditions [74, 75] followed by viscous hydrodynamic evolution. These comparisons have been taken from [76]. The comparisons show that the data are consistent with value of η/s close to 0.2 for the QGP, very close to the quantum lower bound of 0.08 ($1/4\pi$). They also indicate that the IP-Glasma model describes the initial state reasonably well as all the v_n are well reproduced with the same η/s value.

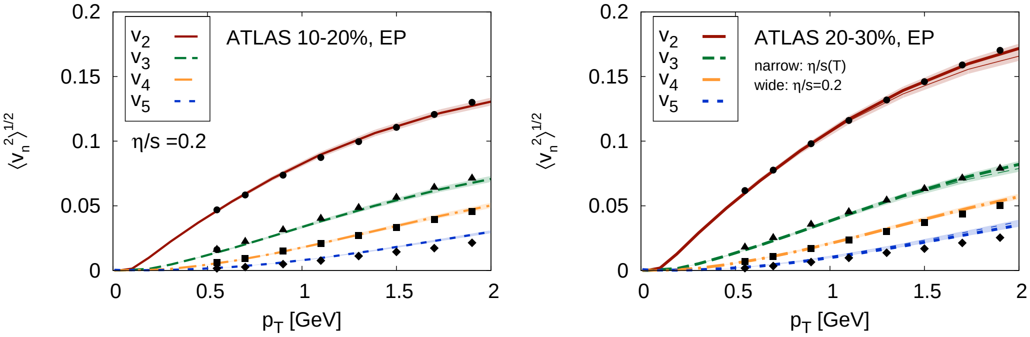

Figure 3.20: p_{T} and centrality of ATLAS v_n^{EP} compared to theory. The theory points are rms v_n and calculated using viscous hydrodynamics starting from an initial state determined using IP-Glasma model. Figure taken from [76].

3.5.5 Summary

In this chapter, measurements of flow harmonics $v_2 - v_6$ using the EP method over $p_{\mathrm{T}} \in (0.5, 20)$ GeV, $\eta \in (-2.5, 2.5)$ and broad centrality ranges were presented. The FCal was used as the event-plane detector, while the ID was used to measure charged-particle tracks. The η dependence of the v_n was shown to be weak indicating that these anisotropies are indeed global anisotropies that characterize the whole event. The presence of odd harmonics, especially large v_3, demonstrated the presence of considerable fluctuations in the initial geometry. It was demonstrated how the v_n measurements can be used to constrain the bulk properties (namely η/s) and initial conditions of the heavy-ion collisions via comparisons to model calculations. Scaling relations were shown in the p_{T} dependence of the v_n which can help in understanding the expansion mechanism.

Chapter 4

Two-particle correlation measurements in Pb+Pb collisions

In this chapter correlations between charged particle pairs, commonly termed two-particle correlations or 2PC are studied. Particle pairs can be correlated due to the global correlations that the individual particles have w.r.t. the event-planes Φ_n. Correlations can also occur due to other phenomena, such as jet fragmentation, back-to-back dijets, decays etc. and more interestingly (at least from a from a heavy-ion perspective) from jet-medium interactions. The features of the 2PCs are investigated and the single-particle v_n including the v_1, which was not measure by the EP method are extracted from the correlations. These measurements are complementary to the EP measurements done in the previous chapter.

The structure of this chapter is as follows: in Section 4.1 the general methodology behind two-particle correlation measurements, applicable to any scenario where particle production takes place is discussed. Following which, the 2PCs in the context of heavy-ion collisions, i.e. the influence of global anisotropies v_n and non-flow on the 2PCs, are discussed. In Section 4.2, the features of the correlations are studied and the phase space region (in p_{T}, centrality etc.) where effects of global anisotropy dominate are identified, to extract the v_n from the correlations. In Section 4.3 the various sources of systematic errors associated with these measurements are discussed. In Section 4.4, the results for v_2-v_6 measurements via the 2PC method and also their comparison to the EP results are presented. Finally in Section 4.5, measurements of the dipolar flow v_1 are presented. The measurements presented in this chapter have been published in [63].

4.1 Methodology

4.1.1 Two-particle correlation method

The correlations between particles produced in any high-energy collision can be studied via two-particle correlations where the yield of associated (or partner) particles (labelled 'b') w.r.t. trigger particles (labelled 'a') in relative azimuthal angle $\Delta\phi$ ($= \phi_a - \phi_b$) and pseudo-rapidity separation $\Delta\eta$ ($= \eta_a - \eta_b$) are measured. The two particles involved in the correlations can be selected using different criteria, for example different p_{T} ranges (hard-soft correlations), different rapidity (forward -backward correlation), different charge sign (same sign or opposite sign correlation) or even different species. In this analysis, the two particles are charged hadrons measured by the ATLAS tracking system, they cover the full azimuth and ± 2.5 in η. Thus, the pair acceptance coverage is ± 5 units in $\Delta\eta$.

In order to account for detector acceptance effects, the correlation is constructed from the ratio of distributions where the trigger and partner particles are taken from the same event (same-event distributions or foreground distributions) and distributions where the trigger and partner particles are taken from two different events (mixed-event distributions or background distributions):

$$C(\Delta\phi, \Delta\eta) = \frac{\langle N_s(\Delta\phi, \Delta\eta)\rangle}{\langle N_m(\Delta\phi, \Delta\eta)\rangle} \tag{4.1}$$

where, the $\langle ...\rangle$ indicates averaging over many events (or mixed-events). The mixed-event distribution is constructed from particles from two different events that have similar centrality and z vertex, so that the detector acceptance effects are similar for the two events. The mixed-event distribution includes the effects of detector inefficiencies and non-uniformity, but contains no physical correlations, while the same-event distribution includes both detector acceptance effects as well as physical correlations. Upon dividing by the mixed-event distribution, the acceptance effects cancel out and only the physical correlations remain (see Appendix B.1 for the derivation of this procedure).

Fig. 4.1 shows example same-event distribution, mixed-event distribution and correlation function for central Pb+Pb collisions. The mixed-event distribution has an almost triangular shape along the $\Delta\eta$ axis since it reflects a convolution of two single particle distributions that are approximately flat in η (for $-2.5 < \eta < 2.5$ [58]). Apart from this triangular shape, there are small modulations in both the $\Delta\eta$ and $\Delta\phi$ directions due to non-uniform acceptance of the detector (arising from holes, dead modules etc.), which are not visible because of the large triangular modulation. A similar triangular shape is also observed for the foreground distribution as it is also largely dominated by combinatorial pairs. Upon dividing the same-event pair distribution by the mixed-event pair distribution, all the acceptance effects (including detector non-uniformity) cancel out leaving behind the physical correlations.

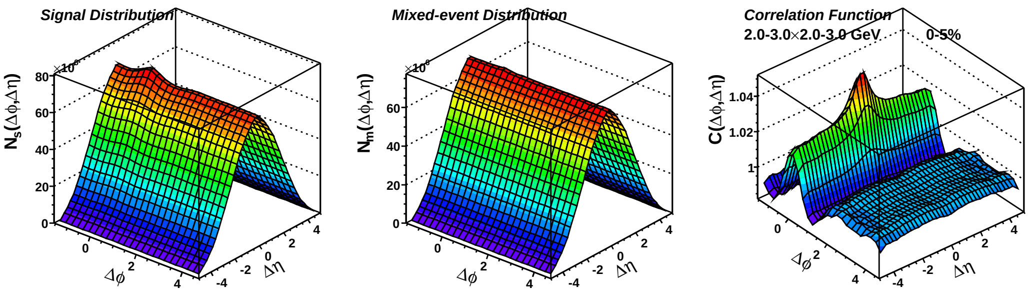

Figure 4.1: The distribution for same event pairs (left), mixed event pairs (middle) and correlation function (right) for $p_{\mathrm{T}}^{a}, p_{\mathrm{T}}^{b} \in$(2,3) GeV for the (0-5)% centrality interval.

To investigate the $\Delta\phi$ dependence in more detail, one-dimensional (1D) $\Delta\phi$ correlation functions can be constructed from the ratio of the same-event and mixed-event pair-distributions both projected to $\Delta\phi$, corresponding to a range in $\Delta\eta$.

$$C(\Delta\phi) = \frac{\langle \int N_s(\Delta\phi, \Delta\eta) d\Delta\eta \rangle}{\langle \int N_m(\Delta\phi, \Delta\eta) d\Delta\eta \rangle} \tag{4.2}$$

Figure 4.2 shows such 1D correlations for several $|\Delta\eta|$ slices along with the corresponding same-event and mixed-event pair distributions. These plots also demonstrate how the mixed-event distribution corrects for detector effects.

In section 4.1.2 it will be demonstrated that only the knowledge of the shape, and not the overall normalization of the correlation function is necessary for studying the v_n. For convenience, the normalization is fixed by rescaling the mixed-event distribution to have the same number of pairs as the same-event distribution in the range $2 < |\Delta\eta| < 5$, so that at large $\Delta\eta$, the correlation has a mean value ~ 1.

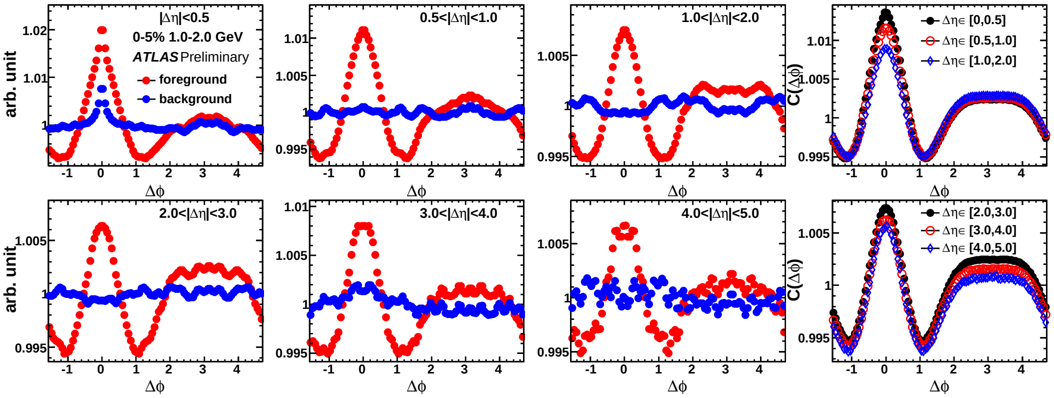

Figure 4.2: The distribution for same-event pairs and mixed-event pairs projected along $\Delta\phi$ for several $|\Delta\eta|$ slices in the (0-5)% centrality interval with $p_{\mathrm{T}}^{a}, p_{\mathrm{T}}^{b} \in (2,3)$ GeV. The last panel shows the correlation functions.

4.1.2 Influence of flow and non-flow on two-particle correlations

The 1D correlation function can be expanded in a Fourier series as:

$$C(\Delta\phi) = A(1 + 2\sum_{n} v_{n,n}(p_{\mathrm{T}}^{\mathrm{a}}, p_{\mathrm{T}}^{\mathrm{b}}) \cos n(\Delta\phi)). \tag{4.3}$$

Where, $p_{\mathrm{T}}^{\mathrm{a}}$ and $p_{\mathrm{T}}^{\mathrm{b}}$ are the trigger and partner p_{T} and $v_{n,n}(p_{\mathrm{T}}^{\mathrm{a}}, p_{\mathrm{T}}^{\mathrm{b}})$ are the Fourier harmonics of the correlation function. In heavy-ion collisions, the physical correlations in 2PCs get contributions from both collective flow, as well as other correlations that involve only a few particles (dijets, decays etc.). As mentioned before, the collective flow leads to an anisotropic distribution of the particles in azimuth:

$$dN/d\phi \propto 1 + 2\sum_{n=1}^{\infty} v_n \cos n(\phi - \Phi_n). \tag{4.4}$$

The influence of flow on two-particle correlation, in the absence of other effects (jets/decays etc.), can be obtained by a simple convolution of two distributions described by Eq. 4.4 as (see Appendix B.2)

$$C(\Delta\phi) \propto dN/d\phi_a \otimes dN/d\phi_b \propto (1 + 2\sum_{n} v_n^a v_n^b \cos n(\Delta\phi)), \tag{4.5}$$

Comparing with Eq. 4.3 the $v_{n,n}(p_{\mathrm{T}}^{\mathrm{a}}, p_{\mathrm{T}}^{\mathrm{b}})$ is related to $v_n(p_{\mathrm{T}}^{\mathrm{a}})$ and $v_n(p_{\mathrm{T}}^{\mathrm{b}})$ as:

$$v_{n,n}(p_{\mathrm{T}}^{a}, p_{\mathrm{T}}^{b}) = v_n(p_{\mathrm{T}}^{a}) v_n(p_{\mathrm{T}}^{b}). \tag{4.6}$$

Thus the Fourier components of the 2PC are simply the products of the v_n of the individual particles. The presence of jets, dijets and other short range correlations such as resonances can modify the correlation function significantly, and hence violate the scaling in Eq. 4.6. For example, pairs from the same jet gives rise to a narrow peak around $(\Delta\phi, \Delta\eta) \sim (0, 0)$ (Fig. 4.1), while the pairs from back-to-back jets are centered around $\Delta\phi \sim \pi$, but elongated along the $\Delta\eta$ direction. These correlations contribute to the $v_{n,n}$. The near-side jet tends to increases the $v_{n,n}$, but its influence is only limited to small $\Delta\eta$. The away-side correlation can potentially influence the $v_{n,n}$ at large $\Delta\eta$. However, it will be shown in Section 4.2 that its influence is negligible in central and mid-central collisions and at low and intermediate p_{T}.

4.1.3 Determining the single particle harmonics from two-particle correlations

If the correlation function is dominated by the contribution from flow, i.e. Eq. 4.6 holds true, then the single particle v_n can be calculated by from the 2PCs. For example by choosing trigger and partner particles from the same p_{T} bin, the $v_n(p_{\mathrm{T}}^{a})$ can be calculated as the square root of $v_{n,n}(p_{\mathrm{T}}^{a}, p_{\mathrm{T}}^{a})$.

$$v_{n,n}(p_{\mathrm{T}}^{a}, p_{\mathrm{T}}^{a}) = v_n(p_{\mathrm{T}}^{a}) v_n(p_{\mathrm{T}}^{a}) = v_n(p_{\mathrm{T}}^{a})^2 \to v_n(p_{\mathrm{T}}^{a}) = \sqrt{v_{n,n}(p_{\mathrm{T}}^{a}, p_{\mathrm{T}}^{a})} \tag{4.7}$$

Such correlations where the trigger and partner are from the same p_{T} bin are termed **fixed-p_{T}** correlations. In some cases, the $v_{n,n}$ become negative, either due to statistical fluctuations, or when Eq. 4.6 is not valid due to non-flow effects. In such case, for continuity the v_n extracted from the 2PC are defined as

$$v_n(p_{\mathrm{T}}^{a}) = -\sqrt{|v_{n,n}(p_{\mathrm{T}}^{a}, p_{\mathrm{T}}^{a})|}, \tag{4.8}$$

This is done only for continuity, clearly the v_n^{2PC} obtained in such cases cannot be interpreted as the single-particle anisotropies.

Figure 4.3 illustrates the steps in the Fourier analysis of the $\Delta\phi$ correlation function for $2 < |\Delta\eta| < 5$ and $p_{\mathrm{T}}^{a}, p_{\mathrm{T}}^{b} \in (2, 3)$ GeV. The second panel shows the 1D correlation function together with the first six Fourier terms and their sum. The first six terms in the Fourier expansion almost completely account for the modulation of the correlation function. The lower panels show the $v_{n,n}$ and $v_n = \sqrt{v_{n,n}}$.

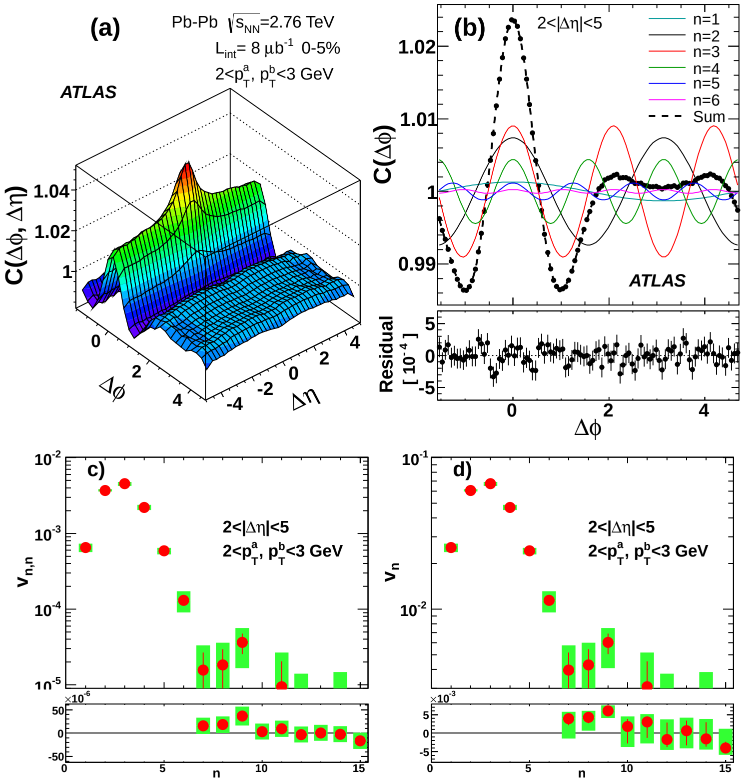

Figure 4.3: The steps involved in extracting the v_n from fixed-p_{T} 2PC: 2D correlation function (top left), 1D projection overlaid with contribution from various Fourier terms as well as the sum (top right), Fourier spectra $v_{n,n}$ vs n (bottom left) and v_n vs n (bottom right). The lower sub-panel of the top right plot shows the residual modulation in the 2PC after removing the first 6 harmonics.

Once the single particle v_n for a given p_{T} bin is determined from the fixed-p_{T} correlation function, particles from this “reference-p_{T}” bin are correlated with particles from another p_{T} bin to obtain the v_n of the second particle as

$$v_n(p_{\mathrm{T}}^b) = \frac{v_{n,n}(p_{\mathrm{T}}^a, p_{\mathrm{T}}^b)}{v_n(p_{\mathrm{T}}^a)}. \tag{4.9}$$

Such correlations, where the two particles are from different p_{T} ranges are termed **mixed-p_{T}** correlations.

It must be emphasized that the factorization relation Eq.4.6 (or Eq. 4.9) is true only when the correlation function is dominated by collective flow. In this case, the v_n extracted using the 2PCs should be consistent with the v_n measured using the EP method, independent of which reference p_{T} is used. On the other hand, if other correlations such as jets, are significant, then the factorization breaks down. In which case, if Eq. 4.9 is used, the $v_n(p_{\mathrm{T}}^{\mathrm{b}})$ extracted using different reference $p_{\mathrm{T}}^{\mathrm{a}}$ will be different. However, it is possible that the collective dynamics dominate one term (say v_3), but not the other (say v_1). In this case the v_n, for those n where the collective dynamics dominates can still be reliably extracted.

4.2 Features of two-particle collisions in heavy-ion collisions

The central aim of the 2PC analysis is to identify the phase space, in terms of p_{T}, $\Delta\eta$ and centrality, over which the correlation functions are dominated by collective flow and then extract the flow harmonics. One check is to systematically study the variation of the $v_{n,n}$ and v_n with $\Delta\eta$. As the $\Delta\eta$ gap between the pair is increased, short-range correlations are reduced. Flow correlations being global, are expected to be less sensitive to the $\Delta\eta$ gap. Another check is to test the validity of the factorization (Eq. 4.9) by measuring the $v_n(p_{\mathrm{T}}^{b})$ using several different reference p_{T}^{a} bins. These two check are performed in this section.

4.2.1 The correlation landscape

Figure 4.4 shows the centrality evolution of the correlation functions for trigger and partner $p_{\mathrm{T}} \in (2,3)$ GeV. The following qualitative features are seen: In all cases, a near-side jet peak centered around $(\Delta\eta, \Delta\phi) = (0,0)$ is observed. The magnitude of the near-side jet peak increases dramatically from the most central events to the peripheral events, indicating the larger contribution from short-range correlations with decreasing centrality. In central and mid-central events, a long range correlation along $\Delta\eta$ at $\Delta\phi = 0$ is observed. This long range correlation was also observed at RHIC [77, 78] and is called the *ridge*. The ridge amplitude increases from central to mid-central collisions, reaching a peak at around the (30-40)% centrality interval, and then decreases for peripheral events. The ridge has only a weak $\Delta\eta$ dependence in central end mid-central events, but beyond the (50-60)% centrality bin its magnitude decreases visibly with increasing $\Delta\eta$. By the (80-90)% centrality bin the near side ridge completely vanishes.

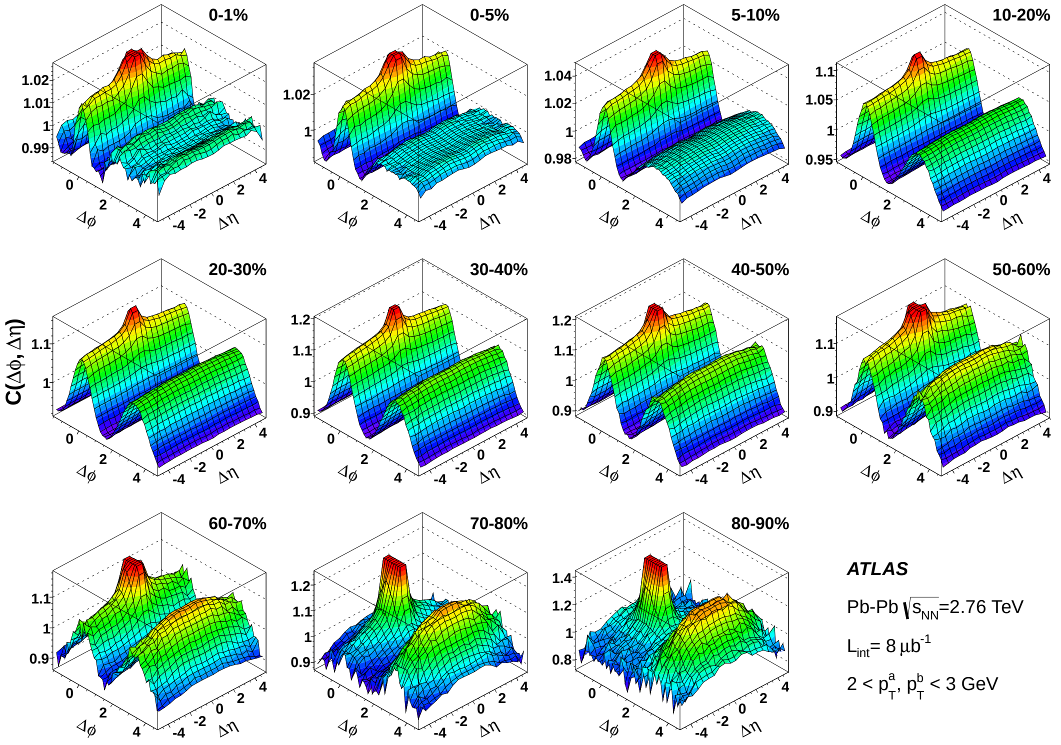

Figure 4.4: Two Particle $\Delta\eta-\Delta\phi$ Correlations $2 < p_T^a$, $p_T^b < 3$ GeV for various centrality selections. The correlation function is truncated from top to better reveal the fine long range structures.

Long-range correlation structures are also seen the away-side ($\Delta\phi \sim \pi$). The away-side correlation structures are also flat in $\Delta\eta$ for central and mid-central events, but their shape in $\Delta\phi$ is centrality dependent. In most central events, namely the (0-1)% and (0-5)% centrality intervals, the away-side is relatively broad and has a *double-hump* structure (also seen at RHIC [79]). The double peak structure disappears for the (0-10)% centrality bin, where a single away-side peak is seen similar to the near-side ridge. The magnitude of this away-side ridge also increases from central to mid-central events, and its width in $\Delta\phi$ narrows. Its magnitude is always smaller than the near side ridge till the (50-60)% centrality interval. The away-side correlation appears to fall off gradually at large $\Delta\eta$ starting in the (50-60)% centrality interval. In more peripheral collisions, the fall off is very evident.

The last panel shows the peripheral centrality of (80-90)%, where the features seen on the away-side are mainly from back-to-back dijets, as collective dynamics or jet-medium interactions are not expected to play an important role here. The away-side correlation is extended in $\Delta\eta$ but its magnitude falls considerably for $|\Delta\eta| > 2$. This shows that the long-range away-side structures seen in central Pb+Pb collisions have much larger extension in $\Delta\eta$ than the swing of the away-side jet.

The long range structures at the near- and away-side could indicate a strong medium modification of jet fragmentation or medium response to the energy lost by quenched jets. In fact, the double-hump structure the away-side in most central events was initially interpreted as the result of shock-waves produced in the medium by the away-side jet [80]. It will be shown in Section 4.4.4 that these structures are accounted for by collective flow. That the ridge and away-side double-hump structure can arise from collective flow was first pointed out in [42]. The measurements presented here were among the first that confirmed this.

4.2.2 Centrality and p_{T} dependence of the long-range correlations

In order to study the long-range correlations in detail, 1D correlations with $2 < |\Delta\eta| < 5$ are analyzed. The $|\Delta\eta|$ cut removes the near-side jet peak and most of the effects of the away-side jet. Figure 4.5 shows such correlations for various centralities and for $p_{\mathrm{T}}^{a}, p_{\mathrm{T}}^{b} \in (3,4)$ GeV together with the individual contributions from the first six $v_{n,n}$ components. If the correlation is dominated by anisotropic flow, its value at $\Delta\phi \sim 0$ should be larger than its value at $\Delta\phi \sim \pi$. This is because in the flow dominated scenario, the $v_{n,n}(p_{\mathrm{T}}^{a}, p_{\mathrm{T}}^{b}) = v_n(p_{\mathrm{T}}^{a})v_n(p_{\mathrm{T}}^{b})$ are positive definite, with their contribution to $C(\Delta\phi)$ adding up on the near-side while on the away-side they alternatively add and subtract[1]. This is the case up to the (40-50)% centrality bin, but beyond that the away-side is larger indicating a significant contribution from the away-side jet. This reversing of the asymmetry between the near- and away-side amplitudes correlates with a continuous decrease of $v_{1,1}$, which eventually becomes negative at around 50% centrality. The correlation function in the (80-90)% centrality interval shows that a broad peak from the away-side jet predominantly generates a negative $v_{1,1}$ and a consequently a positive $v_{2,2}$ that cancel each other at the near-side but add up at the away-side. This behavior shows that, the appearance of a large negative $v_{1,1}$ is a good indicator for a significant contribution of from dijets to $v_{2,2}$.

Next a similar study is done for the p_{T} dependence of the long-range correlation structures. The left panels of Fig. 4.6 show the p_{T} evolution of fixed-

---

[1] As $\cos(n\Delta\phi)$ has a maxima at $\Delta\phi = 0$, and a maxima or minima at $\Delta\phi = \pi$ depending on whether n is odd or even.

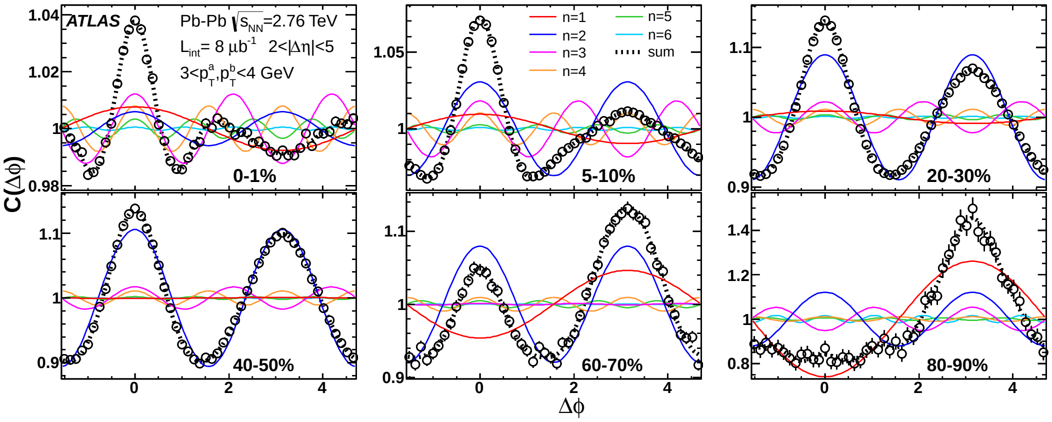

Figure 4.5: Two-particle $\Delta\phi$ correlations for $2 < |\Delta\eta| < 5$ for several centrality intervals. $p_{\mathrm{T}}^{\mathrm{a}}, p_{\mathrm{T}}^{\mathrm{b}} \in (2,3)$ GeV.

p_{T} correlations in the (0-10)% centrality interval. For the upper two panels ($p_{\mathrm{T}} < 6$ GeV) the near-side is larger than the away-side. While for the lower two panels ($p_{\mathrm{T}} > 6$ GeV), the near-side peak completely vanishes while the away-side peak continues to grow. This results in the harmonics $v_{n,n}$ to have alternatively positive and negative signs for even and odd orders, showing the breakdown of the factorization of $v_{n,n}$ (Eq. 4.6) which requires that the $v_{n,n}$ be positive. The right panels of Fig. 4.6 show the centrality evolution of the $v_{n,n}$ for an intermediate p_{T} range $p_{\mathrm{T}} \in (3,4)$ GeV (top panel), and a high p_{T} range $p_{\mathrm{T}} \in (5,6)$ GeV (bottom panel). It is seen that for the 3-4 GeV bin, the sign-flipping of $v_{n,n}$ between even and odd n happens only for peripheral events while for the 5-6 GeV bin the sign-flipping happens over the entire centrality range.

From the analysis done here it can be concluded that the long-range correlation structures seen beyond 50% centrality and for $p_{\mathrm{T}} > 4$ GeV have observable influences from the away-side jet. Next the complementary phase-space i.e. $p_{\mathrm{T}} < 4$ GeV and events more central than 50% are analyzed to explicitly check the factorization of the $v_{n,n}$ (Eq. 4.6).

4.2.3 $\Delta\eta$ dependence of $v_{n,n}$

Fixed p_{T} correlations

A $\Delta\eta$ cut of 2 units was used isolate the long-range correlations in the previous section. Here the $\Delta\eta$ dependence of the $v_{n,n}$ is investigated in detail. Figure 4.7 shows the $|\Delta\eta|$ dependence of the $v_{n,n}$ for several centrality intervals for $p_{\mathrm{T}}^{\mathrm{a}}, p_{\mathrm{T}}^{\mathrm{b}} \in (2,3)$ GeV. The distributions show a narrow peak around

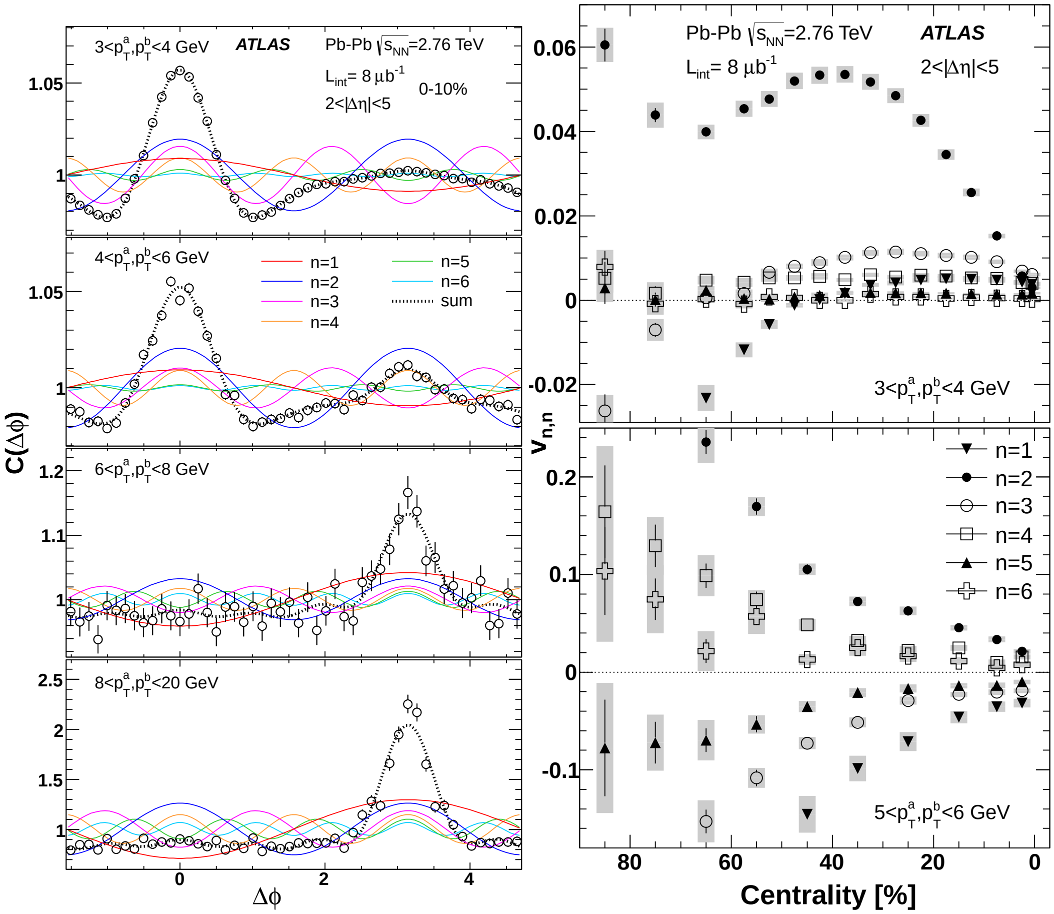

Figure 4.6: Left panels: Two-particle $\Delta\phi$ correlations for $2 < |\Delta\eta| < 5$ for the (0-10)% centrality interval. From top to bottom the panels show correlations with increasing p_{T}. Right panels: the Fourier spectra as a function of centrality for $3 < p_{\mathrm{T}}^{a}, p_{\mathrm{T}}^{b} < 4$ GeV (top panels) and $4 < p_{\mathrm{T}}^{a}, p_{\mathrm{T}}^{b} < 5$ GeV (bottom panels).

$\Delta\eta \sim 0$ and then drop sharply till $|\Delta\eta| \sim$1.5-2.0. However beyond $|\Delta\eta| >$2 the variations in the $v_{2,2}$-$v_{6,6}$ are relatively small. The sharp peak at small $|\Delta\eta|$ reflects the influence of the near-side jet peak, while the gradual fall off at large $\Delta\eta$ might be due to the slow drop of the v_n towards large η (Section 3.5.1), as a larger $\Delta\eta$ gap requires one or both of the particles to be from large η. Figure 4.7 demonstrates that a cut of $|\Delta\eta| > 2$ picks up the long-range correlations while cutting out the near-side jet peak.

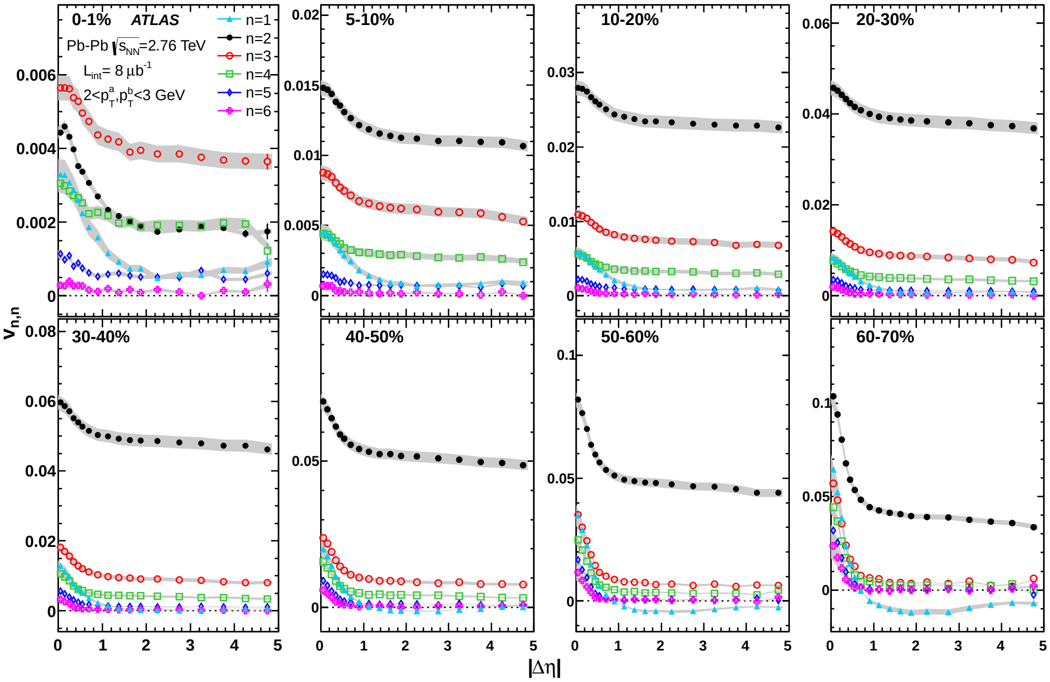

Figure 4.7: $v_{n,n}$ as function of $\Delta\eta$ for $2 < p_T^a, p_T^b < 3$ GeV and various centrality selections.

4.2.4 Mixed-p_T correlations: the factorization of of $v_{n,n}$

The factorization Eq 4.9 is checked using mixed-p_T correlations with several different p_T^a values. Figure 4.8 shows one such study for the (0-10)% centrality interval. The upper panels show the $v_n(p_T^a)$ extracted for four different p_T^a bins of (0.5-1.0), (1-2),(2-3) and (3-4) GeV using fixed-p_T correlations. The middle panels show the $v_{n,n}(p_T^a, p_T^b)$ obtained by correlating these four trigger bins with associated particles having $p_T^b \in (1.4, 1.6)$ GeV. And the lower panels show the $v_n(p_T^b)$ obtained by dividing the plots in the middle panels by the corresponding ones in the top panels (Eq. 4.9). For $\Delta\eta > 1$ we see that while the reference $v_n(p_T^a)$ differ by a factor of 3-10 depending on n, the recovered $v_n(p_T^b)$) are almost identical. There is a small deviation for v_2 when the (3-4) GeV p_T^a bin is used as reference, this is because in the most central events the v_2 signal is small and can have some non-flow bias. For $\Delta\eta \sim 0$ it is seen that the factorization breaks down for all harmonics due to the effect of the near-side jet peak.

Figure 4.9 shows the results of a similar check but for the (20-30)% centrality interval. Similar trends are observed, however the agreement between the different reference p_T bins for v_2 is much better. This is because the elliptic

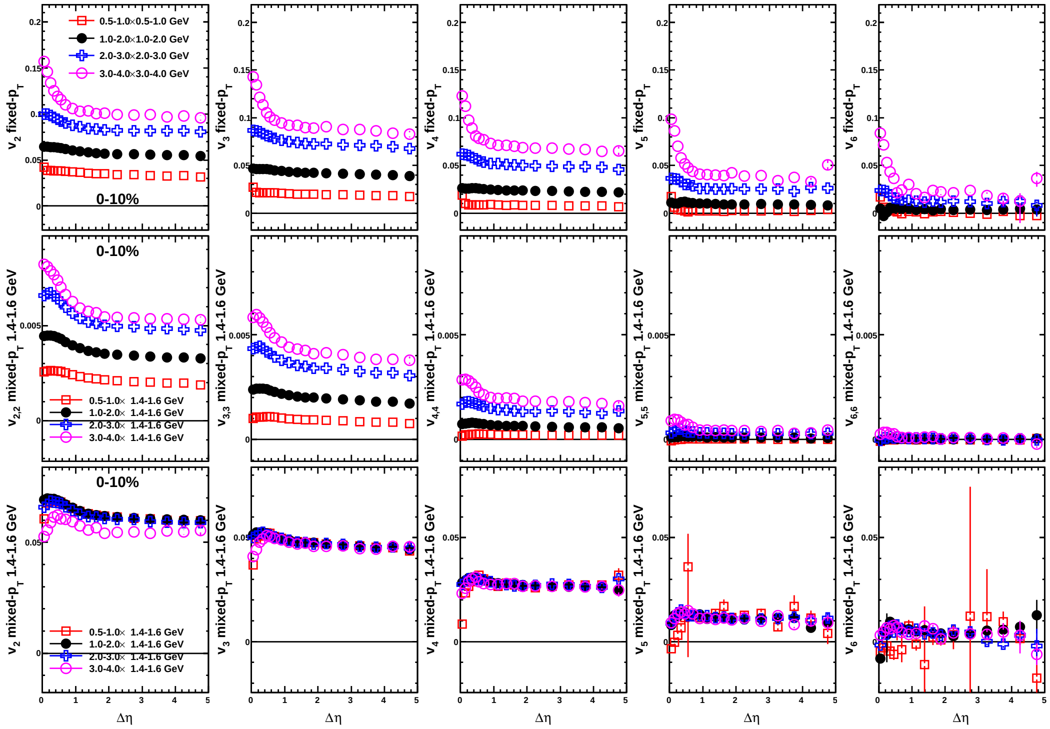

Figure 4.8: Top panels: v_n vs $\Delta\eta$ for four fixed-p_{T} correlations. Middle panels: The $v_{n,n}$ obtained by correlating the four p_{T}^{a} bins shown in the top row with $p_{\mathrm{T}}^{b} \in (1.4, 1.6)$ GeV. Bottom panels: v_n vs $\Delta\eta$ from mixed-p_{T} correlations with target p_{T} of 1.4-1.6 GeV. All plots are for (0-10)% centrality selections.

flow signal in mid-central collisions is much larger than in the (0-10)% bin and thus the influence of the jet bias is smaller (a similar but smaller increase can also be seen for higher order v_n).

In principle, the v_1 can be calculated from $v_{1,1}$. However $v_{1,1}$ is affected by global momentum conservation effects and which break the factorization Eq. 4.9 [81, 82], resulting in $v_{1,1}$ often becoming negative, even for fixed-p_{T} correlations. The $v_{1,1}$ are studied separately Section 4.5. However, the breakdown of the factorization is demonstrated here. The negative $v_{1,1}$ values are handled using Eq. 4.8 for fixed-p_{T} correlations. Figure 4.10 shows the reference and target $v_1(\Delta\eta)$ for the same set of p_{T} bins as shown in Figure 4.8-4.9 but for several centrality bins. The factorization clearly does not work for any $|\Delta\eta|$.

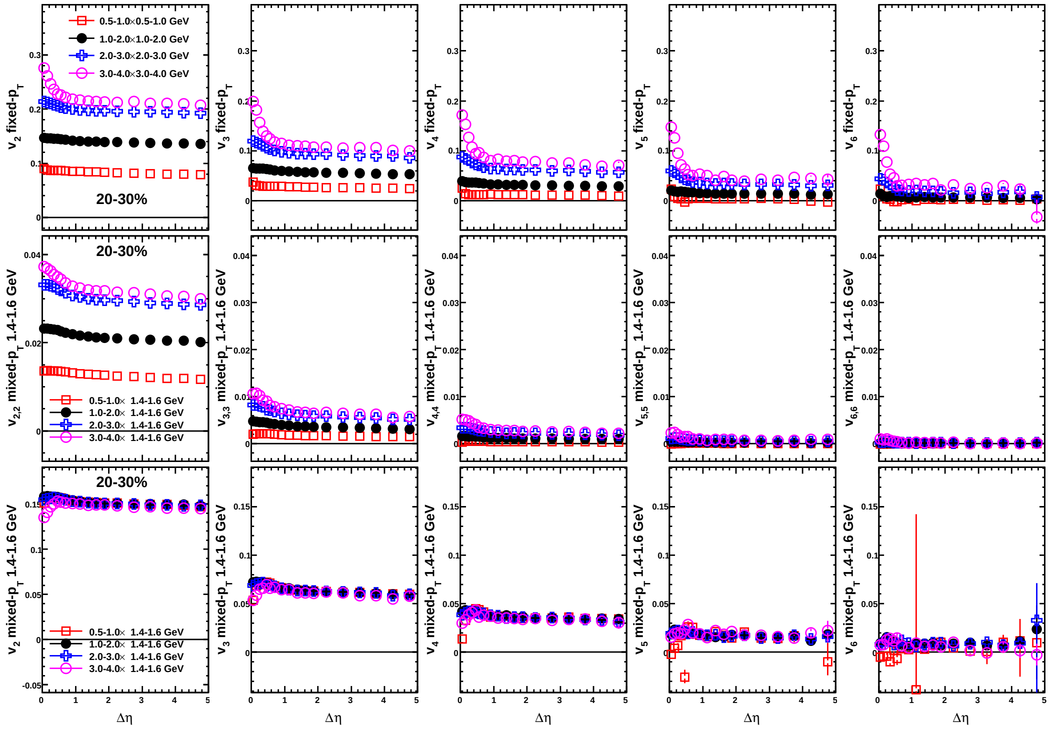

Figure 4.9: Same as previous plot but for (20-30)% centrality interval.

4.2.5 Flow dominated phase space

From the study of the long-range correlation structures presented in this section, it is seen that the factorization relation works well for $p_{\rm T} < 5$ GeV and for centralities up to 50%. The influence of the away-side jet and other non-flow correlations typically make a difference for $p_{\rm T}$ >5 GeV and for centralities (50-60)% and more peripheral. For clarity, it must be pointed out that the effects of the away-side jet are present for all centralities and at all $p_{\rm T}$, however for lower $p_{\rm T}$ and in central and mid-central events, the effects of the single particle anisotropies dominate the 2PC. Similarly, the effects of the single particle anisotropies affect the 2PCs for peripheral centralities, however the jet correlations dominate. There is no hard cutoff in terms of centrality and $p_{\rm T}$ when one switches off and the other takes over. The values of $p_{\rm T}$ and centrality mentioned here are the typical values when we can clearly identify the influence of one or the other. A more detailed evaluation of the non-flow influence is done by comparing the 2PC v_n to the EP v_n in Section 4.4.2. It is also clear that the $v_{1,1}$ values do not factorize for any $p_{\rm T}$ or centrality. This is expected because of the momentum conservation effects that affect v_1. In Section 4.5 a detailed study of the $v_{1,1}$ is done to obtain v_1 by explicitly accounting for the

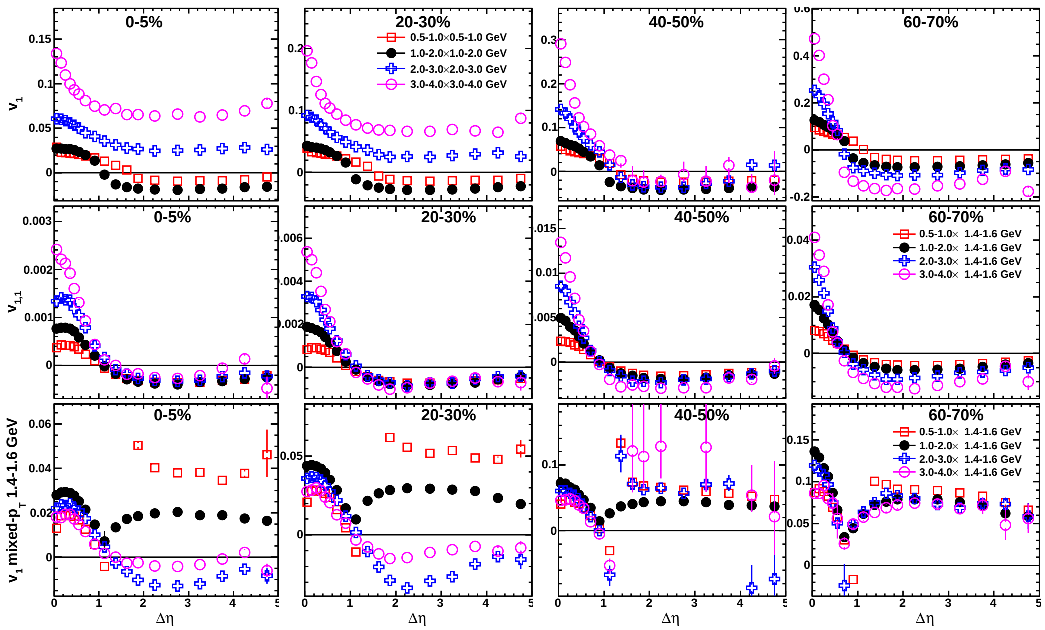

Figure 4.10: Top panels: v_1 vs $|\Delta\eta|$ for four fixed-p_{T} correlations. Middle panels: The $v_{1,1}$ obtained by correlating the four p_{T}^a bins shown in the top row with p_{T}^b in (1.4-1.6) GeV. Bottom panels: v_1 vs $|\Delta\eta|$ from mixed-p_{T} correlations with target p_{T} of 1.4-1.6 GeV. Each column is a different centrality interval.

momentum conservation effects.

4.3 Systematic errors

In this section possible sources that can introduce systematic errors in the correlation analysis are examined. Some of them are identical to the ones that discussed in the Chapter 3 for the EP method. They include

1. Dependence on tracking cuts: The sensitivity of the results to the tracking cuts is studied by varying the $d0$ and $z0\sin(\theta)$ cuts as discussed in Section 3.4.2.

2. Dependence on running period: The total statistics are divided into four running periods and the analysis repeated for each period (Section 3.4.3).

3. Uncertainty in trigger efficiency: This was discussed in Section 3.4.4 and comes from the ±2% uncertainty in the trigger efficiency.

For each of the above checks, the analysis is repeated and the variation in the $v_{n,n}$ and the corresponding variation in v_n are considered as systematic errors. Additional checks using a full ATLAS MC simulation are also performed to evaluate additional errors that can be introduced due to detector inefficiency (see Appendix B.3.1). The errors estimated from these checks are listed in Table 4.1. In some cases the estimated errors have weak centrality and p_{T} dependence. In such cases, the errors are quoted conservatively so as to cover these variations. The total error is taken to be the quadrature sum of the individual errors.

	v_1	v_2	v_3	v_4	v_5	$v_{n\|n\geq 6}$
Track selection[%]	3.0	0.3	0.3	1.0	2.0	4
Running periods[%]	5.0	0.3-1.0	0.7-2.1	1.2-3.1	2.3	7-11
Trigger & event sel.[%]	1.0	0.5-1.0	0.5-1.5	0.5-1	1.0	5
MC consistency[%]	2.0	1.0	1.5	2.0	3.5	5
Total[%]	6.3	1.2-1.8	1.8-3.0	2.6-3.9	4.8	11-14

Table 4.1: Relative systematic uncertainties for v_n, as percentages, from tracking cuts, variation between different running periods, centrality variation, consistency between truth and reconstructed v_n in HIJING simulation, and the quadrature sum of individual terms.

Another source of systematic errors is based on how well the event mixing reproduces the pair acceptance. These are detailed in Appendix B.3.2 and arise because the pair acceptance is not exactly reproduced by the event-mixing procedure because of the finite z-vertex binning (1 mm) and centrality binning (5%) used for the mixed-events. Unlike the errors listed in Table 4.1 which were relative errors, these errors are absolute errors. These errors are summarized in Table 4.2 for the $v_{n,n}$. The errors for the v_n are obtained by propagation of these errors when calculating the v_n via fixed-p_{T} (Eq. 4.7) or mixed-p_{T} (Eq. 4.9) correlations.

	residual $v_{n,n}$ $(\times 10^{-6})$		
p_{T} selections	$2 < \|\Delta\eta\| < 5$	0.1 $\|\Delta\eta\|$ slice	0.5 $\|\Delta\eta\|$ slice
$p_{\mathrm{T}}^a, p_{\mathrm{T}}^b < 2$ GeV	2.5	5.0	3.2
$p_{\mathrm{T}}^a, p_{\mathrm{T}}^b > 2$ GeV	6	8.7	6
$p_{\mathrm{T}}^a > 2$ GeV, $p_{\mathrm{T}}^b <2$ GeV	3.7	8.6	6.6

Table 4.2: The systematic errors for $v_{1,1}$–$v_{6,6}$ estimated for effects not cancelled out by event mixing.

4.4 Results for v_2-v_6

4.4.1 v_n spectra from 2PC

Figures 4.11 shows the v_n as a function of n evaluated from several fixed-p_{T} correlations with $2 < |\Delta\eta| < 5$ for the (0-5)% and (20-30)% centrality intervals. The systematic errors include those from Tables 4.1 and 4.2. The lower sub-panels in these plots also show the harmonics for orders 6 and above on a linear scale, which are typically consistent with zero.

Plotting the power spectrum as a function of n allows us to directly see the relative strength of the different flow harmonics. In the central (0-5)% events (top panels) it is seen that v_3 is comparable and in some cases larger than v_2. The v_4 is fairly comparable to v_2 as well. However, for the mid-central events (bottom panels), an almost exponential decrease with increasing n is seen. This spectra can be compared to results from model calculations of initial geometry and equation of state [83, 84].

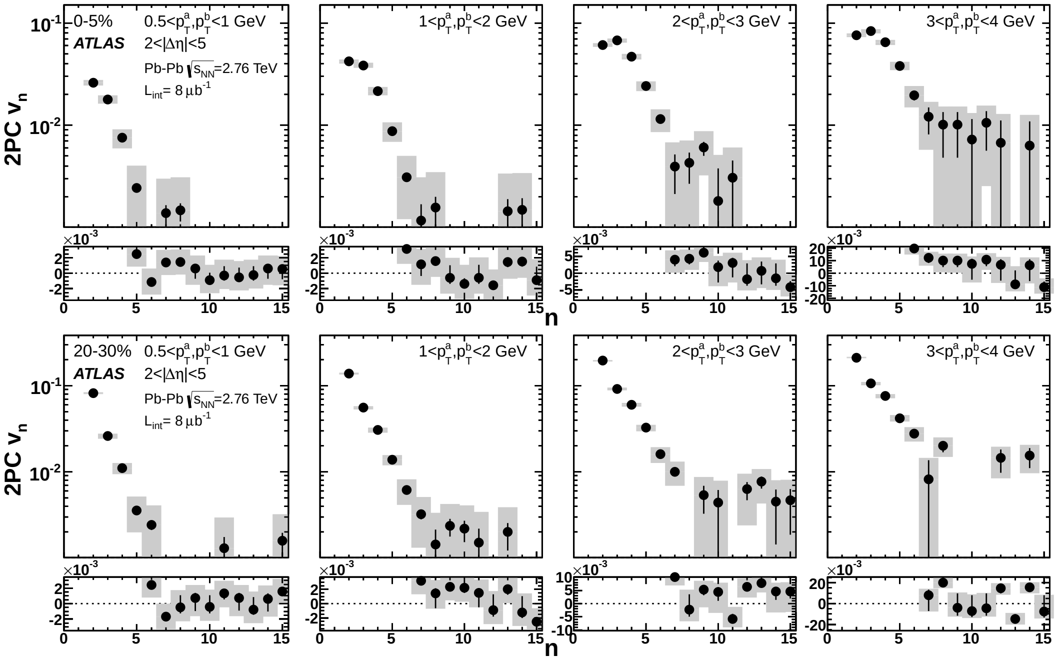

Figure 4.11: v_n vs. n for $n \geq 2$ in the (0-5)% centrality interval (top panels) and in the (20-30)% interval (bottom panels) for four fixed-p_{T} correlations (0.5-1, 1-2, 2-3 and 3-4 GeV from left to right). The error bars and shaded bands indicate the statistical and total systematic uncertainties, respectively.

4.4.2 Comparison with event-plane results: p_{T} dependence

The left panels of Fig. 4.12 compare the p_{T} dependence of the 2PC v_2-v_5 values to the EP values for the (0-10)% centrality interval. For v_2 the results from the two methods are in good agreement within 5-10% till $p_{\mathrm{T}} \sim 4$ GeV, but beyond that the results begin to diverge with the 2PC values being considerably larger, due to contributions from the away-side jet. For $v_3 - v_4$ the agreements are better and also extend out to slightly higher p_{T} values than for the v_2 case. This is because the away-side jet, which produces an excess on the away-side, typically affects $v_{1,1}$ and $v_{2,2}$ while the higher order harmonics are less influenced. For v_5 the statistical errors are too large beyond 4 GeV to make definitive comparisons.

The right panels of Fig. 4.12 show similar comparisons but the 2PC results are obtained using mixed-p_{T} correlations for four different reference-p_{T} bins from relatively low p_{T} ranges. Choosing lower p_{T} reference bins results in the EP and 2PC values agreeing out to much higher values of the associated p_{T}. This is expected as the jet bias is reduced when one of the particles used in the 2PC is from a softer p_{T} range.

Even for the mixed-p_{T} correlations we see that the agreement for v_3 and higher order harmonics is better than that for v_2. However this is only true for most central events where the v_2 values are small. Figure 4.13 shows similar plots for three centrality ranges for $v2$ and $v3$. It is seen that that for mid-central events the agreement for v_2 is nearly as good as that for v_3.

4.4.3 Comparison with event-plane results: Centrality dependence

Figure 4.14 compares the centrality dependence of v_n obtained from the 2PC method and the EP method for three different p_{T} bins. The 2PC results are obtained using the fixed-p_{T} method. The v_n values agree within 5% for v_2-v_4, 10% for v_5 and 15% for v_6 over a broad centrality range, well within the quoted systematic uncertainties for the two methods. The disagreement becomes larger for peripheral events where the influence of non-flow correlations start to become important.

4.4.4 Reconstructing the 2PC from EP v_n

The agreement between the EP and 2PC v_n measurements in central and mid-central events and at low and intermediate p_{T} implies that the features seen

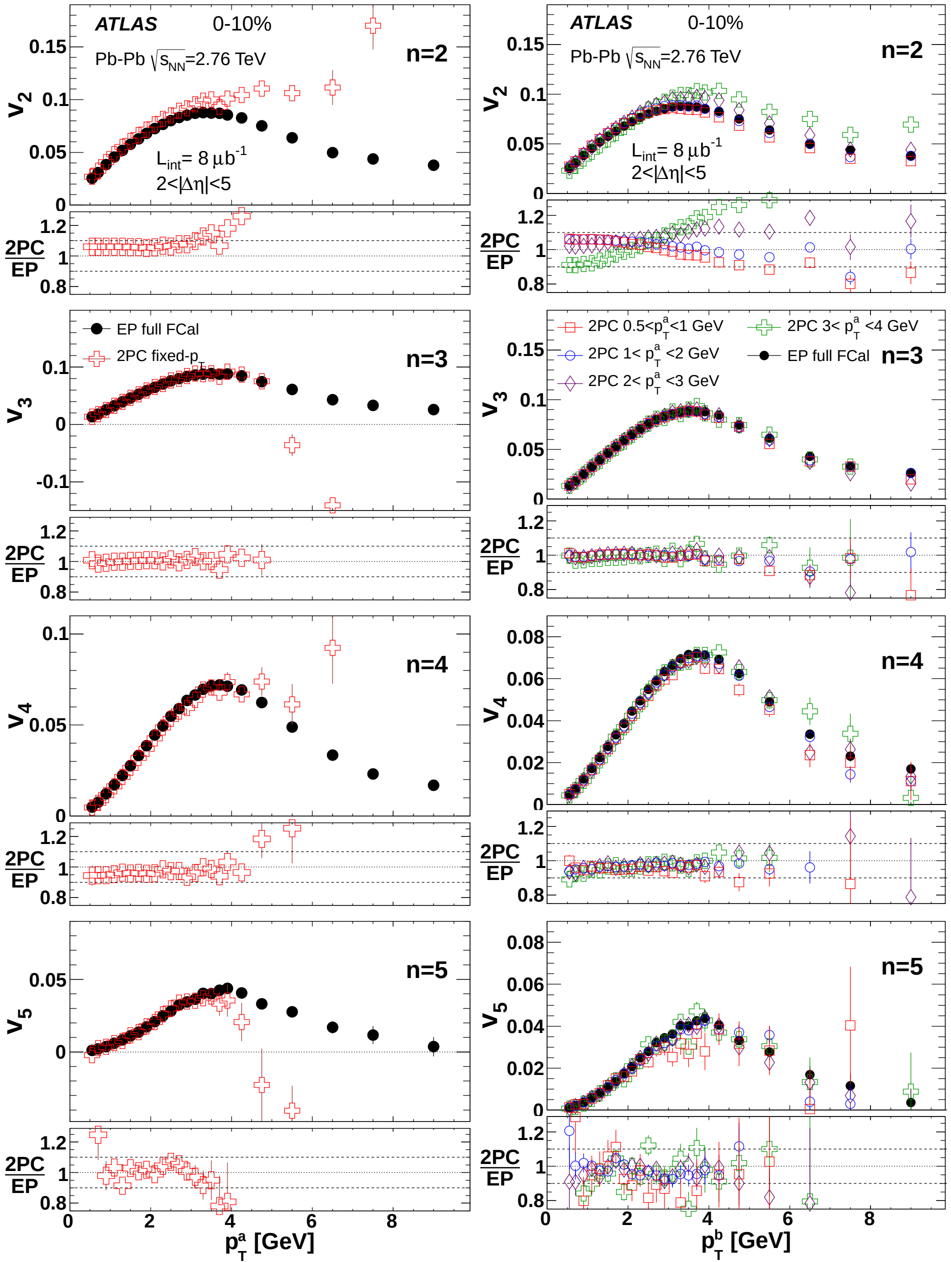

Figure 4.12: Left panels: Comparison of the $v_n(p_\mathrm{T})$ from fixed-p_T 2PC method and EP method. Right panels: Comparison of the $v_n(p_\mathrm{T})$ from mixed-p_T 2PC method with several different reference-p_T bins and the EP method. From top to bottom, the rows are v_2-v_5. The lower sub-panels show the ratios of the 2PC values to the EP values, the dashed lines indicate ±10% lines to guide the eye. All plots are for (0-10)% centrality interval.

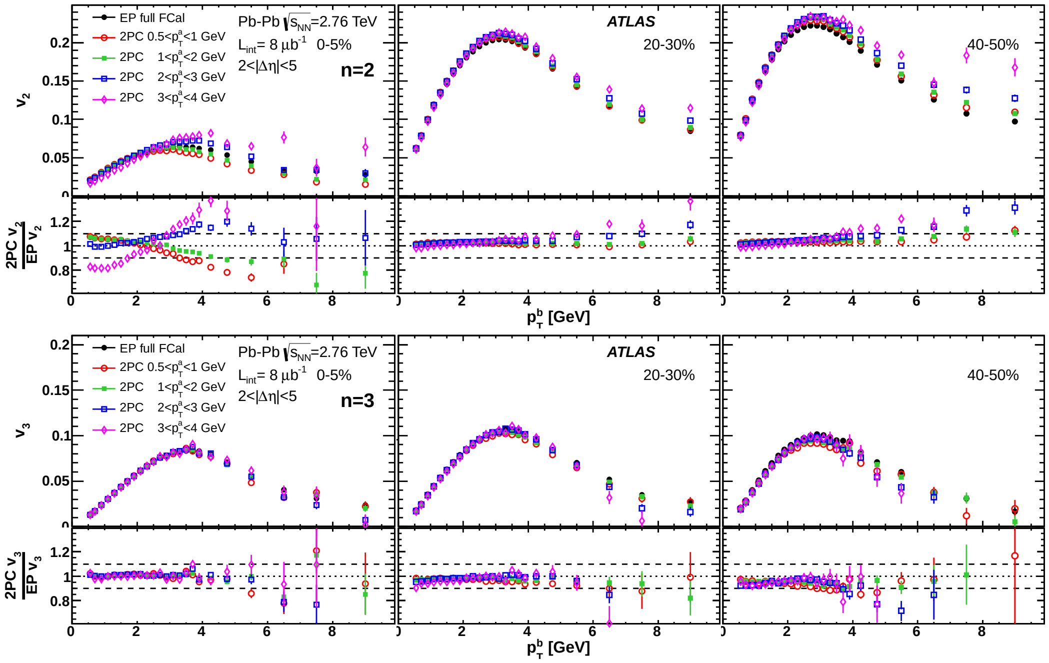

Figure 4.13: Left panels: Comparison of the $v_2(p_\mathrm{T})$ (upper panels) and $v_3(p_\mathrm{T})$ (lower panels) from mixed-p_T 2PCs with several different reference-p_T bins to the EP method. The lower sub-panels show the ratios of the 2PC values to the EP values, the dashed lines indicate ±10% lines to guide the eye. From left to right the plots are for (0-5)%, (20-30)% and (40-50)% centrality intervals respectively.

in the correlation functions, such as the ridge and the double-hump are accounted for by collective flow. In order to demonstrate this more effectively, the 2PCs are reconstructed starting from the EP v_n values. Since there are no v_1 measurements from the EP method, the reconstructed 2PC is assigned a first order component equal to that of the measured 2PC. The overall normalization of the reconstructed 2PC is adjusted to match the measured 2PC. The reconstructed correlation function is constructed as:

$$C^{reco}(\Delta\phi) = N\Big(1 + 2v_{1,1}^{\mathrm{2PC,Measured}}\cos(\Delta\phi) + 2\sum_{i=2}^{6} v_n^{\mathrm{EP,a}} v_n^{\mathrm{EP,a}}\cos(n\Delta\phi)\Big) \tag{4.10}$$

Where, the v_n^{EP} are the values measured by the $\mathrm{FCal}_{\mathrm{P(N)}}$ EP method. Figure 4.15 compares such reconstructed correlation functions for the (0-1)% centrality interval to the measured 2PCs. The measured 2PCs are well reproduced and the ridge and double hump structures recovered. It is clearly seen from

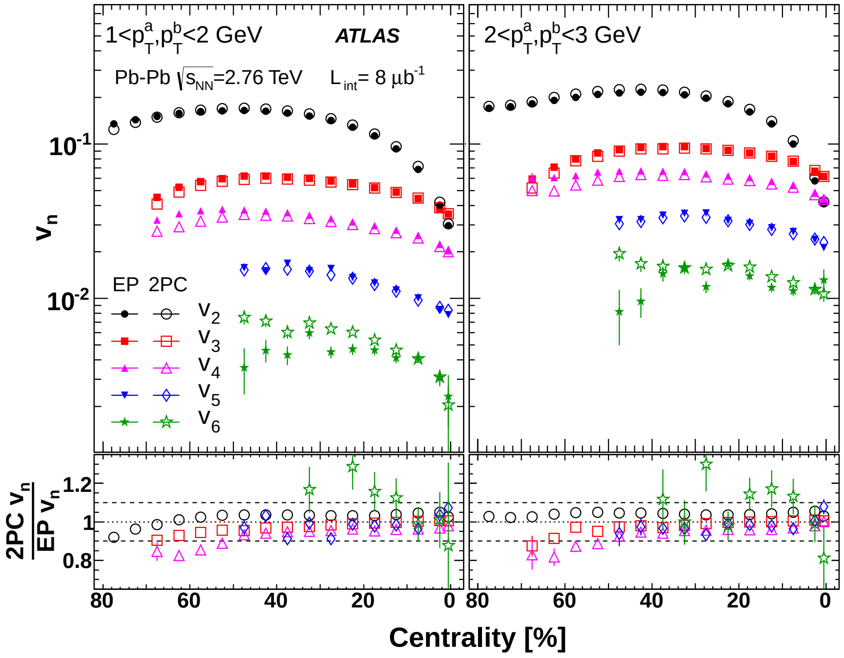

Figure 4.14: Comparison to the Event Plane results where the EP is determined with the full-FCal. The lower sub-panels show the ratio of the 2PC values to the EP values. The dashed lines indicate a ±10% band to guide the eye.

these plots that the double hump structure on the away-side arises from the interplay of even and odd harmonics. Note that in the $p_{\mathrm{T}}^{\mathrm{a}}, p_{\mathrm{T}}^{\mathrm{b}} \in (3,4)$ GeV plot (lower right panel) the $v_{1,1}$ plays a considerable role in producing the cone. However, it will be shown in Section 4.5 that at this p_{T} and centrality, the $v_{1,1}$ is dominated by collective flow. This comparison establishes that the ridge and cone are the product of collective flow and not due to jet-medium interactions as had been previously speculated.

4.5 $v_{1,1}$ and implications for the collective directed flow

Some general features of $v_{1,1}$ data

As shown in Section 4.2.4, the first Fourier coefficient of the correlation function $v_{1,1}$, does not factorize for any p_{T} and centrality. The reason that factorization breaks for $v_{1,1}$ but not for the other Fourier components, is that it is the

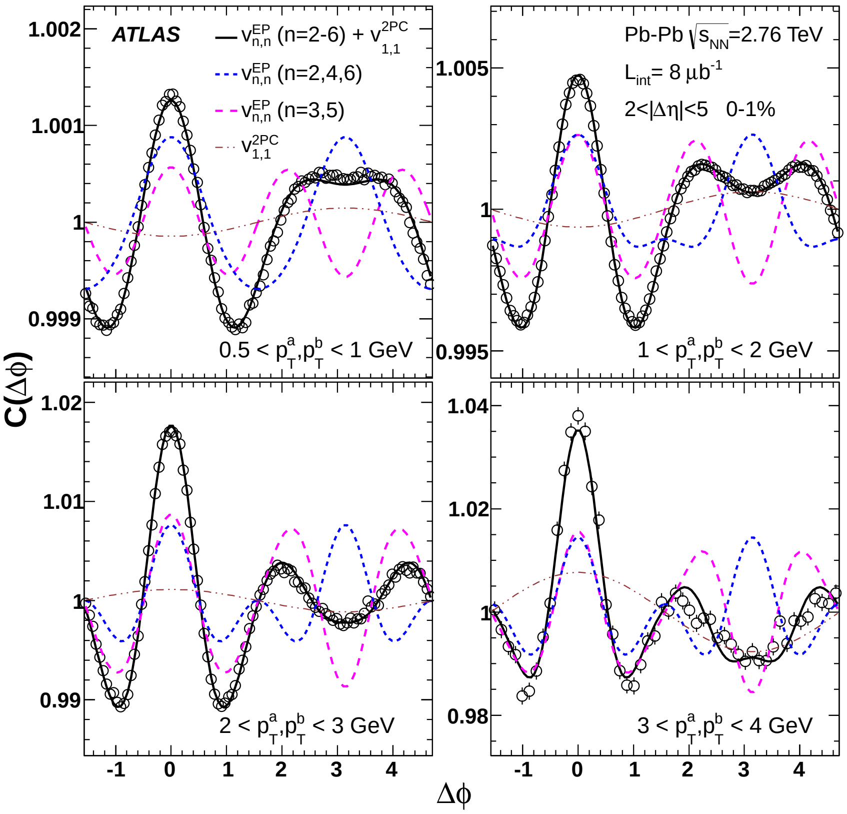

Figure 4.15: The solid black line shows the predicted two-particle correlation function using $v_2 - v_6$ measured by EP method and $v_{1,1}$ from measured two-particle correlation for the (0-1)% centrality interval. The data points are the measured 2PC. The contribution of the $v_{1,1}$ component and of the even and odd harmonics from the EP method are also separately shown.

only term influenced by the effects global momentum conservation [81, 82] – all higher-order coefficients conserve momentum by construction due to their multi-fold symmetry. One example of momentum conservation effect comes from dijets, which tend to give a negative $v_{1,1}$ at large $\Delta\eta$. Several studies on the influence of global momentum conservation on the two-particle correlations have been done [81, 82, 85–88] which show the breakdown of the factorization relation. The modified relation between $v_{1,1}$ and v_1 taking into consideration the effects of momentum conservation, is given by [81, 82]:

$$v_{1,1}({p_{\mathrm{T}}}^{\mathrm{a}}, {p_{\mathrm{T}}}^{\mathrm{b}}) \approx v_1({p_{\mathrm{T}}}^{\mathrm{a}}) v_1({p_{\mathrm{T}}}^{\mathrm{b}}) - \frac{{p_{\mathrm{T}}}^{\mathrm{a}} {p_{\mathrm{T}}}^{\mathrm{b}}}{M \langle {p_{\mathrm{T}}}^2 \rangle} \tag{4.11}$$

where M and $\langle p_{\mathrm{T}}^{2} \rangle$ are the multiplicity and average squared transverse momentum for the whole event respectively. The negative correction term in Eq. 4.11, is the leading order approximation for momentum conservation and is expected to be valid when the correction is small ($\ll$1). As can be seen from its form, the magnitude of the momentum conservation term increases linearly with the p_{T} of the two particles, but decreases with event multiplicity. A natural expectation from Eq. 4.11 is that the global momentum conservation effect is important in peripheral events and high p_{T}, but less so in central events due to the large event multiplicity (large M).

The first term of Eq. 4.11 represents contribution from genuine collective directed flow, whose dependence on η can be generally separated into a η-odd and η-even components[2]. The η-odd v_1 is believed to arise from the "sidewards deflection" of the colliding ions [43], and changes sign going from negative η to positive η [89, 90]. However this η-odd v_1 is measured to be less than 0.5% for $|\eta| < 2$ at the LHC [91]. The resulting contribution to $v_{1,1}$ is expected to be $< 2.5 \times 10^{-5}$, much smaller than the typical $v_{1,1}$ values seen in the data (see below). The η-even v_1 signal is believed to arise from the "dipole asymmetry" of the nuclear overlap region due to initial spatial fluctuations of the nucleons [46, 87]. This spatial asymmetry results in a left-right asymmetry of the pressure gradient, which drives the collective v_1. If the rapidity-even v_1 depends weakly on η similar to the higher-order flow, then its contribution to $v_{1,1}$ is expected to vary weakly with $\Delta\eta$.

Figure 4.16 shows the $\Delta\eta$ dependence of the $v_{1,1}$ extracted from the two-particle correlations for several centrality intervals and p_{T} combinations. The $v_{1,1}$ is always positive at small $\Delta\eta$, due to the contribution from the near-side jet peak and other short range correlations. The large $\Delta\eta$ behavior however changes depending on the p_{T} and centrality. For peripheral events, the $v_{1,1}$ at large $\Delta\eta$ is negative and its magnitude increases with increasing p_{T}. In central events the $v_{1,1}$ at large $\Delta\eta$ is negative at low p_{T}, but becomes positive with increasing p_{T}. Furthermore, the magnitude of $v_{1,1}$ at large $\Delta\eta$ remains relatively flat with $\Delta\eta$ in central collisions, while in peripheral collisions it peaks around $\Delta\eta \sim 2$ and then decreases weakly with $\Delta\eta$. The behavior in central collisions is consistent with a rapidity-even v_1 that is relatively flat in η at high p_{T}, while the behavior in peripheral collisions is consistent with an away-side jet contribution that decreases with $\Delta\eta$.

Since the $\Delta\eta$ dependence of $v_{1,1}$, as seen from Fig. 4.16 is weak at large $\Delta\eta$, especially in central and mid-central events, the $v_{1,1}$ is extracted from the correlation function integrated over $2 < |\Delta\eta| < 5$ to study its dependence on

---

[2] Any function $f(x)$ can be written as the sum of an even and an odd function of x given by: $even(x) = (f(x) + f(-x))/2$ and $odd(x) = (f(x) - f(-x))/2$

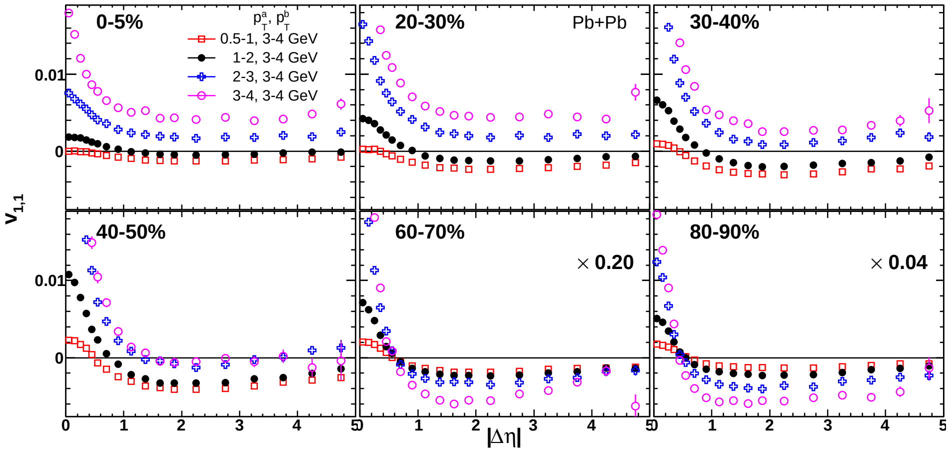

Figure 4.16: $v_{1,1}$ vs $\Delta\eta$ for several different $p_{\mathrm{T}}^{\mathrm{a}}$ bins but with $p_{\mathrm{T}}^{\mathrm{b}} \in (3,4)$ GeV. Each panel corresponds to one centrality bin. In some panels the data are rescaled to fit to the same range, the scale factors are indicated on the panels.

$p_{\mathrm{T}}^{\mathrm{a}}$ and $p_{\mathrm{T}}^{\mathrm{b}}$. The results are shown in Fig. 4.17 as a function of $p_{\mathrm{T}}^{\mathrm{b}}$ for several centralities and $p_{\mathrm{T}}^{\mathrm{a}}$ bins. The $v_{1,1}$ values are always negative in peripheral events and their magnitude increases almost linearly with $p_{\mathrm{T}}^{\mathrm{a}}$ and $p_{\mathrm{T}}^{\mathrm{b}}$, reflecting the influence of the away-side jet. In more central events, however, the magnitude of this negative $v_{1,1}$ decreases, reflecting a weakening of the global momentum conservation term by the large event multiplicity. Furthermore, Fig. 4.17 clearly shows that in central and mid-central events, a positive $v_{1,1}$ is seen for $2 \lesssim p_{\mathrm{T}}^{\mathrm{a}}, p_{\mathrm{T}}^{\mathrm{b}} \lesssim 6$ GeV, with maximum at around 4 GeV, similar to the $n \geq 2$ coefficients. The overall p_{T} and centrality dependence of $v_{1,1}$ is thus qualitatively consistent with the behavior expected from the onset of collective directed flow.

Extracting v_1 from $v_{1,1}$ data via a two component fit

To check is the $v_{1,1}$ data is well described by the two component model of Eq 4.11, a least-square fit of the following form is performed for each centrality interval:

$$\chi^2 = \sum_{a,b} \frac{\left(v_{1,1}(p_{\mathrm{T}}^{\mathrm{a}}, p_{\mathrm{T}}^{\mathrm{b}}) - [v_1^{\mathrm{Fit}}(p_{\mathrm{T}}^{\mathrm{a}}) v_1^{\mathrm{Fit}}(p_{\mathrm{T}}^{\mathrm{b}}) - c p_{\mathrm{T}}^{\mathrm{a}} p_{\mathrm{T}}^{\mathrm{b}}]\right)^2}{\left(\sigma_{a,b}^{\mathrm{stat}}\right)^2 + \left(\sigma_{a,b}^{\mathrm{sys,p2p}}\right)^2} \tag{4.12}$$

where $\sigma_{a,b}^{\mathrm{stat}}$ and $\sigma_{a,b}^{\mathrm{sys,p2p}}$ denote the statistical and point to point systematic error respectively for $v_{1,1}(p_{\mathrm{T}}^{\mathrm{a}}, p_{\mathrm{T}}^{\mathrm{b}})$. The $v_1^{\mathrm{Fit}}(p_{\mathrm{T}})$ function is defined via a smooth interpolation of the v_1 values at m discrete p_{T} points, $v_1^{\mathrm{Fit}}(p_{\mathrm{T,i}})|_{i=1}^{m}$, and these

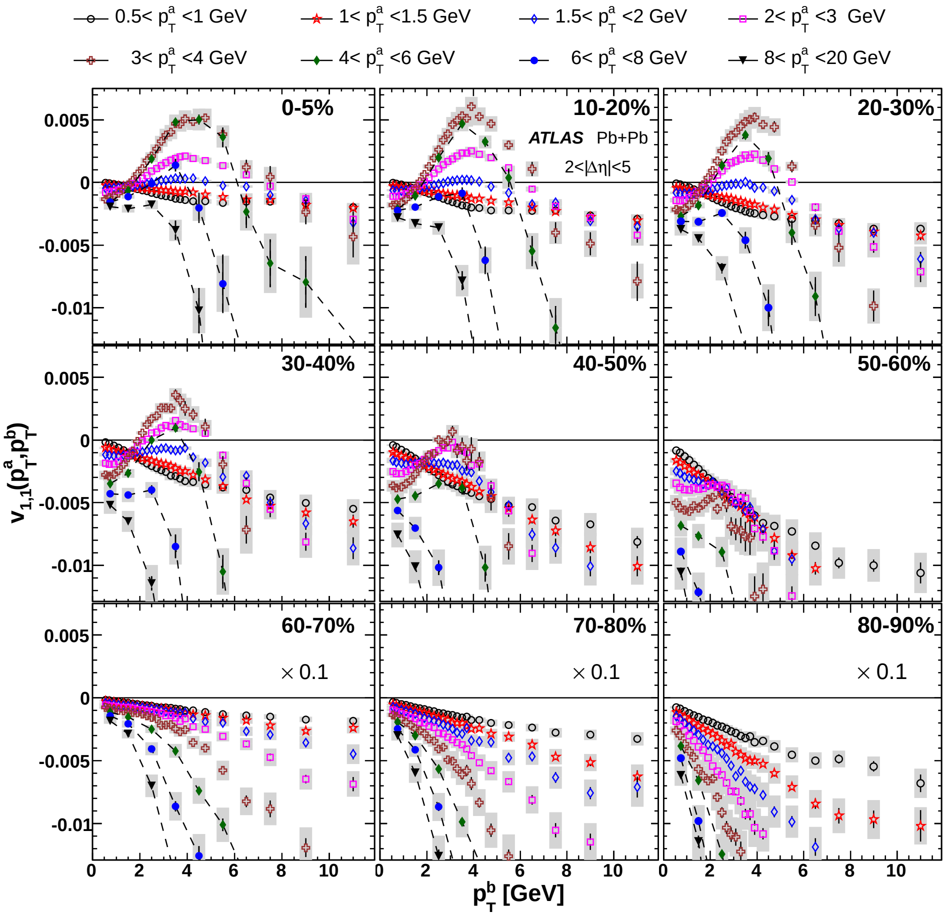

Figure 4.17: $v_{1,1}(p_{\mathrm{T}}^{\mathrm{a}}, p_{\mathrm{T}}^{\mathrm{b}})$ vs $p_{\mathrm{T}}^{\mathrm{b}}$ for several different $p_{\mathrm{T}}^{\mathrm{a}}$ intervals. The error bars and bands represent statistical and systematic uncertainties respectively. The data points for the three highest $p_{\mathrm{T}}^{\mathrm{a}}$ intervals have coarser binning in $p_{\mathrm{T}}^{\mathrm{b}}$, and hence are connected by dashed lines to guide the eye. Each panel represents one centrality interval. The data in the bottom three panels are scaled down by factor of 10 to fit within the same vertical range.

together with parameter c result in a set of $m+1$ fit parameters. The reason behind using an interpolation procedure is that the functional form of $v_1(p_{\mathrm{T}})$ is a priori unknown, but is expected to vary smoothly with p_{T}. The parameter c is introduced as the value of $M\langle p_{\mathrm{T}}^2\rangle$ is not known.

In the default setup, the $v_{1,1}$ data for the fit are restricted to $p_{\mathrm{T}}^{\mathrm{a}} <6$ GeV and $p_{\mathrm{T}}^{\mathrm{b}} <10$ GeV and a cubic spline interpolation procedure is used with the number of interpolation points m=15 (listed in Table 4.3). To account for the p_{T} correlated uncertainty ($\sigma_{a,b}^{\mathrm{sys,corr}}$), the chi-square minimization is repeated after varying all the $v_{1,1}$ data points up or down by $\sigma_{a,b}^{\mathrm{sys,corr}}$. Since $v_{1,1}(p_{\mathrm{T}}^{\mathrm{a}}, p_{\mathrm{T}}^{\mathrm{b}})$ is symmetric in $p_{\mathrm{T}}^{\mathrm{a}}$ and $p_{\mathrm{T}}^{\mathrm{b}}$, this results in the data points for $p_{\mathrm{T}}^{\mathrm{a}} < p_{\mathrm{T}}^{\mathrm{b}}$ to be correlated with those for $p_{\mathrm{T}}^{\mathrm{a}} > p_{\mathrm{T}}^{\mathrm{b}}$. This influence of this correlation is evaluated by repeating the fit using only $v_{1,1}$ data for $p_{\mathrm{T}}^{\mathrm{a}} < p_{\mathrm{T}}^{\mathrm{b}}$ or $v_{1,1}$ data for $p_{\mathrm{T}}^{\mathrm{a}} > p_{\mathrm{T}}^{\mathrm{b}}$. Note that the binning in $p_{\mathrm{T}}^{\mathrm{a}}$ and $p_{\mathrm{T}}^{\mathrm{b}}$ are not identical, so the $v_{1,1}$ data for $p_{\mathrm{T}}^{\mathrm{a}} < p_{\mathrm{T}}^{\mathrm{b}}$ and $p_{\mathrm{T}}^{\mathrm{a}} > p_{\mathrm{T}}^{\mathrm{b}}$ are not identical. The variations from the default fit results are included in the systematic errors.

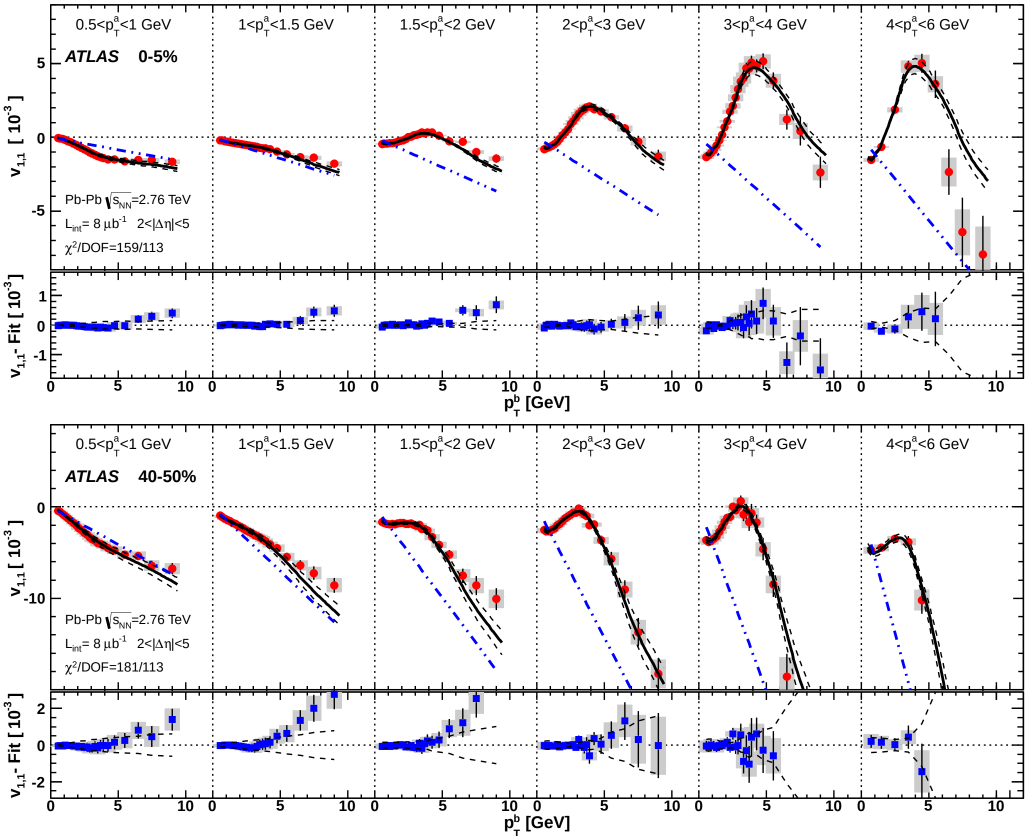

Figure 4.18: Global fit (via Eq. 4.12) of the $v_{1,1}$ data for the (0-5)% centrality interval (top panel) and (40-50)% centrality interval (bottom panel). The data are shown as a function of $p_{\mathrm{T}}^{\mathrm{b}}$ for various $p_{\mathrm{T}}^{\mathrm{a}}$ ranges, with shaded bars indicating the correlated systematic errors. The fit function and the associated systematic uncertainties are indicated by the thick solid lines and surrounding dashed and dotted lines, respectively. The dot-dashed lines (blue, with negative slope) indicate the estimated contribution from the momentum conservation component. The lower part of each panel shows the difference between the data and fit, as well as the systematic uncertainty of the fit (dashed and dotted lines).

Figure 4.18 shows the fit results for two centrality intervals: (0-5)% in the top panel and (40-50)% in the bottom panel. The $v_{1,1}$ data are plotted as a function of $p_{\mathrm{T}}^{\mathrm{b}}$ for six intervals of $p_{\mathrm{T}}^{\mathrm{a}}$. The data are well described by the two component fit (solid black lines) across broad ranges of $p_{\mathrm{T}}^{\mathrm{a}}$ and $p_{\mathrm{T}}^{\mathrm{b}}$. The typical χ^2/DOF of the fits are between 1–2 depending on the centrality, and are listed in Table 4.3. The deviations between the data and the fit, as shown in the bottom sub-panels, are $\lesssim 10^{-4}$ for p_{T} <5 GeV, but increase systematically for higher p_{T} and more peripheral events, possibly indicating the limitations of the two component assumption or the leading order approximation of the momentum conservation term in Eq. 4.11. The final results are restricted to (0-50)% most central events, for which the direct flow term in Eq. 4.11 as extracted from the data, exceeds or at least is comparable in magnitude to the momentum conservation term, and the statistical uncertainties in the fits are not too large. Fit results for other centrality selections are shown in Appendix B.4.

From Fig. 4.18, the contributions of the dipolar flow and the momentum conservation term to $v_{1,1}$ can be directly compared. The dot-dashed lines (blue, with negative slope) indicate the estimated contribution from the momentum conservation term. The difference between the fits to the $v_{1,1}$ data and the momentum conservation component, i.e. the difference between the solid-black line and the dot-dashed line gives the contribution of the dipolar flow.

The estimation of systematic uncertainties associated with the fitting and interpolation procedure is done by the following variations:

1. The interpolation function is changed from cubic spline interpolation (default) to linear interpolation and polynomial interpolation.

2. The number of interpolation points are varied from 15 (default) to 9 and 21 points.

3. The p_{T} range of the fit is varied from $p_{\mathrm{T}}^{\mathrm{a}} \in (0.5, 6)$ GeV, $p_{\mathrm{T}}^{\mathrm{b}} \in (0.5, 10)$ GeV (default) to $p_{\mathrm{T}}^{\mathrm{a}}, p_{\mathrm{T}}^{\mathrm{b}} \in (0.5, 5)$ GeV and $p_{\mathrm{T}}^{\mathrm{a}}, p_{\mathrm{T}}^{\mathrm{b}} \in (0.5, 10)$ GeV.

The total systematic uncertainties of the minimization procedure are calculated as the RMS sum of the above variations. They are small in central events but become substantial in peripheral events, and are important sources of uncertainties at intermediate p_{T}. The total absolute uncertainty is about $\delta v_1 = 0.001 - 0.004$ for p_{T} <3 GeV and increases rapidly for higher p_{T} due to increasingly larger statistical uncertainties.

A final check is done to see if the fit parameter c in Eq. 4.12 which was introduced as a substitute for the unknown $1/M\langle p_{\mathrm{T}}^2\rangle$ has the expected behavior with changing centrality or not. The fit parameter c should be inversely proportional to multiplicity M and $\langle {p_{\mathrm{T}}}^2 \rangle$ of the whole event. This is checked by calculating the product of c and the charged hadron multiplicity at mid-rapidity $\frac{dN}{d\eta}_{|\eta=0}$ from [58], with the assumption that $\frac{dN}{d\eta}_{|\eta=0}$ is proportional to M. The results are summarized in Table 4.3 for each centrality interval. Since $\langle p_{\mathrm{T}}^2 \rangle$ for the whole event is expected to vary weakly with centrality (the $\langle p_{\mathrm{T}} \rangle$ for charged pions at mid-rapidity only varies by $\sim 5\%$ within 0-50% centrality interval at LHC [92]), then the product should also vary weakly with centrality. Table 4.3 show that this is indeed the case, qualitatively supporting the assumptions underlying Eq. 4.11.

Centrality	χ^2/DOF	$c(0.001\mathrm{GeV}^{-2})$	$c\frac{dN}{d\eta}_{\lvert\eta=0}(\mathrm{GeV}^{-2})$
0-5%	159/113	0.24 ± 0.02	0.387 ± 0.035
5-10%	132/113	0.28 ± 0.02	0.374 ± 0.032
10-20%	134/113	0.35 ± 0.03	0.355 ± 0.031
20-30%	165/113	0.50 ± 0.04	0.337 ± 0.028
30-40%	186/113	0.75 ± 0.05	0.326 ± 0.027
40-50%	181/113	1.16 ± 0.09	0.320 ± 0.029

15 interpolation points used in the default fit
0.5, 0.7, 0.9, 1.1, 1.3, 1.5, 2.0, 2.5 3.0, 3.5, 4.5, 5.5, 6.5, 7.5, 9.0 GeV

Table 4.3: Quality of the fit χ^2/DOF, fit parameter c, and corresponding multiplicity scaled values $c\frac{dN}{d\eta}_{|\eta=0}$ for various centrality intervals. The uncertainty of the latter is calculated as quadrature sum of those from c and $\frac{dN}{d\eta}_{|\eta=0}$ of Ref. [58]. The bottom row lists the 15 p_{T} interpolation points used in the default fit.

Figure 4.19 shows the final extracted $v_1(p_{\mathrm{T}})$ from the fits for various centrality intervals. The shaded bands indicate combined statistical and systematic errors. The statistical uncertainty of the fit is important at high p_{T}, while the fit uncertainty from p_{T} correlated error ($\sigma_{a,b}^{\mathrm{sys,corr}}$) is important at low and intermediate p_{T}. A significant v_1 signal is observed for all centrality intervals. It reaches a maximum between 4 GeV and 5 GeV and then falls slightly at higher p_{T}. The magnitude of v_1 is large and its maximum in each centrality is comparable to that for the v_3. The centrality dependence of the v_1 is relatively weak similar to the $n > 2$ harmonics, its maximum shows a $\sim$20% variation with centrality. At $p_{\mathrm{T}} \lesssim 1$ GeV, $v_1(p_{\mathrm{T}})$ becomes negative, confirming a feature expected for collective v_1 as suggested by hydrodynamic model calculations [46, 87]. All these features together with the fact that the $v_{1,1}$

data show little $\Delta\eta$ dependence for $|\Delta\eta| > 2$ (Fig. 4.16), is consistent with the expected behavior of a η-even v_1 contribution, driven primarily by a dipolar deformation in the initial geometry.

In Fig. 4.15 it was seen that the $v_{1,1}$ played a role in producing the double-hump in the $p_T^a, p_T^b \in (3,4)$ GeV range. From The top panel of Fig. 4.18 it can be seen that at this combination of trigger and partner p_T, the contribution from dipolar flow to $v_{1,1}$ is almost thrice as large as the momentum conservation component. This shows that even at this p_T, it is the effects of collective dynamics that produce the double-hump.

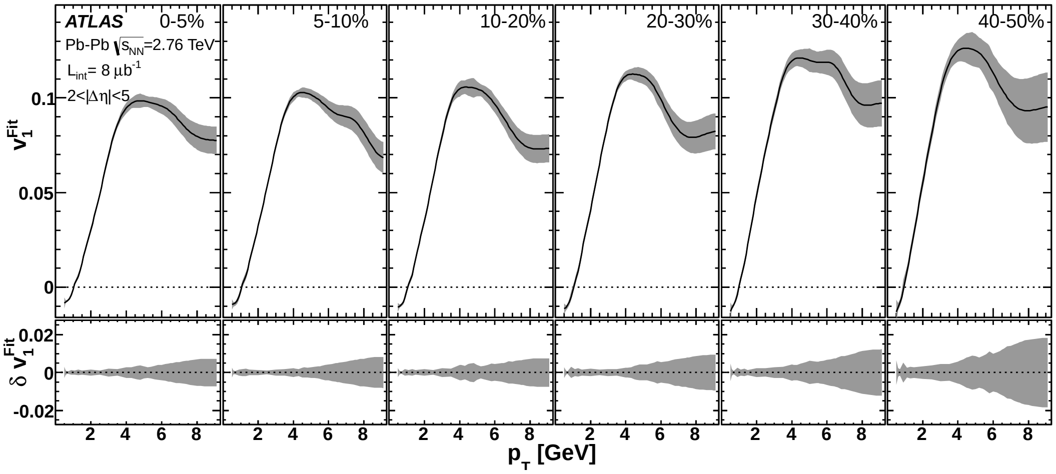

Figure 4.19: v_1 obtained from the global fit vs p_T for various centrality intervals. The shaded bands indicate the total uncertainty and are reproduced in the lower sub-panels for clarity.

4.6 Summary

In this chapter the p_T, $\Delta\eta$ and centrality dependence of the two-particle correlation functions were studied. It was shown that up to $p_T \lesssim 4$ GeV and for centrality $\lesssim 50\%$ almost all of the long-range features seen in the 2PC including the ridge and cone are accounted by collective flow. No additional jet-medium interaction models are needed to describe these structures. In this p_T and centrality range the 2PC v_2-v_6 values were shown to be consistent with the EP results and the factorization relation of the 2PC Fourier coefficients into single particle anisotropies: $v_{n,n}(p_T^a, p_T^b) = v_n(p_T^a)v_n(p_T^b)$ was shown to hold for $|\Delta\eta| > 2$. At higher p_T the factorization was shown to break down, due to the effect of the away-side jet coupled with decreasing flow. However, if the v_n for associated particles were extracted by correlating them with trigger particles having relatively softer p_{T}, the values were consistent with the EP results. This shows that not only soft-soft correlations but also hard-soft correlations are primarily driven by the global event shape.

For $v_{1,1}$ the factorization was shown to not hold for any p_{T} or centrality, because of the effects of global momentum conservation. However using a two-component fit to the $v_{1,1}$ data, the parity-even v_1 associated with the dipole asymmetry of the initial geometry was extracted. Its p_{T} and centrality dependence were studied and its magnitude was shown to be fairly large, comparable to v_3 indicating a significant dipole asymmetry in the initial geometry.

Chapter 5

Measurement of event-by-event distributions of flow harmonics in Pb+Pb collisions

The previous two chapters detailed extensive measurements of the flow harmonics v_1-v_6. The large values of odd harmonics especially v_1 and v_3 indicate the presence of considerable event-by-event (EbyE) fluctuations in the shape of the initial geometry. Such fluctuations have been a topic of considerable theoretical study [44, 93]. Calculations based on the Glauber model have shown that fluctuations in the eccentricity vectors $\boldsymbol{\epsilon}_n$ are well described by 2D-Gaussian distributions about a mean eccentricity vector $\boldsymbol{\epsilon}_n^{\mathrm{RP}}$ which lies along the reaction-plane as [44]:

$$p(\boldsymbol{\epsilon}_n) = \frac{1}{2\pi\delta_{\epsilon_n}^2} e^{-\left(\boldsymbol{\epsilon}_n - \boldsymbol{\epsilon}_n{}^{\mathrm{RP}}\right)^2 / \left(2\delta_{\epsilon_n}^2\right)} \tag{5.1}$$

where, δ_{ϵ_n} quantifies the EbyE fluctuations and $\boldsymbol{\epsilon}_n^{\mathrm{RP}}$ the role of the mean geometry. For the lower order harmonics (n=2,3) hydrodynamic calculations have shown that the v_n are correlated to the ϵ_n in the initial geometry [47, 52]. In such cases the EbyE distributions of the v_n are expected to have a similar form as the EbyE distributions of the ϵ_n:

$$p(\boldsymbol{v}_n) = \frac{1}{2\pi\delta_{v_n}^2} e^{-\left(\boldsymbol{v}_n - \boldsymbol{v}_n{}^{\mathrm{RP}}\right)^2 / \left(2\delta_{v_n}^2\right)} \tag{5.2}$$

where, as in Eq. 5.1, $\boldsymbol{v}_n^{\mathrm{RP}}$ is aligned along the reaction-plane and characterizes the effects of the mean overlap geometry and δ_{v_n} characterizes the fluctuations in the $\boldsymbol{v}_n$. The EbyE distribution of $v_n = |\boldsymbol{v}_n|$ can be obtained by projecting Eq. 5.2 along the radial direction and is given by:

$$p(v_n) = \frac{v_n}{\delta^2_{_{v_n}}} e^{-\frac{(v_n)^2+(v_n^{\mathrm{RP}})^2}{2\delta^2_{v_n}}} I_0\left(\frac{v_n^{\mathrm{RP}} v_n}{\delta^2_{_{v_n}}}\right) , \tag{5.3}$$

where, I_0 is the modified Bessel function of the first kind. The above functional form is commonly called a Bessel-Gaussian function [43]. The parameters v_n^{RP} and $\delta_{_{v_n}}$ in Eq. (5.3) are related to $\langle v_n \rangle$ and σ_{v_n}. For small fluctuations $(\delta_{_{v_n}} \ll v_n^{\mathrm{RP}})$ [44]:

$$\delta_{_{v_n}} \approx \sigma_{v_n}, \quad \left(v_n^{\mathrm{RP}}\right)^2 \approx \langle v_n \rangle^2 - \delta^2_{_{v_n}} . \tag{5.4}$$

For large fluctuations i.e. $\delta_{_{v_n}} \gg v_n^{\mathrm{RP}}$ (e.g. in central collisions), Eq. 5.3 can be approximated by:

$$p(v_n) = \frac{v_n}{\delta^2_{_{v_n}}} e^{-v_n{}^2/\left(2\delta^2_{v_n}\right)}, \tag{5.5}$$

where, the fact that $I_0(0) = 1$ has been used. This is the "fluctuation-only" scenario, i.e. $v_n^{\mathrm{RP}} = 0$. In this case, both the mean and the width are determined by $\delta_{_{v_n}}$ [94]:

$$\langle v_n \rangle = \sqrt{\frac{\pi}{2}}\, \delta_{_{v_n}}, \ \sigma_{v_n} = \sqrt{2 - \frac{\pi}{2}}\, \delta_{_{v_n}}, \tag{5.6}$$

which gives:

$$\frac{\sigma_{v_n}}{\langle v_n \rangle} = \sqrt{\frac{4}{\pi} - 1} = 0.523, \ \sqrt{\langle v_n^2 \rangle} = \frac{2}{\sqrt{\pi}} \langle v_n \rangle = 1.13 \langle v_n \rangle . \tag{5.7}$$

The quantities $\langle v_n \rangle$, σ_{v_n}, $\sqrt{\langle v_n^2 \rangle}$, $\sigma_{v_n}/\langle v_n \rangle$, v_n^{RP} and $\delta_{_{v_n}}$, have been extensively studied both experimentally [66, 95, 96] and in theoretical models [44, 67, 93]. Typically the fluctuation measurements are done using two- and four-particle multi-particle cumulants, which assume that the distributions are Bessel-Gaussian and proceed to evaluate the above quantities [97, 98]. Measurements of higher order multi-particle cumulants suggest that the v_2 distributions are consistent with the Bessel-Gaussian distributions [99, 100]. However, this consistency is inferred indirectly from agreement among four-, six- and eight-particle cumulants.

Direct measurements of the EbyE v_n distributions, presented in this chapter can check whether the Bessel-Gaussian functions correctly describe the data or not. Note that Eq. 5.3 only holds in the limit of linear response ($\boldsymbol{v_n} \propto \boldsymbol{\epsilon_n}$). Thus effects of non-linear response can be quantified by the deviations of the measured v_n distributions from this functional form.

The organization of this chapter is as follows: In Section 5.1 the methodology used to measure the EbyE distributions is described. In Sections 5.2 and 5.3 the implementation of the method as well as estimation of systematic uncertainties are done. The final results as well as comparison to theoretical models are presented in Section 5.4. The measurements presented in this chapter have been submitted for publication [101].

5.1 Methodology

5.1.1 Observed single particle EbyE distributions

The top panels of Figure 5.1 show the azimuthal distribution of reconstructed charged tracks with p_{T} above 0.5 GeV and $|\eta| < 2.5$ in three individual events in the (0-5)% centrality interval. The bottom panels show the corresponding two-particle correlations. The modulations are clearly much larger than the detector acceptance effects (solid red points). The 2PC distributions for the three events show clear two-peak, three-peak and four-peak structure in the first second and third event respectively. This indicates that the dominant harmonic in the three events is n=2, 3 and 4 respectively, even though the three events are from the same centrality interval, indicating the important role of fluctuations.

In the absence of detector effects, the single particle azimuthal distributions as the ones shown in Fig. 5.1 can be expanded into a Fourier series:

$$\begin{aligned} \frac{dN}{d\phi} &\propto 1 + 2\sum_{n=1}^{\infty} v_n^{\mathrm{obs}} \cos n(\phi - \Psi_n) \\ &= 1 + 2\sum_{n=1}^{\infty} \left(v_n^{\mathrm{x,obs}} \cos n\phi + v_n^{\mathrm{y,obs}} \sin n\phi)\right), \end{aligned} \tag{5.8}$$

where,

$$\begin{gathered} v_n^{\mathrm{x,obs}} = \langle \cos n\phi \rangle, v_n^{\mathrm{y,obs}} = \langle \sin n\phi \rangle \\ v_n^{\mathrm{obs}} = \sqrt{\left(v_n^{\mathrm{x,obs}}\right)^2 + \left(v_n^{\mathrm{y,obs}}\right)^2}, \tan n\Psi_n = \frac{v_n^{\mathrm{y,obs}}}{v_n^{\mathrm{x,obs}}}. \end{gathered} \tag{5.9}$$

The averaging $\langle ... \rangle$ is over all particles in a given η range. The v_n^{obs} is simply the magnitude of the observed "flow vector" normalized by the number of

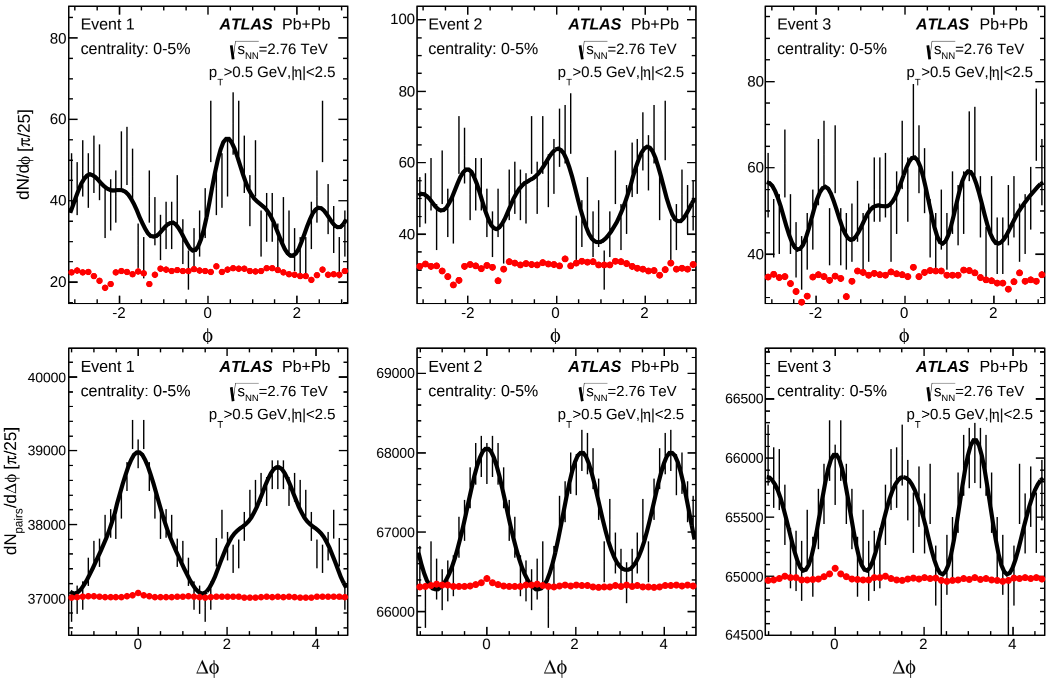

Figure 5.1: Single particle ϕ (top) and pair $\Delta\phi$ (bottom) distributions for three events (from left to right) in the (0-5)% centrality interval. The bars indicate the foreground distributions, the curves indicate a simple Fourier parameterization including first six harmonics, and the red solid points indicate the acceptance functions. Tracks above 0.5 GeV are used.

particles. It is called the observed **per-particle flow vector**. In the limit of infinite multiplicity, it should approach the true flow signal $v_n^{\mathrm{obs}} \rightarrow v_n$ (and $\Psi_n \rightarrow \Phi_n$). However, the finite observed multiplicity of the event leads to smearing of the observed v_n about the true[1] v_n. In order to measure the EbyE v_n distribution, the response function $p(v_n^{\mathrm{obs}}|v_n)$, which gives the probability for measuring a particular v_n^{obs} for a given true v_n has to be determined. This is then used to unfold the measured v_n^{obs} distribution to remove the smearing effects due to the finite multiplicity, to obtain the true EbyE v_n distribution.

The measured distributions need to be corrected to account for the non-uniform detector acceptance. This is achieved by dividing the foreground

---

[1] This smearing effect can make v_n^{obs} both larger and smaller than the true v_n, although on average it will be larger. This is in contrast to the EP method, where the v_n^{obs} was smaller than the true v_n as the phase Ψ_n and the flow harmonic v_n were determined using a different set of particles (or different detectors). Also note that the v_n^{obs} in the EP method is obtained by averaging over many events, while here the v_n^{obs} refers to the anisotropy in a single event.

track distribution ($S(\phi)$) of a given event by the acceptance function ($B(\phi)$) obtained by averaging the track distributions over all events within the same centrality interval (solid red points in Fig. 5.1). In order to account for the tracking efficiency[2] ϵ, which changes as a function of p_{T} and η, each track is weighted by $1/\epsilon(p_{\mathrm{T}}, \eta)$. Weighting by $1/\epsilon(p_{\mathrm{T}}, \eta)$ corrects for the fact that only a fraction $\epsilon(p_{\mathrm{T}}, \eta)$ of tracks are reconstructed. The corrected distribution is thus obtained as:

$$\frac{dN}{d\phi} \propto C(\phi) = \frac{S(\phi)}{B(\phi)} = \frac{1 + 2\sum_{n=1}^{\infty}(v_n^{\mathrm{x,raw}} \cos n\phi + v_n^{\mathrm{y,raw}} \sin n\phi)}{1 + 2\sum_{n=1}^{\infty}(v_n^{\mathrm{x,det}} \cos n\phi + v_n^{\mathrm{y,det}} \sin n\phi)}. \tag{5.10}$$

where, $v_n^{\mathrm{x,raw}}$ and $v_n^{\mathrm{y,raw}}$ are the mean cosine and sine values of the track-phi distributions with each track weighted by $1/\epsilon(p_{\mathrm{T}}, \eta)$:

$$\begin{aligned} v_n^{\mathrm{x,raw}} &= \frac{\sum_i (\cos n\phi_i)/\epsilon(\eta_i, p_{\mathrm{T},i})}{\sum_i 1/\epsilon(\eta_i, p_{\mathrm{T},i})} = \left\langle \frac{\cos n\phi}{\epsilon} \right\rangle \\ v_n^{\mathrm{y,raw}} &= \frac{\sum_i (\sin n\phi_i)/\epsilon(\eta_i, p_{\mathrm{T},i})}{\sum_i 1/\epsilon(\eta_i, p_{\mathrm{T},i})} = \left\langle \frac{\sin n\phi}{\epsilon} \right\rangle \end{aligned} \tag{5.11}$$

and $v_n^{\mathrm{x,det}}$ and $v_n^{\mathrm{y,det}}$ are calculated by averaging over all tracks in all events, and hence represent the Fourier coefficients of the detector acceptance function in azimuth:

$$\begin{aligned} v_n^{\mathrm{x,det}} &= \frac{\sum_{\mathrm{events}} \sum_i \left(\cos n\phi_i\right)/\epsilon(\eta_i, p_{\mathrm{T},i})}{\sum_{\mathrm{events}} \sum_i 1/\epsilon(\eta_i, p_{\mathrm{T},i})} \approx \langle v_n^{\mathrm{x,raw}} \rangle_{\mathrm{events}}, \\ v_n^{\mathrm{y,det}} &= \frac{\sum_{\mathrm{events}} \sum_i \left(\cos n\phi_i\right)/\epsilon(\eta_i, p_{\mathrm{T},i})}{\sum_{\mathrm{events}} \sum_i 1/\epsilon(\eta_i, p_{\mathrm{T},i})} \approx \langle v_n^{\mathrm{y,raw}} \rangle_{\mathrm{events}} \end{aligned} \tag{5.12}$$

From Eq. 5.10 and Eq. 5.8 it follows that for small $v_n^{\mathrm{x,det}}$ and $v_n^{\mathrm{y,det}}$ the acceptance effects can be approximated as:

$$v_n^{\mathrm{x,obs}} \approx v_n^{\mathrm{x,raw}} - v_n^{\mathrm{x,det}}, v_n^{\mathrm{y,obs}} \approx v_n^{\mathrm{y,raw}} - v_n^{\mathrm{y,det}} \tag{5.13}$$

---

[2] The $\epsilon(p_{\mathrm{T}}, \eta)$ is the tracking efficiency which gives the probability that a track with a particular p_{T} and η (but averaged over ϕ) will be reconstructed and is determined from ATLAS MC simulations. The acceptance function $B(\phi)$ is the modulation in the ϕ acceptance and can be obtained by a data driven procedure i.e. averaging the track distribution over several events.

This is similar to the recentering correction that was done in the EP analysis (Chapter 3) for the FCal. From Fig 5.1 it is clear that indeed the $v_n^{\mathrm{x,det}}$ and $v_n^{\mathrm{y,det}}$ are small and this approximation is valid. A more direct way of taking into account the acceptance effect in ϕ, without any approximation is to weight the tracks by $1/B(\phi)$ (besides the $1/\epsilon(p_{\mathrm{T}},\eta)$ weight). This already corrects for the azimuthal detector anisotropy at the $v_n^{\mathrm{x/y,raw}}$ calculation.

$$
\begin{aligned}
v_n^{\mathrm{x,obs}} &= \frac{\sum_i \frac{\cos n\phi_i}{B(\phi_i)\epsilon(\eta_i,p_{T,i})}}{\sum_i \frac{1}{B(\phi_i)\epsilon(\eta_i,p_{T,i})}} = \left\langle \frac{\cos n\phi}{B(\phi)\epsilon} \right\rangle , \\
v_n^{\mathrm{y,obs}} &= \frac{\sum_i \frac{\sin n\phi_i}{B(\phi_i)\epsilon(\eta_i,p_{T,i})}}{\sum_i \frac{1}{B(\phi_i)\epsilon(\eta_i,p_{T,i})}} = \left\langle \frac{\sin n\phi}{B(\phi)\epsilon} \right\rangle
\end{aligned} \tag{5.14}
$$

The differences between using Eq. 5.14 and Eq. 5.13 have been explicitly checked and found to be negligible.

Figure 5.2 shows the EbyE distribution of the observed per-particle flow vector $\boldsymbol{v}_2^{\mathrm{obs}} = (v_2^{\mathrm{x,obs}}, v_2^{\mathrm{y,obs}}) = (v_2^{\mathrm{obs}} \cos 2\Psi_n^{\mathrm{obs}}, v_2^{\mathrm{obs}} \sin 2\Psi_n^{\mathrm{obs}})$, and its magnitude v_2^{obs}, in the (20-25)% centrality interval.

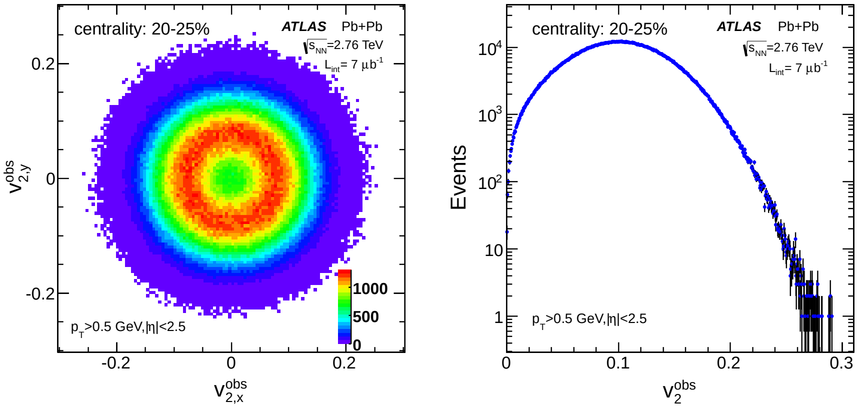

Figure 5.2: The distribution of $\boldsymbol{v_2^{\mathrm{obs}}}$ flow vector (left panel) and the magnitude (right panel) for events in (20-25)% centrality interval.

5.1.2 Determining the response function

Due to finite multiplicity, the measured flow vector is smeared randomly around the true flow vector by a 2D smearing function $p(\boldsymbol{v}_n^{\mathrm{obs}}|\boldsymbol{v}_n)$. This smearing function will be a 2D Gaussian if the smearing is purely statistical. This is shown schematically in Fig. 5.3. The arrow represents the true flow vector $\boldsymbol{v_n}$ in an event. The smaller circle (red) represents the size of the fluctuation of the observed flow vector about the true vector when determined using all tracks within the ATLAS acceptance of $-2.5 < \eta < 2.5$. If only half of the ATLAS tracking acceptance is used in determining the observed flow vector, i.e. $0 < \eta < 2.5$ or $-2.5 < \eta < 0$, the size of the fluctuations will be larger by a factor of $\sqrt{2}$, while the true $\boldsymbol{v_n}$ remains the same. This larger fluctuation for the subevent $\boldsymbol{v_n^{\mathrm{obs}}}$ is indicated by the larger circle (blue) in Fig. 5.3.

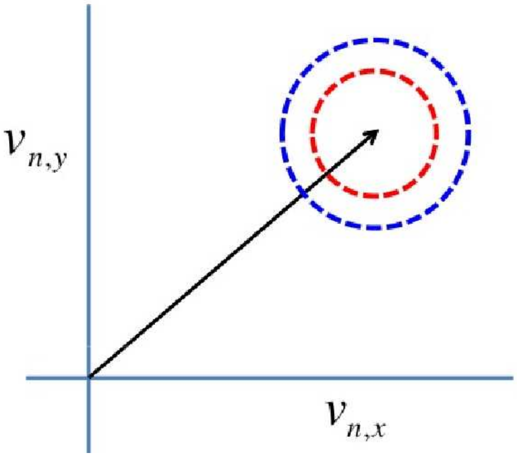

Figure 5.3: Schematic of procedure used to obtain response function. The black line represents the true flow vector in an event. The red circle represents the fluctuation of the observed flow vector about the true vector when determined using all tracks within the ATLAS acceptance of $-2.5 < \eta < 2.5$. The blue circle fluctuation of the observed flow vector about the true vector when using tracks in only half of the ATLAS acceptance i.e. $0 < \eta < 2.5$ or $-2.5 < \eta < 0$. The red circle is $\sqrt{2}$ times larger than the blue circle.

If the observed flow vector measured in the $\eta > 0$ subevent is subtracted from the one measured in the $\eta < 0$ subevent, the physical flow signal cancels, giving a 2D Gaussian distribution that is centered around the origin but is $\sqrt{2}$ larger than the fluctuations in the individual subevents[3]. The response function for the subevents is obtained by scaling down this difference distribution by a factor of $\sqrt{2}$ along the x and y-axes. And scaling it down by another factor of $\sqrt{2}$ gives the response function for the full-event.

The first panel of Fig 5.4 shows the distribution of flow vector differences between the two subevents, $p\left((\boldsymbol{v}_2^{\mathrm{obs}})^{\mathrm{a}} - (\boldsymbol{v}_2^{\mathrm{obs}})^{\mathrm{b}}\right)$ for the (20-25)% centrality

---

[3] The difference between two Gaussian random variables with identical widths is again a Gaussian distribution but with a width that is $\sqrt{2}$ times larger.

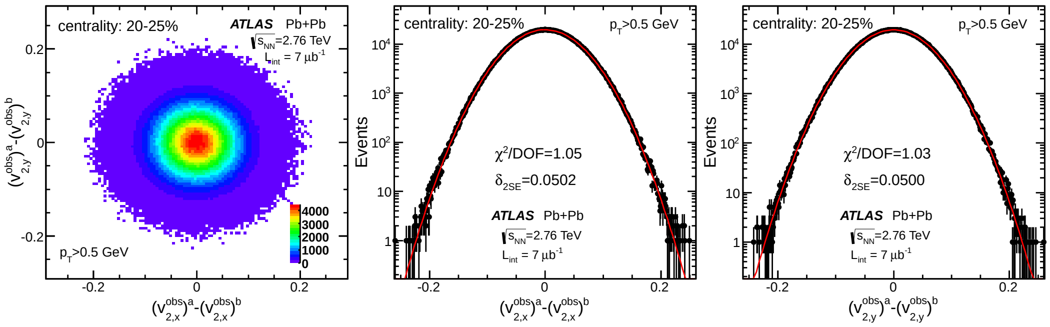

Figure 5.4: (left panel) The distribution of the difference between the flow vectors of the two half ID for events in the (20-25)% centrality interval. (middle panel) The projection on to the x-axis overlaid with a fit to Gaussian function. (right panel) The projection on to the y-axis overlaid with a fit to Gaussian function.

interval. As explained before, the physical flow signal cancels in this distribution and it contains only the effect of statistical smearing. The next two panels of Fig. 5.4 show the x and y projections of this distribution together with fits to a Gaussian function. The fits describe the data across five orders of magnitude with the same widths along both directions, implying that the smearing effect is indeed statistical. The smearing widths are also found to be the same for the x and y-axis directions within 0.1%. Denoting the width of this distribution as $\delta_{\rm 2SE}$, then the width of the response function of the half ID and the full ID should be $\delta_{\rm 2SE}/\sqrt{2}$ and $\delta_{\rm 2SE}/2$, respectively; they can be obtained by rescaling left panel of Figure 5.4 in both dimensions by a constant factor c: $p(\boldsymbol{v}_n^{\rm obs}|\boldsymbol{v}_n) = p\left(c\left[(\boldsymbol{v}_n^{\rm obs})^{\rm a} - (\boldsymbol{v}_n^{\rm obs})^{\rm b}\right]\right)$, with $c = 2$ and $\sqrt{2}$ for the full-ID and half-ID, respectively. The 2D response function for a given true $\boldsymbol{v}_n = (v_n^x, v_n^y)$ is :

$$p(\boldsymbol{v}_n^{\rm obs}|\boldsymbol{v}_n) \propto e^{-\frac{|\boldsymbol{v}_n^{\rm obs}-\boldsymbol{v}_n|^2}{2\delta^2}}, \delta = \begin{cases} \delta_{\rm 2SE}/\sqrt{2} & \text{for half ID} \\ \delta_{\rm 2SE}/2 & \text{for full ID} \end{cases} \tag{5.15}$$

The 1D response function that relates the $v_n^{\rm obs}$ to the v_n, is obtained by expressing Eq. 5.15 in polar coordinates and integrating out the azimuthal angle, which gives:

$$\begin{aligned} p(v_n^{\mathrm{obs}}|v_n) &\propto (v_n^{\mathrm{obs}})e^{-\frac{(v_n^{\mathrm{obs}})^2+v_n^2}{2\delta^2}} I_0\left(\frac{(v_n^{\mathrm{obs}})v_n}{\delta^2}\right) \\ &= (v_n+s)e^{-\frac{(v_n+s)^2+v_n^2}{2\delta^2}} I_0\left(\frac{(v_n+s)v_n}{\delta^2}\right) \end{aligned} \tag{5.16}$$

where I_0 is the modified Bessel function of the first kind, and $s = v_n^{\mathrm{obs}} - v_n$ represents the smearing of the observed v_n about the true v_n. This analytical function, which is a Bessel-Gaussian function, can be used to directly unfold the v_n^{obs} distribution, i.e. the right panel of Figure 5.2.

Figure 5.5 shows the shape of response function given by Eq. 5.16 for $\delta = 0.01$ and $v_n = 0.01 \times i$, with i=0,1,2,.... The response functions are represented by the curves, while the corresponding v_n values are indicated by the vertical lines. Clearly the Bessel-Gaussian function approaches Gaussian function when $v_n >> \delta$.

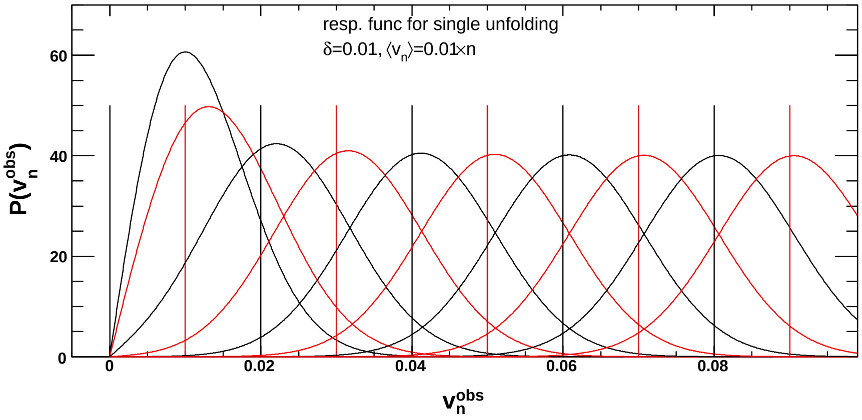

Figure 5.5: The response function Eq. 5.16 for $\delta = 0.01$ and $v_n = 0.01 \times i$, with i=0,1,2,... The response functions are represented by the curves, while the corresponding input v_n values are indicated by the vertical lines.

A detailed investigation of the shape of the response function has been carried out for n=2-6 and for various centrality selections. The details are given in Appendix C.1. In summary, the Gaussian description works very well for centrality interval up to (50-55)%. Beyond that, the distributions become noticeably non-Gaussian, in particular, the tail of the response function is broader than the Gaussian function. Instead, these distributions are described well with the t-distribution, which is the general probability distribution for the difference between two independent estimate of the average. The t-distribution approaches Gaussian-distribution when the degrees of freedom, represented by the number of tracks, becomes large. In this analysis the 1D response functions are obtained numerically from the 2D $(\boldsymbol{v}_2^{\mathrm{obs}})^{\mathrm{a}} - (\boldsymbol{v}_2^{\mathrm{obs}})^{\mathrm{b}}$ distributions, instead of using the analytic form in Eq. 5.16 (which assumes that the 2D response functions are Gaussian). For systematic studies however the analysis is also done with the analytic response function Eq. 5.16.

The two-subevent method discussed here to obtain the response function has been studied extensively in [102], where it was shown that unfolding using this response function not only removes statistical fluctuations, but also removes non-flow effects that are uncorrelated between the two subevents.

5.1.3 Unfolding of the EbyE pair distribution

The unfolding procedure can also be used on EbyE two-particle correlations. Two subevents in opposite hemispheres but with the same η acceptance are chosen, so they have the same response function in the case of the single particle unfolding. The pair distribution is obtained by correlating the tracks in the first subevent with those from the second subevent[4]:

$$\begin{aligned}
\frac{dN^{pairs}}{d\Delta\phi} &\propto \left[1 + 2\sum_n \left(v_n^{\mathrm{x,obs_1}} \cos n\phi_1 + v_n^{\mathrm{y,obs_1}} \sin n\phi_1\right)\right] \\
&\quad \otimes \left[1 + 2\sum_n \left(v_n^{\mathrm{x,obs_2}} \cos n\phi_2 + v_n^{\mathrm{y,obs_2}} \sin n\phi_2\right)\right] \\
&= 1 + 2\sum_n \Bigg(\left(v_n^{\mathrm{x,obs_1}} v_n^{\mathrm{x,obs_2}} + v_n^{\mathrm{y,obs_1}} v_n^{\mathrm{y,obs_2}}\right) \cos n\Delta\phi \\
&\quad + \left(v_n^{\mathrm{x,obs_1}} v_n^{\mathrm{y,obs_2}} - v_n^{\mathrm{y,obs_1}} v_n^{\mathrm{x,obs_2}}\right) \sin n\Delta\phi \Bigg) \\
&\equiv 1 + 2\sum_n \left(A \cos n\Delta\phi + B \sin n\Delta\phi\right) \qquad (5.17)
\end{aligned}$$

where the tracking efficiency weighting has been applied for v_n^x and v_n^y on a track-by-track basis as defined in Eq. 5.10. An EbyE pair variable $v_{n,n}^{\mathrm{obs}}$ is subsequently calculated as :

---

[4] This pair correlation is slightly different than the ones described in chapter 4, where there was no restriction on the η of the particles. Here particle-pairs are made with one particle from $\eta < 0$ and another with $\eta > 0$, i.e. no pairs with both particles from the same η range. For the 2PC's in chapter 4 an EbyE analysis is difficult to do as it is not clear how obtain a response function.

$$\begin{aligned} v_{n,n}^{\mathrm{obs}} &= \sqrt{A^2+B^2} = \sqrt{\left[\left(v_n^{\mathrm{x,obs_1}}\right)^2+\left(v_n^{\mathrm{y,obs_1}}\right)^2\right]\left[\left(v_n^{\mathrm{x,obs_2}}\right)^2+\left(v_n^{\mathrm{y,obs_2}}\right)^2\right]} \\ &= v_n^{\mathrm{obs_1}} v_n^{\mathrm{obs_2}} \end{aligned} \tag{5.18}$$

Note that the term $B \sin n\Delta\phi$ in Eq. 5.17 is essential and captures some additional statistical fluctuations.

The observed flow signal from correlation analysis is defined as

$$v_n^{\mathrm{obs,2PC}} = \sqrt{v_{n,n}^{\mathrm{obs}}} = \sqrt{v_n^{\mathrm{obs_1}} v_n^{\mathrm{obs_2}}} = \sqrt{(v_n+s_1)(v_n+s_2)} \tag{5.19}$$

where s_1 and s_2 are independent smearing functions described by the probability distribution Eq. 5.16 with $\delta = \delta_{\mathrm{2SE}}/\sqrt{2}$. Clearly the smearing for $v_n^{\mathrm{obs,2PC}}$ is very different in nature from that for the single particle $v_n^{\mathrm{obs}} = v_n + s$ defined in the previous section. For example, in the limit of small signal v_n, the $s_1 s_2$ term dominates the smearing, which makes the distribution broader than v_n^{obs}. For large v_n, however, s_1 and s_2 are approximately Gaussian (see Figure 5.5),

$$v_n^{\mathrm{obs,2PC}} \approx \sqrt{v_n^2 + v_n(s_1+s_2)} \approx v_n + \frac{s_1+s_2}{2} = v_n + s_1/\sqrt{2} = v_n + s. \tag{5.20}$$

The last two steps in Eq. 5.20 follow from the fact that the mean of two Gaussian random variables is equivalent to a Gaussian with a $\sqrt{2}$ times narrower width, and that the smearing of half ID (s_1 and s_2) is $\sqrt{2}$ broader than that for the full ID (s). Hence, for sufficiently large v_n, the distribution of $v_n^{\mathrm{obs,2PC}}$ from correlation of the two half ID is expected to approach the v_n^{obs} distributions from the full ID. The 2PC response function can be generated analytically from the measured response function for the single particle v_n (e.g. Figure 5.2). Figure 5.6 shows the shape of 2PC response function generated from Eq. 5.16 and Eq. 5.20 for $\delta = 0.01$ and $v_n = 0.01 \times i$, with i=0,1,2,... (dashed curves). They are compared with the response functions for single particle unfolding (solid curves). The corresponding input true v_n values are indicated by the vertical lines. Clearly the 2PC response function is always broader than the corresponding the single particle response function, and they approach each other when $v_n >> \delta$.

Figure 5.7 shows a comparison between the v_n^{obs} from the full ID and $v_n^{\mathrm{obs,2PC}}$ calculated by correlating the two half IDs, for three centrality intervals. It is seen that the v_n^{obs} and $v_n^{\mathrm{obs,2PC}}$ distributions agree with each other for n=2 and n=3 for $v_n > 0.03$ in central and mid-central collisions. This is where where the condition $v_n > s_1, s_2$ is expected to hold. In all other cases the agreement

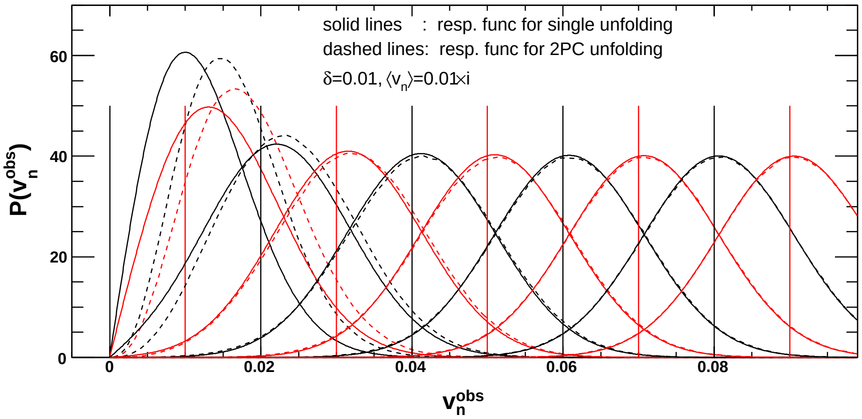

Figure 5.6: The response function for Eq. 5.16 (solid curves) and for Eq. 5.20 (dashed curves) with $\delta = 0.01$ and $v_n = 0.01 \times i$, with i=0,1,2,.... The response functions are represented by the curves, while the corresponding input v_n values are indicated by the vertical lines.

is poor, implying that the $s_1 s_2$ term dominates the 2PC response function.

The aim of performing the analysis on the pair distribution is that it has different susceptibility to non-flow effects than the single particle method. The pair distribution method correlates tracks between two subevents in non-overlapping eta regions and naturally suppresses short-range correlations, since on average there is a large rapidity gap between the particles in each pair. Thus, the results from the 2PC unfolding can be used to estimate systematic effects from short-range correlations.

5.1.4 Bayes unfolding

In this analysis, the standard Bayesian unfolding procedure [103] as implemented in the RooUnfold framework [104] is used. The true distribution (“cause” or c) and the measured distribution (“effect” or e) are related via the response function A, which relates the probability that a cause c_i is mapped on to a measured value e_j

$$Ac = e, \quad A_{ji} = p(e_j|c_i) \tag{5.21}$$

c is obtained via an iterative pseudo-inversion procedure: A unfolding matrix M is determined from the response function and some initial guess of the true

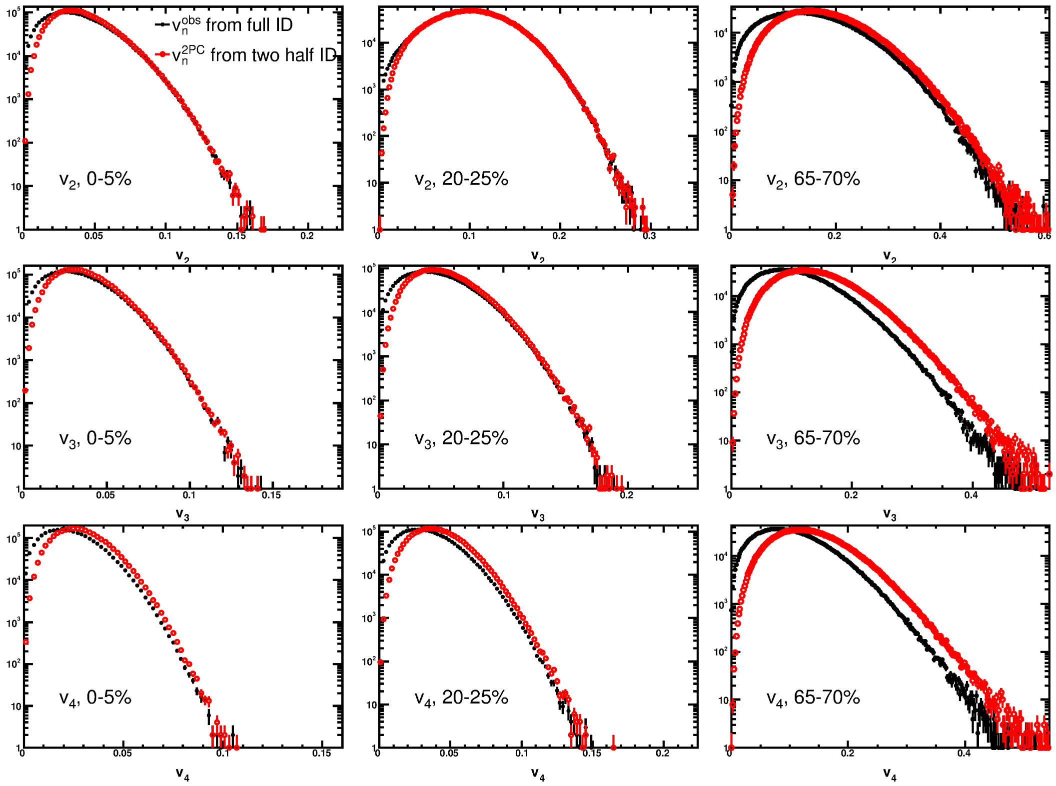

Figure 5.7: Comparison of the EbyE distributions of v_n^{obs} from the full ID and $v_n^{\mathrm{obs,2PC}}$ by correlating the two half IDs for various centrality intervals (left to right) and different harmonic number (top to bottom).

distribution $\hat{c}^0$ (called the **prior**) as :

$$\hat{c}^{\mathrm{iter}+1} = \hat{M}^{\mathrm{iter}} e, \quad \hat{M}_{ij}^{\mathrm{iter}} = \frac{A_{ji}\hat{c}_i^{\mathrm{iter}}}{\sum_{m,k} A_{mi} A_{jk} \hat{c}_k^{\mathrm{iter}}} \tag{5.22}$$

More explicitly, $\hat{M}^0$ is calculated from the initial guess $\hat{c}^0$. The elements of $\hat{M}^0$ are then used to estimate $\hat{c}^1$ and so on. The statistical uncertainties in $\hat{c}^i$ increase rapidly with the number of iterations[5]. Thus the unfolding has to be stopped after a certain number of iterations N_{iter}, which is tuned according to the sample statistics. Due to the large statistics of the Run-10 dataset, which has ~ 2.4 million events for each 5% centrality interval, the N_{iter} can be chosen to be a large enough such that the $\hat{c}^i$ converge, yet the statistical uncertainties are still fairly small.

---

[5] This is a general feature of the Bayesian unfolding.

The response function is determined from the subevent correlation as described in Sections 5.1.2 and 5.1.3. The v_n^{obs} distribution from the full ID (or $v_n^{\mathrm{obs,2PC}}$ distribution from correlations between the two half IDs) can be used as the prior $\hat{c}^0$ i.e. $\hat{c}^0 = e$ in Eq. 5.22. The convergence improves when using a prior that is closer to the true distribution, while using a prior that is very different than the true distribution converges slower. The priors used in this analysis are obtained by rescaling the v_n^{obs} distributions by a factor R as:

$$v_n^{\mathrm{obs}} \rightarrow R v_n^{\mathrm{obs}}, \qquad R = \frac{v_n^{\mathrm{EP}}}{\langle v_n^{\mathrm{obs}} \rangle + \left(\langle (v_n^{\mathrm{obs}})^2 \rangle - \langle v_n^{\mathrm{obs}} \rangle \right) f}, \tag{5.23}$$

with f=0, 0.5, 1, 1.5, 2 and 2.5. The $\langle v_n^{\mathrm{obs}} \rangle$ and $\langle (v_n^{\mathrm{obs}})^2 \rangle$ are the mean and the RMS of the v_n^{obs} distribution respectively and v_n^{EP} is the integral v_n for $p_{\mathrm{T}} >$0.5 GeV measured using the event-plane method (Chapter 3). The v_n^{EP} is typically close to the RMS of the true v_n distribution (see Section 3.2.5). Thus, choosing f=1 in Eq. 5.23 gives a prior close to the true distribution (as its RMS is equal to the v_n^{EP}). While f<1 (f>1) gives priors that are typically broader (narrower) than the final answer, and can be used to check the stability of the unfolding. The f=0 prior is used as the default prior.

The unfolding problem in this analysis has several nice features that greatly improves its convergence behavior:

1. The response function is obtained from a data-driven method, without any need for Monte Carlo.

2. Each event provides one entry to the input distribution and the response function, they can be determined with great precision given the large event statistics of the Pb+Pb dataset: roughly 2.4 million events for each 5% centrality interval.

3. There is no efficiency loss, as each event provides one value of v_n^{obs}, and the effect of the tracking inefficiency is simply to smear the observed distribution. In other words an event is never lost i.e. the integral of the unfolded distribution and of the true distribution are the same, and the unfolding does not have to correct for efficiency loss.

4. There is no leakage problem: the corrected v_n distribution is always narrower than the observed distribution and contained within the available range.

In this analysis, the unfolding of the single-particle EbyE v_n^{obs} is used as the primary method. The unfolding of $v_n^{\mathrm{obs,2PC}}$, with its very different response function and sensitivity to non-flow effects, is used to assess systematic uncertainties. Additional checks on the non-flow effects are provided by varying the gap between the two half IDs, or by measuring v_n^{obs} for tracks with different p_{T} threshold.

5.2 Data analysis

In this section the performance of the unfolding as well as several cross-checks to check its convergence and stability are discussed. The analysis done here form the basis of the systematic uncertainties estimated for the EbyE distributions.

5.2.1 Basic performance of the unfolding

The top row of Fig. 5.8 shows the performance of the Bayesian unfolding for the v_2 distribution in the (20-25)% centrality interval. The first panel shows the unfolded distributions for different number of iterations N_{iter}. The second panel shows the ratio of the different iterations to the 128th iteration. The unfolding converges within a few percent around the peak region by N_{iter}=8. Additional iterations bring about improvements in the tails. The third panel shows the ratio of the refolded distribution – obtained by convoluting the unfolding distribution with the response function – to the v_n^{obs} distribution. This sanity check shows that that the measured distribution is recovered by smearing the unfolded distribution by the response function. Similar plots for v_3 and v_4 are shown in the second and third rows Figs. 5.8. The performance is similar but the convergence is slower as the physical signals are smaller for v_3 and v_4 as compared to v_2. The statistical uncertainties in the unfolded distributions increase with increasing N_{iter} and are close to $\sqrt{N}$ error, where the N is the number of events in each bin in the unfolded distribution for $64 < N_{\mathrm{iter}} < 128$. Thus iteration 128 is used as the final iteration and the results are presented only over the centrality range where the difference between the 32nd and 128th iterations is less than 10% when statistics allow for a meaningful comparison. The centrality ranges for harmonics 2, 3 and 4 are (0-70)%, (0-60)% and (0-45)% respectively.

5.2.2 Unfolding subevent v_n distributions

To show that the method yields a consistent answer, the unfolding procedure is performed independently for the half ID and the full ID, assuming the width of the smearing function for half ID is $\sqrt{2}$ times that for the full

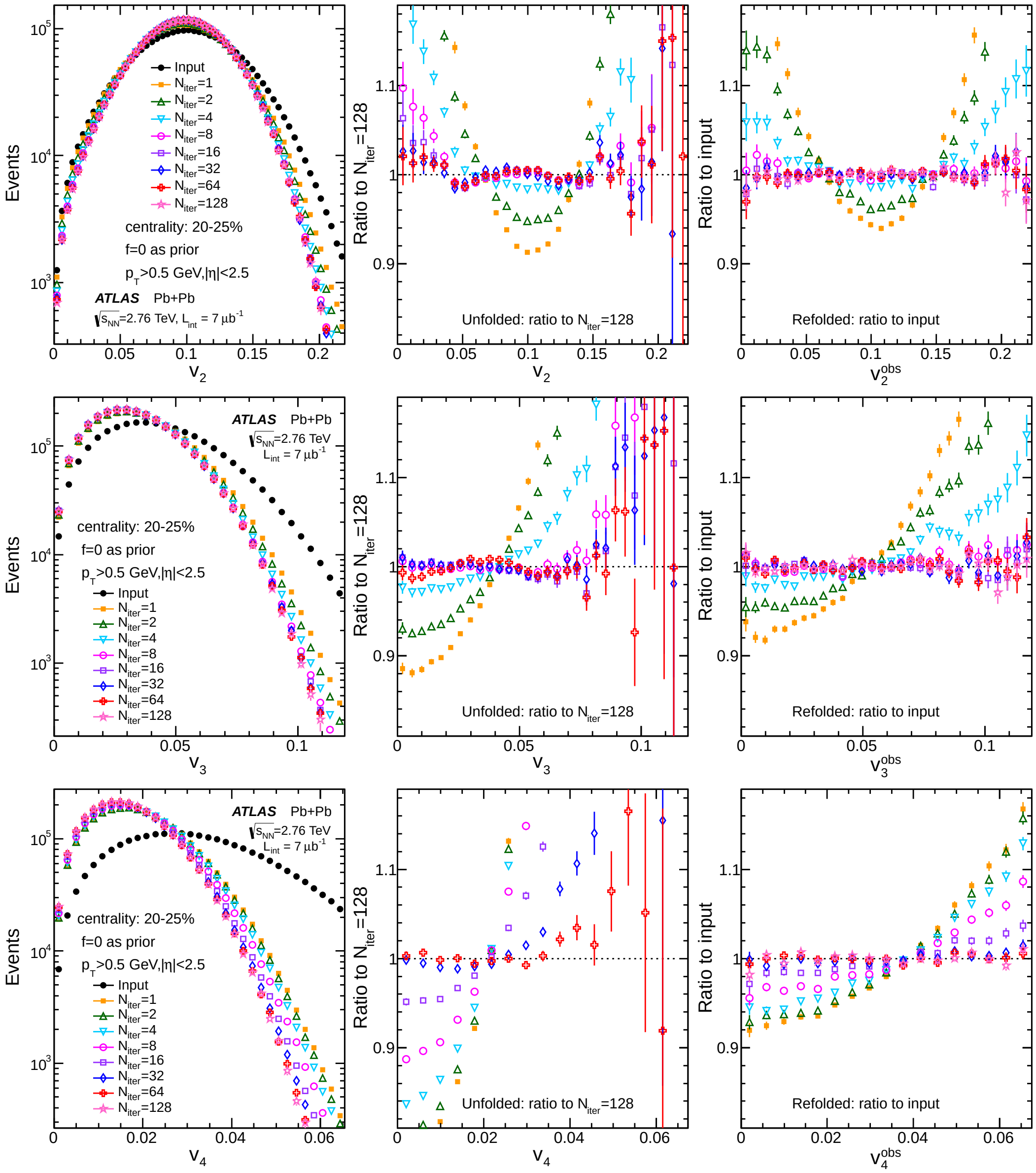

Figure 5.8: The unfolding performance for the v_n distribution for the (20-25)% centrality interval for various $\mathrm{N_{iter}}$ (left panels), the ratios of the unfolded distributions to the results after 128 iterations (middle panels), and the ratios of the refolded distributions to the measured v_n^{obs} (right panels). From top to bottom the rows correspond to v_2, v_3 and v_4.

ID (Eq. 5.15). The results for this study are shown in Fig. 5.9 for N_{iter}=128 for the (20-25)% centrality interval. Despite the substantial difference in the initial distributions, the final unfolded results converge within a few percent. Some systematic deviations are seen in the tail of the v_4 distribution, which mainly reflects the remaining non-convergence of the half ID unfolding, since the response function is $\sqrt{2}$ broader than that for than the full ID.

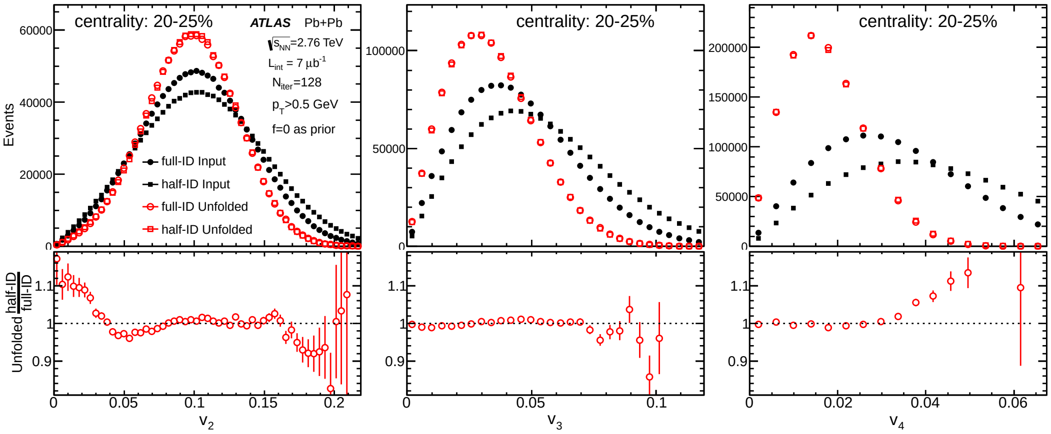

Figure 5.9: Comparison of the input distributions (solid symbols) and unfolded distributions for N_{iter}=128 (open symbols) between the half-ID and the full-ID in the (20-25)% centrality interval. The ratios of half-ID to full-ID unfolded results are shown in the bottom panels. The results are shown for v_2 (left panels), v_3 (middle panels) and v_4 (right panels).

5.2.3 Dependence on the prior

The convergence of the results starting with different priors is used to check the stability of the unfolding. Figure 5.10 shows the convergence behavior for different choices of priors for v_2 to v_4 in the (20-25)% centrality interval. Five difference priors are used: Eq. 5.23 with f=0, 0.5, 1.5, 2.5 as well as the observed v_n^{obs} distribution. Clearly a better choice of prior improves the convergence, however all priors eventually converge to the same distribution. Even when choosing a prior that is narrower than the true distribution (f¿1), the results still converge showing the robustness of the unfolding. A caveat though is that a narrow prior can result in some information loss in the tail, and typically has larger fluctuations (in the tail).

5.2.4 Dependence on the response function

In the default analysis an explicit dependence of the widths δ_{2SE}, of the 2D response function on v_n^{obs} are not considered. However, as shown in Fig. 5.11, the

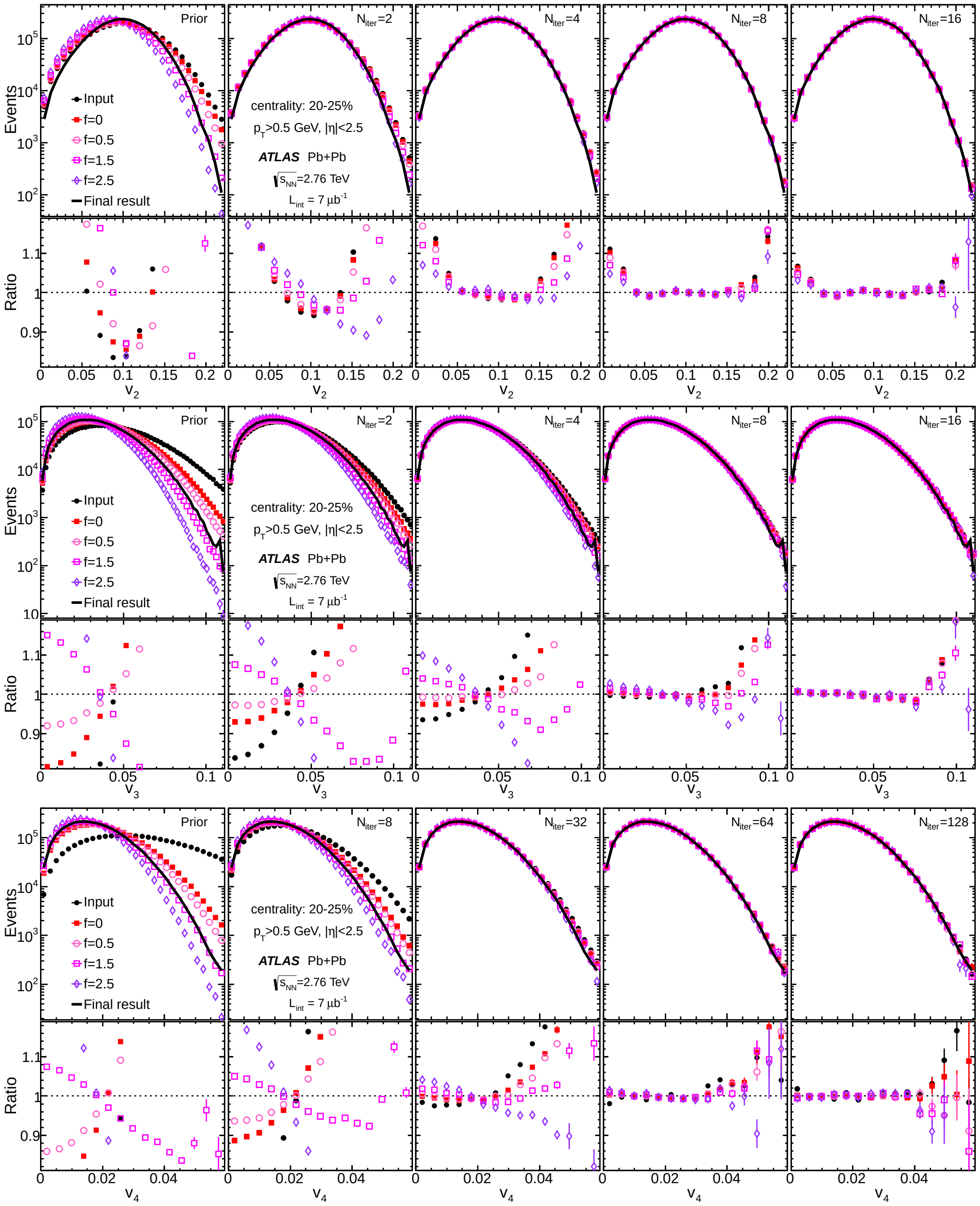

Figure 5.10: Convergence behavior in the (20-25)% centrality interval for five choices of priors for several values of $N_{\rm iter}$, increasing from left to right. The lower sub-panels show the ratios to the result for $N_{\rm iter}$=128. A common reference, shown by the solid lines in the upper sub-panels, is calculated by averaging the result for $f = 0$ and $f = 0.5$ with $N_{\rm iter}$=128.

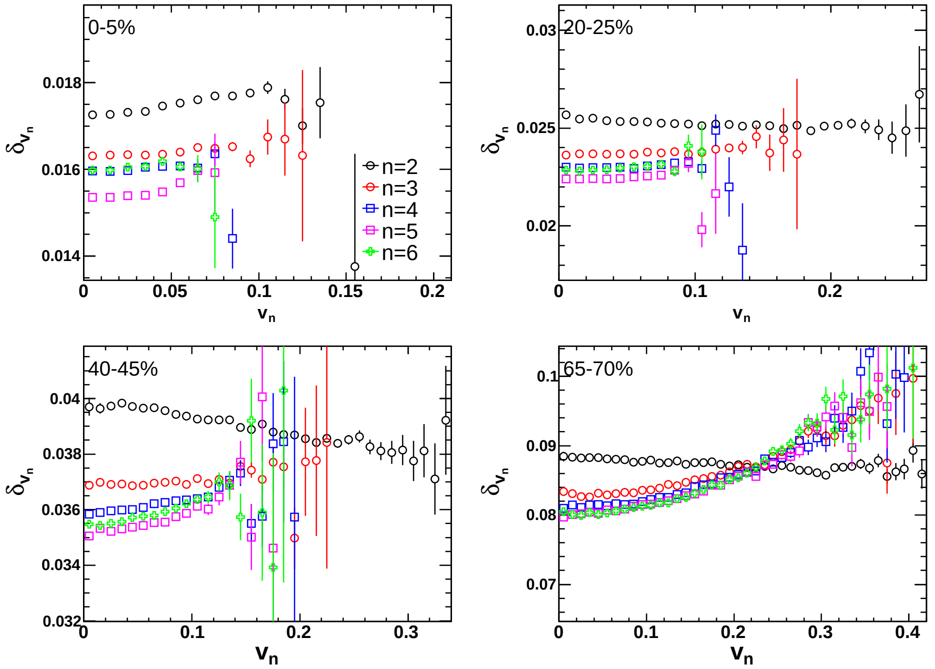

Figure 5.11: The width of the 2D response functions obtained by fitting distribution of the flow vector difference $\left((\boldsymbol{v}_2^{\rm obs})^{\rm a} - (\boldsymbol{v}_2^{\rm obs})^{\rm b}\right)/2$ between the two half ID for $n = 2-6$ for several centrality selections. Note that the y-axes are zero suppressed. The variation in the width with $v_n^{\rm obs}$ is a few %, except in the last panel where the variation is much larger for n >2.

width of the response function does have a weak dependence on the v_n^{obs}. The variation is typically a few percent, but can be larger in peripheral collisions. To quantify the uncertainty associated with the shape and the width of the response function, the unfolding is performed using four different variations of the response function:

1. The measured response function obtained numerically from the two subevent $\left((\boldsymbol{v}_2^{\mathrm{obs}})^{\mathrm{a}} - (\boldsymbol{v}_2^{\mathrm{obs}})^{\mathrm{b}}\right)$ distribution but integrated over the full v_n^{obs} i.e. ignoring any dependence on v_n^{obs}. This is the default case.
2. The analytical response function obtained using Eq. 5.16. δ_{2SE} is obtained by fitting the $\left((\boldsymbol{v}_2^{\mathrm{obs}})^{\mathrm{a}} - (\boldsymbol{v}_2^{\mathrm{obs}})^{\mathrm{b}}\right)$ distribution integrated over the full v_n^{obs}.

The other two cases are when the dependence of the response function on v_n^{obs} is taken into consideration by measuring the $\left((\boldsymbol{v}_2^{\mathrm{obs}})^{\mathrm{a}} - (\boldsymbol{v}_2^{\mathrm{obs}})^{\mathrm{b}}\right)$ distributions in bins of v_n^{obs}. The differences between the default and the other three cases are used to assess the systematic uncertainties.

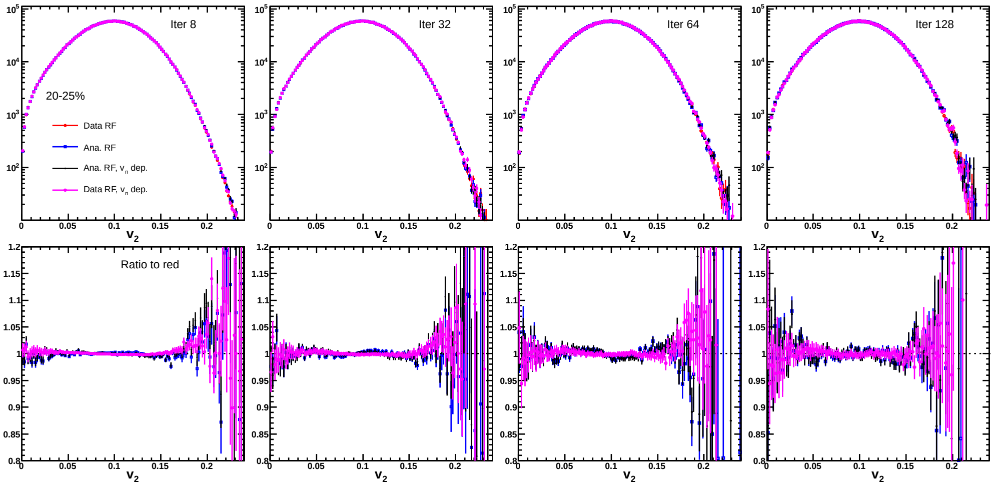

Figure 5.12: The unfolded results for four different implementations of the response functions mentioned in the text for v_2 in (20-25)% centrality interval. The difference are quantified by the ratios relative to the default response function in the bottom panels.

Figure 5.12 shows the unfolded results in (20-25)% centrality interval obtained using these four response functions for v_2. Good agreement is observed in most cases. In general, there are no differences between using the analytical response function and using the measured response function. But there are

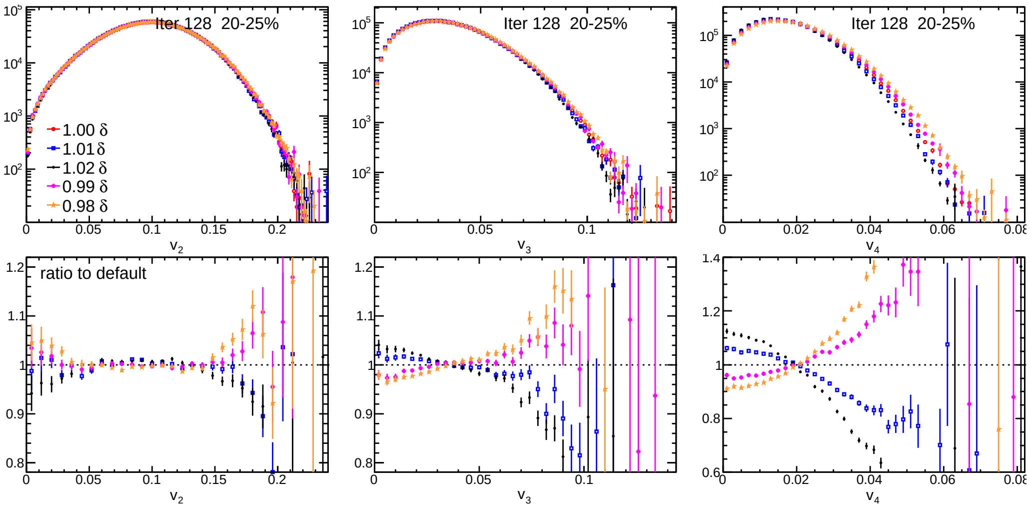

Figure 5.13: The sensitivity of the unfolded results on the width of the response functions in (20-25)% central collisions. These results are obtained by rescaling the width of the default response function by a small factor: 1.01, 1.02, 0.99 or 0.98.

some small systematic differences of the order of a few percent depending on whether or not the width is parameterized as a function of v_n^{obs}.

The sensitivity of the unfolding on the width of the response function is also checked explicitly by rescaling the measured integrated response function to be slightly narrower or broader by 1%-2%. The rescaled response functions are then used in the unfolding and the variations are shown in Figure 5.13 for the (20-25)% centrality interval. In general, the changes are small for n=2 but can be large for n=4, especially in the tail.

5.2.5 Comparison to unfolding of EbyE pair distributions

Comparing the unfolded distributions from the single-particle unfolding and the pair-unfolding is an important systematic check, as the bias of non-flow effects on the two methods is expected to be different. In Fig. 5.14 the observed and unfolded distributions for the single-particle and pair distributions are compared. Despite substantial differences in the observed distributions, the unfolded distributions are very consistent with each other except in the tail for the v_3 and v_4 distributions. This is expected as the response functions for the 2PC are wider and the convergence is slower.

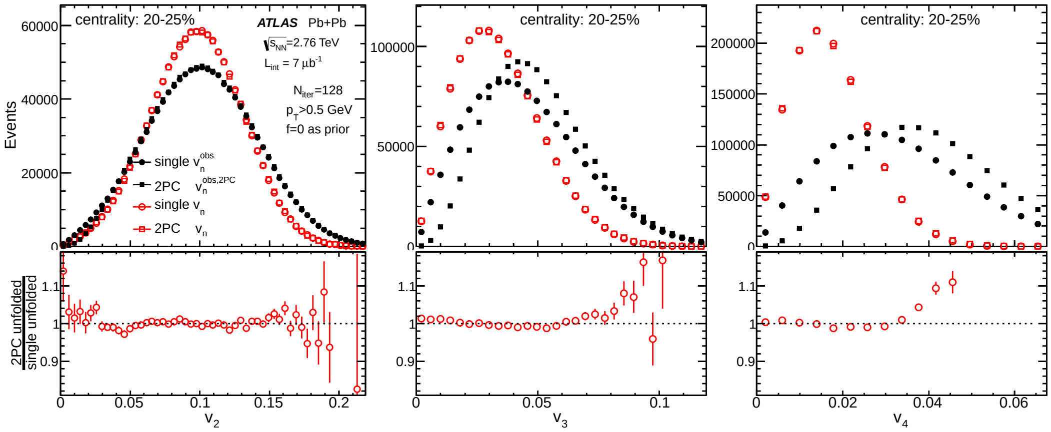

Figure 5.14: Comparison of the input distributions (solid symbols) and unfolded distributions for N_{iter}= 128 (open symbols) between the single-particle unfolding and 2PC unfolding in the (20-25)% centrality interval for v_2 (left panels), v_3 (middle panels) and v_4 (right panels). The ratios of 2PC to single-particle unfolded results are shown in the bottom panels.

5.2.6 Dependence on the η gaps

In the default setup, the response functions are determined from the two half IDs without any gap in between. Another way of systematically studying the effect of short-range correlation on the v_n distributions is to repeat both the single particle and two-particle EbyE v_n measurements with varying amounts of η gap between the two subevents. Six additional cases are studied with successively increasing the minimum η gap between the two subevents: > 0.2, > 0.4, > 0.6, > 0.8, > 1.0 and > 2.0. For each case, the full analysis chain is repeated and the results are compared with the default case.

The upper two panels of Fig. 5.15 show the final unfolded distributions (128 iteration) with these rapidity gaps from both the single particle method and correlation method for v_2 in the (0-5)% centrality interval. Fig. 5.16 shows similar plots for the v_3 distribution. The bottom left panel shows the ratio of the single particle distributions to the default case. Systematic deviations are seen when the gap is increased (see bottom left panel), with the unfolded distributions being narrower for larger η gap. However, this narrowing is not necessarily from changing non-flow effects, and in fact is expected from the slight decrease of v_n with increasing η (Section 3.5.1), since a larger η gap on average selects particles at forward η. The bottom right panel shows the ratios between the correlation method and single particle method for the different η gaps. The ratio is independent of the η gap indicating that the effect of the

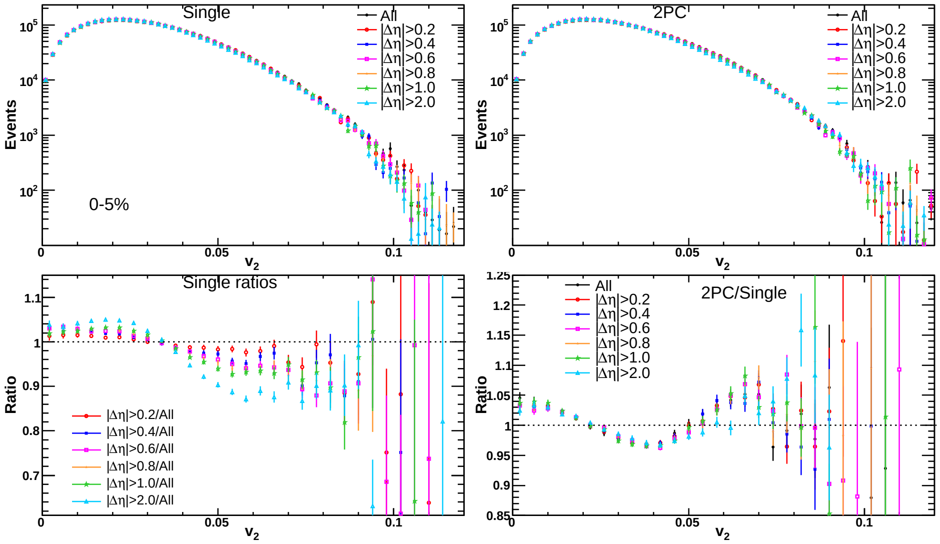

Figure 5.15: The unfolded distributions of EbyE v_2 with various $\Delta\eta$ gaps between the two subevents from single particle method (top left) and correlation method (top right) for the (0-5)% centrality interval. Bottom left panel shows ratios between results with gap and without gap from single particle method. The bottom right panel shows the ratio between the two methods.

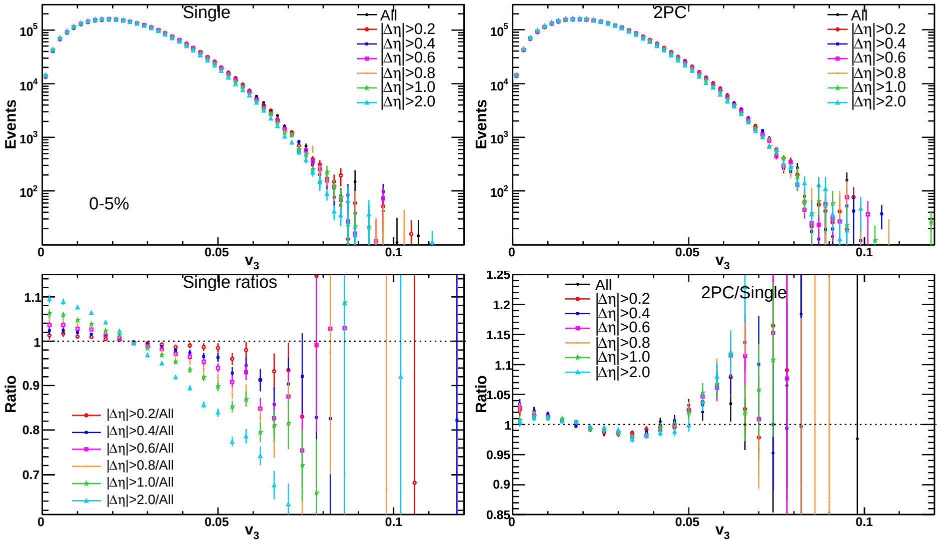

Figure 5.16: Same as previous plot but for v_3.

η gap is identical on the 2PC and single-particle distributions, indicating that the non-flow influence is not being affected by varying the η gap.

Based on this observation, the η gap dependence is not used to quote additional systematic errors. However, the difference between the 2PC and the single-particle results for the default case is included as a systematic error.

5.2.7 Dependence on the p_{T} cuts

In this analysis, the EbyE v_n is calculated using tracks with $p_{\mathrm{T}} > 0.5$ GeV. Studying how the EbyE distributions change with the p_{T} binning can a give better understanding of the fluctuations. It can also help in understanding the non-flow biases, as they are expected to be more dominant at higher p_{T}. For this, the tracks are divided into two categories: those with $0.5 < p_{\mathrm{T}} < 1.0$ GeV and those with $p_{\mathrm{T}} > 1.0$ GeV. It is not possible to make finer bins in p_{T} as the number of tracks/event has to be kept at a substantial level for the unfolding to work. About 60% of all tracks are within the $0.5 < p_{\mathrm{T}} < 1.0$ GeV bin, although this fraction varies slightly with centrality. The full analysis chain is repeated independently for the two classes of tracks.

The top panels of Figure 5.17 show the unfolded EbyE v_n distributions for the two p_{T} bins as well as the combined p_{T} bin in the (0-5)% centrality interval. The unfolded distributions for the $p_{\mathrm{T}} > 1.0$ GeV bin are much wider and thus the associated $\langle v_n \rangle$ values are larger than that for the $0.5 < p_{\mathrm{T}} < 1.0$ GeV bin. This simply indicates that the v_n increase with increasing p_{T}. However, the overall shape of the distributions are quite similar. In fact once these distributions are rescaled to have the same mean value, they fall on top of each other as indicated by the bottom panels of Figure 5.17. Only a small deviation is observed in the tails of the distributions.

The similarity of shape between the EbyE v_n in different p_{T} ranges implies that the hydrodynamic response of the medium to the initial geometry is independent of the p_{T} up to an overall scaling, i.e. the change of the distribution is largely captured by an increase of the average v_n with p_{T}. It also indicates that the change in non-flow effects are minimal between the two bins, further establishing the robustness of the unfolding to non-flow influence.

5.3 Systematic errors

In Section 5.2 the basic steps and important cross-checks of the analysis were laid out. The default results are obtained from single particle unfolding with full-ID using a prior distribution that is rescaled to have the same mean value as the event-plane measurement ($f = 0$), and the response function is obtained from correlations between two half IDs without rapidity gap in between (followed by scaling by 1/2). The systematic uncertainties are studied by varying

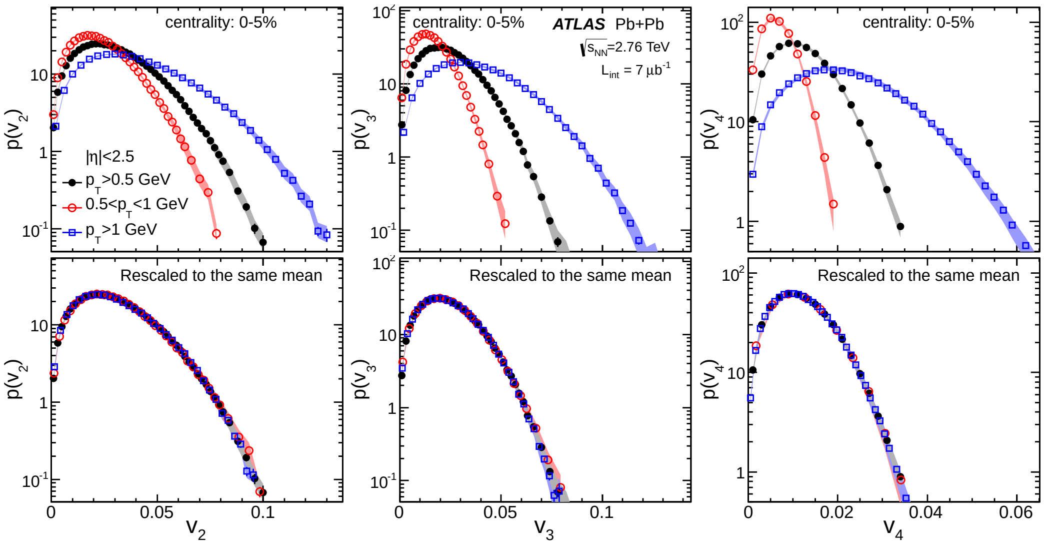

Figure 5.17: Top panels: The v_n unfolded distributions in (0-5)% centrality interval for all tracks with $p_{\mathrm{T}} > 0.5$ GeV, $1.0 > p_{\mathrm{T}} > 0.5$ GeV and $p_{\mathrm{T}} > 1$ GeV. Bottom panels: The distributions scaled to have the same $\langle v_n \rangle$ as the $p_{\mathrm{T}} > 0.5$ distribution.

the ingredients associated with analysis. Results in Section 5.2.7 showed that the overall shape of the unfolded distributions, when rescaled to the same $\langle v_n \rangle$, are very stable against the change of the p_{T} selection cut. Motivated by this observation, all the sources of systematic uncertainties are decomposed into two components: the uncertainty associated with the $\langle v_n \rangle$ or the v_n-scale, and the uncertainty of the shape after adjusting to the same $\langle v_n \rangle$. This approach simplifies the presentation of the systematic uncertainties, as most uncertainties can be attributed to a change of $\langle v_n \rangle$ while keeping the overall shape almost unchanged.

The sources of systematic errors already discussed in Section 5.2 are:

1. Residual non-convergence: This is taken as the difference between the results of iteration 32 and 128, or between the results from full-ID unfolding and half-ID unfolding. These two are strongly correlated and the error is taken to be the larger of the two bin by bin in the unfolded distribution.

2. Dependence on prior: This is taken as the difference in results obtained between the $f = 0$ and $f = 2.5$ priors.

3. Uncertainty in response function: This is taken as the change using the four variants of the response function described in section 5.2.4 as well

as the change when varying the width of the response function by ±1%. The variation from these two sources are added in quadrature.

4. Two-particle EbyE distributions: The difference between the results of the default (without any η gap) 2PC unfolding and the single particle unfolding is included as a source of systematic error.

Additional sources of systematic uncertainties are discussed below:

5.3.1 Tracking efficiency

As discussed in Section 5.1.1 while calculating the EbyE v_n^{obs}, the tracks are weighted by the inverse of the tracking efficiency $1/\epsilon$. Thus any uncertainty on the efficiency ϵ translates into an error in the EbyE v_n measurement. The tracking efficiency used in this analysis is based on the tracking performance study done in [60] and shown in Fig. 2.11. The uncertainty in the tracking efficiency is roughly ±3% independent of p_{T} and η. An overall scaling of the tracking efficiency does not alter the v_n^{obs} measured in an event, as it affects all tracks equally. This can be seen from Eq. 5.11, where it is clear that a scale change of $\epsilon(\eta, p_{\mathrm{T}})$ cancels in the numerator and denominator. Thus scaling the efficiency up or down by its ±3% uncertainty does not affect the EbyE distributions. Instead, the effect of the tracking efficiency uncertainty is determined by assuming that the errors in it are completely anti-correlated at the low-p_{T} and high-p_{T} end. The tracking efficiency is varied as a function of p_{T} as:

$$\epsilon_{\pm}(p_{\mathrm{T}}) = \epsilon(p_{\mathrm{T}}) \pm 0.03 \frac{\epsilon(p_{\mathrm{T}}) - \epsilon(p_{\mathrm{T}}^{\mathrm{low}})}{\epsilon(p_{\mathrm{T}}^{\mathrm{up}}) - \epsilon(p_{\mathrm{T}}^{\mathrm{low}})} \mp 0.03 \tag{5.24}$$

This variation lowers(raises) the efficiency by 3% at $p_{\mathrm{T}}^{\mathrm{low}} = 0.5$ GeV and raises(lowers) it by 3% at $p_{\mathrm{T}}^{\mathrm{up}} = 10$ GeV with a smooth interpolation in between. Such a variation covers the maximum effect that the uncertainty in the efficiency can have.

5.3.2 Other uncertainties

There are other potential uncertainties that haven't been considered so far, such as track selection, trigger-efficiency and event selection, and run by run dependence. The track selection accounts for influence of fakes, the trigger-efficiency and event selection is associated with the definition of centrality intervals, while the run by run dependence is associated with the instability of the detector acceptance and efficiency. These three sources of systematics are expected to only change the v_n scale, and have been studied in detail the EP v_n analysis (Chapter 3). As this analysis uses the same dataset and track selection cuts, the errors on the scale are quoted as the corresponding errors from the EP analysis (Tables 3.3–3.5).

5.3.3 Summary of systematic uncertainties

As discussed before, each source is decomposed into two components: the uncertainty on the mean $\langle v_n \rangle$ or v_n scale, and the uncertainty on the shape of the v_n distribution with respect to the same $\langle v_n \rangle$.

Uncertainty of the v_n scale

Figure 5.18 summarizes the various sources of systematic uncertainties for $\langle v_n \rangle$, σ_{v_n} and $\sigma_{v_n}/\langle v_n \rangle$. Here the results are plotted as a function of the mean number of participating nucleons $\langle N_{\text{part}} \rangle$ by mapping the centrality intervals to $\langle N_{\text{part}} \rangle$ (see Table 2.1)[6]. The first five points with highest $\langle N_{\text{part}} \rangle$ correspond to the (0-5)% centrality in 1% centrality bins, the subsequent points are bins of 5% centrality.

The uncertainty for $\langle v_n \rangle$ and σ_{v_n} are strongly correlated, indicating that many of the sources of errors affect the overall scale but not the shape. These uncertainties are summarized in Table 5.1. They are listed for four groups of centrality intervals 0-10%, 10-30%, 30-50% and 50-70%, the numbers are given as percentage. Most uncertainties are asymmetric, the quoted numbers correspond to the range spanned by the largest uncertainty for all centrality intervals in each group. The net uncertainty in the scale is obtained by adding the uncertainties in quadrature.

Uncertainty of the v_n shape

Once the $\langle v_n \rangle$ is determined for each systematic check, the full unfolded distribution is rescaled horizontally to match the $\langle v_n \rangle$ value from the default unfolding. The rescaled distribution is then divided by the distribution from the default unfolding. The ratio thus obtained quantifies the level of residual shape variation. Figure 5.19 summarizes these ratios for all the major systematic checks for each of the 19 centrality intervals for v_2. The uncertainty associated with the residual non-convergence is taken as the larger of the following two numbers: the difference between $N_{\text{iter}} = 32$ and 128 and the difference between the half-ID and full-ID results. The upper and lower bounds of this

---

[6] From here on, all centrality dependence results are presented as a function of N_{part} for easier comparison to theory.

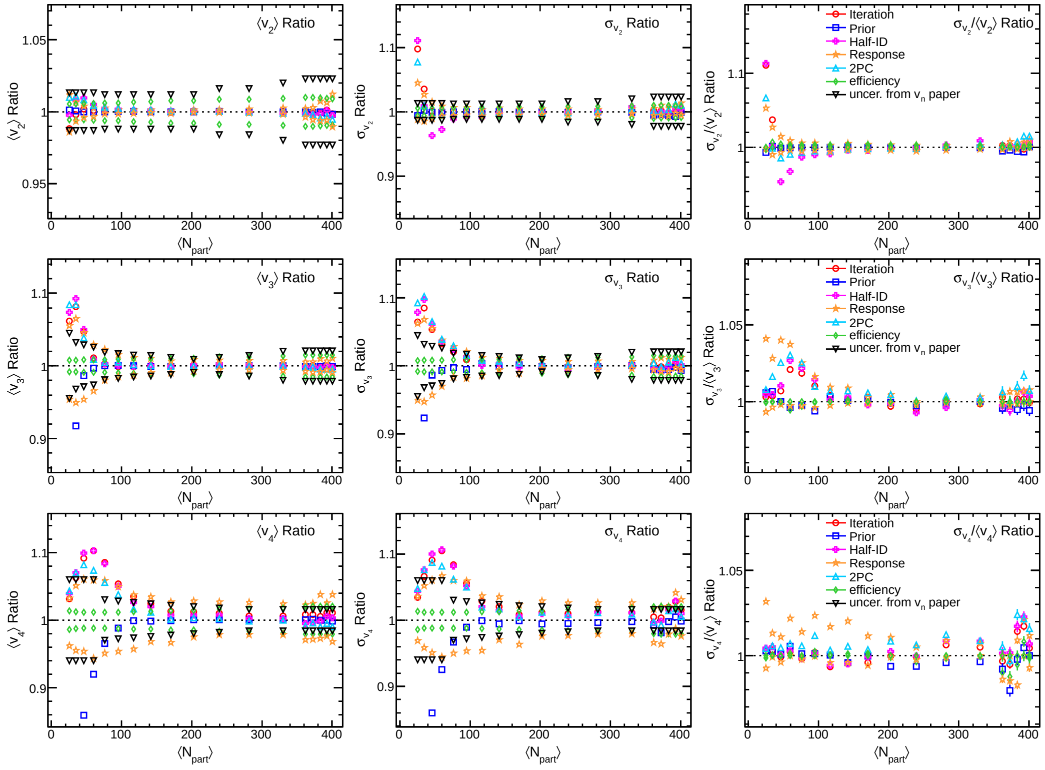

Figure 5.18: Fractional change of $\langle v_n \rangle$ (left column), σ_{v_n} (middle column) and $\sigma_{v_n}/\langle v_n \rangle$ (right column) for various sources of systematic uncertainties. Each row corresponds to a different harmonic number: n=2 (top row), n=3 (middle row) and n=4 (bottom row). Note that, changes for some sources are indicated by a upper and lower bounds (for example efficiency), while only one bound is shown for other sources (i.e. comparison to 2PC).

	Uncertainty in $\langle v_2 \rangle$ or σ_{v_2}				Uncertainty in $\sigma_{v_2}/\langle v_2 \rangle$			
Centrality	0–10%	10–30%	30–50%	50–70%	0–10%	10–30%	30–50%	50–70%
Non-convergence [%]	<0.1	<0.1	<0.2	3–12	0.9	0.3	0.5–1.4	3–11
Prior [%]	<0.1	<0.1	<0.1	0.1–0.2	0.6	<0.3	<0.2	0.2–0.7
Response function [%]	0.3–1	0.1	0.1	0.2–1	1.0	0.5	0.6	0.6–3
Compare to 2PC [%]	<0.1	<0.1	<0.1	0.2–7	0.5–1.5	<0.4	0.4–0.8	1–7
Efficiency [%]	1	0.6-0.8	0.7	0.6	0.4	0.4	0.4	0.4–0.8
Track selection, trigger, stability [%]	2.2	1.7	1.5	1.5				
Total [%]	2.5	1.9	1.7	3.5–14	1.6–2.2	1	1–1.8	3.4–14

	Uncertainty in $\langle v_3 \rangle$ or σ_{v_3}				Uncertainty in $\sigma_{v_3}/\langle v_3 \rangle$			
Centrality	0–10%	10–30%	30–50%	50–60%	0–10%	10–30%	30–50%	50–60%
Non-convergence [%]	0.2	0.3	0.3	1.2–5	0.2–0.8	0.3–0.8	0.4–2	0.5–4
Prior [%]	<0.1	<0.1	<0.1	0.5–1.4	0.6	0.2–0.4	0.2–1.0	3.0
Response function [%]	0.6	0.8	0.8–2.4	2.9–4.6	0.3–0.7	0.2–0.5	0.9–2.5	3–5
Compare to 2PC [%]	0.5	0.2–0.7	0.1	0.2	0.3–1.6	0.4–0.6	0.7–2.5	1–3
Efficiency [%]	1.5	1.2	1	0.9	<0.2	<0.2	<0.3	<0.3
Track selection, trigger, stability [%]	2.1	1.4	1.5–2	2.5–4.5				
Total [%]	2.7	2.2	2–3.3	4.2–8.3	0.8–2	0.6–1.2	1.3–4.2	4.2–7.0

	Uncertainty in $\langle v_4 \rangle$ or σ_{v_4}				Uncertainty in $\sigma_{v_4}/\langle v_4 \rangle$			
Centrality	0–10%	10–30%	30–45%		0–10%	10–30%	30–45%	
Non-convergence [%]	1–2.0	1–1.5	3.0–5.5		1–2	0.5–1	2.0–4.0	
Prior [%]	3.0	3.0	5.0–7.0		2.0	3.0	5.0	
Response function [%]	2.5–4.0	3.0	3.0–5.0		0.5–2	0.6–1.2	2.0–2.3	
Compare to 2PC[%]	0.2-1	0.3	1–4.7		1–2.5	1.2	0.5–1.2	
Efficiency [%]	2.0	1.5	1.2		1	0.4	<0.3	
Track selection, trigger, stability [%]	3.0	2.7	3–6					
Total [%]	5.4	5.4	8–11		3.0	4.0	5-7	

Table 5.1: Summary of systematic uncertainties for $\langle v_n \rangle$, σ_{v_n} and $\sigma_{v_n}/\langle v_n \rangle$ ($n = 2$–4) obtained using charged particles with $p_{\mathrm{T}} > 0.5$ GeV. The uncertainties for $\langle v_n \rangle$ and σ_{v_n} are similar so the larger of the two is quoted. Most uncertainties are asymmetric; the quoted numbers refer to the maximum uncertainty range spanned by various centrality intervals in each group.

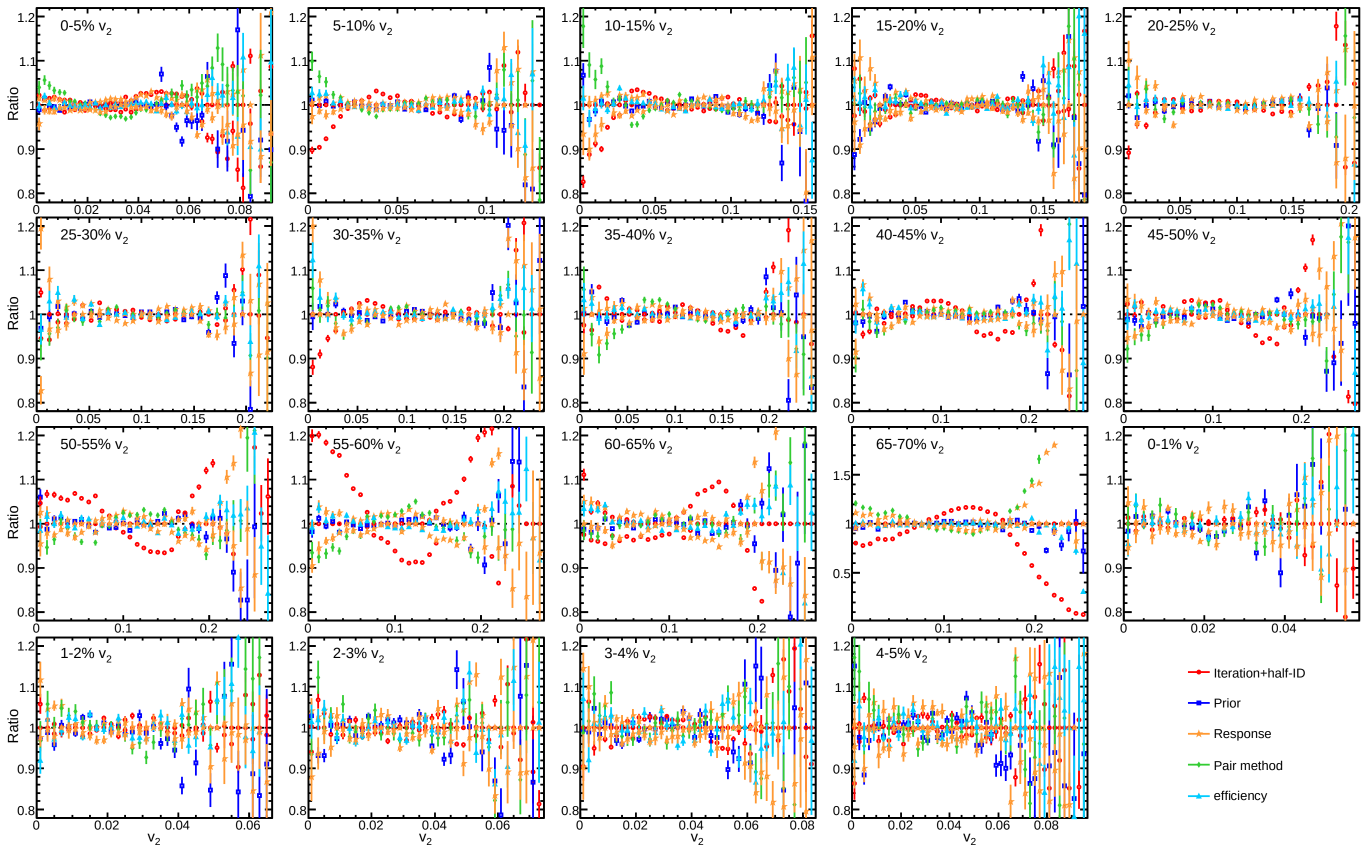

Figure 5.19: The residual shape variations associated with various systematic checks as a function of v_2. Each panels represent result in one centrality interval.

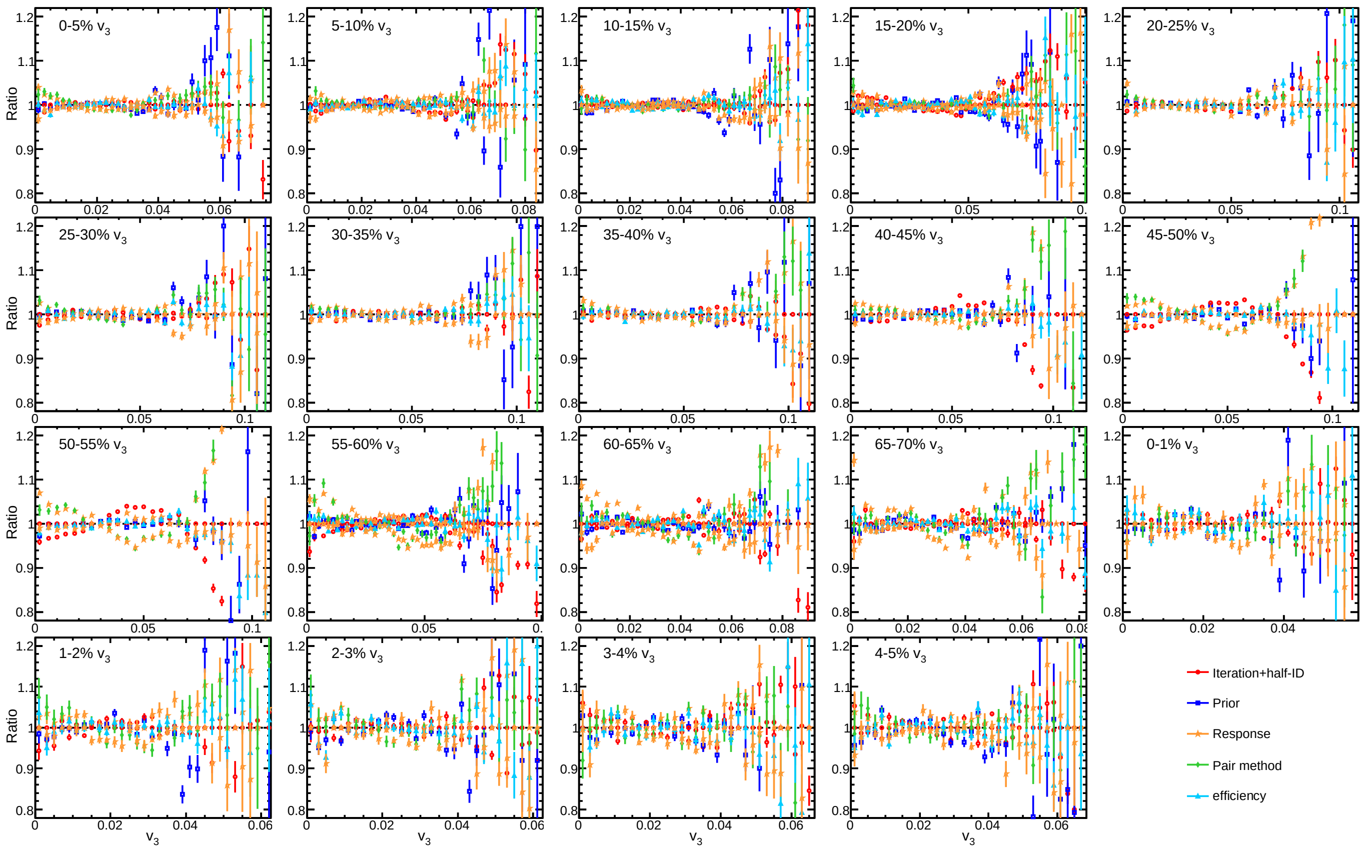

Figure 5.20: Same as previous plot but for v_3.

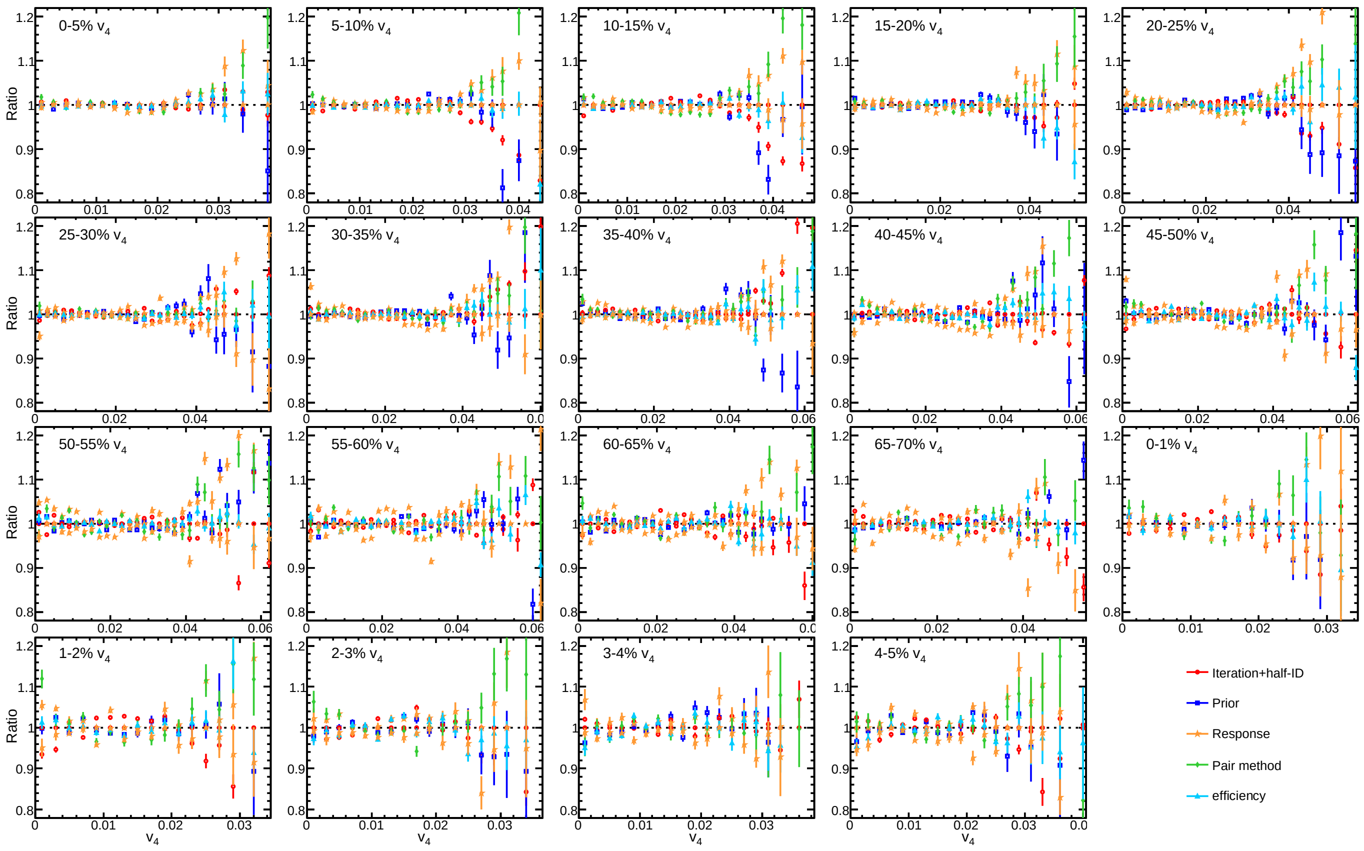

Figure 5.21: Same as previous plot but for v_4.

uncertainty are represented by red symbols. The uncertainty associated with the response function is also represented by upper and lower bounds (brown symbols). However the uncertainty associated with the remaining sources are each represented by one single ratio. Every ratio usually crosses 1.0 in at least two locations, because of the fact that the distributions in the numerator and denominator have the same mean. The deviations are larger in the tails of the v_2 distributions. Figure 5.20 and Figure 5.21 summarize similar results for v_3 and v_4. The deviations from unity are smaller than that for the v_2, which is mainly due to the fact that the unfolded v_3 and v_4 distributions themselves are almost Gaussian, while the response functions themselves are also Gaussian, hence the unfolding procedure does not lead to much shape distortions.

These different sources of systematic uncertainties are then added in quadrature. The combined uncertainties have quite large point to point fluctuations and are smoothed out to enclose the global trend of the systematic uncertainties.

The ranges of the unfolded distributions shown for Figure 5.19-5.21 are chosen such that the statistical error in each bin is less than 15%, and the upper limit of distributions has to be less than $\langle v_n \rangle + 4\sigma_{v_n}$. This is to ensure that the fluctuations in the unfolded distributions are not too large, usually much less than the quoted systematic uncertainties. The fraction of events outside this limit ranges from 0.1% to 0.5%, depending on the centrality and harmonic number. These fractions are summarized in Figure 5.22.

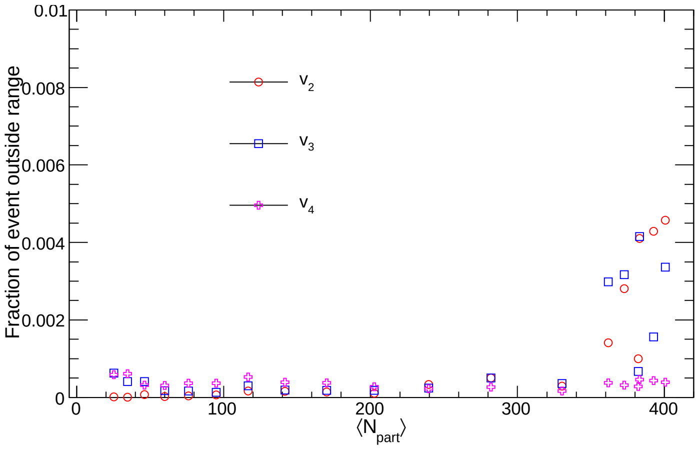

Figure 5.22: Fraction of events outside the range of the unfolded distributions as function of $\langle N_{\text{part}} \rangle$ for $v_2 - v_4$.

5.4 Results

EbyE v_n distributions

Figure 5.23 shows the main result of the EbyE v_n measurements. These are the probability distribution of the EbyE v_n in several centrality intervals for charged particles with $p_{\mathrm{T}} > 0.5$ GeV and $|\eta| < 2.5$. The shaded bands indicate the systematic uncertainties associated with the reduced shape and are fully correlated: the data points are allowed to change the shape of the distribution within the band while keeping the $\langle v_n \rangle$ unchanged. The ranges of these distributions are chosen such that the statistical uncertainties in all bins are less than 15%. This choice ensures that the statistical uncertainties are always smaller than the systematic uncertainties, and that the total integral outside these ranges is < 0.1% for 5% centrality intervals and < 0.5% for the 1% centrality intervals.

The v_2 distribution changes considerably between the different centralities, indicating the important role of the changing average geometry. For the v_3 and v_4 distributions the change is more gradual. This was already seen in the EP and 2PC analyses where it was shown the $v_2^{\mathrm{EP/2PC}}$ changes quite strongly with centrality but the $v_3^{\mathrm{EP/2PC}}$ and $v_4^{\mathrm{EP/2PC}}$ change much slowly. These distributions are compared with the fluctuations-only scenario (Eq. 5.5 and 5.6) given by:

$$P(v_n) = \frac{v_n}{\delta_n^2} e^{-\frac{v_n^2}{2\delta_n^2}}, \delta_n = \sqrt{\frac{2}{\pi}} \langle v_n \rangle \tag{5.25}$$

These functions, as indicated by the solid curves, are calculated directly from the measured $\langle v_n \rangle$ values for each distributions. The fluctuations-only description works well for v_3 and v_4 over the measured centrality range. However, a small systematic difference in the tails of the v_3 distributions is noticed in mid-central collisions where the v_3 values exceed 0.1. For v_2 the fluctuations-only description works only for the (0-2)% centrality intervals (only (0-1)% is shown on the plot), and is not shown for the other centralities. It will be shown later that they are better described by Bessel-Gaussian distributions with $v_n^{\mathrm{RP}} > 0$, indicating the effects of the average geometry on the v_2.

p_{T} scaling of v_n distributions

The top panels of Figs. 5.24-5.25 compare the unfolded EbyE v_n distribution in three p_{T} ranges: $p_{\mathrm{T}} \in (0.5, 1.0)$ GeV, $p_{\mathrm{T}} > 1.0$ GeV and $p_{\mathrm{T}} > 0.5$ GeV, for the (20-25)% and (40-45)% centrality intervals respectively (also see Fig. 5.17). The distributions are much broader for the higher p_{T} range, however, once they

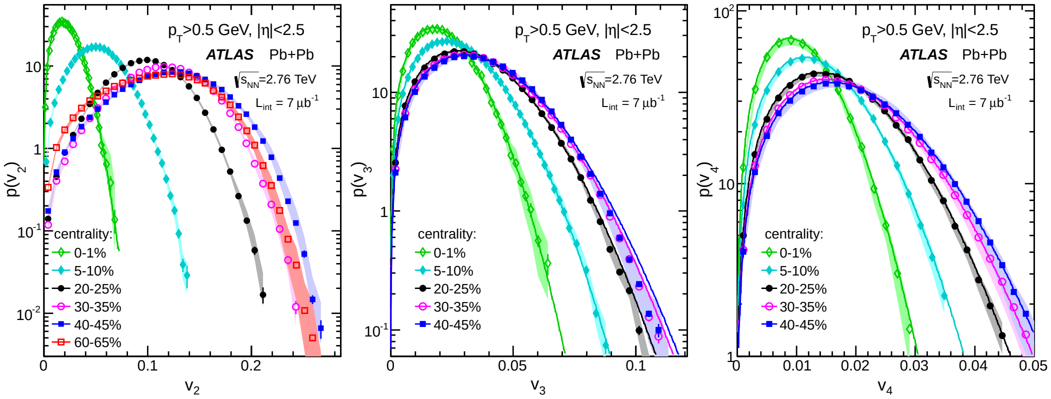

Figure 5.23: The v_n distributions normalized to unity in several centrality intervals for $n = 2$ (left panel), $n = 3$ (middle panel) and $n = 4$ (right panel). The errors bars are statistical uncertainties, and the shaded bands are uncertainties on the v_n-shape. The solid curves are functions calculated from the measured $\langle v_n \rangle$ according to Eq. 5.25 (shown for the (0-1)% centrality interval for v_2, and all centrality intervals for v_3 and v_4).

are rescaled[7] to the same $\langle v_n \rangle$ values (bottom panels), all three distributions almost completely match with each other[8]. This suggests that the hydrodynamic response of the medium factorizes into a p_{T} dependent function and an initial-geometry dependent function.

Starting from the EbyE distributions, quantities such as the mean v_n ($\langle v_n \rangle$) and the rms width σ_{v_n} can be obtained. These are shown in Fig. 5.26 as a function of $\langle N_{\mathrm{part}} \rangle$ for the $p_{\mathrm{T}} \in (0.5, 1.0)$ GeV, $p_{\mathrm{T}} > 1.0$ GeV and the $p_{\mathrm{T}} > 0.5$ GeV bins. The shaded bands represent the systematic uncertainties listed in Table 5.1, which in general are asymmetric. It is seen that while the $\langle v_n \rangle$ and σ_{v_n} have considerable p_{T} dependence, the ratio σ_{v_n}/v_n is nearly identical for the three bins. This shows that the scaling feature shown in Figs. 5.24–5.25 is in fact true for all centralities. For v_2, the value of $\sigma_{v_n}/\langle v_n \rangle$ varies strongly with $\langle N_{\mathrm{part}} \rangle$ and reaches a minimum of about 0.34 at $\langle N_{\mathrm{part}} \rangle \sim 200$ or (20-30)% centrality range. For v_3 and v_4, the value of $\sigma_{v_n}/\langle v_n \rangle$ is almost independent of $\langle N_{\mathrm{part}} \rangle$, and is consistent with the value expected from pure Gaussian fluctuations scenario: $\sqrt{\frac{4}{\pi} - 1} = 0.523$ (Eq. 5.7) as indicated by the dashed lines. This was already expected from the EbyE distributions (Fig. 5.23) where it

---

[7] Note that these are probability distributions and are constrained to have an integral equal to 1.0, thus after scaling along the x-axis they are renormalized again.

[8] Note that only two of these bins are independent, as the $p_{\mathrm{T}} > 0.5$ GeV bin is simply the sum of the other two.

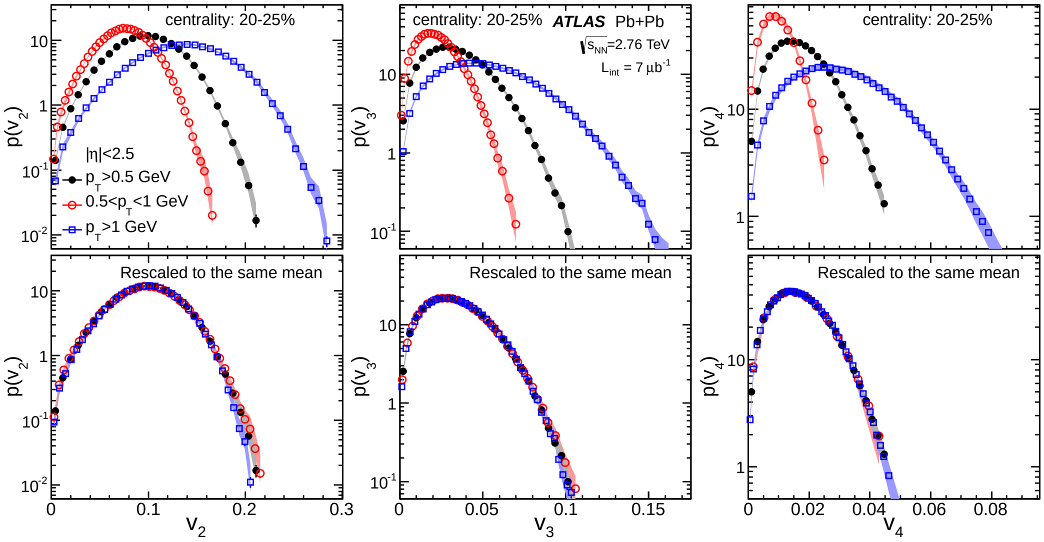

Figure 5.24: Top panels: The unfolded distributions for v_n in the (20-25)% centrality interval for charged particles in the $p_{\rm T} > 0.5$ GeV, 0.5< $p_{\rm T} < 1$ GeV and $p_{\rm T} > 1$ GeV ranges. Bottom panels: same distributions but rescaled horizontally so the $\langle v_n \rangle$ values match that for the $p_{\rm T} > 0.5$ GeV range. The shaded bands represent the systematic uncertainties on the v_n-shape.

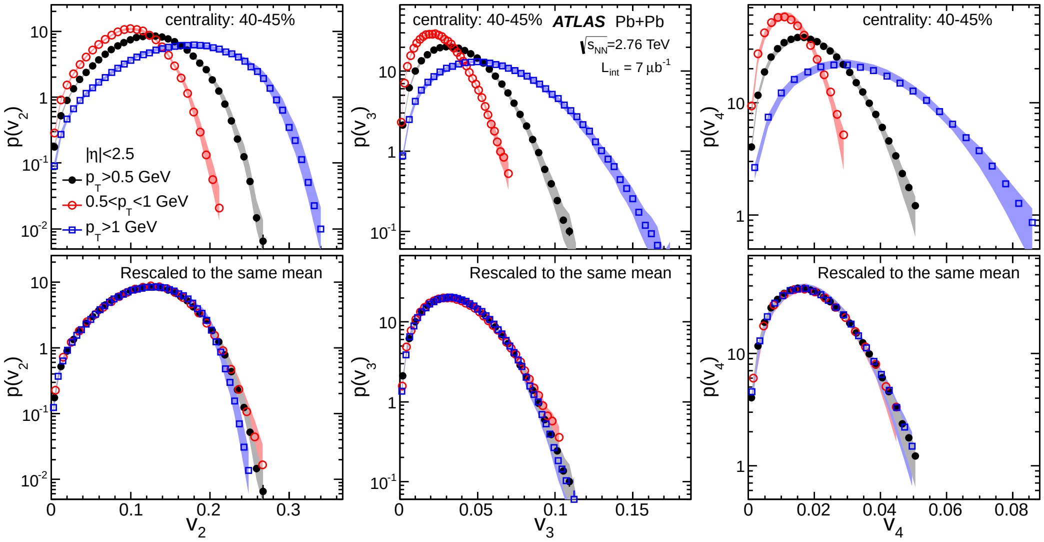

Figure 5.25: Same as previous plot but for (40-45)% centrality interval.

was shown that the v_3 and v_4 distributions were consistent with the pure-fluctuations scenario. Note that for v_2, the pure-fluctuations limit is also reached in most central collisions, indicating the lack of mean geometry effects on the EbyE v_2 distributions in very central events. The values of $\sigma_{v_n}/\langle v_n\rangle$ are also compared to those obtained from the Glauber model [53] and MC-KLN model [105]. The comparisons to these two models are discussed in more detail in Section 5.4.2.

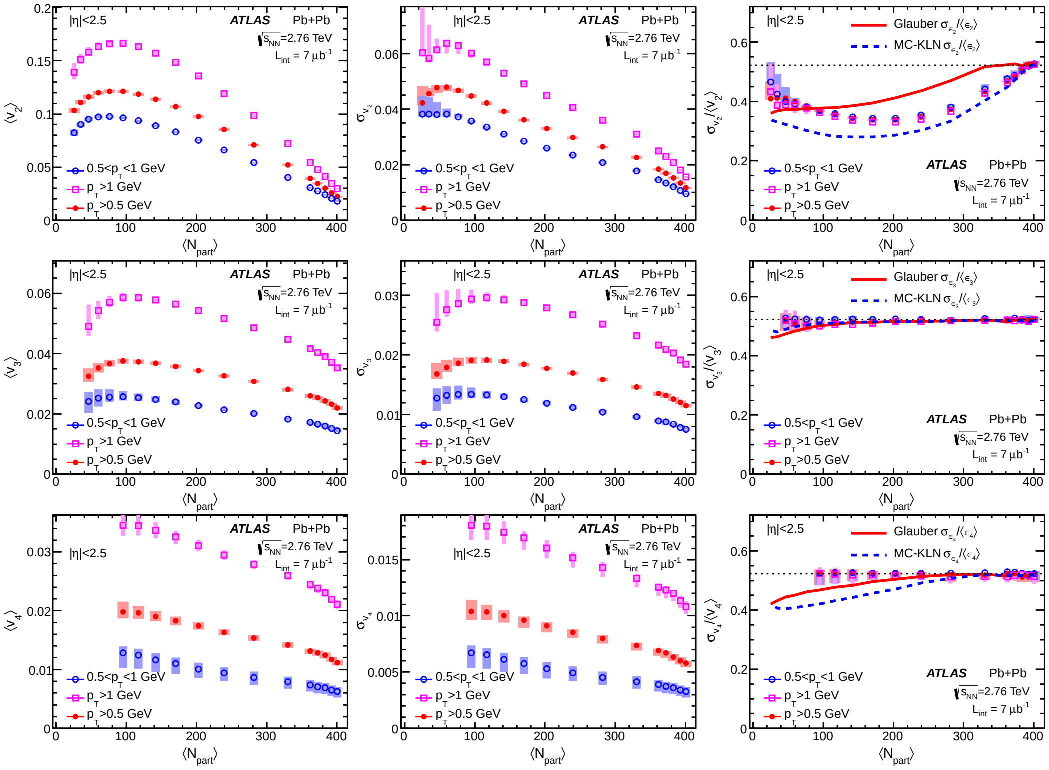

Figure 5.26: The $\langle N_{\text{part}}\rangle$ dependence of $\langle v_n\rangle$ (left column), σ_{v_n} (middle column) and $\sigma_{v_n}/\langle v_n\rangle$ (right column) for $n = 2$ (top row), $n = 3$ (middle row) and $n = 4$ (bottom row). Each panel shows the results for three p_{T} ranges together with the total systematic uncertainties. The dashed lines in the right column indicate the $\sqrt{\frac{4}{\pi} - 1} = 0.523$ expected for pure Gaussian distributions. The values of $\sigma_{v_n}/\langle v_n\rangle$ are compared with the $\sigma_{\epsilon_n}/\langle\epsilon_n\rangle$ given by the Glauber model [53] and MC-KLN model [105].

Figure 5.27 compares the $\langle v_n\rangle$ and $\sqrt{\langle v_n^2\rangle} \equiv \sqrt{\langle v_n\rangle^2 + \sigma_{v_n}^2}$ from the EbyE distributions with the v_n measured using the event-plane method for tracks with $p_{\text{T}} > 0.5$ GeV. Since the fractional systematic uncertainties for $\langle v_n\rangle$ and σ_{v_n} are almost the same and fully correlated, hence the fractional uncertainties for $\sqrt{\langle v_n^2\rangle}$ is taken to be the same as those for $\langle v_n\rangle$. The values of the v_3^{EP} are almost identical to $\sqrt{\langle v_3^2\rangle}$. For v_4 a slight systematic shift of the EP values from the $\sqrt{\langle v_4^2 \rangle}$ can be seen, but this difference is comfortably covered by the systematic errors. For v_2 however, the EP values are in general in between $\langle v_2 \rangle$ and $\sqrt{\langle v_2^2 \rangle}$, and only approach the $\sqrt{\langle v_2^2 \rangle}$ values in peripheral collisions. This is qualitatively consistent with the behavior expected for v_n measured by event-plane method i.e. $v_n^{\mathrm{EP}} \to \sqrt{\langle v_n^2 \rangle}$ when the event-plane resolution is poor as it is for v_3 and v_4 (and for v_2 for peripheral events).

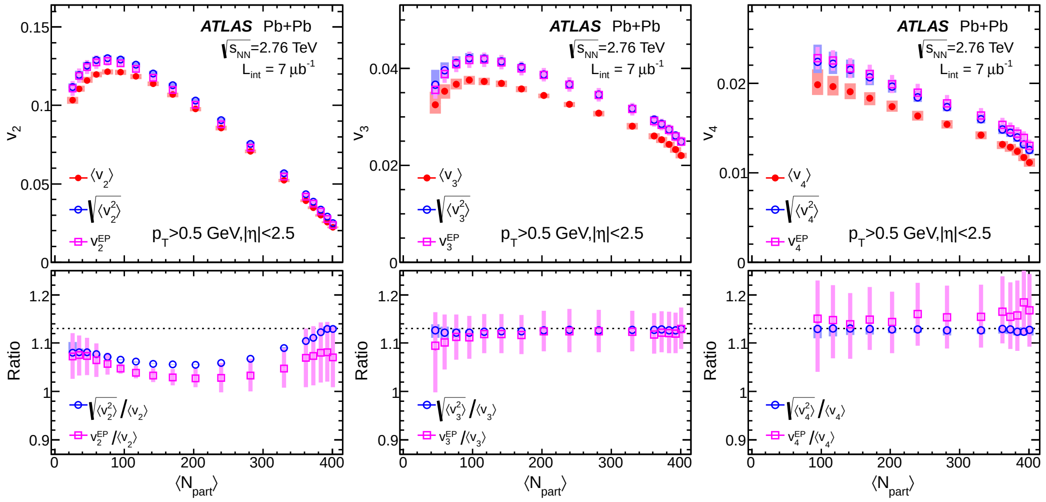

Figure 5.27: The $\langle v_n \rangle$ and $\sqrt{\langle v_n^2 \rangle} \equiv \sqrt{\langle v_n \rangle^2 + \sigma_{v_n}^2}$ derived from the EbyE v_n distribution, compared with the EP v_n for tracks with $p_{\mathrm{T}} > 0.5$ GeV. The shaded bands represent the total systematic uncertainties. The dotted lines in bottom panels indicate $\sqrt{\langle v_n^2 \rangle}/\langle v_n \rangle = 1.13$, the value expected for the radial projection of a 2D Gaussian distribution.

5.4.1 Derived quantities from the v_2 distributions

The measured v_n distributions can be fitted with the Bessel-Gaussian function to extract the mean-geometry component (v_n^{RP}) and the fluctuation component (δ_{v_n}). However, as demonstrated by Figs 5.23 and 5.26, the distributions for v_2 in most central (0-2)% events and for v_3 and v_4 for all centralities are well described by the pure Gaussian fluctuations scenario. Thus the Bessel-Gaussian fits are only done for v_2 and in the (2-70)% centrality range. The results of the fits are shown in Fig. 5.28. The fits work reasonably well up to the (25-30)% centrality interval. However, systematic deviations are observed in the tails of the distributions already in the (15–20)% centrality interval which increase for more peripheral collisions. These deviations may indicate that the fluctuations of ϵ_2 are not Gaussian in peripheral collisions where N_{part} is small [66]. They may also indicate that the linear response assumption breaks down for peripheral events.

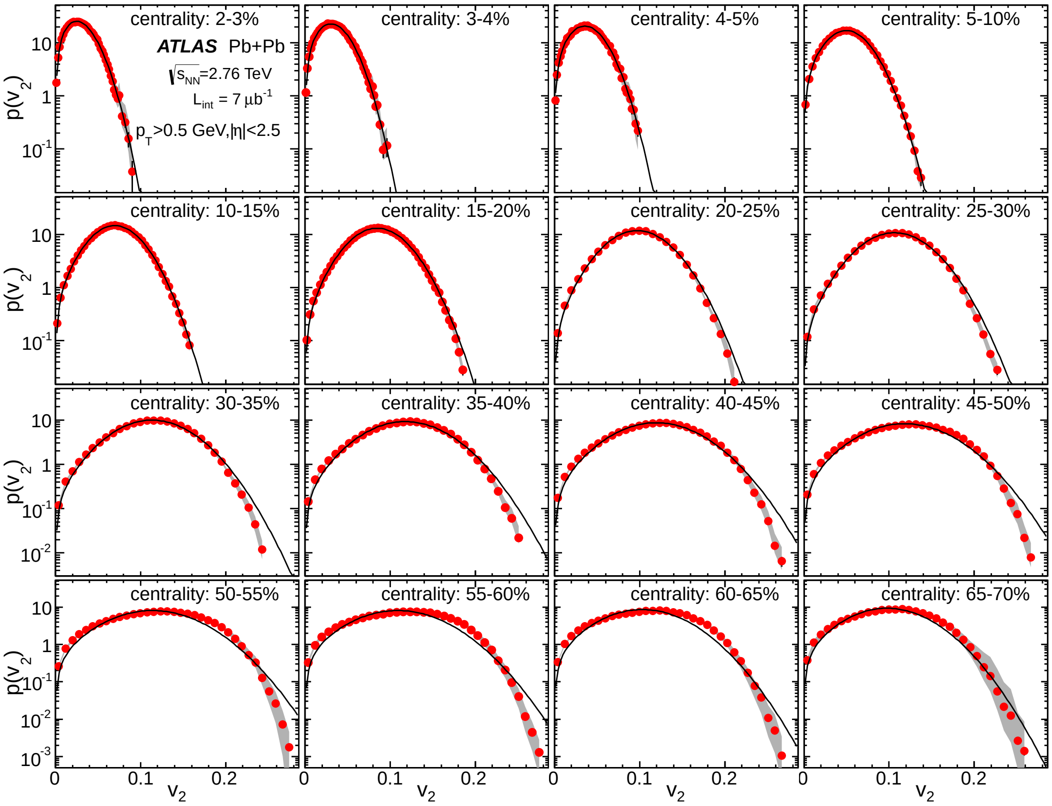

Figure 5.28: The probability distribution of v_2 in several centrality intervals for $p_T > 0.5$ GeV, together with fits to the Bessel-Gaussian function Eq. 5.3. The fit for (0-2)% are not shown but they can be well described by Bessel-Gaussian function with $v_2^{\mathrm{RP}} = 0$ (see discussion of Fig. 5.26).

The v_2^{RP} extracted from the fits is shown in the left panel of Fig. 5.29 as a function of N_{part}. Also shown for comparison is the $\langle v_2 \rangle$ obtained directly from the v_2 distributions. The v_2^{RP} is always smaller than the $\langle v_2 \rangle$. In the (0-2)% central collisions (top two N_{part} bins) it is consistent with zero, as expected from the results shown in Figure 5.26. The second panel shows the comparison of δ_{v_2} from the fits to the σ_{v_2} of the distributions. The δ_{v_2} is comparable to σ_{v_2} except in the most central collisions. The third panel shows the ratio $\delta_{v_2}/v_2^{\mathrm{RP}}$ which is a measure of the relative influence of the fluctuations and the mean geometry on the v_2. Also shown for comparison is the $\sigma_{v_2}/\langle v_2 \rangle$. The value of $\delta_{v_2}/v_2^{\mathrm{RP}}$ decreases with N_{part} and reaches a minimum of 0.38 ± 0.02 at $N_{\mathrm{part}} \approx 200$ (or (20–25)% centrality), and then increases and is greater than one in central collisions. Note that the two points corresponding to (0–1)% and (1–2)% most central collisions are omitted as their v_2^{RP} values are consistent with zero. This result shows that the impact of the fluctuations on the v_2 distributions is largest in central events, lowest in mid-central events and again increases for peripheral events.

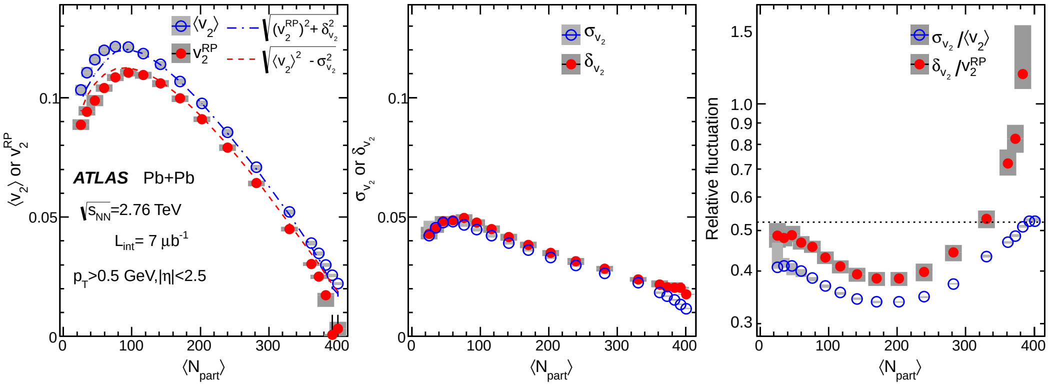

Figure 5.29: The dependence of v_2^{RP} and $\langle v_2 \rangle$ (left), δ_{v_2} and σ_{v_2} (middle) and $\delta_{v_2}/v_2^{\mathrm{RP}}$ and $\sigma_{v_2}/\langle v_2 \rangle$ (right) on N_{part}. The error bars and shaded bands indicate the statistical and systematic uncertainties, respectively. The dashed and dotted lines in the left panel indicate the calculated values for $\sqrt{\left(v_2^{\mathrm{RP}}\right)^2 + \delta_{v_2}^2}$ and $\sqrt{\langle v_2 \rangle^2 - \sigma_{v_2}^2}$, respectively.

According to Eq. 5.4, when the relative fluctuation is small the value of $\langle v_n \rangle$ can be approximated by:

$$\langle v_n \rangle \approx \sqrt{\left(v_n^{\mathrm{RP}}\right)^2 + \delta_{v_n}^2} \; . \tag{5.26}$$

Similarly the value of v_n^{RP} can be estimated from σ_{v_n} and $\langle v_n \rangle$ without relying on the fit as:

$$v_n^{\mathrm{RP}} \approx \sqrt{\langle v_n \rangle^2 - \sigma_{v_n}^2} \; . \tag{5.27}$$

Both relations are calculated and indicated by the dashed and dotted lines in the left panel of Fig. 5.29 for v_2. Good agreement is observed for $100 < N_{\mathrm{part}} < 350$, corresponding to the (5–45)% centrality range. However, systematic deviations are observed both in central collisions where the fluctuation are dominating, and in peripheral collisions where the Bessel-Gaussian function fails to describe the shape of the v_2 distributions.

The elliptic flow fluctuations have also been studied using multi-particle

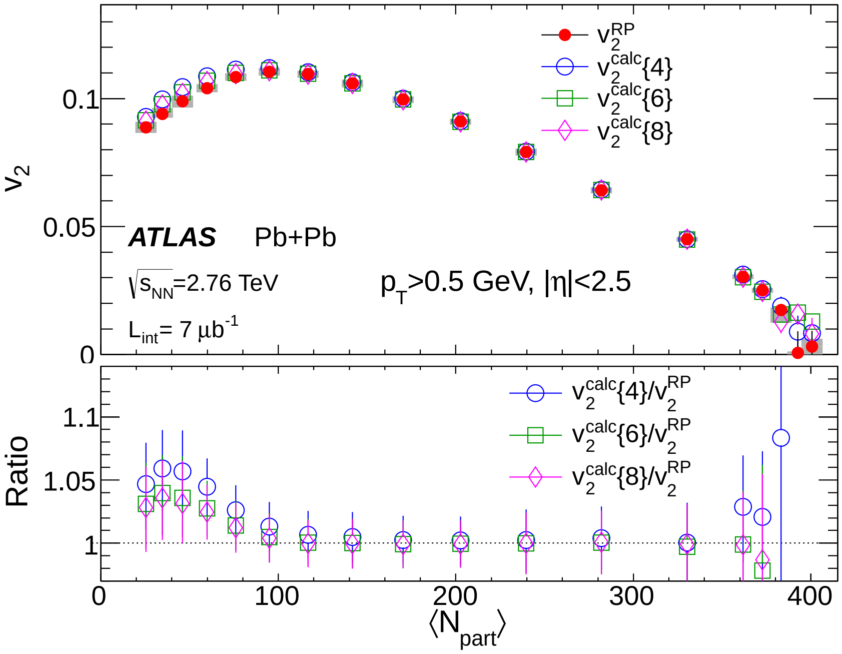

Figure 5.30: Comparison of the v_2^{RP} obtained from the Bessel-Gaussian fit of the v_n distribution with the four-particle ($v_2^{\mathrm{calc}}\{4\}$), six-particle ($v_2^{\mathrm{calc}}\{6\}$) and eight-particle ($v_2^{\mathrm{calc}}\{8\}$) cumulant results calculated directly from the v_n distribution via Eq. 5.28. The lower sub-panel shows the ratios of the cumulants to the fit result, with the error bars representing the total uncertainties.

cumulants [97, 100, 106]. The first few cumulants are defined as [44]:

$$\begin{aligned}
v_2\{2\}^2 &\equiv \langle v_2^2\rangle \approx \left(v_2^{\mathrm{RP}}\right)^2 + 2\delta_{v_2}^2 \ , \\
v_2\{4\}^4 &\equiv -\langle v_2^4\rangle + 2\langle v_2^2\rangle^2 \approx \left(v_2^{\mathrm{RP}}\right)^4 \ , \\
v_2\{6\}^6 &\equiv \left(\langle v_2^6\rangle^2 - 9\langle v_2^4\rangle\langle v_2^2\rangle + 12\langle v_2^2\rangle^3\right)/4 \approx \left(v_2^{\mathrm{RP}}\right)^6 \ , \\
v_2\{8\}^8 &\equiv -\left(\langle v_2^8\rangle^2 - 16\langle v_2^6\rangle\langle v_2^2\rangle - 18\langle v_2^4\rangle^2 + 144\langle v_2^4\rangle\langle v_2^2\rangle^2 - 144\langle v_2^2\rangle^4\right)/33 \\
&\approx \left(v_2^{\mathrm{RP}}\right)^8 \ . \qquad (5.28)
\end{aligned}$$

where, the second part of the equations are exact in the Bessel-Gaussian limit. In this limit all the $v_n\{2k\}$ for $k \geq 2$ are identical to v_n^{RP}. Thus consistency between the higher order cumulants is considered to be indicative of Bessel-Gaussian flow fluctuations. In a recent measurement, the ALICE collaboration has shown such consistency between the $v_2\{4\}$, $v_2\{6\}$ and $v_2\{8\}$ [100]. This is in apparent contradiction with the deviations seen in the tails of the v_2 distributions from the Bessel-Gaussian fits. In order to resolve this, the cumulants

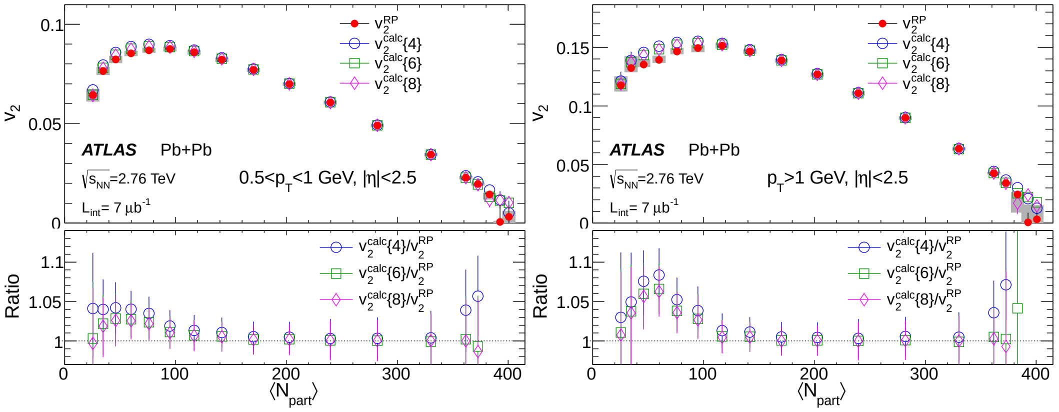

Figure 5.31: Comparison for $0.5 < p_{\mathrm{T}} < 1$ GeV (left panel) and $p_{\mathrm{T}} > 1$ GeV (right panel) of the v_2^{RP} obtained from the Bessel-Gaussian fit of the v_2 distributions with the values for four-particle ($v_2^{\mathrm{calc}}\{4\}$), six-particle ($v_2^{\mathrm{calc}}\{6\}$) and eight-particle ($v_2^{\mathrm{calc}}\{8\}$) cumulants calculated directly from the v_2 distributions via Eq. (5.28). The lower sub-panels show the ratios of the cumulants to the fit results, with the error bars representing the total uncertainties.

are directly calculated starting from the EbyE v_2 distributions. They are denoted by $v_2^{\mathrm{calc}}\{2k\}$ (k=2–4) and are shown in Figure 5.30 as a function of N_{part} along with the v_n^{RP} parameter from the Bessel-Gaussian fits (from Fig. 5.28). It is seen that the cumulants agree with v_n^{RP} within ∼1% till N_{part} ∼100 (or (40-45)% centrality), while the deviations from the Bessial-Gaussian fits already showed up in the (15-20)% centrality bin (or $N_{\mathrm{part}} \approx$240). Even for N_{part} <100, while the cumulants show deviation from v_n^{RP} they are still consistent with each other. This indicates that the 4–8 particle cumulants are not sensitive enough to measure the deviations from Bessel-Gaussian distributions that are seen in the v_2 distributions. Figure 5.31 shows similar comparisons separately for the for the $0.5 < p_{\mathrm{T}} < 1$ GeV and $p_{\mathrm{T}} > 1$ GeV ranges. The trends are similar to those seen in figure 5.30. However a slightly bigger deviation between v_2^{RP} and $v_2^{\mathrm{calc}}\{2k\}$ is observed in peripheral collisions for the $p_{\mathrm{T}} > 1$ GeV range.

5.4.2 Comparison to initial geometry models

The EbyE v_n distributions can be compared with the distributions of eccentricities ϵ_n calculated from commonly used models of initial geometry. Two geometry models, a Glauber model [53] and CGC model [105] are used for this comparison. The CGC model is based on Glauber model but takes into account the corrections to the initial geometry due to gluon saturation effects.

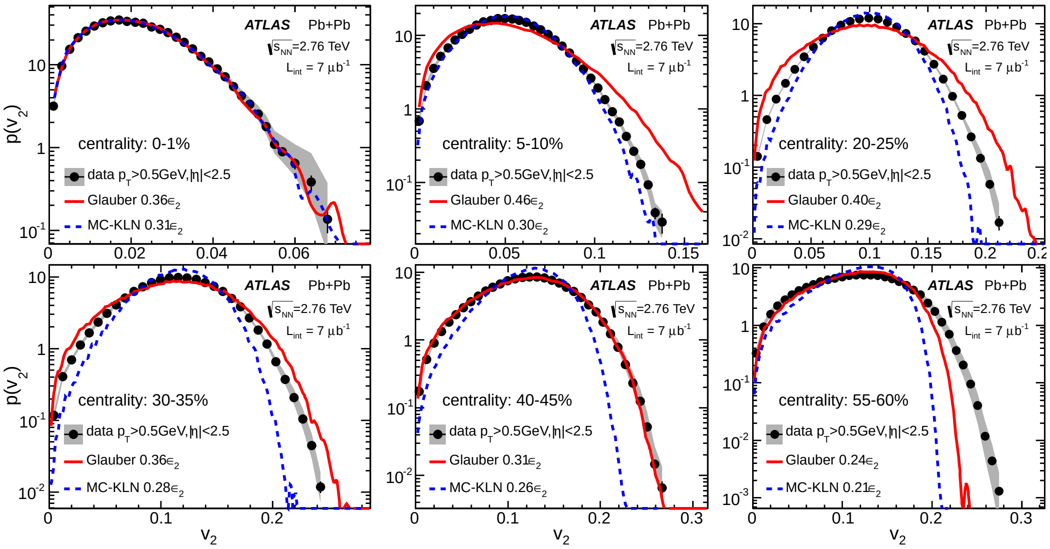

Figure 5.32: The EbyE v_2 distributions compared with the eccentricity distributions from two initial geometry models: Glauber model (red lines) and CGC model (blue lines).

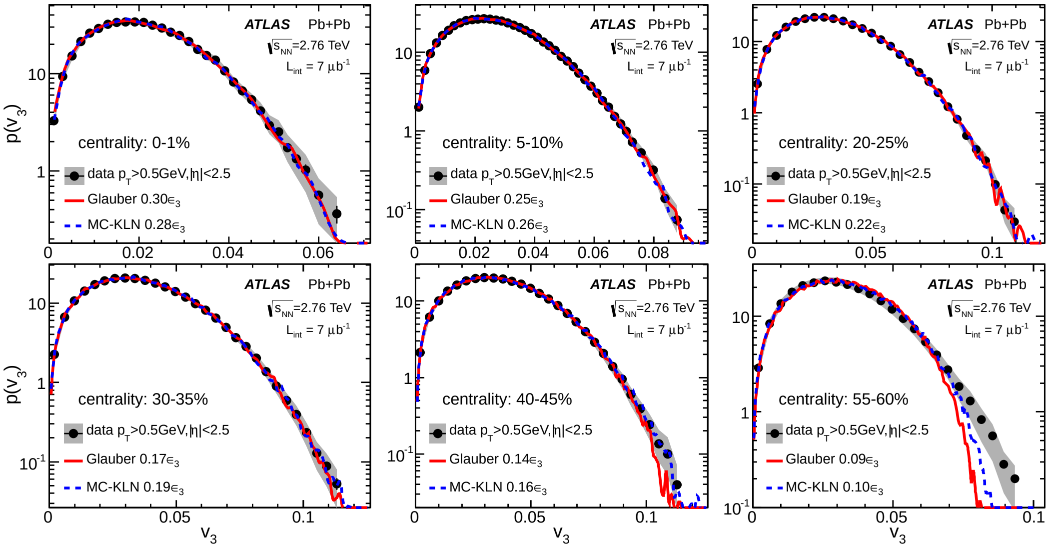

Figure 5.33: The EbyE v_3 distributions compared with the eccentricity distributions from two initial geometry models: Glauber model (red lines) and CGC model (blue lines).

Three million events are generated for either model and grouped into centrality intervals by selecting on their impact parameter. Figure 5.32 compares

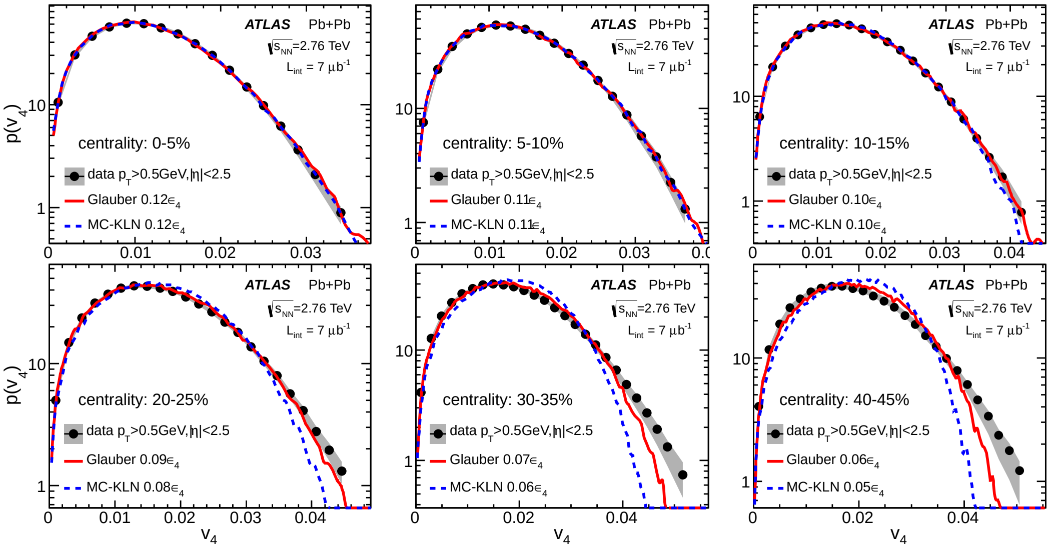

Figure 5.34: The EbyE v_4 distributions compared with the eccentricity distributions from two initial geometry models: Glauber model (red lines) and CGC model (blue lines).

the EbyE v_2 distributions with the distribution of the eccentricities ϵ_2 of the initial geometry calculated in these two models. The ϵ_2 distribution for each centrality interval is rescaled to match the $\langle v_2 \rangle$ of the data, the scale factors are indicated on the plots. The rescaled ϵ_2 distributions match the data in the most central (0-1)%collisions, but start to fail in more peripheral collisions. Similar comparisons between v_n and ϵ_n for n=3 and 4 are shown in Fig. 5.33 and Fig. 5.34, respectively. The agreement with the models are better than the n=2 case, but even here deviations are seen in the tails for the less central events, beginning with (40-45)% for v_3 and (20-25)% for v_4. It has been shown that in hydrodynamic models the shape of the EbyE v_n distributions are very well correlated with the EbyE ϵ_n distributions [107]. Thus, such large deviations seen in the Glauber and MC-KLN ϵ_n distributions from the measured v_n distributions, are strong indicators of the inadequacy of these models in describing the initial geometry.

Figure 5.35 shows similar comparisons of the v_n distributions measured in this work to the ϵ_n distributions from the IP-Glasma Model, and the v_n distributions obtained after evolving the IP-Glasma initial conditions via viscous hydro. These comparisons have been taken from from [76, 108]. The model ϵ_n values are in fairly good agreement with the measured EbyE v_n distributions, although some disagreements in the tails are visible in the (20-25)% centrality interval. However, no such deviations are seen when comparing the model v_n

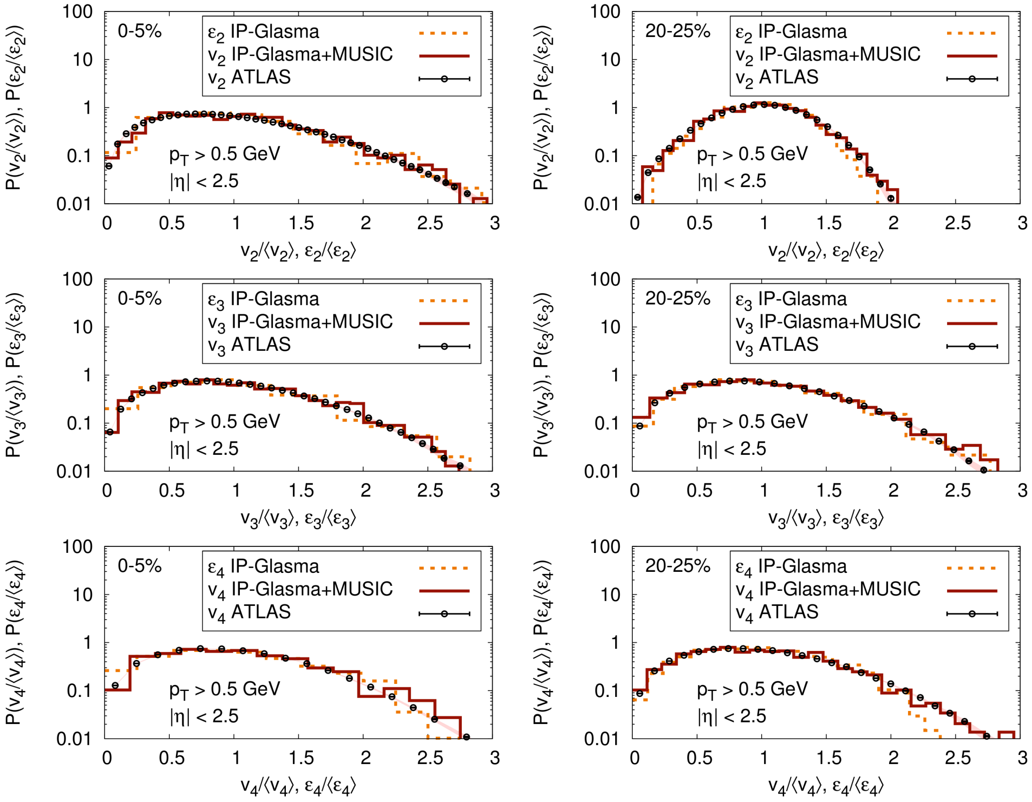

Figure 5.35: The EbyE v_n distributions compared with the ϵ_n distributions from the IP-Glasma Model [76] and the v_n distributions obtained after viscous hydro (MUSIC) evolution. Figure taken from [108].

distributions, obtained after hydro-evolution, to the measured distributions. This indicates that the tails of the EbyE v_n distributions are sensitive to the effects of non-linear hydro response.

These comparisons show the power of these measurements in constraining models of initial geometry.

5.5 Summary

In this chapter, measurements of the EbyE v_n distributions for n=2, 3 and 4 for several centrality intervals were presented. The v_3 and v_4 distributions were shown to be consistent with a pure Gaussian fluctuation scenario (i.e. $v_n^{\mathrm{RP}} = 0$) over the entire measured centrality range. However, for the v_2 distribution, this was true only in the (0-2)% most central collisions, and it showed significant deviations from this scenario for other centralities, indicating a considerable influence from the average collision geometry. The shape of the distributions, when rescaled to the same $\langle v_n \rangle$, were shown to be nearly identical for $p_{\mathrm{T}} \in (0.5, 1)$ GeV and $p_{\mathrm{T}} > 1$ GeV, suggesting that the hydrodynamic response to the initial geometry depends on p_{T} only up to an overall scaling. The ratio of the width to the mean, $\sigma_{v_n}/\langle v_n \rangle$, was calculated from these distributions and studied as a function of $\langle N_{\mathrm{part}} \rangle$ and p_{T}. The values of $\sigma_{v_2}/\langle v_2 \rangle$ are observed to reach a minimum of 0.34 for $\langle N_{\mathrm{part}} \rangle \sim 200$, while the values of $\sigma_{v_3}/\langle v_3 \rangle$ and $\sigma_{v_4}/\langle v_4 \rangle$ are consistent with the value expected from a pure Gaussian fluctuation scenario independent of $\langle N_{\mathrm{part}} \rangle$.

To further understand the role of average geometry and fluctuations on the v_2 distributions, they were fitted with Bessel-Gaussian functions to estimate the value of v_2^{RP} and the width of the fluctuation δ_{v_2}. The value of $\delta_{v_2}/v_2^{\mathrm{RP}}$ was found to decrease with increasing N_{part} and reach a minimum of 0.38 ± 0.02 at $N_{\mathrm{part}} \approx 200$, and then increase again and eventually become greater than one in central collisions, showing that the influence of the fluctuations on the v_2 is largest in central events, lowest in mid-central events and again increases for peripheral events.

A systematic deviation of the v_2 data from Bessel-Gaussian distributions was observed for the (15-20)% centrality interval, with the deviations increasing for more peripheral collisions. This suggests significant non-Gaussian behaviour in the flow fluctuations for collisions with small N_{part}. The Multi-particle cumulants were shown to be not sensitive enough to identify such deviations. The ability of the EbyE v_n distributions to rule out models of initial geometry was demonstrated by comparing them to ϵ_n distributions obtained from various models.

Chapter 6

Measurement of event-plane correlations in Pb+Pb collisions

In this chapter correlations between sets of two or three event-planes Φ_n are measured. Correlations between the Φ_n can be generated due to correlations in the initial geometry between the eccentricities ϵ_n, which drive the hydrodynamic response. If the medium response were purely linear i.e. $v_n \propto \epsilon_n$, then the Φ_n would be oriented along the minor axes of the ϵ_n, and any correlations between the ϵ_n in the initial geometry would result in correlations between the Φ_n in the final state. Hydrodynamic calculations exist that show that the Ψ_2 and Ψ_3 are strongly correlated with the ϵ_2 and ϵ_3 in the initial state [47, 52].

However such linearity in the response has been shown to break for higher order harmonics [47]. In such cases the v_n also receive non-linear contributions from the lower order ϵ_m with $m<n$ [109]. For example, including non-linear response, the magnitude and phases of v_4 and v_5 are related to the ϵ_n as [47]:

$$\begin{aligned} v_4 e^{i4\Phi_4} &= k_{4,4}\epsilon_4 e^{i4\Phi'_4} + k_{4,2,2}\epsilon_2^2 e^{i4\Phi'_2} \\ v_5 e^{i5\Phi_5} &= k_{5,5}\epsilon_5 e^{i5\Phi'_5} + k_{5,2,3}\epsilon_2 e^{i2\Phi'_2}\epsilon_3 e^{i3\Phi'_3}. \end{aligned} \tag{6.1}$$

where, the k's characterize the strength of the linear or non-linear response, and the Φ'_n are the orientations of the minor axes of the ϵ_n. Eq. 6.1 suggests that the non-linear response can lead to Φ_2-Φ_4 correlations and Φ_2-Φ_3-Φ_5 correlations. The response can be influenced by viscous effects, which damp out the higher order ϵ_n and thus enhance the relative contribution of the non-linear response to the lower order ϵ_m ($m<n$). Thus measurements of event-plane correlations can be used to simultaneously study the non-linear response as well as to constrain η/s.

Previous measurements at RHIC and the LHC support a strong correlation between Φ_2 and Φ_4 [73], and a weak correlation between Φ_2 and Φ_3 [110, 111]. Although the methodology used in those measurements and the observables were different than those presented here. The correlations among three event planes of different order have been investigated in model calculations [46, 112–114], but no experimental measurements exist to date.

The outline of this chapter is as follows: In Section 6.1 the observables are defined and the analysis framework is discussed. In Sections 6.2 and 6.3, the two-plane and three-plane measurements as well as all the systematic cross-checks are described. Finally in Section 6.5 the final results as well as comparisons to theory are presented. The measurements presented here are summarized in an ATLAS CONF-NOTE [115].

6.1 Methodology

6.1.1 Observables

Correlations between two event-planes (Φ_n, Φ_m) can be studied by measuring the generalized relative distribution of one w.r.t. the other, i.e. distributions of the form

$$a_n\Phi_n + a_m\Phi_m, \tag{6.2}$$

where a_n and a_m are integers. As illustrated in Fig. 6.1, the n^{th}-order harmonic plane Φ_n has a n-fold symmetry in azimuth. Thus any physical correlation between two event-planes of the form Eq 6.2 has to be invariant under a phase shift:

$$\Phi_n \to \Phi_n + p\frac{2\pi}{n} \text{ and } \Phi_m \to \Phi_m + q\frac{2\pi}{m} \tag{6.3}$$

for arbitrary integers p and q. Also the combination must be invariant under a global rotation (along the beam axis) by an arbitrary angle θ:

$$\Phi_n \to \Phi_n + \theta \text{ and } \Phi_m \to \Phi_m + \theta \tag{6.4}$$

The above condition simply means that the correlation should not depend on the choice of transverse coordinates used to measure it.

The first condition requires that a_n (a_m) has to be a multiple of n (m), while the second condition requires that the sum of the coefficients has to be zero i.e. a_n=$-a_m$. The relative angle $\Phi_{n,m} = k(\Phi_n - \Phi_m)$, with k being the least common multiple of n and m, satisfies these constraints. Any other relative angle that satisfies these constraints can only be an integral multiple of $\Phi_{n,m}$. Thus the correlation between the event-planes Φ_n and Φ_m is completely described by the differential distribution $dN_{\text{events}}/(d\,(k(\Phi_n - \Phi_m))$ of the EbyE values of $k(\Phi_n - \Phi_m)$. This distribution is an even function due to symmetry, hence it can be expanded into the following Fourier series [1]:

$$\frac{dN_{\text{events}}}{d\,(k(\Phi_n - \Phi_m))} \quad \propto \quad 1 + 2\sum_{j=1}^{\infty} V^{j}_{n,m} \cos jk(\Phi_n - \Phi_m) \tag{6.5}$$

where the **correlators** $V^{j}_{n,m}$ are given by:

$$V^{j}_{n,m} \quad = \quad \langle \cos jk(\Phi_n - \Phi_m)\rangle. \tag{6.6}$$

The measurement of the two-plane correlation is thus equivalent to measuring the event average of a set of cosine functions $\langle \cos jk(\Phi_n - \Phi_m)\rangle$. The reason why the Fourier coefficients are measured, rather than directly measuring the distribution, is that the coefficients can be corrected to account for detector resolution effects while the raw distribution cannot.

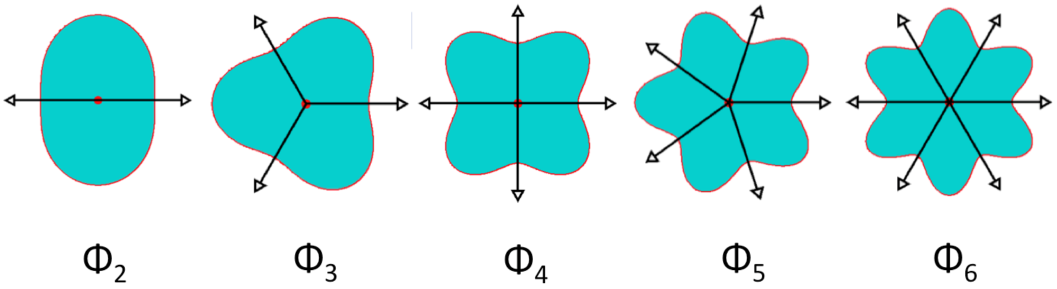

Figure 6.1: Illustration of the azimuthal shape of the harmonic component n=2-6. The angle of n^{th}-order harmonic shape Φ_n has n-fold ambiguity, i.e. $dN_{\text{evts}}/d\Phi_n$ has to be invariant under transformation: $\Phi_n \rightarrow \Phi_n + \frac{2\pi}{n}$.

This discussion can be generalized for correlations involving three or more EPs. The multi-plane correlator can be written as $\langle \cos(c_1\Phi_1 + 2c_2\Phi_2 ... + lc_l\Phi_l)\rangle$, where the n^{th}-order EP angle Φ_n always has a coefficient that is a multiple of n. The coefficients must also satisfy the constraint [112]:

$$c_1 + 2c_2 ... + lc_l = 0, \tag{6.7}$$

which ensures that measured angle is invariant under an arbitrary global rotation along the beam axis.

---

[1] There cannot be sine terms in this expansion as the colliding system Pb+Pb is symmetric w.r.t. to a parity transformation (when averaged over many events) while sine terms have odd parity.

The idea behind three-plane correlations can be understood from Eq. 6.1. Another way of understanding them at them is to express them as a linear combination of two-plane relative angles. For example:

$$\begin{aligned} 2\Phi_2 + 4\Phi_4 - 6\Phi_6 &= 4(\Phi_4 - \Phi_2) - 6(\Phi_6 - \Phi_2) \\ -10\Phi_2 + 4\Phi_4 + 6\Phi_6 &= 4(\Phi_4 - \Phi_2) + 6(\Phi_6 - \Phi_2) \end{aligned} \tag{6.8}$$

and

$$\begin{aligned} 2\Phi_2 + 3\Phi_3 - 5\Phi_5 &= 3(\Phi_3 - \Phi_2) - 5(\Phi_5 - \Phi_2) \\ -8\Phi_2 + 3\Phi_3 + 5\Phi_5 &= 3(\Phi_3 - \Phi_2) + 5(\Phi_5 - \Phi_2) \end{aligned} \tag{6.9}$$

Therefore the combination of two three-plane correlators reflects the correlation of two EPs relative to the third.

Event-plane resolution

As discussed in Chapter 3, the measured event-plane angles Ψ_n fluctuate about the true event-plane angles Φ_n. The measured correlators thus need to be corrected to account for the event plane resolution as (see Appendix D.1:

$$\langle \cos(c_1\Phi_1 + ... + lc_l\Phi_l)\rangle = \frac{\langle \cos(c_1\Psi_1 + ... + lc_l\Psi_l)\rangle}{\mathrm{Res}\{c_1\Psi_1\}...\mathrm{Res}\{c_l l\Psi_l\}} \tag{6.10}$$

$$\mathrm{Res}\{c_n n\Psi_n\} = \langle \cos c_n n(\Psi_n - \Phi_n)\rangle \tag{6.11}$$

For convenience, the combined resolution for the correlator is referred to by the notation:

$$\mathrm{Res}\{c_1\Psi_1 + ... + lc_l\Psi_l\} \equiv \mathrm{Res}\{c_1\Psi_1\}...\mathrm{Res}\{c_l l\Psi_l\}. \tag{6.12}$$

Note that the combined resolution is simply a product of the individual event-plane resolutions involved in the correlator and can become very small especially when higher order harmonics are involved.

In principle a large number of correlators can be studied. However, the measurability of these correlators is limited by the event-plane resolutions, as the correlators can not be measurable reliably if the associated resolutions for the event-planes are poor. Table 6.1 lists the set of two-plane correlations and required resolution terms in this analysis. The corresponding information for the three-plane correlations is listed in Table 6.2. The list of correlations includes all two and three-plane combinations for $n = 2-6$, that satisfy Eq. 6.7, and where the combined resolution is good enough for the correlations to be measurable. The two-plane and three-plane correlations are listed separately, because different detectors are used in their measurements, which requires the separate evaluation of the resolution corrections.

Correlator	Associated EP resolutions
$\langle\cos 4(\Phi_2 - \Phi_4)\rangle$	Res$\{4\Psi_2\}$, Res$\{4\Psi_4\}$
$\langle\cos 8(\Phi_2 - \Phi_4)\rangle$	Res$\{8\Psi_2\}$, Res$\{8\Psi_4\}$
$\langle\cos 12(\Phi_2 - \Phi_4)\rangle$	Res$\{12\Psi_2\}$, Res$\{12\Psi_4\}$
$\langle\cos 6(\Phi_2 - \Phi_3)\rangle$	Res$\{6\Psi_2\}$, Res$\{6\Psi_3\}$
$\langle\cos 6(\Phi_2 - \Phi_6)\rangle$	Res$\{6\Psi_2\}$, Res$\{6\Psi_6\}$
$\langle\cos 6(\Phi_3 - \Phi_6)\rangle$	Res$\{6\Psi_3\}$, Res$\{6\Psi_6\}$
$\langle\cos 12(\Phi_3 - \Phi_4)\rangle$	Res$\{12\Psi_3\}$, Res$\{12\Psi_4\}$
$\langle\cos 10(\Phi_2 - \Phi_5)\rangle$	Res$\{10\Psi_2\}$, Res$\{10\Psi_5\}$

Table 6.1: The list of two-plane correlators and associated event-plane resolution factors that need to be measured.

Correlator	Associated EP resolutions
$\langle\cos(2\Phi_2 + 3\Phi_3 - 5\Phi_5)\rangle$	Res$\{2\Psi_2\}$, Res$\{3\Psi_3\}$, Res$\{5\Psi_5\}$
$\langle\cos(2\Phi_2 + 4\Phi_4 - 6\Phi_6)\rangle$	Res$\{2\Psi_2\}$, Res$\{4\Psi_4\}$, Res$\{6\Psi_6\}$
$\langle\cos(-8\Phi_2 + 3\Phi_3 + 5\Phi_5)\rangle$	Res$\{8\Psi_2\}$, Res$\{3\Psi_3\}$, Res$\{5\Psi_5\}$
$\langle\cos(-10\Phi_2 + 4\Phi_4 + 6\Phi_6)\rangle$	Res$\{10\Psi_2\}$, Res$\{4\Psi_4\}$, Res$\{6\Psi_6\}$
$\langle\cos(2\Phi_2 - 6\Phi_3 + 4\Phi_4)\rangle$	Res$\{2\Psi_2\}$, Res$\{6\Psi_3\}$, Res$\{4\Psi_4\}$
$\langle\cos(-10\Phi_2 + 6\Phi_3 + 4\Phi_4)\rangle$	Res$\{10\Psi_2\}$, Res$\{6\Psi_3\}$, Res$\{4\Psi_4\}$

Table 6.2: The list of three plane correlators and associated event-plane resolution factors that need to be measured.

Figure 6.2 shows the two and three-plane correlators as a function of N_{part} calculated in a Glauber model initial geometry, by correlating the minor axes of the ϵ_n [113, 116]. The measured correlators would have similar N_{part} dependence as these only in the linear response limit. Nevertheless, it is interesting that the Glauber model predicts strong signals for the $\langle\cos 4(\Phi'_2 - \Phi'_4)\rangle$, $\langle\cos 6(\Phi'_3 - \Phi'_6)\rangle$, and $\langle\cos 6(\Phi'_2 - \Phi'_6)\rangle$ two-plane correlators. For the three-plane correlators, strong signals are predicted for $\langle\cos(2\Phi'_2 + 3\Phi'_3 - 5\Phi'_5)\rangle$, $\langle\cos(2\Phi'_2 + 4\Phi'_4 - 6\Phi'_6)\rangle$, and $\langle\cos(10\Phi'_2 - 4\Phi'_4 - 6\Phi'_6)\rangle$.

6.1.2 Procedure for obtaining correlation function and applying the resolution correction

In the event-plane analysis (Chapter 3), the FCal was used as the event-plane detector, primarily to maintain a clear separation in rapidity from the ID,

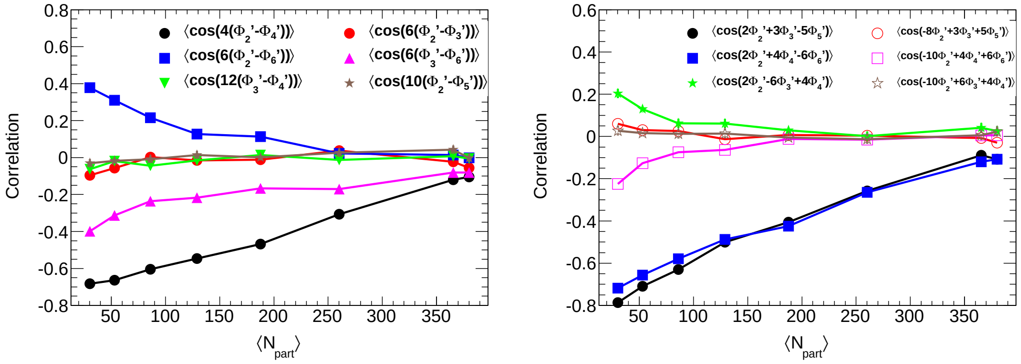

Figure 6.2: The correlation between the minor axes of the eccentricities, calculated in Glauber initial geometry [113, 116].

where the charged tracks were measured. Since this analysis is concerned only with the event-planes, the full ATLAS EM calorimetry (-4.8< η <4.8) is used.

Each detector provides its own measurement of event-plane Ψ_n for n=2-6. However, to avoid auto-correlations, no two planes involved in the correlation are measured in the same detector. For example, in calculating the relative angle $4(\Psi_2 - \Psi_4)$, the Ψ_2 and Ψ_4 are measured in non-overlapping detectors A and B, and the correlation calculated as:

$$\langle \cos 4(\Phi_2 - \Phi_4)\rangle = \frac{\langle \cos 4(\Psi_2^A - \Psi_4^B)\rangle}{\mathrm{Res}\{4\Psi_2^A\}\mathrm{Res}\{4\Psi_4^B\}}. \tag{6.13}$$

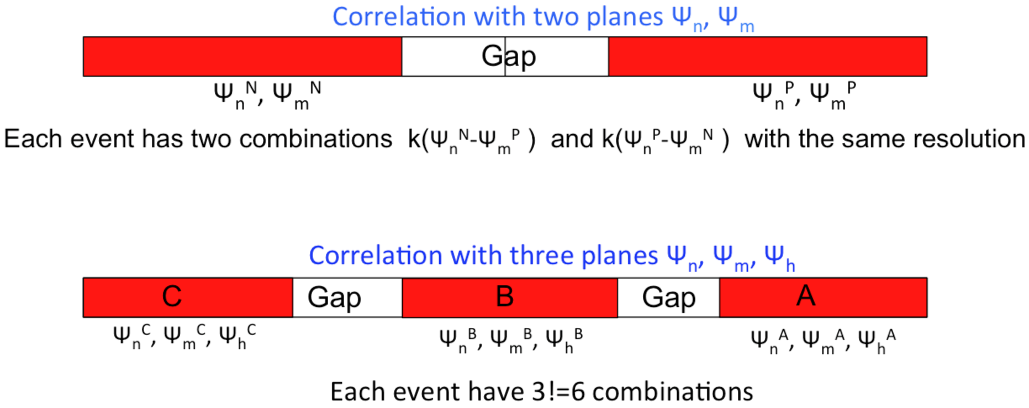

Figure 6.3: Schematic illustration of sub-detectors used to obtain the raw signal for two-plane correlations (top) and three-plane correlations (bottom).

Figure 6.3 illustrates the idea behind choosing the detectors (or subevents) for the two-plane and three-plane correlations. In the two-plane correlation, the two subevents are chosen to be symmetric around the center of ATLAS, so they have identical resolutions. Each subevent provides its own measurement of the two event-planes: $\Psi_n^{\rm P}$ and $\Psi_m^{\rm P}$ for positive η, and $\Psi_n^{\rm N}$ and $\Psi_m^{\rm N}$ for negative η, resulting in two independent measurements of the correlations:

$$\langle\cos k(\Phi_n - \Phi_m)\rangle = \frac{\left\langle\cos k(\Psi_n^{\rm P} - \Psi_m^{\rm N})\right\rangle}{{\rm Res}\{k\Psi_n^{\rm P}\}{\rm Res}\{k\Psi_m^{\rm N}\}} = \frac{\left\langle\cos k(\Psi_n^{\rm N} - \Psi_m^{\rm P})\right\rangle}{{\rm Res}\{k\Psi_n^{\rm N}\}{\rm Res}\{k\Psi_m^{\rm P}\}} \quad (6.14)$$

Since ${\rm Res}\{k\Psi_n^{\rm P}\}{\rm Res}\{k\Psi_m^{\rm N}\} = {\rm Res}\{k\Psi_n^{\rm N}\}{\rm Res}\{k\Psi_m^{\rm P}\}$ for symmetric detectors, two measurements are combined for increased precision:

$$\langle\cos k(\Phi_n - \Phi_m)\rangle = \frac{\left\langle\cos k(\Psi_n^{\rm P} - \Psi_m^{\rm N})\right\rangle + \left\langle\cos k(\Psi_n^{\rm N} - \Psi_m^{\rm P})\right\rangle}{{\rm Res}\{k\Psi_n^{\rm P}\}{\rm Res}\{k\Psi_m^{\rm N}\} + {\rm Res}\{k\Psi_n^{\rm N}\}{\rm Res}\{k\Psi_m^{\rm P}\}} \quad (6.15)$$

To measure three-plane correlations, three non-overlapping subevents, labeled as A, B and C, are chosen such that they have approximately the same η coverage. The guiding principle for choosing the subevents is that they should have as large η acceptance as possible, but still have a sufficient η gap from each other. Here, subevents A and C are chosen to be symmetric and have identical η acceptance (hence same resolution), while the resolution of B in general could be different. There are $3! = 6$ independent ways of obtaining the three-plane correlators from these three detectors, based on which detector is used to determine which plane. Since A and C have same resolutions, the cases where the planes are swapped between A and C are combined into a single measurement, resulting in three independent estimates for the three-plane correlation. For example, the three estimations for the correlation $2\Phi_2 + 3\Phi_3 - 5\Phi_5$, denoted by subscripts Type1-Type3, are

$$\langle\cos(2\Phi_2 + 3\Phi_3 - 5\Phi_5)\rangle_{\rm Type1} = \frac{\left\langle\cos(2\Psi_2^B + 3\Psi_3^A - 5\Psi_5^C)\right\rangle + \left\langle\cos(2\Psi_2^B + 3\Psi_3^C - 5\Psi_5^A)\right\rangle}{{\rm Res}\{2\Psi_2^B\}{\rm Res}\{3\Psi_3^A\}{\rm Res}\{5\Psi_5^C\} + {\rm Res}\{2\Psi_2^B\}{\rm Res}\{3\Psi_3^C\}{\rm Res}\{5\Psi_5^A\}}, \quad (6.16)$$

$$\langle\cos(2\Phi_2 + 3\Phi_3 - 5\Phi_5)\rangle_{\rm Type2} = \frac{\left\langle\cos(2\Psi_2^A + 3\Psi_3^B - 5\Psi_5^C)\right\rangle + \left\langle\cos(2\Psi_2^C + 3\Psi_3^B - 5\Psi_5^A)\right\rangle}{{\rm Res}\{2\Psi_2^A\}{\rm Res}\{3\Psi_3^B\}{\rm Res}\{5\Psi_5^C\} + {\rm Res}\{2\Psi_2^C\}{\rm Res}\{3\Psi_3^B\}{\rm Res}\{5\Psi_5^A\}}, \quad (6.17)$$

$$\left\langle \cos(2\Phi_2+3\Phi_3-5\Phi_5)\right\rangle_{\mathrm{Type3}} = \frac{\left\langle \cos(2\Psi_2^A+3\Psi_3^C-5\Psi_5^B)\right\rangle + \left\langle \cos(2\Psi_2^C+3\Psi_3^A-5\Psi_5^B)\right\rangle}{\mathrm{Res}\{2\Psi_2^A\}\mathrm{Res}\{3\Psi_3^C\}\mathrm{Res}\{5\Psi_5^B\}+\mathrm{Res}\{2\Psi_2^C\}\mathrm{Res}\{3\Psi_3^A\}\mathrm{Res}\{5\Psi_5^B\}}, \quad (6.18)$$

These three measurements are statistically combined, and the spreads between them are used as estimation for the systematic uncertainty.

The resolutions for the detectors used in the two and three-plane correlation analysis are determined via two-subevent or three-subevent methods[2] (Appendix A.1.3). The two-subevent method can be used only for detectors that form a symmetric pair about $\eta = 0$ i.e. have same resolutions. The three-subevent method can however be used to determine the resolution for any detector. All the detectors used in the measurements as well as for the cross-checks, are calibrated by the recentering-flattening procedure that was used for the FCal in the EP analysis (Appendix A.1.4).

6.1.3 Sources of systematic uncertainties

There are two primary sources of systematic uncertainties.

1. Detector effects can bias the determination of the event-plane angle Ψ_n, and hence can influence both the correlation signal as well as the resolution correction. Most of these detector effects should be removed by the event-plane calibration. The residual detector systematics can be estimated as:
   - Non-vanishing sine terms in the correlation function $\langle \sin jk\left(\Psi_n - \Psi_m\right)\rangle$, $\langle \sin\left(c_n n\Psi_n + c_m m\Psi_m + c_h h\Psi_h\right)\rangle$.
   - The detector effects can also result in sine terms the 2SE and 3SE resolution calculations: $\left\langle \sin jn\left(\Psi_n^A - \Psi_n^B\right)\right\rangle$ that are used to determine the resolution.
2. Correlations other than flow (non-flow) such as resonance decays and jet fragmentations. These correlations typically have limited range in rapidity, and can be suppressed by requiring an η gap between the subevents used in measuring the correlation or resolution determination.
   - The remaining non-flow effects can influence the resolution determination. For a given detector, several independent measurements of the resolution from 2SE and 3SE methods should be done.

---

[2] Note that the two-subevent/three-subevent method for determining resolutions have nothing to do with the two-plane/three-plane correlations. They are simply methods of obtaining the resolution.

- Due to the large η coverage of the ATLAS detector, a given two-plane or three-plane correlation can be measured independently using detectors at different η. It is useful to compare the results obtained using different detectors. However, one caveat is that the differences could also be due to η dependence of the flow physics itself.

6.2 Two-plane correlation analysis

The default detector used for the two-plane analysis includes the FCal, EM end-cap and EM Barrel. The towers from all three sub-detectors are combined to make two symmetric subevents covering $\eta \in (0.5, 4.8)$ and $\eta \in (-4.8, -0.5)$. The one unit η gap between the two detectors is sufficient to suppress short-range correlations (will be shown in Section 6.2.3). This combined detector is denoted as ECalFCal, with subscripts P and N to denote its positive and negative η sides.

6.2.1 Measurements of raw signals and resolutions

Figures 6.4 shows the raw two-plane relative angle distributions for the (20-30)% centrality interval. The red and blue histograms are foreground and background distributions, respectively. The background distributions are calculated from mixed events, i.e. by combining the Ψ_n from one event with Ψ_m from another event with similar centrality (matched within 5%) and z-vertex (matched within 3 cm). Both the foreground and mixed-event distributions are normalized to have a mean value of 1.0. The mixed-event distribution provides an estimate of detector effects, while the foreground distribution contains both detector effects and physics. The background distributions are almost flat, but do indicate some small variations on the order of about 1/1000. To cancel these non-physical structures, the correlation functions are obtained by dividing the foreground (S) by the mixed-event distributions(B):

$$C(k(\Psi_n - \Psi_m)) = \frac{S(k(\Psi_n - \Psi_m))}{B(k(\Psi_n - \Psi_m))} \tag{6.19}$$

The correlation functions show significant positive signal for $4(\Psi_2 - \Psi_4)$, $6(\Psi_2 - \Psi_6)$ and $6(\Psi_3 - \Psi_6)$, a very weak signal for $6(\Psi_2 - \Psi_3)$, while $12(\Psi_3 - \Psi_4)$ and $10(\Psi_2 - \Psi_5)$ are consistent with zero.

Starting from these correlation functions, the various raw correlators $\langle \cos jk(\Psi_n - \Psi_m)\rangle$ listed in Table 6.1 are calculated. The associated sine terms $\langle \sin jk(\Psi_n - \Psi_m)\rangle$

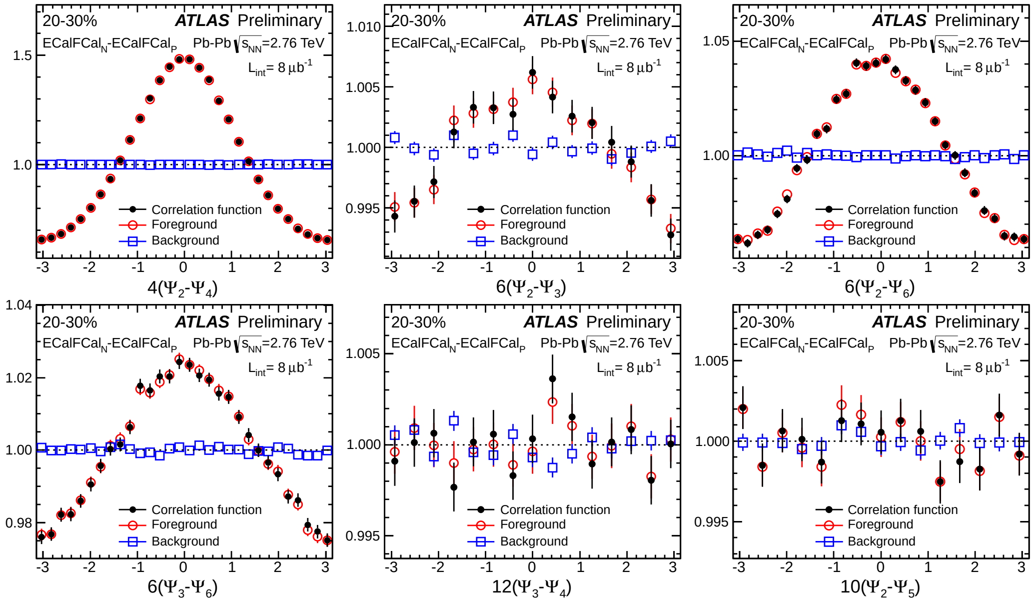

Figure 6.4: Two-plane relative angle distributions for the (20-30)% centrality interval measured by the ECalFCal.

as well as the sine and cosine components of the background distributions are also evaluated, and their quadrature sum is used as the systematic error for the $\langle\cos jk(\Psi_n - \Psi_m)\rangle$. Figure 6.5 summarizes the centrality dependence of the raw signal together with the estimated systematic uncertainties.

Resolution results

The nominal resolution factors for the ECalFCal are obtained via the two-subevent method as $\sqrt{\langle\cos jn\,(\Psi_n^N - \Psi_n^P)\rangle}$, with the sine terms $\left\langle\sin jn\left(\Psi_n^N - \Psi_n^P\right)\right\rangle$ are used as estimates of the systematic errors. Additional measurements are done the three-subevent method and the differences from the two-subevent results are included as systematic errors. The systematic uncertainties from the two sources are quoted as centrality independent (conservatively) and then added in quadrature. Figure 6.6 shows the event-plane resolutions for n=2-6 used in this analysis together with their systematic uncertainties. The details of the resolution calculation are given in Appendix D.2.1.

Figure 6.7 shows the combined resolution terms for the eight two-plane correlators in Table 6.1, evaluated from the single-plane resolutions using Eq. 6.12. These combined resolution values lie in the range of a few percent up to about 40%. They also show quite different centrality dependence trends. The systematic uncertainties for combined resolutions are propagated from individual

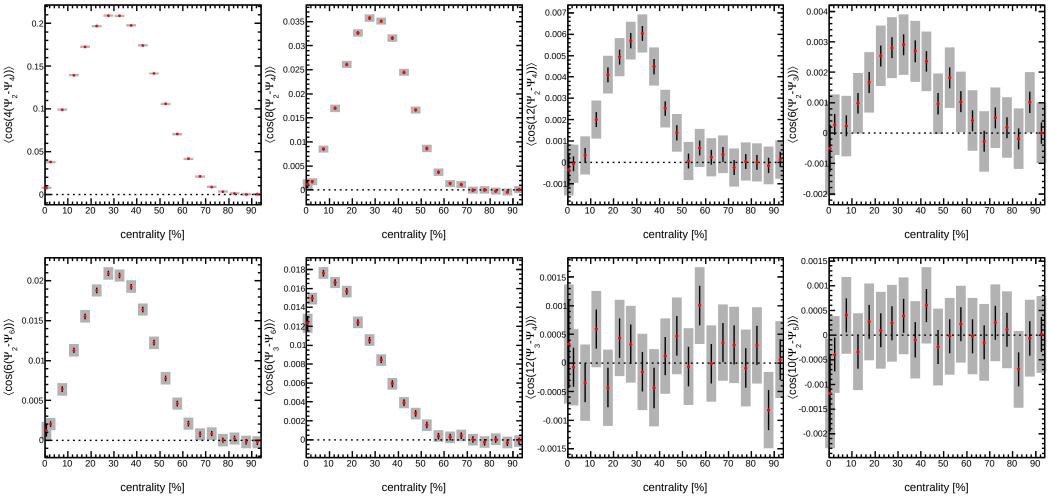

Figure 6.5: The centrality dependence of raw correlation signals for the eight two-plane correlators studied in this note. They are presented for 5% centrality intervals, together with a 0-1% centrality bin. Bars and bands are statistical and systematic errors respectively.

resolution terms, and they are summarized in Table 6.3.

6.2.2 Corrected results

The final event-plane correlations are obtained by dividing the raw signals (Fig. 6.5) by the combined resolution factors (Fig. 6.7). The results are presented as a function of N_{part}, shown in Fig. 6.8. The highest N_{part} bin corresponds to the (0-1)% centrality interval, subsequent points are 5% centrality bins starting with (0-5)% centrality. Some of the peripheral bins where the uncertainties were too large are removed from the final results.

The various sources of the systematic uncertainties are summarized in Table 6.3 and include the uncertainty for the raw cosine signal of the correlation function and the combined event-plane resolution. The former is evaluated as the absolute values of the sine terms and the sine and cosine terms of the mixed-events distribution and is quoted as the absolute error on the raw signal. This error is important when either the raw signal is small or the resolution is poor. The latter is calculated via Eq. 6.12 using standard error propagation. Also included are two additional sources which account for the uncertainly in the trigger efficiency and dependence on running periods. These are discussed later in Section 6.4.

For the two-plane correlators, the “2-4”, “2-6” and “3-6” correlations are

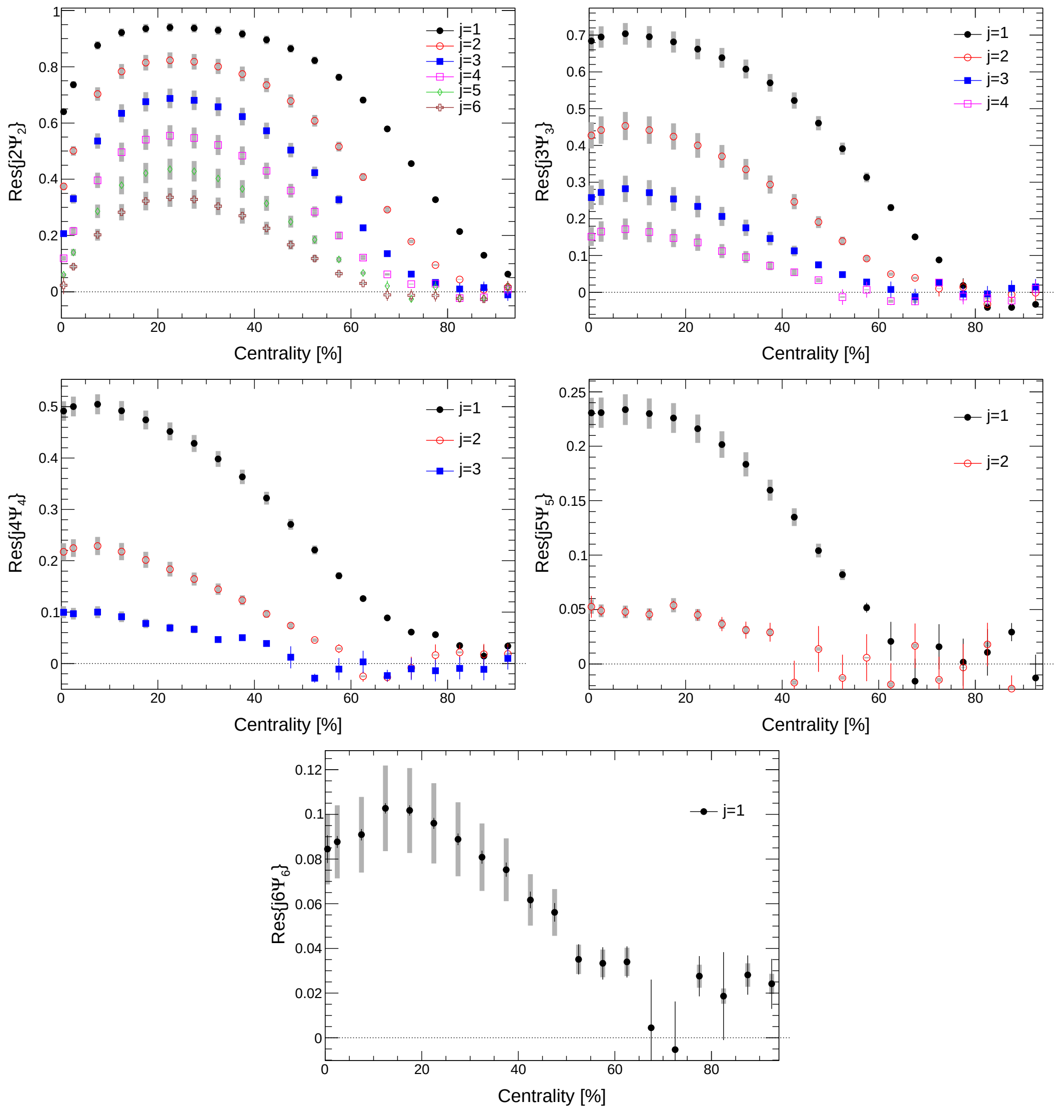

Figure 6.6: Summary of the event-plane resolution Res$\{jn\Psi_n\}$ for n=2-6 and different values of j. Bars and bands are statistical and systematic errors respectively.

particularly strong while the '3-4" and "2-5" correlators are consistent with zero for all centralities. The "2-3" correlation though weak, is non-zero and has some centrality dependence. The physical implications of these results will be discussed in Section 6.5.

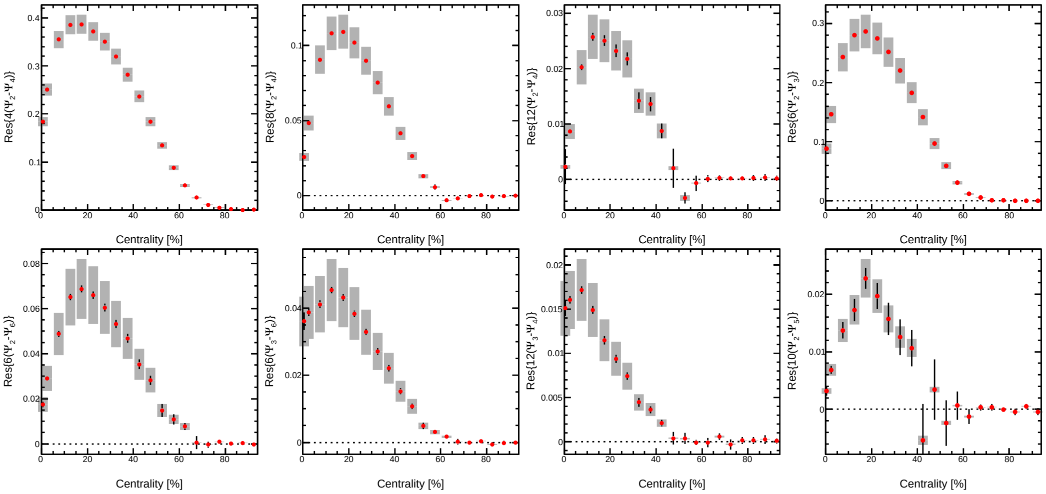

Figure 6.7: Combined resolution for the eight two-plane correlators Res$\{k(\Psi_n - \Psi_m)\}$. Bars and bands are statistical and systematic errors respectively.

Error for $\langle\cos jk(\Phi_n - \Phi_m)\rangle$ correlators								
(j,n,m)	(1,2,4)	(2,2,4)	(3,2,4)	(1,2,3)	(1,2,6)	(1,3,6)	(1,3,4)	(1,2,5)
Res$\{jk(\Psi_n - \Psi_m)\}$	5.14%	10.3%	15.4%	9.84%	19.4%	20.5%	20.4%	14.8%
sine and mixed-events for raw distribution (absolute error $\times 10^{-4}$)	5-15	5-10	5-10	5-8	5-10	5-10	5-10	5-10
Trigger&event selection	0.5-2%	1-4%	3%	3%	1-2%	0.5-2%	$< 1\%$	$< 1\%$
Run periods	$< 0.5\%$	1%	5%	0.004	3%	3%	0.02	0.02

Table 6.3: Summary of systematic uncertainties for various two-plane correlators. Some of the uncertainties are as a percentage (of the signal) while others are absolute.

6.2.3 Cross checks

One potential source of the systematic uncertainty arises from non-flow effects. These effects can lead to correlations between the subevents, and hence influence the correlation function and the determination of the event-plane resolutions. Therefore, it is important to check the sensitivity of the final correlation on the rapidity gap between the subevents, and/or compare the correlations obtained independently from different subevents. This is the main goal of this section.

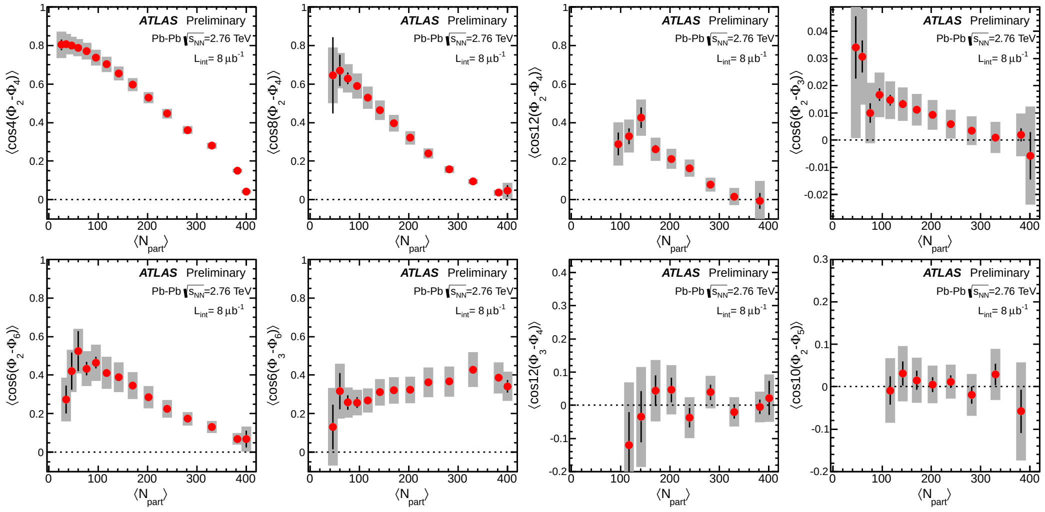

Figure 6.8: N_{part} dependence of the two-plane correlators. Bars and bands are statistical and systematic errors respectively.

Dependence on the η gap

An η gap between the P-side and the N-side subevents is necessary to reduce short-range correlations. By increasing the η gap, the influence of short-range can be decreased, however this also decreases the acceptance of the sub-detectors and hence reduces the resolution and raw correlation signal. Therefore a compromise must be made between maximizing the signal and suppressing the auto-correlations. For this purpose, the two-plane correlation measurements are repeated using symmetric sub-detectors but with varying rapidity separation between them. This is done by choosing the two sub-detectors to have an acceptance of (η_{min},4.8) and (-4.8,-η_{min}) in η. The segmentation of the calorimeter towers in 0.1 units in η allows for a flexible choice of η_{min} . A total of 17 cases of η_{min} are studied.

Figures 6.9-6.12 show the raw signal, combined resolution, as well as the corrected correlations for some of the two-plane correlators, as a function of the minimum η of the sub-detector. The η gap between the two sub-detectors is $2\eta_{min}$, while the acceptance of the sub-detectors is $4.8-\eta_{min}$. The $\eta_{min} = 0.5$ case corresponds to the default detector (ECalFCal). The correlation function and the resolution decrease considerably with increasing η_{min}, often by more than a factor of 4, but the corrected correlations are remarkably stable.

In most cases, the raw correlation signal changes smoothly with η_{min}, even at small η_{min} values. In contrast, the estimated event-plane resolution factors have a sharp jump at small η_{min} in some cases (Figs. 6.10 and 6.11). Such en-

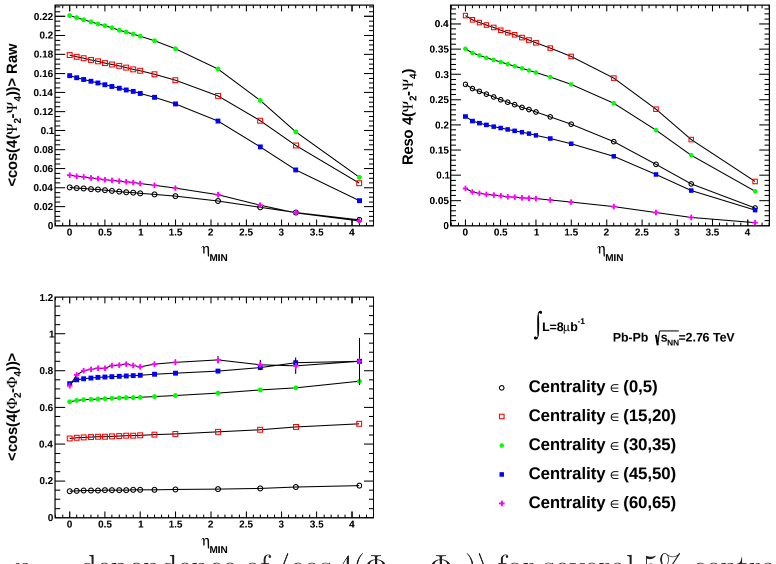

Figure 6.9: η_{min} dependence of $\langle\cos 4(\Phi_2 - \Phi_4)\rangle$ for several 5% centrality intervals. Top-left panel: Correlation before resolution corrections. Second panel: The resolution factor. Third Panel: Correlation after resolution correction.

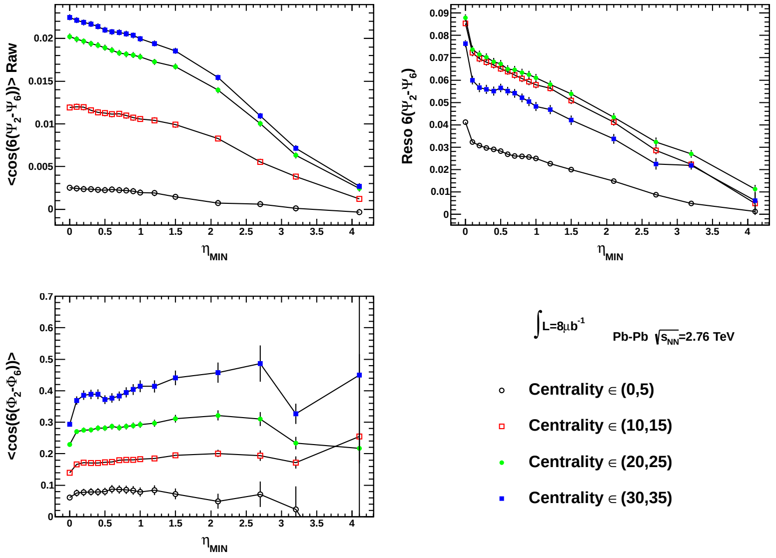

Figure 6.10: Same as previous plot but for $\langle\cos 6(\Phi_2 - \Phi_6)\rangle$

hancement of the resolution leads to a suppression of the corrected correlation signal at small η_{min}. This indicates that while the short-range correlations influence individual harmonics, they only weakly correlate EPs of different order. Since the EP resolution is estimated from the subevent correlation of the

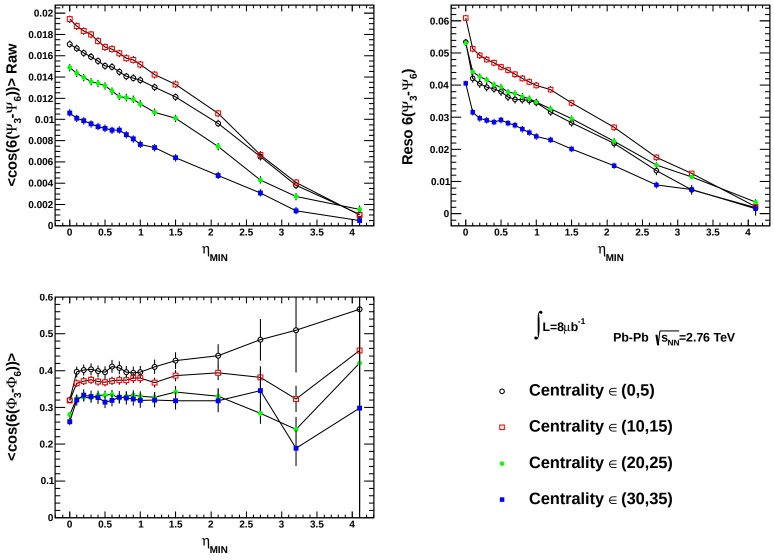

Figure 6.11: Same as previous plot but for $\langle\cos 6(\Phi_3 - \Phi_6)\rangle$.

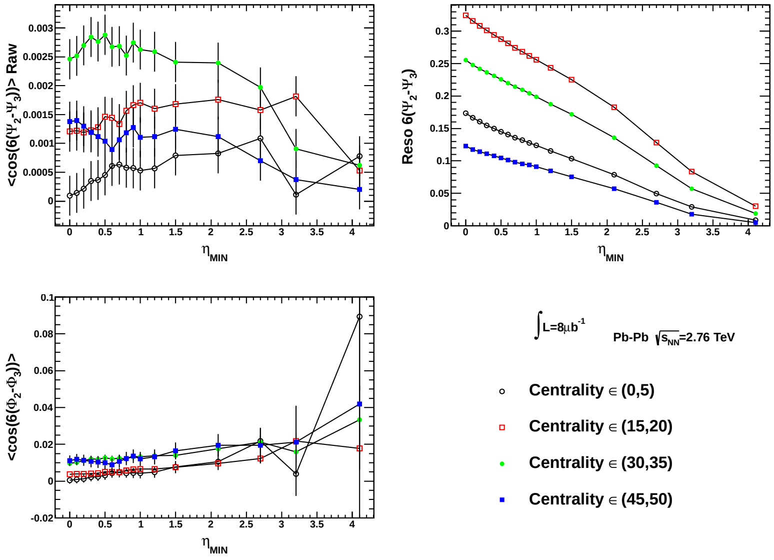

Figure 6.12: Same as previous plot but for $\langle\cos 6(\Phi_2 - \Phi_3)\rangle$.

same order planes, they are more affected by the short-range correlations. The short-range correlations do not seem to have an influence on the resolutions for $4(\Phi_2 - \Phi_4)$ and $6(\Phi_2 - \Phi_3)$ (Figs. 6.9 and 6.12). This is because the flow signal is strong for harmonics 2, 3 and 4, and so the corresponding planes are less sensitive to the non-flow effects.

In all cases, the influence of these short-range correlations, if any, is only limited to a small η gap between the two sub-detectors, and becomes negligible for $\eta_{min} > 0.2$ (or equivalently $\Delta\eta > 0.4$). The default detectors have a gap of 1 unit in η between them, which is thus sufficient to suppress these short-range correlations. In some cases, there is a slight variation of the corrected correlation even at large values of η_{min}, however it is not clear if this is due to systematics introduced by the procedure or is a physical effect. Thus, this variation is not quoted as a systematic error.

Comparison to results obtained from tracking detectors

As a cross-check, the full analysis chain is repeated using the ID including estimation of systematic errors. The two subevents used in the ID based analysis are made using all good-quality[3] charged tracks with $\eta \in (0.5, 2.5)$ and $\eta \in (-2.5, -0.5)$. The subevents thus have a gap of 1.0 in η which is sufficient to suppress non-flow correlations. Note that the acceptance of the ID based subevents is much smaller than the calorimeter based ones, consequently the ID analysis has larger systematic and statistical errors.

Figure 6.13 compares the ID results to the ECalFCal results. For all the correlators, the results are in good agreement between the measurements. Any differences between the two are easily covered by the systematic errors. The comparison with the ID is only used as a cross-check, it is not used to quote additional systematic errors.

6.3 Three-plane correlation analysis

6.3.1 Analysis with default detector

For three-plane correlation, the three subevents are built from calorimeter towers as:

1. Subevent A: Towers with $\eta \in (0.5, 2.7)$, this consists of parts of the EM barrel and parts of the EM end-cap. This is labelled as $\mathrm{ECal_P}$ (or DetA).
2. Subevent B: The full-FCal with $3.3 < |\eta| < 4.8$. This is labelled as FCal (or DetB).
3. Subevent C: Towers with $\eta \in (-2.7, -0.5)$, this consists of parts of the EM barrel and parts of the EM end-cap. This is symmetric with A. This is labelled as $\mathrm{ECal_N}$ (or DetC).

---

[3] Same quality cuts as used in the EP and 2PC analysis. Also $p_{\mathrm{T}} > 0.5$ GeV is required.

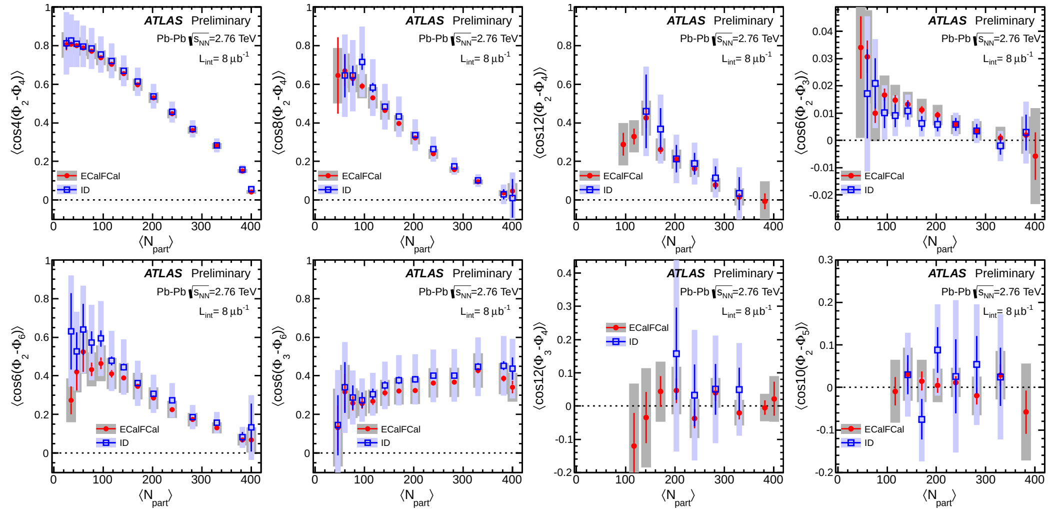

Figure 6.13: Comparison of two-plane correlations measured with Calorimeters and ID. Bars and bands are statistical and systematic errors respectively.

Utilising the symmetry between the A and C subevents, the measurements are combined into three independent measurements (cf Eq. 6.16-6.18), labelled as Type 1, 2 and 3.

Figure 6.14 shows the Type-1 correlation functions for the six three-plane correlators studied in this analysis. The red and blue histograms are foreground and background distributions, respectively. The background distributions are calculated from mixed events, i.e. the three individual plane angles are obtained from three different events with similar centrality and z-vertex. Both the foreground and mixed-event distributions are normalized to have a mean value of 1. Strong correlations are already observed at the raw level for $(2\Psi_2 + 3\Psi_3 - 5\Psi_5)$ and $(2\Psi_2 + 4\Psi_4 - 6\Psi_6)$. A clear anti-correlation is seen for $(2\Psi_2 - 6\Psi_4 + 4\Psi_4)$ with a dip at zero rather than a peak. A weak signal is seen for $(-10\Psi_2 + 4\Psi_4 + 6\Psi_6)$. The mixed event distributions are consistent with zero signal in all cases, showing minimal influence of detector effects. The raw signals are extracted from these correlation functions. The sine terms in the correlations as well as the sine and cosine terms in the mixed-event background are used as estimates of systematic errors for the raw signals. The raw signals are plotted for the three Types for each of the six three plane correlators in Fig. 6.15.

Figure 6.16 shows the resolution terms for individual event-planes for different values of n and j (as in $\mathrm{Res}\{jn\Psi_n\}$), for subevents A, B and C. They are obtained via 2SE and 3SE methods. The systematic uncertainties are estimated from the sine term in the 2SE correlation, as well as the deviations

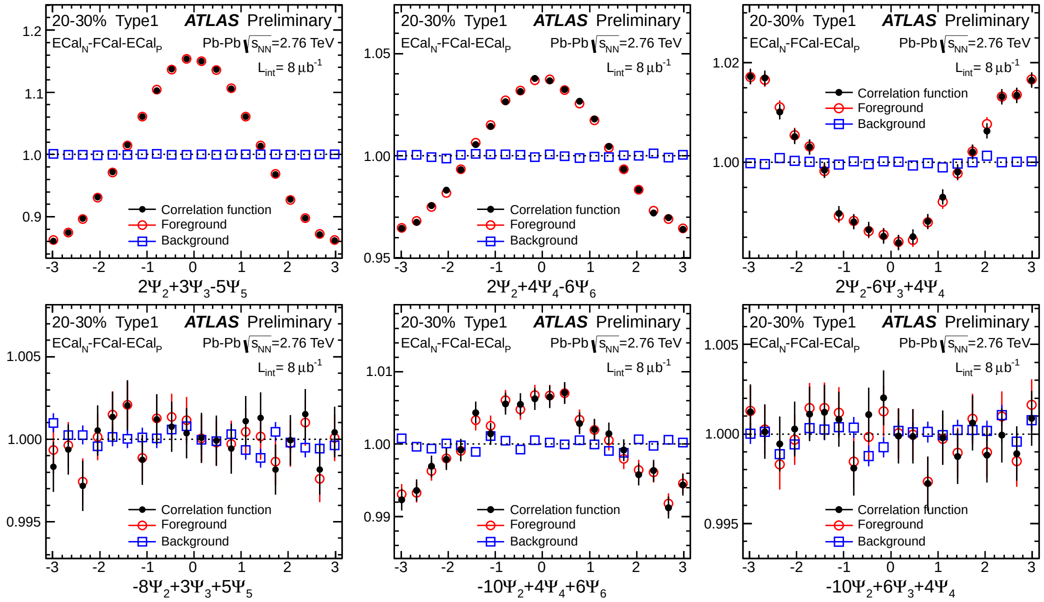

Figure 6.14: Three-plane relative angle distributions for the (20-30)% centrality interval. These plots correspond to Type-1 distributions.

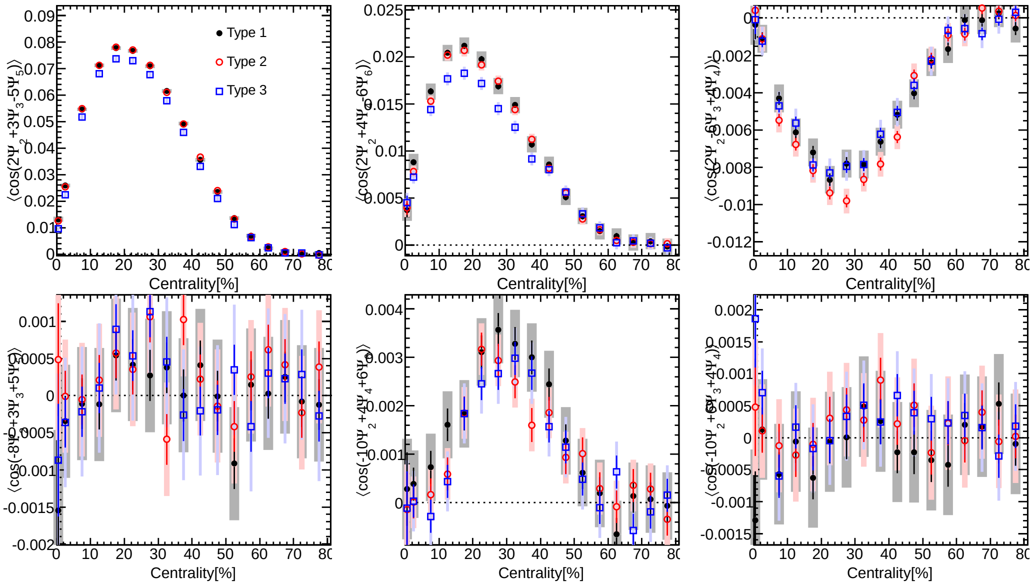

Figure 6.15: Centrality dependence of the raw cosine signal for the six three-plane correlators. Bars and bands are statistical and systematic errors respectively.

between the 3SE and/or 2SE results.They are summarized in Table 6.4. Note that the uncertainty of Res$\{jn\Psi_n\}$ are found to be proportional to values of j. The resolution and systematic uncertainties associated with DetA and DetC are almost the same as they are completely symmetric.

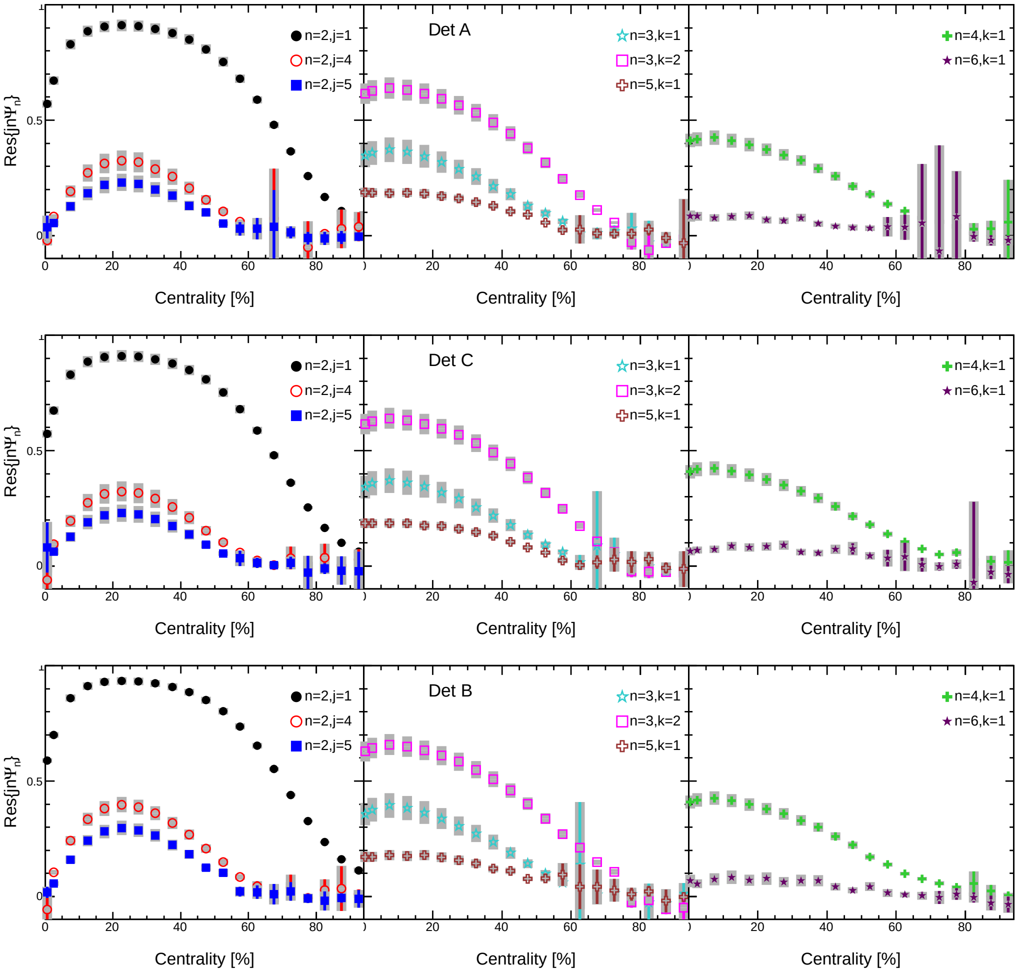

Figure 6.16: Centrality dependence of the resolution for individual event-planes associated with the three detectors used in the three-plane correlations. From top to bottom the three rows correspond to DetA, DetC and DetB respectively. Bars and bands are statistical and systematic errors respectively.

The individual event-plane resolutions are combined to give the total resolution for the three-plane correlators (Eq. 6.12). The combined resolutions are plotted as a function of centrality in Fig. 6.17. The resolution corrected correlators are evaluated by dividing the raw signal in Fig 6.15 with the combined resolutions in Fig. 6.17 (separately for the Type1-3 combinations). The

Error for Res$\{jn\Psi_n\}$					
n	2	3	4	5	6
Detector A&C	$2.7j\%$	$7.2j\%$	$7.3j\%$	$10.3j\%$	$20.6j\%$
Detector B	$1.7j\%$	$6.8j\%$	$6.9j\%$	$12.4j\%$	$34j\%$

Table 6.4: Summary of systematic uncertainties for individual Res$\{jn\Psi_n\}$ for detectors used in three-plane correlations.

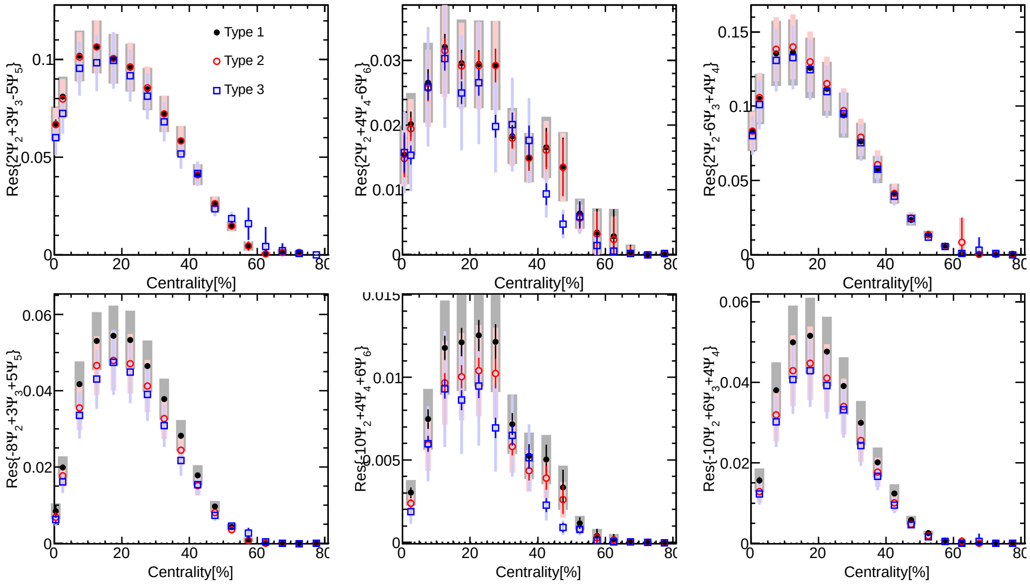

Figure 6.17: Centrality dependence of the combined three-plane resolutions. Bars and bands are statistical and systematic errors respectively.

results are shown in Fig. 6.18. The systematic uncertainty comes from both the raw signal and resolution correction and are summarized in Table 6.5. The uncertainties for the raw cosine signals are evaluated as the quadrature sum of the sine terms in the raw-correlations and the sine and cosine terms of the mixed-events distribution, and are quoted as absolute errors. The uncertainties for the combined resolutions are obtained by a simple error propagation of the individual single-plane resolutions given in Table 6.4. As one can see from Table 6.5, most of the uncertainty arises from the resolution correction. For each three-plane correlator, the three independent estimates agree with each other within their uncertainties.

The final corrected results are obtained as a weighted average between the three independent measurements. The results are shown in Fig. 6.19 as a function of N_{part}. The systematic uncertainties are calculated as the quadrature sum of two sources:

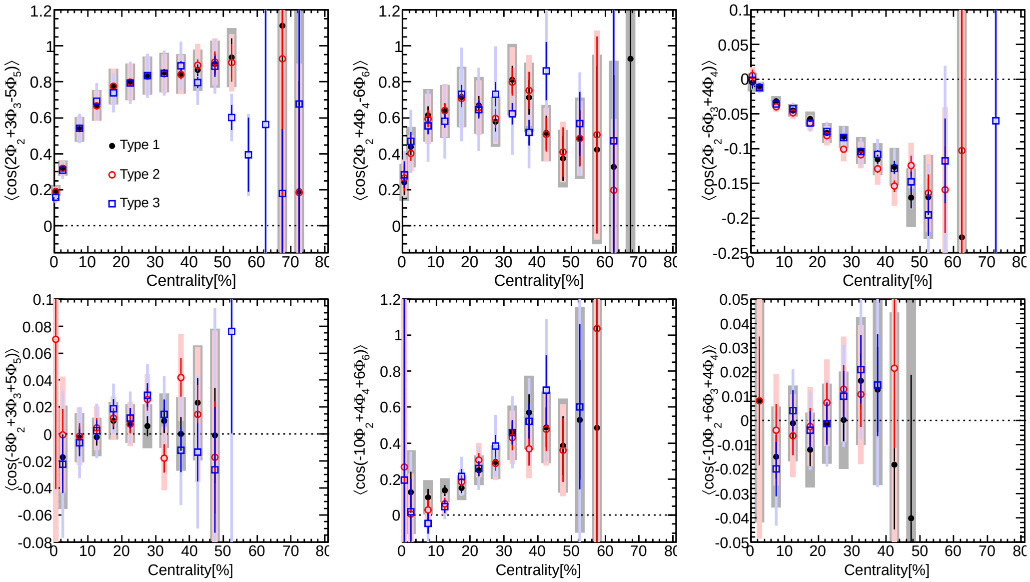

Figure 6.18: Centrality dependence of the three-plane correlators. The three set of data points correspond to the three types of correlations in Eq. 6.16-6.18. Bars and bands are statistical and systematic errors respectively.

Systematic errors for the three-plane correlators: $\langle\cos(\sum\Phi)\rangle$				
$\sum\Phi$	Combined Resolution [%]			Raw distribution $\times10^{-4}$
	Type-1	Type-2	Type-3	Type-1 Type-2 Type-3
$2\Phi_2+3\Phi_3-5\Phi_3$	12.7	12.7	14.6	7–15
$-8\Phi_2+3\Phi_3+5\Phi_5$	14.3	16.4	18.0	5–10
$2\Phi_2+4\Phi_4-6\Phi_6$	21.9	21.9	34.9	6–13
$-10\Phi_2+4\Phi_4+6\Phi_6$	23.5	25.6	37.3	5–10
$2\Phi_2-6\Phi_3+4\Phi_4$	16.3	15.7	16.2	6–13
$-10\Phi_2+6\Phi_3+4\Phi_4$	18.3	20.6	21.0	5–10

Table 6.5: Summary of systematic uncertainties for the three-plane correlators. The errors from resolution correction are in percentage while the errors from the raw correlation are in absolute values.

1. The weighted-average of the systematic uncertainties for the three individual measurements.
2. The point-to-point differences between the three measurements.

Additional systematic uncertainties listed in Table 6.6 are also added in quadrature to the above errors. These errors are explained in Section 6.4. As with the two-plane results, the peripheral bins where the systematic uncertainties were too large have been removed from the final results. The physical implications of these results along with the two-plane ones will be discussed in Section 6.5.

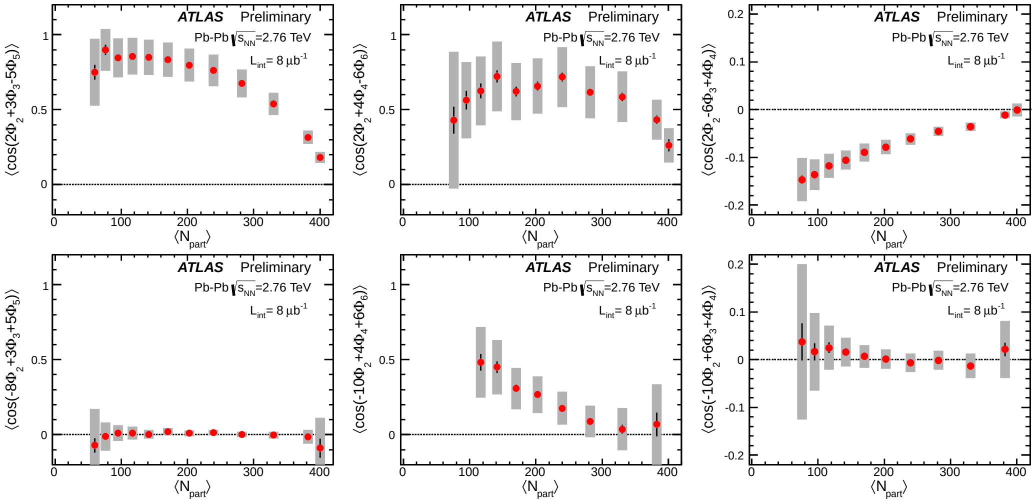

Figure 6.19: $\mathrm{N_{part}}$ dependence of the three-plane correlators. Bars and bands are statistical and systematic errors respectively.

Additional systematic errors for the three-plane correlators $\langle\cos(\sum\Phi)\rangle$			
$\sum\Phi$	$2\Phi_2+3\Phi_3-5\Phi_5$	$2\Phi_2+4\Phi_4-6\Phi_6$	$2\Phi_2-6\Phi_3+4\Phi_4$
Trigger&event sel.	1-2%	1%	3-4%
Run periods	1.5%	5%	5%
$\sum\Phi$	$-8\Phi_2+3\Phi_3+5\Phi_5$	$-10\Phi_2+4\Phi_4+6\Phi_6$	$-10\Phi_2+6\Phi_3+4\Phi_4$
Trigger&event sel.	1-3%	1-3%	1-3%
Run periods	0.01	0.07	0.03

Table 6.6: Additional systematic uncertainties for the three-plane correlators.

6.3.2 Cross-checks using tracking detectors

As with the two-plane case, the three-plane correlations are cross-checked with using the ID, including its own estimation of systematic errors. The three subevents used in the ID based analysis are made using tracks over the following ranges: $\eta \in (-2.5, 1.5)$, $\eta \in (-1.0, 1.0)$ and $\eta \in (1.5, 2.5)$ for subevents A, B and C respectively. Unfortunately it is not possible to maintain a 1 unit η gap between all three detectors and at the same time have good acceptance. Thus the minimum gap is relaxed to 0.5 unit η gap. Figure 6.20 compares the ID results to the Calorimeter results. For all the correlators, the results are in good agreement between the measurements with only small systematic differences, which are covered by the systematic errors. As with the two-plane case, the comparison with the ID is only used as a cross-check, and not used for additional systematic errors.

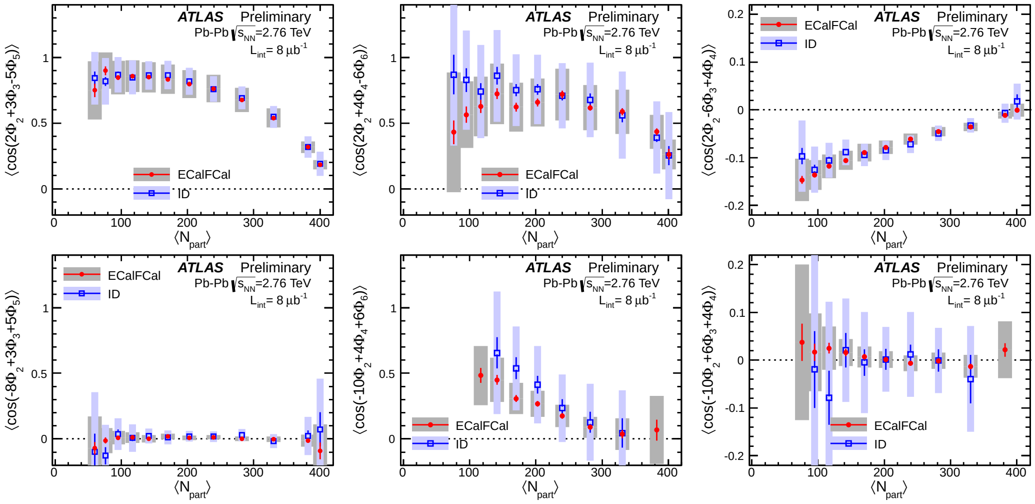

Figure 6.20: Comparison of three-plane correlations measured with Calorimeters and ID.

6.4 Other systematics

Some additional sources of errors are discussed here. They were already included in the final results and tabulated in Tables 6.3 and 6.6 for the two and three-plane correlators respectively.

Trigger and event selections

As described in Section 3.4.4, the ±2% uncertainty in the trigger efficiency (which has a nominal value of 98%) leads to an uncertainty in the definition of the centrality classes. The change of the centrality definition mainly leads to a rescaling of the centrality-axis (x-axis) by ±2% while keeping the origin fixed. This scaling mostly affects the most peripheral events, but has very little influence for the central events (as the centrality=0 end of the centrality-axis is fixed). The changes in centrality range can be approximated as $\delta_x = \pm 0.02 x_i$ for i^{th} data point. The influence for each data point is estimated based on a interpolation procedure between the neighboring bins: $\delta_i = (y_{i+1} - yi) \times \frac{\pm 0.02 x_i}{x_{i+1} - x_i}$.

For the two-plane correlators, the estimated changes when converted into percentage values, are typically less than 1-3% most cases (and centrality dependent); In some cases, the changes are slightly bigger, but they are typically associated with the large point-to-point statistical fluctuations and/or because the values themselves are very small. Similarly for the three-plane correlators, relative variation is on the order of 1-4% depending on centrality and the type of the correlator.

Run-by-run dependence

As with the EP and 2PC analyses, the dependence of the results on different running periods is checked. This is done by grouping all the runs into into three groups with approximately the same statistics. The variation is checked by comparing the results in each group with the those for the full statistics. Overall no clear systematic variations are seen between the three groups. The level of deviations beyond statistical fluctuation are conservatively estimated in terms of either percentage (when the signals are large) or as absolute values (when signals are small).

6.5 Results and summary

The final results for the two and three-plane correlations were shown in Fig. 6.8 and Fig. 6.19 respectively. In this they are compared to theoretical calculations.

Figure 6.21 compares the correlations the initial geometry between the minor axes of the ϵ_n (Φ'_n), calculated in two different initial geometry models: MC-Glauber and MC-KLN, as well as the corresponding correlations in the final state after viscous hydrodynamic evolution to the measured two-plane correlators. The MC calculations are taken from [116]. It is clear that for some of the correlators, the correlations in the initial state are both quantitatively and qualitatively different than the measured correlations. For example the $\langle\cos 4(\Phi_2 - \Phi_4)\rangle$ and $\langle\cos 12(\Phi_2 - \Phi_4)\rangle$ correlations in the initial geometry are close to zero in most central events (highest $\mathrm{N_{part}}$) and then become more and more negative with decreasing $\mathrm{N_{part}}$, while the measured correlations increase with decreasing $\mathrm{N_{part}}$ become more and more positive. Qualitative differences are also seen for the $\langle\cos 6(\Phi_3 - \Phi_6)\rangle$ correlation. However hydro-evolution qualitatively recovers all the two-plane correlations as shown in the bottom panels of Fig. 6.21. In fact, the hydro evolution starting with the MC-KLN initial conditions and $\eta/s = 0.2$ describes the data quite well.

Similar comparisons are shown for the three-plane correlations in Fig 6.22.

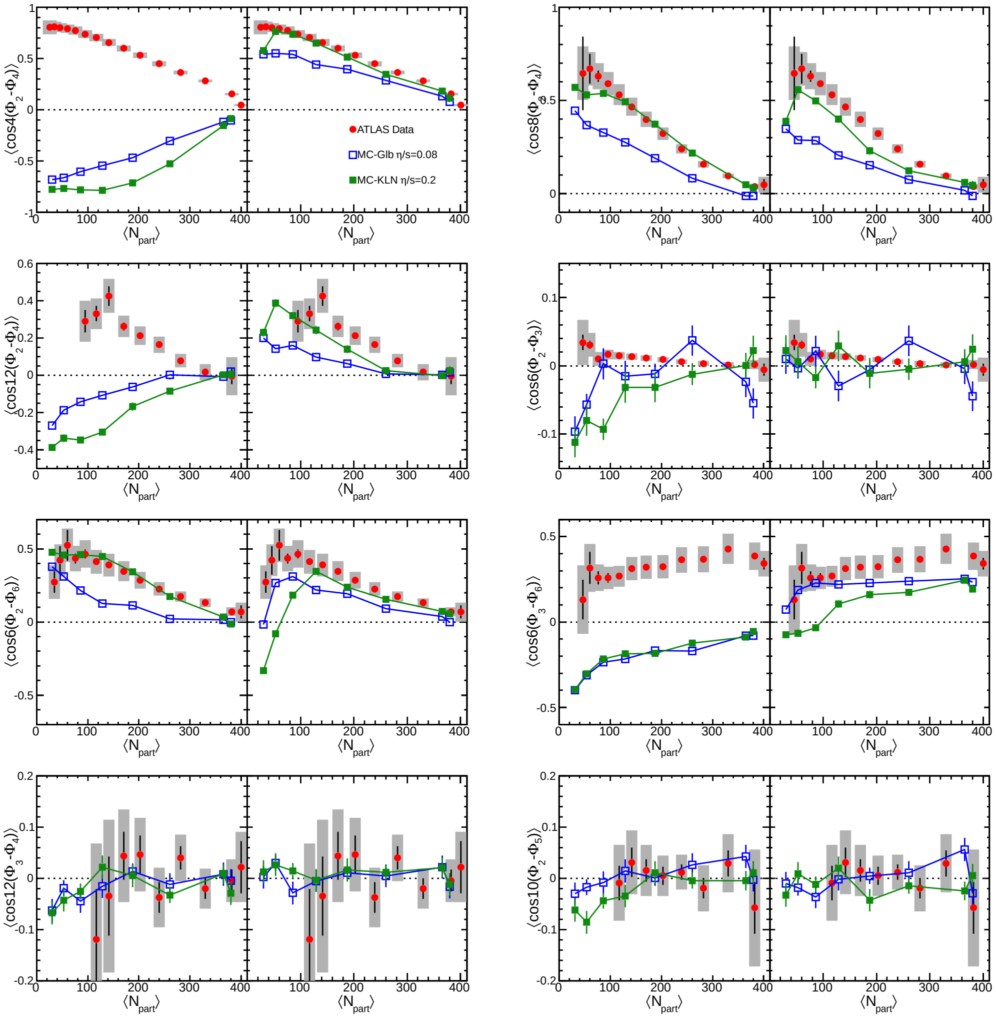

Figure 6.21: Left sub-panels: Two-plane correlations between the Φ'_n in two initial geometry models. Right sub-panels: corresponding correlations between final particles after hydro evolution. Each composite panel corresponds to one correlator. The measured correlators are also plotted. MC calculations taken from [116].

It is seen that for the four non-zero correlators, the correlations in the initial geometry are much different than the measured correlations. However as with the two-plane correlations hydro-evolution reproduces the qualitative nature of the measured correlators.

These results clearly show that the non-linear response to the ϵ_n play an important role in generating the measured correlations. They also indicate that viscous effects might be playing a role in the correlations by dissipating out the higher order ϵ_n and thus enhancing the relative influence of non-linear response to the lower ϵ_n. In fact the MC-KLN based hydro calculations that have larger η/s show better agreement with the measured correlators. A cleaner comparison of the viscous effects can be seen by calculations starting from the same initial geometry, but using different η/s values during the hydro evolution. Figure 6.23 shows such a comparison for the $\langle\cos 4(\Phi_2 - \Phi_4)\rangle$ (left) and $\langle\cos(2\Phi_2 + 3\Phi_3 - 5\Phi_5)\rangle$ (right) where the correlators are calculated starting from a Glauber initial geometry but after ideal (η/s=0, red points) and viscous (η/s=0.16, green points) hydro evolution. This figure is taken from [116]. It is clearly seen that the correlators are larger for the viscous hydro case and in better agreement with the data. These comparisons show the ability of these measurements to constrain the η/s of the medium.

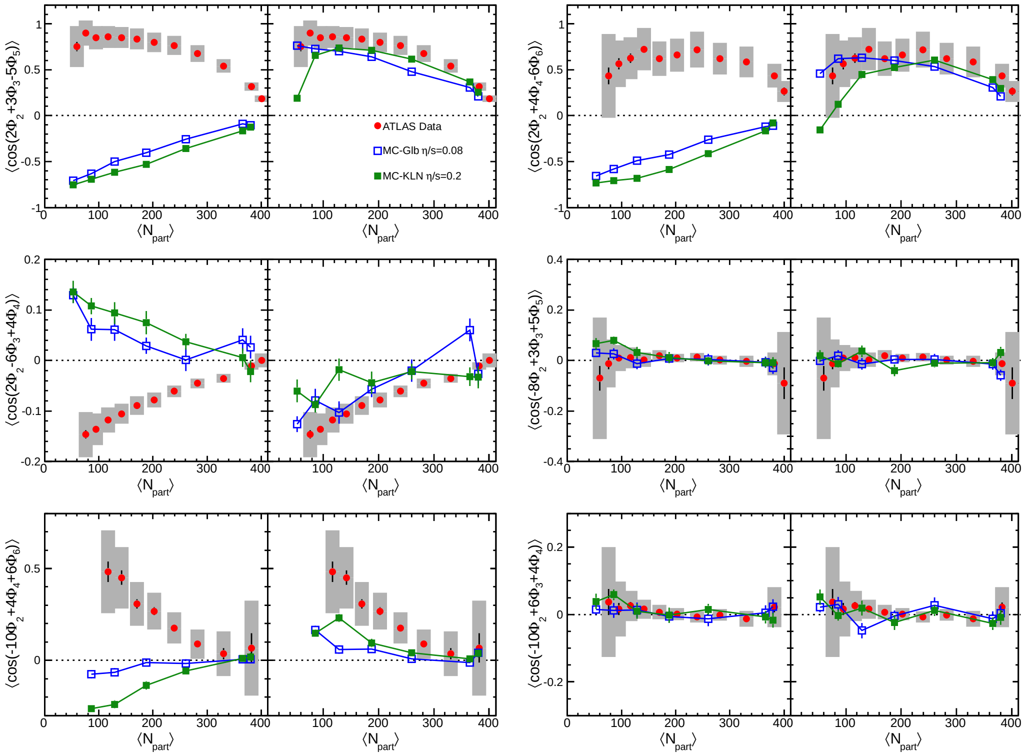

Figure 6.22: Left sub-panels: Three-plane correlations between the Φ'_n in two initial geometry models. Right sub-panels: corresponding correlations between final particles after hydro evolution. Each composite panel corresponds to one correlator. The measured correlators are also plotted. MC calculations taken from [116].

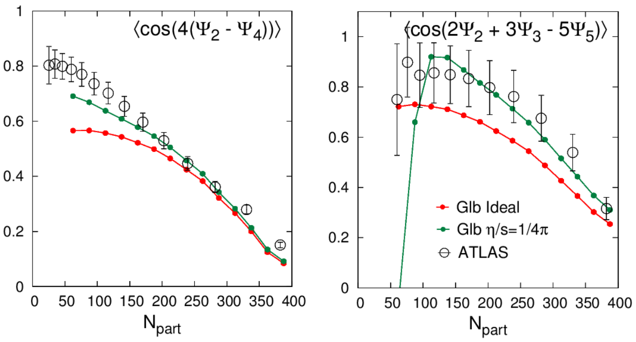

Figure 6.23: Comparison of the $\langle\cos 4(\Phi_2 - \Phi_4)\rangle$ (left) and $\langle\cos(2\Phi_2 + 3\Phi_3 - 5\Phi_5)\rangle$ (right) correlations in viscous and ideal hydro calculations to the ATLAS data measured here. Figure taken from [117]. Note that the Ψ_n in this plot refer to the Φ_n in the notation used here.

Chapter 7

Two-particle correlation measurements in p+Pb collisions

In Chapter 4, the long-range correlations seen in Pb+Pb two-particle correlations (i.e. the ridge and cone), were shown to be a manifestation of the single-particle anisotropies v_n, which originate due to the hydrodynamic expansion of the medium. Thus, such long-range correlations are not expected to be seen in smaller colliding systems, hydrodynamic or collective phenomena are not expected to develop. Recently, the CMS Collaboration analyzed the two-particle correlations in high-multiplicity proton-proton collisions [54] and showed the presence of a ridge like correlation on the near-side ($\Delta\phi \sim 0$) for events that produce $\gtrsim 100$ charged particles. Many models argue that this ridge is due to initial state effects [118–124], e.g. multi-parton processes which color connect partons across a large η range. These processes can be enhanced due to gluon saturation effects in central proton-proton collisions where the gluon density is high [118, 120]. However, a second class of calculations argue that the ridge in proton-proton collisions arises from the mechanism similar to heavy ion collisions: i.e. elliptic flow, with the initial eccentricities produced by fluctuations of the sub-nucleonic structures [125–129]. It suffices to say that current theoretical understanding of the long range ridge in proton-proton collisions is far from clear, and hence measuring similar structures in proton-nucleus collision might shed light on the underlying physics picture.

In this chapter two-particle correlations in p+Pb events at $\sqrt{s_{\mathrm{NN}}} = 5.02$ TeV are measured. The presence of such long-range correlations both on the near-side ($\Delta\phi \sim 0$) as well as on the away-side ($\Delta\phi \sim \pi$) is shown. The dependence of the long-range correlations on p_{T} and event-activity is studied in detail and the final results are compared to theoretical calculations. The measurements presented in this chapter have been published in [130].

7.1 Methodology

The 2PC procedure is similar to the one used for the Pb+Pb analysis in Chapter 4. The 2D and 1D correlation functions are built by dividing foreground pairs by mixed-event pairs. However here track-by-track efficiency re-weighting $1/\epsilon(\eta, p_{\mathrm{T}})$ is also applied for both trigger and partner tracks, i.e. the pair has a weight $1/\epsilon(\eta^a, {p_{\mathrm{T}}}^a) \times 1/\epsilon(\eta^b, {p_{\mathrm{T}}}^b)$. The reason for applying this explicit weighting will be clarified later.

Figure 7.1 shows the 2D correlation functions for $p_{\mathrm{T}}^a, p_{\mathrm{T}}^b \in (0.5, 4)$ GeV for several event-activity classes based on $N_{\mathrm{ch}}^{\mathrm{rec}}$ (as defined is Section 2.2.2) . In the low-multiplicity events only the jet peak is seen on the near-side, however as the multiplicity increases a clear ridge structure develops on the near-side.

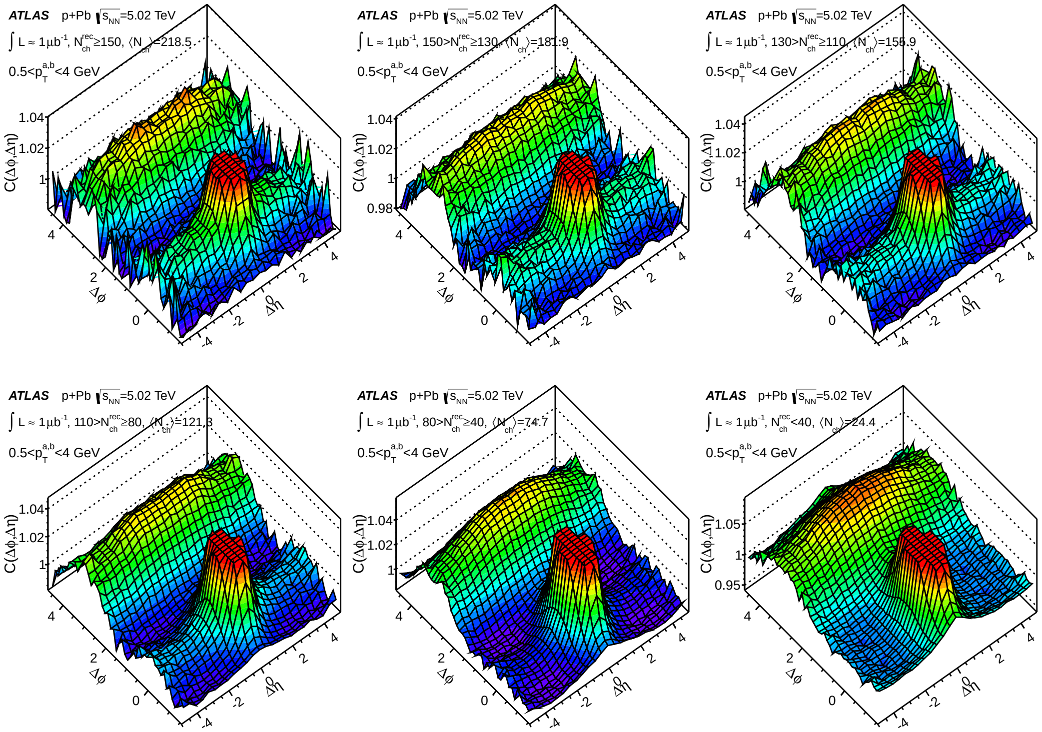

Figure 7.1: The 2D correlation function $C(\Delta\phi, \Delta\eta)$ for tracks in $0.5 < p_{\mathrm{T}} < 4$ GeV in various event activity classes, defined by the number of reconstructed tracks with $p_{\mathrm{T}} > 0.4$ GeV.

This can be seen more clearly in the 1D correlation functions shown in

Fig. 7.2. The top panels show the long range correlations ($|\Delta\eta| > 2$) where one can clearly see the ridge evolving with increasing $N_{\mathrm{ch}}^{\mathrm{rec}}$ with identical shape for like-charge and unlike-charge correlations. The lower panels show similar figures but for $|\Delta\eta| < 2$ where the near-side jet peak is seen at $\Delta\phi \sim 0$. The two like-charge and unlike-charge correlations show a clear separation which is expected for jet fragmentation. That the long-range correlations do not show this separation, clearly indicates that they are not coming from jet-fragmentation.

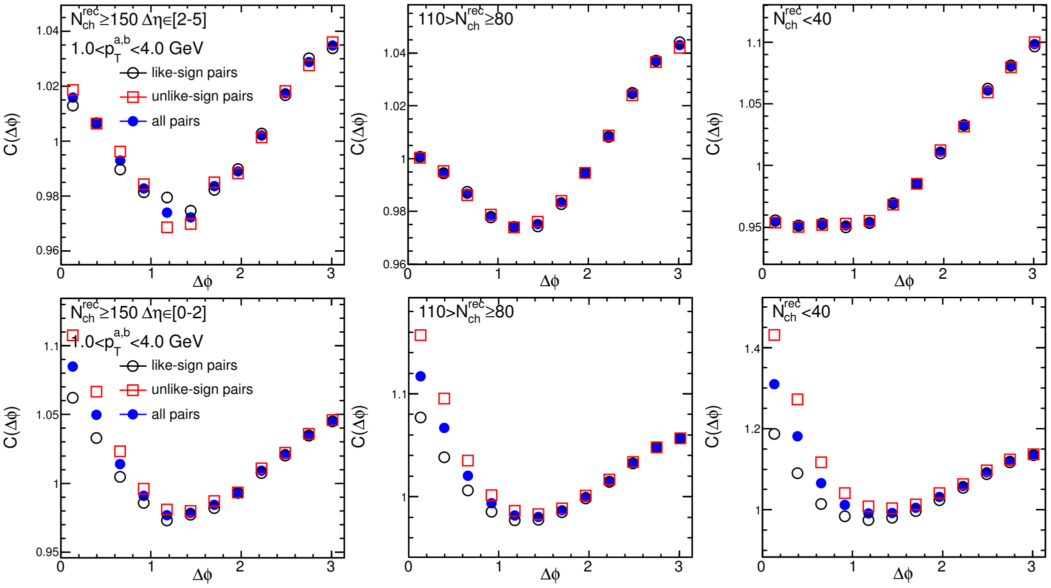

Figure 7.2: The correlation function in $\Delta\phi$ distributions integrated over $2 < |\Delta\eta| < 5$ (upper panels) and over $|\Delta\eta| < 2$ (lower panels) for like-sign, unlike-sign and all pairs. Each panel shows the distributions for one multiplicity interval.

7.1.1 Per-trigger yield

The ridge magnitude can be quantified by the per-trigger yield [79] (PTY or Y for short), which is defined as the number of associated particles per trigger particle, over a flat pedestal. It can be obtained for the same-event and mixed-event pairs as:

$$Y(\Delta\phi) = \frac{1}{N^a} \frac{\int B(\Delta\phi) d\Delta\phi}{\int d\Delta\phi} \left[\frac{S(\Delta\phi)}{B(\Delta\phi)}\right] - b_{\mathrm{ZYAM}} \tag{7.1}$$

where, N^a in the number of triggers, corrected to account for tracking efficiency, contributing to the same-event pair distribution, i.e.:

$$N^a = \sum_{Triggers} 1/\epsilon(\eta^a, p_{\mathrm{T}}^a) \tag{7.2}$$

and b_{ZYAM} is a flat pedestal which is subtracted such that $Y(\Delta\phi)$ has Zero Yield At Minimum (ZYAM [79]). Eq. 7.2 can be understood as the following: The same-event pairs $S(\Delta\phi)$ is the distribution of associated particles in $\Delta\phi$ for N^a trigger particles. The division by $B(\Delta\phi)$ corrects for the $\Delta\phi$ acceptance but changes the normalization. The overall multiplication by $(\int B(\Delta\phi)d\Delta\phi)/(\int d\Delta\phi)^1$, which is the mean value of $B(\Delta\phi)$, restores the correct normalization. The division by N^a converts this into a *per-trigger* quantity. Finally a flat pedestal b_{ZYAM} is removed so that only truly correlated pairs are considered[2]. The end goal of measuring the PTY was the main reason why the efficiency re-weighting $1/\epsilon(\eta^a, {p_{\mathrm{T}}}^a) \times 1/\epsilon(\eta^b, {p_{\mathrm{T}}}^b)$ was applied while measuring the $S(\Delta\phi)^3$.

Figure 7.3 shows the procedure for obtaining the PTY. The first panel shows the correlation function for $|\Delta\eta| \in (2, 5)$. The correlation function is normalized such that the $S(\Delta\phi)$ and $B(\Delta\phi)$ have the same integral. The second panel shows the PTY before the pedestal subtraction. This is identical to the correlation function up to an overall normalization. The final panel shows the PTY. For locating the minimum for ZYAM subtraction, the following procedure is followed: first a scan with a fixed width of $\pi/12$ is used, corresponding to twice the bin width of the histograms in Figure 7.3, this gives an approximate estimation of the minimum, however may suffer from large statistical uncertainties as well as the tendency to pick the point with largest downward fluctuation. This is followed by, a second order polynomial fit to redetermine the minimum and the pedestal. The default fit range used is $\Delta\phi_{\mathrm{ZYAM}} \pm 0.5$ radian, and is varied over ±0.4 and ±0.6 for systematic checks.

The reason why the PTY is measured is that it can be directly compared across different event-activity classes, since its normalization is well defined and physical. The left panels of Fig. 7.4 show the PTY for several activity classes defined via $\Sigma E_{\mathrm{T}}^{\mathrm{Pb}}$ (left) and $N_{\mathrm{ch}}^{\mathrm{rec}}$ (right) for pairs in $2 < |\Delta\eta| < 5$ constructed from charged tracks with $0.5 < p_{\mathrm{T}} < 4$ GeV. From these plots

---

[1] $\int d\Delta\phi = \pi$ or 2π depending on whether the PTY is folded into $(0, \pi)$ or not.

[2] The ZYAM procedure assumes that at its minimum, the correlation function gets contributions only from combinatorial pairs

[3] The efficiency re-weighting must consequently also be applied for $B(\Delta\phi)$ for the mixing procedure to work.

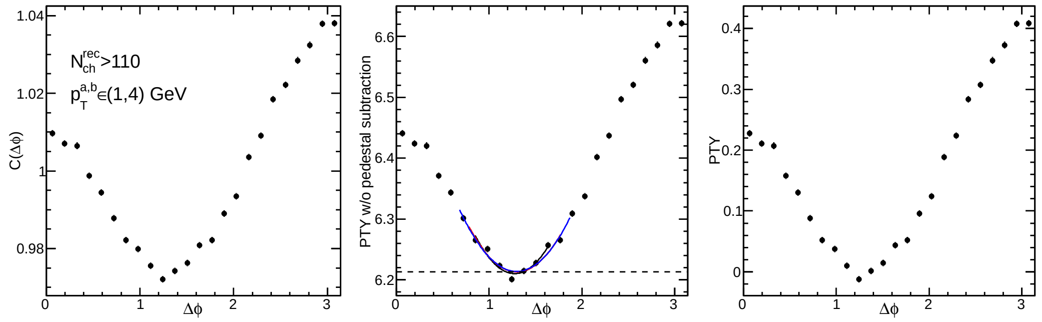

Figure 7.3: Left panel: The correlation function. Middle panel: The per-trigger yield before pedestal subtraction together with second order polynomial fits to determine the minimum. Right panel: The per-trigger yield after pedestal subtraction.

the development of the ridge with increasing event-activity can be easily seen. Interestingly the yield of associated particles also increases on the away side with the magnitude of the increase almost identical. This clearly indicates that an away side ridge is also present but masked by the away-side jet correlations. In order to better reveal the development of the away-side ridge, the PTY in the lowest event-activity class is used as a measure of the jet correlations and subtracted from the PTY of the other classes. The quantity thus obtained is called the **recoil subtracted PTY** (or peripheral subtracted PTY) $\Delta Y(\Delta\phi)$:

$$\Delta Y(\Delta\phi) = \begin{cases} Y(\Delta\phi)|_{\Sigma E_{\mathrm{T}}^{\mathrm{FCal_{Pb}}}} - Y(\Delta\phi)|_{\Sigma E_{\mathrm{T}}^{\mathrm{FCal_{Pb}}}<20\ \mathrm{GeV}} & \Sigma E_{\mathrm{T}}^{\mathrm{Pb}}\ \text{based} \\ Y(\Delta\phi)|_{N_{\mathrm{ch}}^{\mathrm{rec}}} - Y(\Delta\phi)|_{20<N_{\mathrm{ch}}^{\mathrm{rec}}<40} & N_{\mathrm{ch}}^{\mathrm{rec}}\ \text{based} \end{cases} \tag{7.3}$$

Note that the low activity bin chosen for the subtraction have almost no long-range correlations on the near-side, as can be seen from the left panels of Fig. 7.4. This subtraction assumes that the jet-like correlations are identical, at the per-trigger level, between low-activity and high-activity events. The right panels of Fig. 7.4 show the recoil subtracted PTY. The development of the away-side ridge is clearly seen and parallels that of the near-side. This can be seen more clearly by fitting these distributions by fitting the distributions with functions of the form:

$$\Delta Y(\Delta\phi) = a_0 + 2a_2\cos(2\Delta\phi) \tag{7.4}$$

These fits are also shown on the $\Delta Y(\Delta\phi)$ plots.

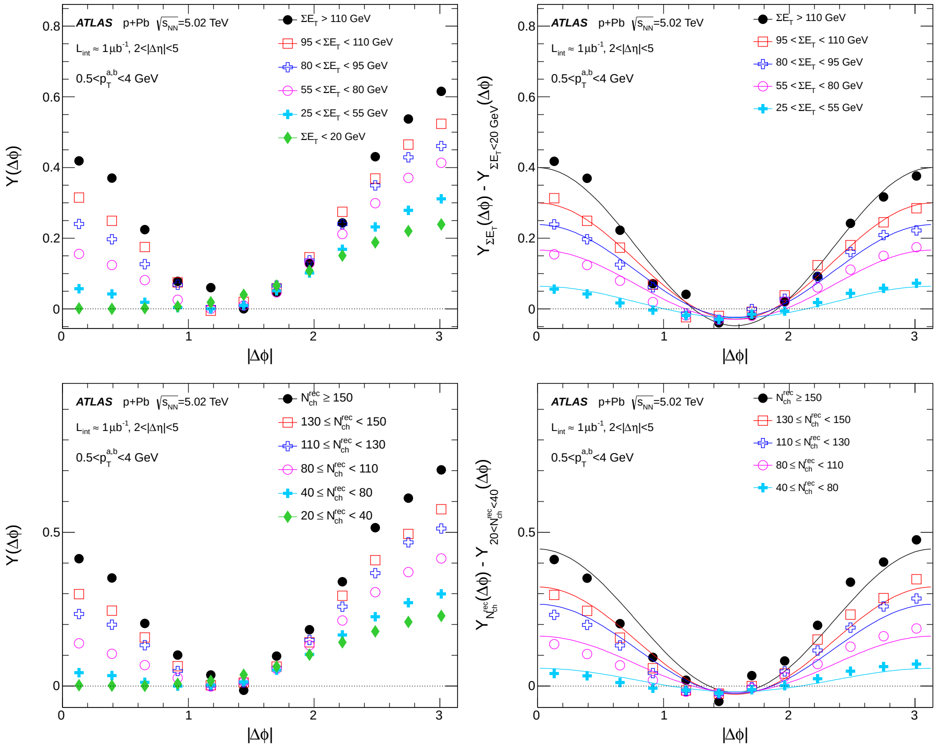

Figure 7.4: Left Panels: $Y(\Delta\phi)$ in several event activity classes. Right panels: $\Delta Y(\Delta\phi)$ obtained by subtracting $Y(\Delta\phi)$ in the low event activity class (see Eq. 7.3), for pairs in $2 < |\Delta\eta| < 5$ constructed from charged tracks with $0.5 < p_{\mathrm{T}} < 4$ GeV. The event classes are defined by $\Sigma E_{\mathrm{T}}^{\mathrm{Pb}}$ (left panel) and $N_{\mathrm{ch}}^{\mathrm{rec}}$ (right panel) respectively. The lines indicate a fit to a $a_0 + 2a_2 \cos 2\Delta\phi$ function.

7.2 Systematic errors

The main results for the p+Pb analysis are the per-trigger yields $Y(\Delta\phi)$ and $\Delta Y(\Delta\phi)$. All other observables (to be presented in Section 7.3) are directly derived from them. In this section, the list of checks that were done to determine the systematic uncertainties associated with the PTY are discussed. The errors on the other derived observables are obtained by a propagation of these errors. The following sources of systematic uncertainties are identified for the PTY:

1. Uncertainty of tracking efficiency: In this analysis the same-pair and mixed-pair distributions are corrected by the tracking efficiency $\epsilon(p_{\mathrm{T}}, \eta)$. The uncertainties in the tracking efficiencies thus affect our results. The

influence of the tracking efficiency are evaluated by varying the tracking selection criteria in both the data and simulation, re-calculating the efficiency map $\epsilon(p_{\rm T}, \eta)$, and evaluating the change in the PTY and correlation functions.

2. Material uncertainty: The tracking efficiency is determined using MC which requires a description of the ATLAS geometry. The material budget in ATLAS has some uncertainty which introduces additional η and $p_{\rm T}$ dependent uncertainty to the tracking efficiency.

3. ZYAM uncertainty: This is related to the errors introduced when identifying the minimum of the PTY for ZYAM subtraction.

4. Acceptance & event-mixing procedure: The acceptance changes slightly with event multiplicity and collision vertex. Thus it is important to check whether the shape of background distribution depends on the multiplicity and z-vertex matching in constructing the mixed event distributions.

5. Monte Carlo closure: This is an independent check of the robustness of the analysis procedure. This is done by repeating the whole analysis in a full ATLAS simulation using the HIJING event generator. The correlation functions and the PTY at the generator (truth) level and the reconstructed level are compared to check for differences.

Table 7.1 summarizes the errors from each source. In general, ZYAM uncertainty is mostly systematic when the PTY has very small statistical uncertainty, but when the $\Delta\phi$ distribution has poor statistics, the ZYAM uncertainty becomes correlated with the statistical uncertainty. This is usually the case at high $p_{\rm T}$ or for event classes with low multiplicity. The event mixing procedure introduces an uncertainty that is only related to the detector and does not depend on the event multiplicity, and it has been estimated to be a fixed fraction of the pedestal level (about 0.0003). The uncertainty from all other sources can be expressed as a percentage of the true PTY.

7.3 Results

2D correlation functions

Figure 7.5 shows the 2D correlation function for $p_{\rm T}^a, p_{\rm T}^b \in (0.5, 4)$ GeV for several FCal$_{\sum \rm E_T^{Pb}}$ event-activity classes. Similar plots were shown in Fig 7.1 for the $\rm N_{ch}^{rec}$ based centrality classes. The development of the near-side ridge with increasing event-activity is clearly seen. A more careful look shows that the

ZYAM procedure	0.0003 – 0.001 of background level when stat error is small. Comparable to stat error when stat error is large.
Acceptance& event mixing	0.0003 of background level
Tracking efficiency due to cuts	2.5%
Tracking efficiency due to material	3%
Monte Carlo Closure	3%

Table 7.1: Sources of systematic uncertainties for PTY.

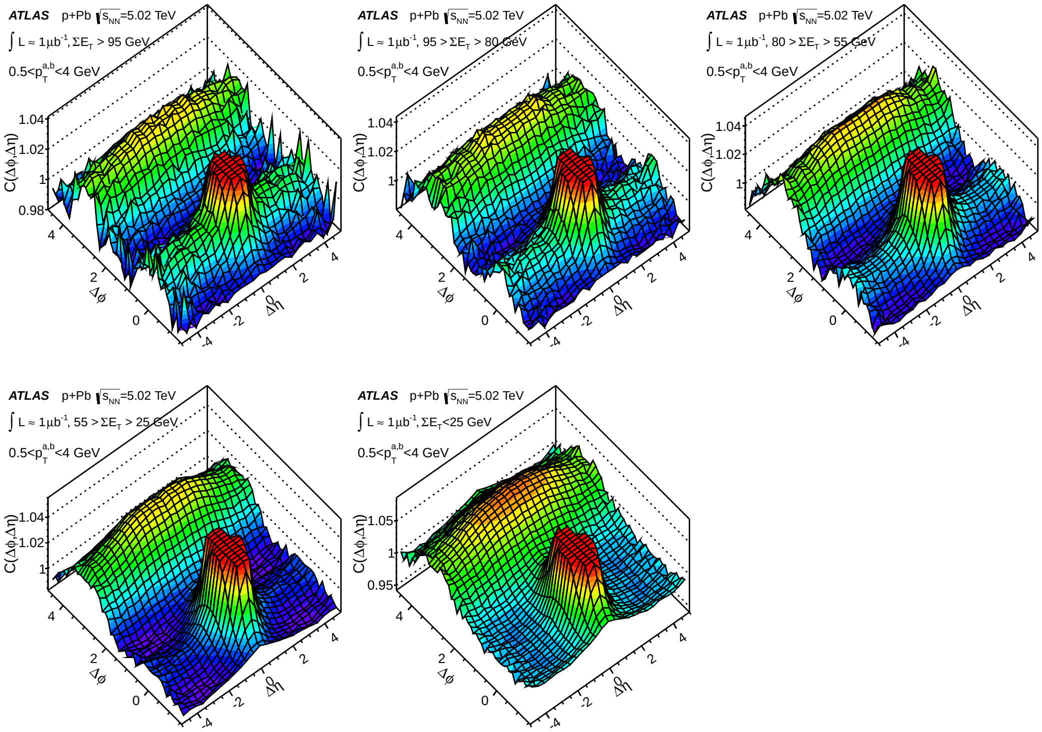

Figure 7.5: The 2D correlation functions for tracks with $p_{\mathrm{T}}^{a}, p_{\mathrm{T}}^{b} \in (0.5, 4)$ GeV in various event activity classes, defined by the $\sum E_{\mathrm{T}}^{Pb}$. The evolution of the near-side ridge is clearly seen.

away side, which has considerable $\Delta\eta$ dependence in the lowest event-activity case (lower right plot), also becomes flatter with increasing event-activity, indicating the development of the away-side ridge.

PTY and PTY Difference

As mentioned before the development of the ridge can be studied in more detail by the $Y(\Delta\phi)$ and $\Delta Y(\Delta\phi)$ integrated over $|\Delta\eta| \in (2, 5)$. The centrality evolution of these quantities was shown in Fig 7.4. In order to further investigate the development of the ridge, the $Y(\Delta\phi)$ is integrated in $2\pi/3$ windows around the near side ($|\Delta\phi| < \pi/3$) and away-side ($|\Delta\phi - \pi| < \pi/3$). This quantity is termed as the **integrated per-trigger-yield** or Y_{int}. Figure 7.6 shows the variation of the near-side and away-side Y_{int} with $\sum E_{\mathrm{T}}^{Pb}$ (left plot) and $\mathrm{N}_{\mathrm{ch}}^{\mathrm{rec}}$ (right plot) as well as the difference between the two. For the $\Sigma E_{\mathrm{T}}^{\mathrm{Pb}}$ based results, the near-side yield is close to zero for $\Sigma E_{\mathrm{T}}^{\mathrm{Pb}} < 20$ GeV, and increases with increasing $\Sigma E_{\mathrm{T}}^{\mathrm{Pb}}$. The away-side yield shows a similar variation as a function of $\Sigma E_{\mathrm{T}}^{\mathrm{Pb}}$, except that it starts at a non-zero value, due to the contribution of the away-side jet. The yield difference between these two regions is found to be approximately independent of $\Sigma E_{\mathrm{T}}^{\mathrm{Pb}}$, indicating the symmetry of the ridge.

For the N_{ch} based results qualitatively see similar trends are seen. However, the away-side Y_{int} shows a sharp drop at low N_{ch}. This is because requiring small $\mathrm{N}_{\mathrm{ch}}^{\mathrm{rec}}$ in the event reduces the number of pairs in the events, hence it suppresses the per-trigger yield as well. This auto-correlation effect can introduce further bias when the recoil subtraction (Eq. 7.3) is done. The $\Sigma E_{\mathrm{T}}^{\mathrm{Pb}}$ based results do not have this problem. Thus they are used for presenting the final results.

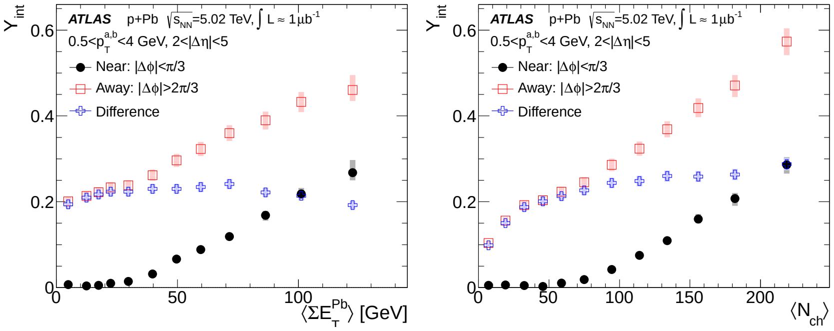

Figure 7.6: Y_{int} for ${p_{\mathrm{T}}}^a, p_{\mathrm{T}}^b \in (0.5, 4)$ GeV measured vs $\sum E_{\mathrm{T}}^{Pb}$ (left) and $\mathrm{N}_{\mathrm{ch}}^{\mathrm{rec}}$ (right). The data points are plotted at the mean values of $\sum E_{\mathrm{T}}^{Pb}$ or N_{ch} for each interval.

p_{T} dependence of Y and ΔY

It is also interesting to study the p_{T} dependence of the yields. Figure 7.7 shows the $Y(\Delta\phi)$ for a high activity ($\Sigma E_{\mathrm{T}}^{\mathrm{Pb}} > 80$ GeV) and the lowest activity

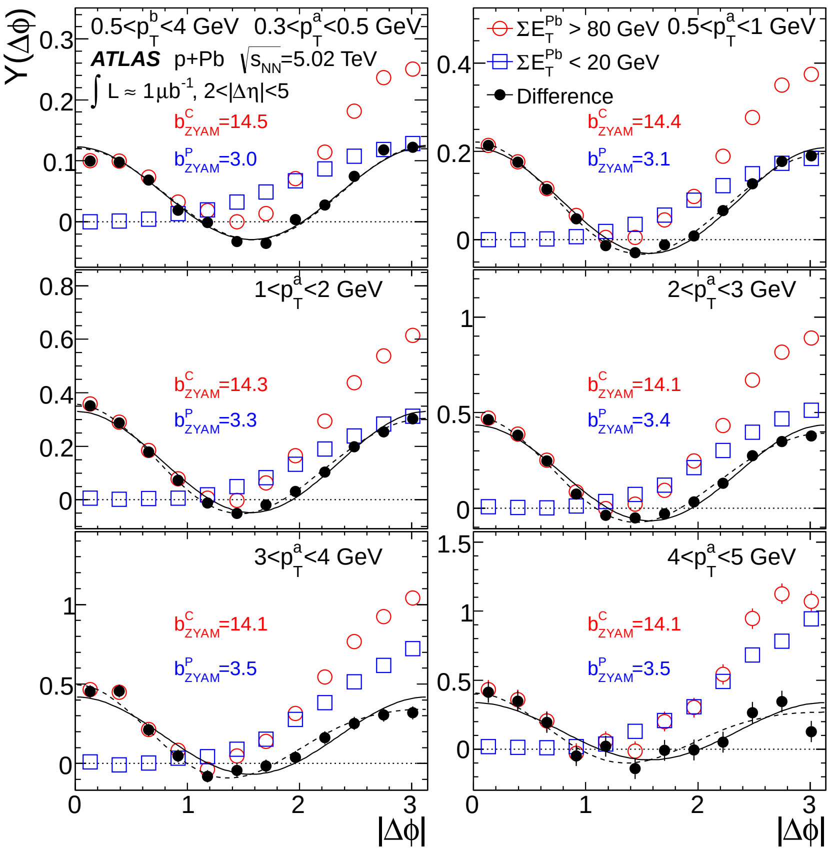

Figure 7.7: $Y(\Delta\phi)$ in $\Sigma E_{\mathrm{T}}^{\mathrm{Pb}} < 20$ GeV (blue points) and $\Sigma E_{\mathrm{T}}^{\mathrm{Pb}} > 80$ GeV (red points) classes and their difference (black points) for $p_{\mathrm{T}}^{b} \in (0.5, 4)$ GeV. Each panel is for a different range of ${p_{\mathrm{T}}}^{a}$. The lines indicate a fit to $\Delta Y(\Delta\phi)$ with functions $a_0 + 2a_2\cos(2\Delta\phi)$ (solid line) and $a_0 + 2a_2\cos(2\Delta\phi) + a_3\cos(3\Delta\phi)$.

($\Sigma E_{\mathrm{T}}^{\mathrm{Pb}} <$ 20 GeV) class for $p_{\mathrm{T}}^{b} \in (0.5, 4)$ GeV. Each panel is a different p_{T}^{a} going from lower p_{T} (top left) to higher p_{T} (bottom right). The black points indicate the yield difference $\Delta Y(\Delta\phi)$. Across all the p_{T}^{a} ranges, the $\Delta Y(\Delta\phi)$ largely described by a functional form $a_0 + 2a_2\cos(2\Delta\phi)$ (solid lines) showing the symmetric nature of the ridge. Including a third order modulation term $a_3\cos(3\Delta\phi)$ only improves the fits a little (dashed lines).

The p_{T} dependence can be studied more quantitatively by the integrated yield Y_{int}. This is shown in the top panels of Figure 7.8 for the near-side (left plot) and the away-side (right plot), for three different activity classes. The near-side plot has a dependence that is remarkably similar to the p_{T} dependence of the v_n that was seen in the Pb+Pb analysis (Section 3.5.2). The behavior of the away side is qualitatively different due to the away-side jet. However for the yields obtained after recoil subtraction, shown in the lower panels, the behavior of both the near and away-side is nearly identical.

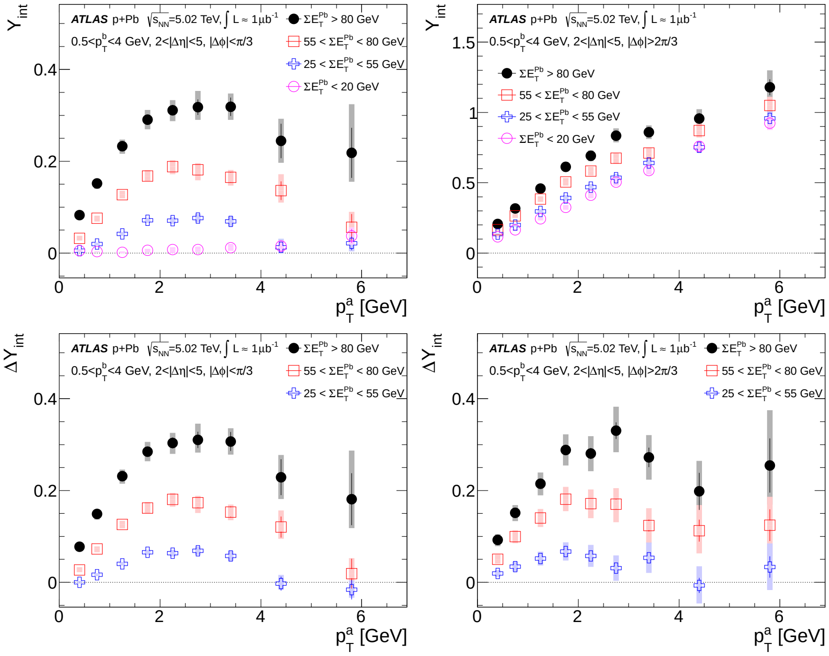

Figure 7.8: Top panels: The near-side (left) and away-side (right) Y_{int} vs p_T^a for $p_T^b \in (0.5, 4)$ GeV for several $\sum E_T^{Pb}$ classes. Lower Panels : similar plots but for ΔY_{int}.

Fourier analysis of correlation functions

The qualitative similarity between the p_T^a dependence of the $\Delta Y_{\rm int}$ and the v_n, suggests that these correlations could have similar hydrodynamic origin. In such a scenario the single-particle azimuthal distributions can be parameterized, similar to the ones in heavy-ion collisions, as:

$$dN/d\phi \propto (1 + 2\sum ns_n \cos(n(\phi - \Phi_n)) \tag{7.5}$$

where, the s_n are the magnitudes of the single-particle anisotropies (analogous the v_n in the Pb+Pb analysis). One way to check if this is true is to expand the two-particle correlations in a Fourier series:

$$C(\Delta\phi) \propto (1 + 2\sum nc_n \cos(n\Delta\phi)) \tag{7.6}$$

and check if the Fourier coefficients $c_n(p_{\mathrm{T}}^a, p_{\mathrm{T}}^b)$ factorize into $s_n(p_{\mathrm{T}}^a)$ and $s_n(p_{\mathrm{T}}^b)$, i.e. one should get the same $s_n(p_{\mathrm{T}}^a)$ independent of the p_{T}^b which was used in the 2PC. Similar to the $v_{n,n}$ factorization in the Pb+Pb analysis. However, the significant contribution of the away-side jet will already break this factorization (as in peripheral Pb+Pb events). Thus before the factorization of the c_n can be tested, the jet influence must be removed from the correlation function.

This is done by subtracting out the jet contribution at the PTY level and then converting it into a correlation function as follows:

$$\begin{aligned} C_{\Delta}(\Delta\phi) &\propto Y(\Delta\phi)_{\sum E_{\mathrm{T}}^{\mathrm{Pb}}} + b_{\mathrm{ZYAM},\sum E_{\mathrm{T}}^{\mathrm{Pb}}} - Y(\Delta\phi)_{\sum E_{\mathrm{T}}^{\mathrm{Pb}}<20\,GeV} \\ &= \Delta Y(\Delta\phi)_{\sum E_{\mathrm{T}}^{\mathrm{Pb}}} + b_{\mathrm{ZYAM},\sum E_{\mathrm{T}}^{\mathrm{Pb}}} \end{aligned} \tag{7.7}$$

The way to understand the above is as follows: The correlation function $C(\Delta\phi)$ is proportional to the $Y(\Delta\phi)+b_{\mathrm{ZYAM}}$ (see Eq. 7.1). The contribution from the jet-like correlations can be removed at the per-trigger level by subtracting out the $Y(\Delta\phi)_{\sum E_{\mathrm{T}}^{\mathrm{Pb}}<20\,GeV}$. The remaining quantity which is $\Delta Y(\Delta\phi) + b_{\mathrm{ZYAM}}$, would only contain the genuine long-range correlations. The recoil subtracted correlation function is $C_{\Delta}(\Delta\phi)$ thus proportional to this quantity.

Once the peripheral subtracted correlations are obtained, the Fourier coefficients $c_n(p_{\mathrm{T}}^a, p_{\mathrm{T}}^b)$ can be extracted. The $s_n(p_{\mathrm{T}}^a)$ for different p_{T}^b can be calculated as (c.f. Eq. 4.9):

$$s_n(p_{\mathrm{T}}^a) = c_n(p_{\mathrm{T}}^a, p_{\mathrm{T}}^b)/s_n(p_{\mathrm{T}}^b) = c_n(p_{\mathrm{T}}^a, p_{\mathrm{T}}^b)/\sqrt{c_n(p_{\mathrm{T}}^b, p_{\mathrm{T}}^b)} \tag{7.8}$$

The left panels of Fig 7.9 show the c_2 and c_3 as a function of p_{T}^a with $p_{\mathrm{T}}^b \in (0.5, 4)$ GeV for three different event-activity classes. The right panels show the s_2 and s_3. As expected, the c_2 and s_2 behave very similar to the v_2 in Pb+Pb collisions: they increase linearly with p_{T} at low p_{T} to reach a maximum at ~ 3 GeV then decrease. Unfortunately for c_3 and s_3 there is not enough statistical precision to measure them out till 6 GeV as for the s_2. They do show a linear increase at low p_{T} but it is difficult to ascertain if they turn around at 3 GeV like the s_2.

The left panel of Fig. 7.9 shows the $s_2(p_{\mathrm{T}}^a)$ obtained using three different p_{T}^b bins. Overall the three estimates of s_2 agree with each other within 20%, with agreement being better at lower p_{T}^a. The right plot shows a similar check for s_3. Unfortunately there is not enough statistical precision in the data to check the factorization at the same level as for s_2.

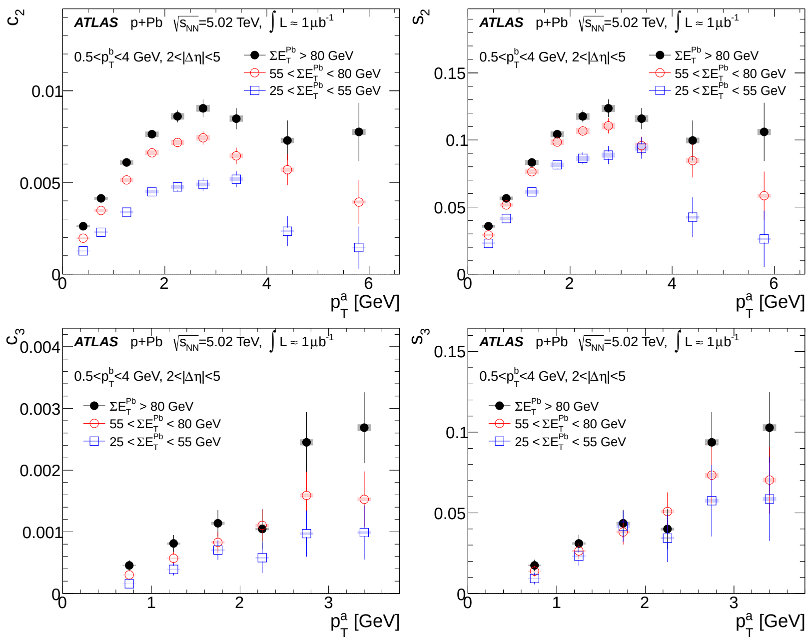

Figure 7.9: The c_n (left) and s_n (right) vs ${p_\mathrm{T}}^a$ for ${p_\mathrm{T}}^b \in (0.5, 4)$ GeV in three different $\Sigma E_\mathrm{T}^\mathrm{Pb}$ event-classes.

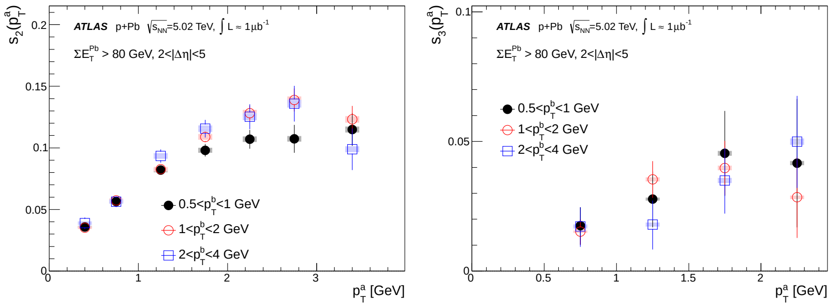

Figure 7.10: $s_n(p_\mathrm{T}^a)$ obtained using Eq. 7.8 for three different p_T^b for $\Sigma E_\mathrm{T}^\mathrm{Pb} >$ 80 GeV event-class.

7.4 Summary

In this chapter two-particle correlations in p+Pb events were studied. Long-range correlations along $\Delta\eta$ were seen on the near-side whose strength increased with event activity ($\Sigma E_\mathrm{T}^\mathrm{Pb}$ or $\mathrm{N}_\mathrm{ch}^\mathrm{rec}$). A more detailed analysis via the study of per-trigger-yields showed that such long-range correlation structures are also present on the away-side but contaminated by the away-side jet. The strength of the jet-like contribution was estimated using low event-activity collisions and subtracted. The peripheral subtracted $\Delta Y(\Delta\phi)$ thus obtained showed that the away-side ridge had nearly identical strength as the near-side ridge.

The p_{T} dependence of the ridges was found to be qualitatively similar in shape to the v_n in Pb+Pb events. Peripheral subtracted correlation functions were constructed, similar to the ΔY, and their Fourier coefficients c_n were extracted. The factorization of the $c_n(p_{\mathrm{T}}^a, p_{\mathrm{T}}^b)$ into products of $s_n(p_{\mathrm{T}}^a)$ and $s_n(p_{\mathrm{T}}^b)$, much like the factorization of $v_{n,n}$ into v_n in the Pb+Pb case, was tested and showed to hold at the 20% level for s_2.

The measurements qualitatively suggest the presence of global correlations in p+Pb events with sufficiently large event-activity, similar to those in Pb+Pb events. However recent theoretical calculations based on the CGC framework show that such correlations are possible from gluon saturation effects [131]. Figure 7.11 shows a comparison to the $Y(\Delta\phi)$ and $\Delta Y(\Delta\phi)$ data to CGC calculations [131], which show good agreement with the data. Further analysis of the Pb+Pb data including the measurement of higher order c_n can possibly enable us to understand the origin of these long-range correlations. Also with the much larger dataset recorded in the 2013 run, EbyE v_n analysis could be possible for the highest multiplicity events.

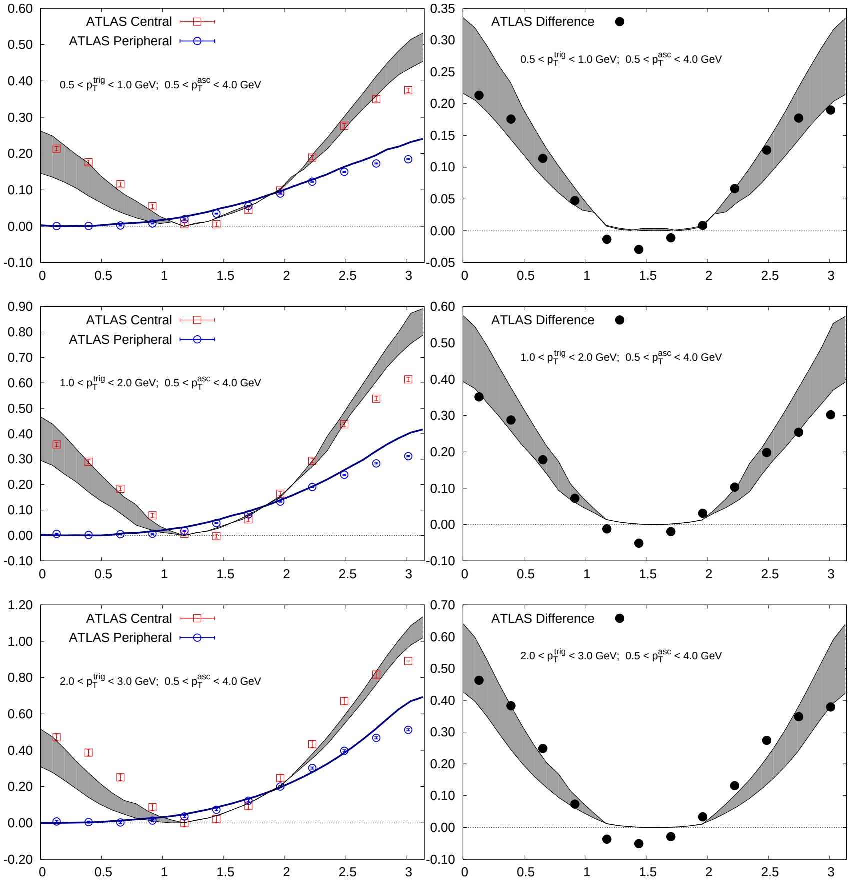

Figure 7.11: Left Panels: Comparison of $Y(\Delta\phi)$ for $\Sigma E_{\mathrm{T}}^{\mathrm{Pb}} > 80$ GeV (red squares) and $\Sigma E_{\mathrm{T}}^{\mathrm{Pb}} < 20$ GeV (blue circles) to CGC calculations (blue line and shaded band). Right Panels: Similar comparison for the $\Delta Y(\Delta\phi)$. From top to bottom the panels are for different p_{T}^{a} with $p_{\mathrm{T}}^{b} \in (0.5, 4)$ GeV. Figure taken from [131].

Chapter 8

Conclusions

8.1 Summary of results

In this work details measurements of azimuthal the anisotropies of charged particle distributions in Pb+Pb as well as in p+Pb collisions were presented. The ultimate goal of these measurements was to understand the nature of the initial geometry and the hydrodynamic response to that initial geometry in heavy-ion collisions. To acheieve this end comprehensive measurements of the p_{T}, η and centrality dependence of the flow harmonics v_n were done (Fig 8.1). These four dimentional measurements –in n, p_{T}, η and centrality– can precisely constrain the η/s of the medium and at the same time constrain initial geometry models.

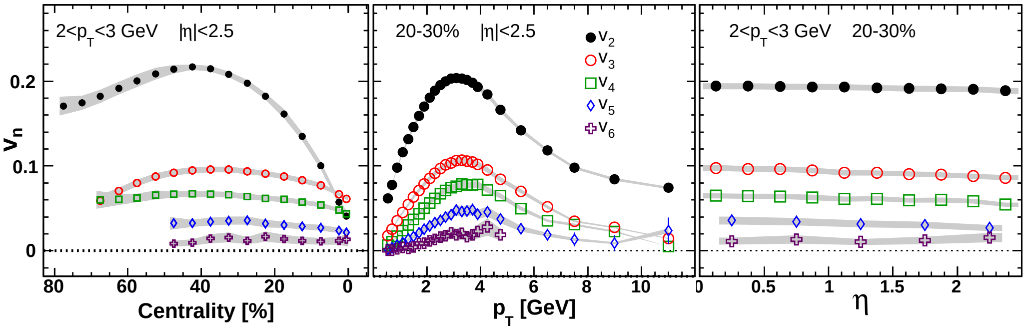

Figure 8.1: The EP v_n measurements.

The cone and ridge structures seen in the 2PC were shown to be a manifestation of collective flow (Fig 8.2), dismissing the previous notions that these structures were the result from jet-medium interactions. Similar ridge like correlations were also seen in two-particle correlations for p+Pb events with large multiplicities. By subtracting out the contribution of the away-side jet, it was shown that such correlations were also present on the away-side. The p_{T} dependence of the p+Pb double-ridge was shown to be similar to that in Pb+Pb, indicating the possible presence of collective phenomena in smaller systems.

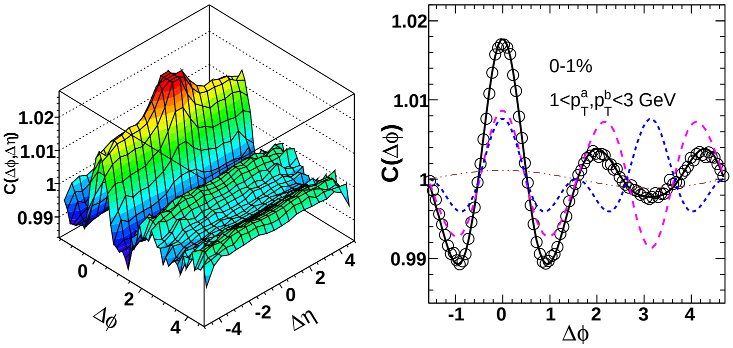

Figure 8.2: Left Panel: 2PC in Pb+Pb. Right: The long-range correlations (open symbols) along with the expected correlations from single particle v_n (black line).

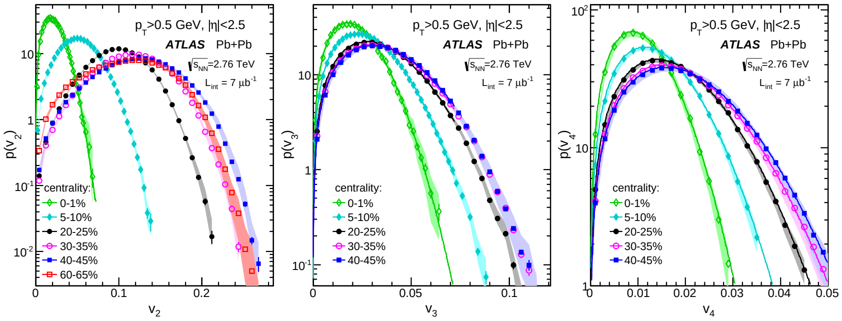

Figure 8.3: The EbyE distributions for v_2 (left), v_3 (center) and v_4 (right).

The fluctuations in the initial geometry were investigated by measuring EbyE distributions of flow harmonics v_2-v_4 (Fig 8.3). The EbyE distributions for $p_{\mathrm{T}} > 1$ GeV and $p_{\mathrm{T}} \in (0.5, 1)$ GeV were shown to have identical shapes, implying that the hydrodynamic response to the initial geometry factorizes into a p_{T} dependent, and a geometry dependent function. The v_3 and v_4 distributions were shown to be consistent with the pure Gaussian fluctuation scenario, uncorrelated with the mean geometry. For v_2 this was true only for most central-events (0-2%) beyond which a the role of the mean geometry effects became important and the v_2 distributions were better described by Bessel-Gaussian functions. However, in the (15-20)% and more peripheral centralities, a systematic deviation of the Bessel-Gaussian fit from the v_2 data was observed, suggesting either non-Gaussian behavior in the flow fluctuations, and/or the presence of non-linear hydrodynamic response to the ϵ_n. The measured v_2 distributions were shown to be qualitatively different than the ϵ_n distributions in the Glauber and MC-KLN models. However, the ϵ_n distributions from the IP-Glasma model were in good agreement with the v_n distributions with the agreement further improving after viscous-hydro evolution, showing the importance of non-linear hydrodynamic response to the ϵ_n. The non-linear response was further investigated by measurement of event-plane correlations (Fig 8.4). Comparisons with hydro calculations showed that these correlations are the result of non-linear response and also sensitive to viscous effests.

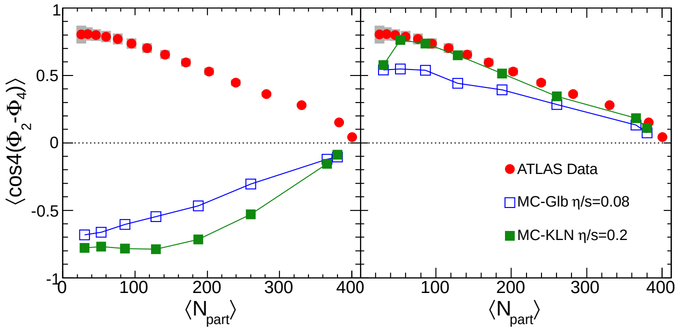

Figure 8.4: The measured $\langle \cos 4(\Phi_2\text{-}\Phi_4)\rangle$ correlatior compated to initial geometry models(left) and EbyE hydro simulations (right).

While all the five analyses presented here are independent measurements relying on different experimental techniques, they complement and supplement each other in terms of the physical conclusions that are drawn from them. Together they give a fairly complete picture of the collective phenomena in heavy-ion collisions.

8.2 Possible future flow analyses

At the end it is worthwhile to point out the analyses that are possible in the future starting from the foundation laid out in this work. Both the EbyE ane EP correlation measurements are the first of their kind in heavy-ion physics, and have considerable potential for future work, whereas the EP and 2PC measurements in have been around for quite some time and explored in detail. However they can be stil be extended to measure new quantities. For example the EP analysis can be extended to study mixed harmonics, such as v_4 in the Φ_2 plane:

$$v_{4,\Phi_2} = \langle \cos 4(\phi - \Phi_2) \rangle \tag{8.1}$$

where the subscript Φ_2 indicates that this is the v_4 measured in the Φ_2 plane (as opposed to the Φ_4 plane). The ratio of v_{4,Φ_2} and v_4 gives the correlation between Φ_2 and Φ_4:

$$\frac{v_{4,\Phi_2}}{v_4} = \langle \cos 4(\Phi_2 - \Phi_4) \rangle \tag{8.2}$$

and is an alternative way of measuring the two-plane correlations. However this method has the advantage that the correlations can be studied differentially as a function of p_{T}. This can be used as a check of the implicit assumption in all flow measurements of the constancy of the harmonic planes Ψ_n over the whole event, i.e. that the Φ_n are independent of the p_{T} of the measured particles. This assumption is largely valid as is seen by the good agreement between the 2PC v_n using mixed harmonics, where one does not explicitly determine the event-planes, and the v_n from the EP method. However as the flow measurements become more and more precise, this assumption needs to be explicitly checked and can be done by the above method. Hydro calculations that suggest such variations in Φ_n as a function of p_{T} already exist [132, 133]. Measurements of the mixed harmonics have been done previously at RHIC [73] for v_{4,Φ_2}, but they were not interpreted along the lines of event-plane correlations.

The EP and 2PC methods can also be extended to do event-shape-engineering (ESE) measurements proposed in [134] (also see [135]) where one cuts on the Q_n^{obs} in one detector and measures the v_k^{EP} or v_k^{2PC} in another detector for both $k = n$ and $k \neq n$. These observables would give information about the correlations between the magnitude of the v_n for different n. However there are two drawbacks: the first is that the evnts are divided into classes based on Q_n^{obs} in a detector rather than the true $\boldsymbol{Q}_n$ and the second is that the EP and 2PC methods loose some information on the fluctuations due to averaging over many events. However this method still improves our current understanding of flow correlations.

The future of most flow analyses seems to be going in the direction of identifying new observables that are sensitive to the detailed nature of fluctuations in the v_n, as in the EbyE analysis. It is difficult to extend the EbyE v_n measurements to be more differential in p_{T} and η that what has been presented here, as we are statistics limited by the number of particles in an event rather than by number of events. However they can be extended for ESE studies by measuring correlations between the magnitudes of different v_n, for example v_2-v_4 or v_2-v_3, on an EbyE basis. For the v_2-v_4 correlations, we expect events with larger v_2 to have larger v_4 based on the study of the event-plane correlations. Nominally the analysis would involve making a 2D distribution of v_2^{obs} vs v_4^{obs}(or v_3^{obs}) and then unfolding that with a data driven response function. The EbyE ESE measurements would not suffer from the drawbacks that were mentioned earlier for the EP and 2PC based ESE analyses[1]. However, the analysis would be complicated as it would require a 2D unfolding and be more susceptible to systematic as well as statistical errors than the 1D method used here. Another possibility would be to measure the EbyE v_4 and v_3 distributions in rather broad bins of v_2^{obs}. This would limit the unfolding to be one-dimensional but would have the disadvantage that the binning is in v_2^{obs} rather than the true v_2.

As described at the end of Section 3.2, a draw-back of the EP method is that it assumes that the event-plane resolution is the same for all events in a centrality class. which is not true when there are large EbyE fluctuations in the v_n. This also affects the event-plane correlation measurements. An improvement to the event-plane correlations measurement was described in [136], where it was suggested to define the observables as:

$$\langle\cos(c_1\Phi_1 + ... + lc_l\Phi_l)\rangle \rightarrow \frac{\langle v_1^{c_1} v_2^{c_2} ... \cos(c_1\Phi_1 + ... + lc_l\Phi_l)\rangle}{\langle v_1^{c_1} v_2^{c_2} ...\rangle} \tag{8.3}$$

$$\langle\cos 4(\Phi_2 - \Phi_4) = \frac{4(\Psi_2 - \Psi_4)}{\sqrt{(\Psi_2^A - \Psi_2^B)}}\rangle \tag{8.4}$$

where, the assertion was that the observable on the r.h.s. of the above equation can be measured in a detector independent manner (i.e. it would not depend on the resolution of the detector). This modified method is called the scalar-product method. This also requires making corresponding changes in the formulae for the raw measured signal and resolution correction as described in [136]. Figure 8.5 shows comparisons of the two-plane correlations measured in this work to the ones calculated by both methods in the AMPT ([137]) transport model. In general, only a small difference is seen between

---

[1] as the unfolding would give the correlations between the true v_n rather that the v_n^{obs} and by construction the EbyE measurements give the full distribution rather than the mean value as was the case for the 2PC and EP methods.

the two methods. However in the future, measurements via the scalar product method would be more beneficial for comparison with theory. Another possible improvement would be to study the correlations not only in bins to centrality but also in bins of v_n. This would further clarify the nature of the correlations by explicitly showing how the correlations change for fixed multiplicity (centrality) but changing v_n. This is similar in nature to the ESE measurements.

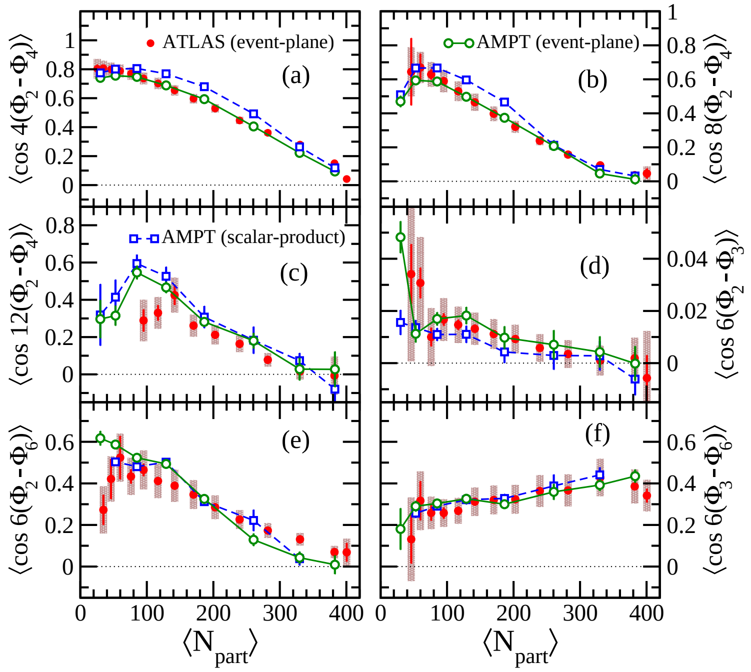

Figure 8.5: Two-plane correlations calculated in the in AMPT simulations of Pb+Pb collisions at $\sqrt{s_{NN}} = 2.76$ TeV. The red points corresponds to the ATLAS measurements (Chapter 6) the green and blue points are AMPT results via EP method and scalar-product method respectively. Figure taken from [136].

For the p+Pb data a wealth of new analyses are possible. The analysis done here was based only on ∼2 million min-bias events. In January of this year (2013) ATLAS recorded a much larger p+Pb dataset. The new data can be used to push the ridge analysis to higher multiplicities, and to measure higher order harmonics (a_n and c_n). The highest multiplicity p+Pb events have multiplicities comparable to the 65% central Pb+Pb events, allowing for the possibility to study EbyE v_2 distributions in p+Pb. The EbyE v_n and higher order harmonic measurements can determine the origin of the ridge, as to whether it comes from final state interactions (hydro) or from initial state effects (CGC).

All these possible measurements can extend the analyses done in this work to improve our understanding of both the initial geometry, and how the collective phenomena develop in heavy-ion collisions.

Bibliography

[1] E. V. Shuryak, "Theory of Hadronic Plasma," *Sov.Phys.JETP* **47** (1978) 212–219.

[2] E. V. Shuryak, "Quark-Gluon Plasma and Hadronic Production of Leptons, Photons and Psions," *Phys.Lett.* **B78** (1978) 150.

[3] E. Shuryak, "Quantum chromodynamics and the theory of superdense matter," *Physics Reports* **61** no. 2, (1980) 71–158.

[4] F. Karsch, E. Laermann, and A. Peikert, "The Pressure in two flavor, (2+1)-flavor and three flavor QCD," *Phys.Lett.* **B478** (2000) 447–455, `arXiv:hep-lat/0002003 [hep-lat]`.

[5] F. Karsch, "Lattice QCD at high temperature and density," *Lect.Notes Phys.* **583** (2002) 209–249, `arXiv:hep-lat/0106019 [hep-lat]`.

[6] A. Bazavov, T. Bhattacharya, M. Cheng, N. Christ, C. DeTar, *et al.*, "Equation of state and QCD transition at finite temperature," *Phys.Rev.* **D80** (2009) 014504, `arXiv:0903.4379 [hep-lat]`.

[7] Z. Fodor and S. Katz, "Critical point of QCD at finite T and mu, lattice results for physical quark masses," *JHEP* **0404** (2004) 050, `arXiv:hep-lat/0402006 [hep-lat]`.

[8] R. T. et al., "2007 Long Range Plan: The Frontiers of Nuclear Science, Report to the Nuclear Science Advisory Committee.,".

[9] **PHOBOS** Collaboration, B. Alver *et al.*, "System size, energy, pseudorapidity, and centrality dependence of elliptic flow," *Phys.Rev.Lett.* **98** (2007) 242302, `arXiv:nucl-ex/0610037 [nucl-ex]`.

[10] H. Heiselberg and A.-M. Levy, "Elliptic flow and hanbury-brown˘twiss correlations in noncentral nuclear collisions," *Phys. Rev. C* **59** (May, 1999) 2716–2727. `http://link.aps.org/doi/10.1103/PhysRevC.59.2716`.

[11] E. Iancu, "QCD in heavy ion collisions," `arXiv:1205.0579 [hep-ph]`.

[12] U. W. Heinz and P. F. Kolb, "Early thermalization at RHIC," *Nucl.Phys.* **A702** (2002) 269–280, `arXiv:hep-ph/0111075 [hep-ph]`.

[13] **PHENIX** Collaboration, A. Adare *et al.*, "Detailed measurement of the e^+e^- pair continuum in $p+p$ and Au+Au collisions at $\sqrt{s_{\rm NN}} = 200$ GeV and implications for direct photon production," *Phys.Rev.* **C81** (2010) 034911, `arXiv:0912.0244 [nucl-ex]`.

[14] D. Teaney, "The Effects of viscosity on spectra, elliptic flow, and HBT radii," *Phys.Rev.* **C68** (2003) 034913, `arXiv:nucl-th/0301099 [nucl-th]`.

[15] P. Romatschke and U. Romatschke, "Viscosity Information from Relativistic Nuclear Collisions: How Perfect is the Fluid Observed at RHIC?," *Phys.Rev.Lett.* **99** (2007) 172301, `arXiv:0706.1522 [nucl-th]`.

[16] H. Song, S. A. Bass, U. Heinz, T. Hirano, and C. Shen, "Hadron spectra and elliptic flow for 200 A GeV Au+Au collisions from viscous hydrodynamics coupled to a Boltzmann cascade," *Phys.Rev.* **C83** (2011) 054910, `arXiv:1101.4638 [nucl-th]`.

[17] **PHENIX** Collaboration, K. Adcox *et al.*, "Flow measurements via two particle azimuthal correlations in Au+Au collisions at $\sqrt{s_{\rm NN}} =$ 130 GeV," *Phys.Rev.Lett.* **89** (2002) 212301, `arXiv:nucl-ex/0204005 [nucl-ex]`.

[18] **STAR** Collaboration, J. Adams *et al.*, "Evidence from d + Au measurements for final state suppression of high p(T) hadrons in Au+Au collisions at RHIC," *Phys.Rev.Lett.* **91** (2003) 072304, `arXiv:nucl-ex/0306024 [nucl-ex]`.

[19] **PHENIX** Collaboration, S. Adler *et al.*, "Dense-Medium Modifications to Jet-Induced Hadron Pair Distributions in Au+Au Collisions at $\sqrt{s_{\rm NN}}$= 200 GeV," *Phys.Rev.Lett.* **97** (2006) 052301, `arXiv:nucl-ex/0507004 [nucl-ex]`.

[20] **ATLAS** Collaboration, G. Aad *et al.*, "Observation of a Centrality-Dependent Dijet Asymmetry in Lead-Lead Collisions at $\sqrt{s_{\rm NN}} = 2.77$ TeV with the ATLAS Detector at the LHC," *Phys.Rev.Lett.* **105** (2010) 252303, `arXiv:1011.6182 [hep-ex]`.

[21] **CMS** Collaboration, S. Chatrchyan *et al.*, "Observation and studies of jet quenching in PbPb collisions at nucleon-nucleon center-of-mass energy = 2.76 TeV," *Phys.Rev.* **C84** (2011) 024906, `arXiv:1102.1957 [nucl-ex]`.

[22] **ATLAS** Collaboration, G. Aad *et al.*, "Measurement of the jet radius and transverse momentum dependence of inclusive jet suppression in lead-lead collisions at $\sqrt{s_{\mathrm{NN}}}$= 2.76 TeV with the ATLAS detector," *Phys.Lett.* **B719** (2013) 220–241, `arXiv:1208.1967 [hep-ex]`.

[23] **PHENIX** Collaboration, A. Adare *et al.*, "Scaling properties of azimuthal anisotropy in Au+Au and Cu+Cu collisions at s(NN) = 200-GeV," *Phys.Rev.Lett.* **98** (2007) 162301, `arXiv:nucl-ex/0608033 [nucl-ex]`.

[24] **STAR Collaboration** Collaboration, K. Ackermann *et al.*, "Elliptic flow in Au + Au collisions at (S(NN))**(1/2) = 130 GeV," *Phys.Rev.Lett.* **86** (2001) 402–407, `arXiv:nucl-ex/0009011 [nucl-ex]`.

[25] **PHENIX** Collaboration, K. Adcox *et al.*, "Formation of dense partonic matter in relativistic nucleus-nucleus collisions at RHIC: Experimental evaluation by the PHENIX collaboration," *Nucl.Phys.* **A757** (2005) 184–283, `arXiv:nucl-ex/0410003 [nucl-ex]`.

[26] B. Back, M. Baker, M. Ballintijn, D. Barton, B. Becker, *et al.*, "The PHOBOS perspective on discoveries at RHIC," *Nucl.Phys.* **A757** (2005) 28–101, `arXiv:nucl-ex/0410022 [nucl-ex]`.

[27] **BRAHMS** Collaboration, I. Arsene *et al.*, "Quark gluon plasma and color glass condensate at RHIC? The Perspective from the BRAHMS experiment," *Nucl.Phys.* **A757** (2005) 1–27, `arXiv:nucl-ex/0410020 [nucl-ex]`.

[28] P. Huovinen, P. Kolb, U. W. Heinz, P. Ruuskanen, and S. Voloshin, "Radial and elliptic flow at RHIC: Further predictions," *Phys.Lett.* **B503** (2001) 58–64, `arXiv:hep-ph/0101136 [hep-ph]`.

[29] M. Luzum and P. Romatschke, "Conformal Relativistic Viscous Hydrodynamics: Applications to RHIC results at s(NN)**(1/2) = 200-GeV," *Phys.Rev.* **C78** (2008) 034915, `arXiv:0804.4015 [nucl-th]`.

[30] G. Policastro, D. Son, and A. Starinets, "The Shear viscosity of strongly coupled N=4 supersymmetric Yang-Mills plasma," *Phys.Rev.Lett.* **87** (2001) 081601, `arXiv:hep-th/0104066 [hep-th]`.

[31] P. Kovtun, D. Son, and A. Starinets, "Viscosity in strongly interacting quantum field theories from black hole physics," *Phys.Rev.Lett.* **94** (2005) 111601, `arXiv:hep-th/0405231 [hep-th]`.

[32] **STAR** Collaboration, B. Abelev *et al.*, "Centrality dependence of charged hadron and strange hadron elliptic flow from $\sqrt{s_{\mathrm{NN}}}$=200 GeV Au+Au collisions," *Phys.Rev.* **C77** (2008) 054901, `arXiv:0801.3466 [nucl-ex]`.

[33] R. J. Glauber, "Cross sections in deuterium at high energies," *Phys. Rev.* **100** (Oct, 1955) 242–248. `http://link.aps.org/doi/10.1103/PhysRev.100.242`.

[34] E. Iancu and R. Venugopalan, "The Color glass condensate and high-energy scattering in QCD," `arXiv:hep-ph/0303204 [hep-ph]`.

[35] A. Shor, "ϕ-Meson Production as a Probe of the Quark-Gluon Plasma," *Phys. Rev. Lett.* **54** (Mar, 1985) 1122–1125. `http://link.aps.org/doi/10.1103/PhysRevLett.54.1122`.

[36] **PHENIX** Collaboration, S. Afanasiev *et al.*, "Elliptic flow for phi mesons and (anti)deuterons in Au + Au collisions at $\sqrt{s_{\mathrm{NN}}}$=200 GeV," *Phys.Rev.Lett.* **99** (2007) 052301, `arXiv:nucl-ex/0703024 [NUCL-EX]`.

[37] **PHENIX Collaboration** Collaboration, A. Adare *et al.*, "Suppression pattern of neutral pions at high transverse momentum in Au + Au collisions at s(NN)**(1/2) = 200-GeV and constraints on medium transport coefficients," *Phys.Rev.Lett.* **101** (2008) 232301, `arXiv:0801.4020 [nucl-ex]`.

[38] **PHENIX** Collaboration, A. Adare *et al.*, "Transverse momentum dependence of meson suppression η suppression in Au+Au collisions at $\sqrt{s_{\mathrm{NN}}}$ =200 GeV," *Phys.Rev.* **C82** (2010) 011902, `arXiv:1005.4916 [nucl-ex]`.

[39] **PHENIX** Collaboration, A. Adare *et al.*, "Identified charged hadron production in $p+p$ collisions at $\sqrt{s}$=200 and 62.4 GeV," *Phys.Rev.* **C83** (2011) 064903, `arXiv:1102.0753 [nucl-ex]`.

[40] A. Adare, S. Afanasiev, C. Aidala, N. Ajitanand, Y. Akiba, *et al.*, "Production of ω mesons in $p+p$, d+Au, Cu+Cu, and Au+Au collisions at $\sqrt{s_{\mathrm{NN}}}$=200 GeV," *Phys.Rev.* **C84** (2011) 044902, `arXiv:1105.3467 [nucl-ex]`.

[41] **PHENIX Collaboration** Collaboration, S. Afanasiev *et al.*, "Measurement of Direct Photons in Au+Au Collisions at $\sqrt{s_{NN}} = 200$ GeV," *Phys.Rev.Lett.* **109** (2012) 152302, `arXiv:1205.5759 [nucl-ex]`.

[42] B. Alver and G. Roland, "Collision geometry fluctuations and triangular flow in heavy-ion collisions," *Phys.Rev.* **C81** (2010) 054905, `arXiv:1003.0194 [nucl-th]`.

[43] S. A. Voloshin, A. M. Poskanzer, and R. Snellings, "Collective phenomena in non-central nuclear collisions," `arXiv:0809.2949 [nucl-ex]`.

[44] S. A. Voloshin, A. M. Poskanzer, A. Tang, and G. Wang, "Elliptic flow in the Gaussian model of eccentricity fluctuations," *Phys.Lett.* **B659** (2008) 537–541, `arXiv:0708.0800 [nucl-th]`.

[45] B. H. Alver, C. Gombeaud, M. Luzum, and J.-Y. Ollitrault, "Triangular flow in hydrodynamics and transport theory," *Phys.Rev.* **C82** (2010) 034913, `arXiv:1007.5469 [nucl-th]`.

[46] D. Teaney and L. Yan, "Triangularity and Dipole Asymmetry in Heavy Ion Collisions," *Phys.Rev.* **C83** (2011) 064904, `arXiv:1010.1876 [nucl-th]`.

[47] F. G. Gardim, F. Grassi, M. Luzum, and J.-Y. Ollitrault, "Mapping the hydrodynamic response to the initial geometry in heavy-ion collisions," *Phys.Rev.* **C85** (2012) 024908, `arXiv:1111.6538 [nucl-th]`.

[48] N. Borghini, P. M. Dinh, and J.-Y. Ollitrault, "A New method for measuring azimuthal distributions in nucleus-nucleus collisions," *Phys.Rev.* **C63** (2001) 054906, `arXiv:nucl-th/0007063 [nucl-th]`.

[49] N. Borghini, R. Bhalerao, and J. Ollitrault, "Anisotropic flow from Lee-Yang zeroes: A Practical guide," *J.Phys.* **G30** (2004) S1213–S1216, `arXiv:nucl-th/0402053 [nucl-th]`.

[50] B. Schenke, S. Jeon, and C. Gale, "Elliptic and triangular flow in event-by-event (3+1)D viscous hydrodynamics," *Phys.Rev.Lett.* **106** (2011) 042301, `arXiv:1009.3244 [hep-ph]`.

[51] B. Schenke, S. Jeon, and C. Gale, "Anisotropic flow in $\sqrt{s} = 2.76$ TeV Pb+Pb collisions at the LHC," *Phys.Lett.* **B702** (2011) 59–63, `arXiv:1102.0575 [hep-ph]`.

[52] Z. Qiu and U. W. Heinz, "Event-by-event shape and flow fluctuations of relativistic heavy-ion collision fireballs," *Phys.Rev.* **C84** (2011) 024911, `arXiv:1104.0650 [nucl-th]`.

[53] M. L. Miller, K. Reygers, S. J. Sanders, and P. Steinberg, "Glauber modeling in high energy nuclear collisions," *Ann.Rev.Nucl.Part.Sci.* **57** (2007) 205–243, `arXiv:nucl-ex/0701025 [nucl-ex]`.

[54] **CMS** Collaboration, V. Khachatryan *et al.*, "Observation of Long-Range Near-Side Angular Correlations in Proton-Proton Collisions at the LHC," *JHEP* **1009** (2010) 091, `arXiv:1009.4122 [hep-ex]`.

[55] L. Evans and P. Bryant, "LHC Machine," *JINST* **3** (2008) S08001.

[56] **ATLAS** Collaboration, G. Aad *et al.*, "The ATLAS Experiment at the CERN Large Hadron Collider," *JINST* **3** (2008) S08003.

[57] D. Kharzeev and M. Nardi, "Hadron production in nuclear collisions at RHIC and high density QCD," *Phys.Lett.* **B507** (2001) 121–128, `arXiv:nucl-th/0012025 [nucl-th]`.

[58] **ATLAS** Collaboration, G. Aad *et al.*, "Measurement of the centrality dependence of the charged particle pseudorapidity distribution in lead-lead collisions at $\sqrt{s_{NN}} = 2.76$ TeV with the ATLAS detector," *Phys.Lett.* **B710** (2012) 363–382, `arXiv:1108.6027 [hep-ex]`.

[59] **ATLAS** Collaboration, G. Aad *et al.*, "Charged-particle multiplicities in pp interactions at $\sqrt{s} = 900$ GeV measured with the ATLAS detector at the LHC," *Phys.Lett.* **B688** (2010) 21–42, `arXiv:1003.3124 [hep-ex]`.

[60] **ATLAS** Collaboration, "Measurement of the centrality dependence of charged particle spectra and $\mathrm{R_{CP}}$ in lead-lead collisions at $\sqrt{s_{\mathrm{NN}}} =$ 2.76 TeV with the ATLAS detector at the LHC," Tech. Rep. ATLAS-CONF-2011-079, CERN, Geneva, Jun, 2011.

[61] A. M. Poskanzer and S. Voloshin, "Methods for analyzing anisotropic flow in relativistic nuclear collisions," *Phys.Rev.* **C58** (1998) 1671–1678, `arXiv:nucl-ex/9805001 [nucl-ex]`.

[62] J.-Y. Ollitrault, "On the measurement of azimuthal anisotropies in nucleus-nucleus collisions," `arXiv:nucl-ex/9711003 [nucl-ex]`.

[63] **ATLAS** Collaboration, G. Aad *et al.*, "Measurement of the azimuthal anisotropy for charged particle production in $\sqrt{s_{\mathrm{NN}}} = 2.76$ TeV lead-lead collisions with the ATLAS detector," *Phys.Rev.* **C86** (2012) 014907, `arXiv:1203.3087 [hep-ex]`.

[64] **PHENIX** Collaboration, S. Afanasiev *et al.*, "Systematic Studies of Elliptic Flow Measurements in Au+Au Collisions at $\sqrt{s_{\mathrm{NN}}} =$ 200-GeV," *Phys.Rev.* **C80** (2009) 024909, `arXiv:0905.1070 [nucl-ex]`.

[65] **E877** Collaboration, J. Barrette *et al.*, "Proton and pion production relative to the reaction plane in Au + Au collisions at AGS energies," *Phys.Rev.* **C56** (1997) 3254–3264, `arXiv:nucl-ex/9707002 [nucl-ex]`.

[66] B. Alver, B. Back, M. Baker, M. Ballintijn, D. Barton, *et al.*, "Importance of correlations and fluctuations on the initial source eccentricity in high-energy nucleus-nucleus collisions," *Phys.Rev.* **C77** (2008) 014906, `arXiv:0711.3724 [nucl-ex]`.

[67] J.-Y. Ollitrault, A. M. Poskanzer, and S. A. Voloshin, "Effect of flow fluctuations and nonflow on elliptic flow methods," *Phys.Rev.* **C80** (2009) 014904, `arXiv:0904.2315 [nucl-ex]`.

[68] **PHENIX** Collaboration, A. Adare *et al.*, "Azimuthal anisotropy of neutral pion production in Au+Au collisions at $\sqrt{(s_N N)} = 200$ GeV: Path-length dependence of jet quenching and the role of initial geometry," *Phys.Rev.Lett.* **105** (2010) 142301, `arXiv:1006.3740 [nucl-ex]`.

[69] **STAR** Collaboration, J. Adams *et al.*, "Azimuthal anisotropy and correlations at large transverse momenta in p+p and Au+Au collisions at $\sqrt{s_{\mathrm{NN}}}$=200 GeV," *Phys.Rev.Lett.* **93** (2004) 252301, `arXiv:nucl-ex/0407007 [nucl-ex]`.

[70] M. Gyulassy, I. Vitev, and X. Wang, "High p(T) azimuthal asymmetry in noncentral A+A at RHIC," *Phys.Rev.Lett.* **86** (2001) 2537–2540, `arXiv:nucl-th/0012092 [nucl-th]`.

[71] B. Betz, M. Gyulassy, and G. Torrieri, "Fourier Harmonics of High-pT Particles Probing the Fluctuating Intitial Condition Geometries in

Heavy-Ion Collisions," *Phys.Rev.* **C84** (2011) 024913, `arXiv:1102.5416 [nucl-th]`.

[72] **STAR** Collaboration, J. Adams *et al.*, "Azimuthal anisotropy at RHIC: The First and fourth harmonics," *Phys.Rev.Lett.* **92** (2004) 062301, `arXiv:nucl-ex/0310029 [nucl-ex]`.

[73] **PHENIX** Collaboration, A. Adare *et al.*, "Elliptic and hexadecapole flow of charged hadrons in Au+Au collisions at $\sqrt{s_{NN}} = 200$ GeV," *Phys.Rev.Lett.* **105** (2010) 062301, `arXiv:1003.5586 [nucl-ex]`.

[74] B. Schenke, P. Tribedy, and R. Venugopalan, "Fluctuating Glasma initial conditions and flow in heavy ion collisions," *Phys.Rev.Lett.* **108** (2012) 252301, `arXiv:1202.6646 [nucl-th]`.

[75] B. Schenke, P. Tribedy, and R. Venugopalan, "Event-by-event gluon multiplicity, energy density, and eccentricities in ultrarelativistic heavy-ion collisions," *Phys.Rev.* **C86** (2012) 034908, `arXiv:1206.6805 [hep-ph]`.

[76] C. Gale, S. Jeon, B. Schenke, P. Tribedy, and R. Venugopalan, "Event-by-event anisotropic flow in heavy-ion collisions from combined Yang-Mills and viscous fluid dynamics," *Phys.Rev.Lett.* **110** (2013) 012302, `arXiv:1209.6330 [nucl-th]`.

[77] **STAR** Collaboration, B. Abelev *et al.*, "Long range rapidity correlations and jet production in high energy nuclear collisions," *Phys.Rev.* **C80** (2009) 064912, `arXiv:0909.0191 [nucl-ex]`.

[78] **PHOBOS** Collaboration, B. Alver *et al.*, "High transverse momentum triggered correlations over a large pseudorapidity acceptance in Au+Au collisions at $\sqrt{s_{\rm NN}} = 200$ GeV," *Phys.Rev.Lett.* **104** (2010) 062301, `arXiv:0903.2811 [nucl-ex]`.

[79] **PHENIX** Collaboration, A. Adare *et al.*, "Dihadron azimuthal correlations in Au+Au collisions at $\sqrt{s_{NN}} = 200$ GeV," *Phys.Rev.* **C78** (2008) 014901, `arXiv:0801.4545 [nucl-ex]`.

[80] J. Casalderrey-Solana, E. Shuryak, and D. Teaney, "Conical flow induced by quenched QCD jets," *J.Phys.Conf.Ser.* **27** (2005) 22–31, `arXiv:hep-ph/0411315 [hep-ph]`.

[81] N. Borghini, P. M. Dinh, and J.-Y. Ollitrault, "Are flow measurements at SPS reliable?," *Phys.Rev.* **C62** (2000) 034902, `arXiv:nucl-th/0004026 [nucl-th]`.

[82] N. Borghini, P. Dinh, J.-Y. Ollitrault, A. M. Poskanzer, and S. Voloshin, "Effects of momentum conservation on the analysis of anisotropic flow," *Phys.Rev.* **C66** (2002) 014901, `arXiv:nucl-th/0202013 [nucl-th]`.

[83] P. Staig and E. Shuryak, "The Fate of the Initial State Fluctuations in Heavy Ion Collisions. III The Second Act of Hydrodynamics," *Phys.Rev.* **C84** (2011) 044912, `arXiv:1105.0676 [nucl-th]`.

[84] U. W. Heinz and R. Snellings, "Collective flow and viscosity in relativistic heavy-ion collisions," `arXiv:1301.2826 [nucl-th]`.

[85] M. Luzum and J.-Y. Ollitrault, "Directed flow at midrapidity in heavy-ion collisions," *Phys.Rev.Lett.* **106** (2011) 102301, `arXiv:1011.6361 [nucl-ex]`.

[86] N. Borghini, "Momentum conservation and correlation analyses in heavy-ion collisions at ultrarelativistic energies," *Phys.Rev.* **C75** (2007) 021904, `arXiv:nucl-th/0612093 [nucl-th]`.

[87] F. G. Gardim, F. Grassi, Y. Hama, M. Luzum, and J.-Y. Ollitrault, "Directed flow at mid-rapidity in event-by-event hydrodynamics," *Phys.Rev.* **C83** (2011) 064901, `arXiv:1103.4605 [nucl-th]`.

[88] J. Jia, S. K. Radhakrishnan, and S. Mohapatra, "A study of the anisotropy associated with dipole asymmetry in heavy ion collisions," `arXiv:1203.3410 [nucl-th]`.

[89] **PHOBOS** Collaboration, B. Back *et al.*, "Energy dependence of directed flow over a wide range of pseudorapidity in Au + Au collisions at RHIC," *Phys.Rev.Lett.* **97** (2006) 012301, `arXiv:nucl-ex/0511045 [nucl-ex]`.

[90] **STAR** Collaboration, B. Abelev *et al.*, "System-size independence of directed flow at the Relativistic Heavy-Ion Collider," *Phys.Rev.Lett.* **101** (2008) 252301, `arXiv:0807.1518 [nucl-ex]`.

[91] I. Selyuzhenkov, "Charged particle directed flow in Pb-Pb collisions at $\sqrt{s_{\mathrm{NN}}} = 2.76$ TeV measured with ALICE at the LHC," *J.Phys.* **G38** (2011) 124167, `arXiv:1106.5425 [nucl-ex]`.

[92] **ALICE** Collaboration, R. Preghenella, "Transverse momentum spectra of identified charged hadrons with the ALICE detector in Pb-Pb collisions at $\sqrt{s_{NN}} = 2.76$ TeV," *PoS* **EPS-HEP2011** (2011) 118, `arXiv:1111.0763 [nucl-ex]`.

[93] R. S. Bhalerao and J.-Y. Ollitrault, "Eccentricity fluctuations and elliptic flow at RHIC," *Phys.Lett.* **B641** (2006) 260–264, `arXiv:nucl-th/0607009 [nucl-th]`.

[94] W. Broniowski, P. Bozek, and M. Rybczynski, "Fluctuating initial conditions in heavy-ion collisions from the Glauber approach," *Phys.Rev.* **C76** (2007) 054905, `arXiv:0706.4266 [nucl-th]`.

[95] **PHOBOS** Collaboration, B. Alver *et al.*, "Event-by-Event Fluctuations of Azimuthal Particle Anisotropy in Au + Au Collisions at $\sqrt{s_{\mathrm{NN}}} = 200$ GeV," *Phys.Rev.Lett.* **104** (2010) 142301, `arXiv:nucl-ex/0702036 [nucl-ex]`.

[96] **ALICE** Collaboration, B. Abelev *et al.*, "Anisotropic flow of charged hadrons, pions and (anti-)protons measured at high transverse momentum in Pb-Pb collisions at $\sqrt{s_{\mathrm{NN}}}$=2.76 TeV," *Phys.Lett.B* **719** (2013) 18–28, `arXiv:1205.5761 [nucl-ex]`.

[97] **ATLAS** Collaboration, "Measurement of the elliptic flow with multi-particle cumulants in lead-lead collisions at $\sqrt{s_{\mathrm{NN}}} = 2.76$ TeV with the ATLAS detector at the LHC," Tech. Rep. ATLAS-CONF-2012-118, CERN, Geneva, Aug, 2012.

[98] R. Snellings, "Anisotropic flow at the LHC measured with the ALICE detector," *J.Phys.* **G38** (2011) 124013, `arXiv:1106.6284 [nucl-ex]`.

[99] **STAR** Collaboration, J. Adams *et al.*, "Azimuthal anisotropy in Au+Au collisions at $\sqrt{s_{\mathrm{NN}}}$ =200 GeV," *Phys.Rev.* **C72** (2005) 014904, `arXiv:nucl-ex/0409033 [nucl-ex]`.

[100] **ALICE** Collaboration, A. Bilandzic, "Anisotropic flow of charged particles at $\sqrt{s_{\mathrm{NN}}}$=2.76 TeV measured with the ALICE detector," *J.Phys.* **G38** (2011) 124052, `arXiv:1106.6209 [nucl-ex]`.

[101] **ATLAS** Collaboration, G. Aad *et al.*, "Measurement of the distributions of event-by-event flow harmonics in lead–lead collisions at $\sqrt{s_{NN}}$=2.76 TeV with the ATLAS detector at the LHC," `arXiv:1305.2942 [hep-ex]`.

[102] J. Jia and S. Mohapatra, "Disentangling flow and nonflow correlations via Bayesian unfolding of the event-by-event distributions of harmonic coefficients in ultrarelativistic heavy-ion collisions," *Phys Rev C. 75.* **031901** (2013) , `arXiv:1304.1471 [nucl-ex]`.

[103] G. D'Agostini, "A Multidimensional unfolding method based on Bayes' theorem," *Nucl.Instrum.Meth.* **A362** (1995) 487–498.

[104] T. Adye, K. Tackmann, and F. Wilson, "http://hepunx.rl.ac.uk/adye/software/unfold/RooUnfold.html,".

[105] H.-J. Drescher, A. Dumitru, A. Hayashigaki, and Y. Nara, "The Eccentricity in heavy-ion collisions from color glass condensate initial conditions," *Phys.Rev.* **C74** (2006) 044905, `arXiv:nucl-th/0605012 [nucl-th]`.

[106] **CMS Collaboration** Collaboration, S. Chatrchyan *et al.*, "Measurement of the elliptic anisotropy of charged particles produced in PbPb collisions at nucleon-nucleon center-of-mass energy = 2.76 TeV," *Phys.Rev.* **C87** (2013) 014902, `arXiv:1204.1409 [nucl-ex]`.

[107] H. Niemi, G. Denicol, H. Holopainen, and P. Huovinen, "Event-by-event distributions of azimuthal asymmetries in ultrarelativistic heavy-ion collisions," `arXiv:1212.1008 [nucl-th]`.

[108] C. Gale, S. Jeon, and B. Schenke, "Hydrodynamic Modeling of Heavy-Ion Collisions," *Int.J.Mod.Phys.* **A28** (2013) 1340011, `arXiv:1301.5893 [nucl-th]`.

[109] D. Teaney and L. Yan, "Non linearities in the harmonic spectrum of heavy ion collisions with ideal and viscous hydrodynamics," *Phys.Rev.* **C86** (2012) 044908, `arXiv:1206.1905 [nucl-th]`.

[110] **ALICE** Collaboration, K. Aamodt *et al.*, "Higher harmonic anisotropic flow measurements of charged particles in Pb-Pb collisions at $\sqrt{s_{\rm NN}}$=2.76 TeV," *Phys.Rev.Lett.* **107** (2011) 032301, `arXiv:1105.3865 [nucl-ex]`.

[111] R. Bhalerao, M. Luzum, and J. Ollitrault, "New flow observables," *J.Phys.* **G38** (2011) 124055, `arXiv:1106.4940 [nucl-ex]`.

[112] R. S. Bhalerao, M. Luzum, and J.-Y. Ollitrault, "Determining initial-state fluctuations from flow measurements in heavy-ion collisions," *Phys.Rev.* **C84** (2011) 034910, `arXiv:1104.4740 [nucl-th]`.

[113] J. Jia and S. Mohapatra, "A Method for studying initial geometry fluctuations via event plane correlations in heavy ion collisions," *Eur. Phys. J. C73,* **2510** (2013) , `arXiv:1203.5095 [nucl-th]`.

[114] J. Jia and D. Teaney, "Study on initial geometry fluctuations via participant plane correlations in heavy ion collisions: part II," `arXiv:1205.3585 [nucl-ex]`.

[115] **ATLAS** Collaboration, "Measurement of reaction plane correlations in pb-pb collisions at $\sqrt{s_{\mathrm{NN}}}$=2.76 tev," Tech. Rep. ATLAS-CONF-2012-049, CERN, Geneva, May, 2012.

[116] Z. Qiu and U. Heinz, "Hydrodynamic event-plane correlations in Pb+Pb collisions at $\sqrt{s} = 2.76$ATeV," *Phys.Lett.* **B717** (2012) 261–265, `arXiv:1208.1200 [nucl-th]`.

[117] D. Teaney and L. Yan, "Non-linear flow response and reaction plane correlations," *Nucl.Phys.A904-905* **2013** (2013) 365c–368c, `arXiv:1210.5026 [nucl-th]`.

[118] A. Dumitru, K. Dusling, F. Gelis, J. Jalilian-Marian, T. Lappi, *et al.*, "The Ridge in proton-proton collisions at the LHC," *Phys.Lett.* **B697** (2011) 21–25, `arXiv:1009.5295 [hep-ph]`.

[119] M. Diehl and A. Schafer, "Theoretical considerations on multiparton interactions in QCD," *Phys.Lett.* **B698** (2011) 389–402, `arXiv:1102.3081 [hep-ph]`.

[120] A. Kovner and M. Lublinsky, "Angular Correlations in Gluon Production at High Energy," *Phys.Rev.* **D83** (2011) 034017, `arXiv:1012.3398 [hep-ph]`.

[121] T. Altinoluk and A. Kovner, "Particle Production at High Energy and Large Transverse Momentum - 'The Hybrid Formalism' Revisited," *Phys.Rev.* **D83** (2011) 105004, `arXiv:1102.5327 [hep-ph]`.

[122] K. Dusling and R. Venugopalan, "Azimuthal collimation of long range rapidity correlations by strong color fields in high multiplicity hadron-hadron collisions," *Phys.Rev.Lett.* **108** (2012) 262001, `arXiv:1201.2658 [hep-ph]`.

[123] E. Levin and A. H. Rezaeian, "The Ridge from the BFKL evolution and beyond," *Phys.Rev.* **D84** (2011) 034031, `arXiv:1105.3275 [hep-ph]`.

[124] M. Strikman, "Transverse Nucleon Structure and Multiparton Interactions," *Acta Phys.Polon.* **B42** (2011) 2607–2630, `arXiv:1112.3834 [hep-ph]`.

[125] J. Casalderrey-Solana and U. A. Wiedemann, "Eccentricity fluctuations make flow measurable in high multiplicity p-p collisions," *Phys.Rev.Lett.* **104** (2010) 102301, `arXiv:0911.4400 [hep-ph]`.

[126] E. Shuryak, "Comments on the CMS discovery of the 'Ridge' in High Multiplicity pp collisions at LHC," `arXiv:1009.4635 [hep-ph]`.

[127] K. Werner, I. Karpenko, and T. Pierog, "The 'Ridge' in Proton-Proton Scattering at 7 TeV," *Phys.Rev.Lett.* **106** (2011) 122004, `arXiv:1011.0375 [hep-ph]`.

[128] P. Bozek, "Elliptic flow in proton-proton collisions at $\sqrt{s} = 7$ TeV," *Eur.Phys.J.* **C71** (2011) 1530, `arXiv:1010.0405 [hep-ph]`.

[129] P. Bozek, "Collective flow in p-Pb and d-Pd collisions at TeV energies," *Phys.Rev.* **C85** (2012) 014911, `arXiv:1112.0915 [hep-ph]`.

[130] **ATLAS** Collaboration, G. Aad *et al.*, "Observation of Associated Near-side and Away-side Long-range Correlations in $\sqrt{s_{\rm NN}}$=5.02 TeV Proton-lead Collisions with the ATLAS Detector," *Phys.Rev.Lett.* **110** (2013) 182302, `arXiv:1212.5198 [hep-ex]`.

[131] K. Dusling and R. Venugopalan, "Comparison of the Color Glass Condensate to di-hadron correlations in proton-proton and proton-nucleus collisions," `arXiv:1302.7018 [hep-ph]`.

[132] F. G. Gardim, F. Grassi, M. Luzum, and J.-Y. Ollitrault, "Breaking of factorization of two-particle correlations in hydrodynamics," *Phys.Rev.* **C87** (2012) 031901, `arXiv:1211.0989 [nucl-th]`.

[133] U. W. Heinz, Z. Qiu, and C. Shen, "Fluctuating flow angles and anisotropic flow measurements," *Phys.Rev.* **C87** (2013) 034913, `arXiv:1302.3535 [nucl-th]`.

[134] J. Schukraft, A. Timmins, and S. A. Voloshin, "Ultra-relativistic nuclear collisions: event shape engineering," *Phys.Lett.* **B719** (2013) 394–398, `arXiv:1208.4563 [nucl-ex]`.

[135] **ALICE** Collaboration, A. Dobrin, "Event shape engineering with ALICE," *Nucl.Phys.A904-905* **2013** (2013) 455c–458c, `arXiv:1211.5348 [nucl-ex]`.

[136] R. S. Bhalerao, J.-Y. Ollitrault, and S. Pal, "Event-plane correlators," `arXiv:1307.0980 [nucl-th]`.

[137] Z.-W. Lin, C. M. Ko, B.-A. Li, B. Zhang, and S. Pal, "A Multi-phase transport model for relativistic heavy ion collisions," *Phys.Rev.* **C72** (2005) 064901, `arXiv:nucl-th/0411110 [nucl-th]`.

[138] M. Gyulassy and X.-N. Wang, "HIJING 1.0: A Monte Carlo program for parton and particle production in high-energy hadronic and nuclear collisions," *Comput.Phys.Commun.* **83** (1994) 307, `arXiv:nucl-th/9502021 [nucl-th]`.

Appendix A

Event plane analysis

A.1 Methodology

A.1.1 Determining the event-plane angles

Here the method used for determining the event-plane angles is described. The measured anisotropy in a given detector, where the EP angle is estimated, can be expressed as a Fourier series:

$$\begin{aligned}2\pi dN/d\phi &= Q_0 + \sum_n \left(2Q_{x,n}\cos n\phi + 2Q_{y,n}\sin n\phi\right)\\ &= Q_0 + \sum_n 2Q_n \cos n(\phi - \Psi_n), \\ &= Q_0(1 + \sum_n 2v_n^{\mathrm{obs}} \cos n(\phi - \Psi_n)),\end{aligned} \tag{A.1}$$

with

$$\begin{aligned}&Q_{x,n} = \sum_i w_i \cos n\phi_i,\ Q_{y,n} = \sum_i w_i \sin n\phi_i,\\ &Q_n^2 = Q_{x,n}^2 + Q_{y,n}^2,\ \Psi_n = \frac{1}{n}\tan^{-1}\left(\frac{Q_{y,n}}{Q_{x,n}}\right),\end{aligned} \tag{A.2}$$

where, w_i is the appropriate weight for each detector channel, (number of charged particles, or total transverse energy) and Ψ_n is the measured n^{th} order event-plane defined by the n^{th} order flow vector

A.1.2 Event-plane resolution

Due to finite statistics in the determination of the event-plane (or Q-vector), the measured event-plane is different than the true event-plane. The following derivation shows how the difference between the true event-plane and the observed event-plane affects the measured flow harmonics and how the measured harmonics can be corrected. The true n^{th} order event-plane is denoted by Φ_n and the observed event-plane by Ψ_n. The distribution of particles about the true event-plane is given as:

$$2\pi dN/d\phi \quad = \quad N_0 \left(1 + 2\sum_{n'=1}^{\infty} v_{n'} \cos(n'(\phi - \Phi_{n'}))\right) \tag{A.3}$$

However as the measured n^{th} order event-plane is Ψ_n, the observed v_n is calculated by the distribution of particles about the Ψ_n as:

$$v_n^{\text{obs}} = \langle \cos(n(\phi - \Psi_n)) dN/d\phi \rangle = v_n \cos(n(\Psi_n - \Phi_n)) \tag{A.4}$$

where, $\langle ... \rangle$ implies averaging over all tracks and Eq. A.3 is substituted for $dN/d\phi$. The Last equality in Eq. A.4 follows from the conditions:

$$\begin{aligned} \int_0^{2\pi} \cos(n(\phi - \Psi_n)) \cos(n'(\phi - \Phi_{n'})) d\phi &= \pi \delta_{n,n'} \cos(n(\Psi_n - \Phi_{n'})), \\ \int_0^{2\pi} \cos(n(\phi - \Psi_n)) d\phi &= 0 \end{aligned} \tag{A.5}$$

where, $\delta_{n,n'}$ is the Kronecker delta function. Averaging Eq. A.4 over many events gives[1]:

$$\langle v_n^{\text{obs}} \rangle_{\text{events}} = \langle v_n \cos(n(\Psi_n - \Phi_n)) \rangle_{\text{events}} \tag{A.6}$$

If it is assumed that the fluctuation of Ψ_n about Φ_n is independent[2] of v_n then the above equation becomes:

$$\langle v_n^{\text{obs}} \rangle_{\text{events}} = \langle v_n \rangle_{\text{events}} \langle \cos(n(\Psi_n - \Phi_n)) \rangle_{\text{events}} \tag{A.7}$$

---

[1] The averaging is actually a weighted average, with each event being weighted by its multiplicity N_0.

[2] This is one of the assumptions of the EP method. This is true if the multiplicity and the v_n do not change appreciably from one event to another within a centrality class.

Thus averaged over many events, the difference between the measured event-plane and the true event-plane effectively reduces the measured value of v_n by a factor of $\langle \cos(n(\Psi_n - \Phi_n))\rangle$. This factor is defined as the event-plane resolution (for the n^{th}-order harmonic) of the detector:

$$\text{Resolution} = \langle \cos(n(\Psi_n - \Phi_n))\rangle \tag{A.8}$$

Once the resolution is determined, the true value of v_n can me obtained by dividing the observed value by the resolution. That is:

$$v_n = \frac{v_n^{\text{obs}}}{\langle \cos(n(\Psi_n - \Phi_n))\rangle} = \frac{v_n^{\text{obs}}}{\text{Res}\{n\Psi_n\}} \tag{A.9}$$

Note that in the above derivation Ψ_n indicates the measured event-plane after accounting for all detector effects. Thus any difference between Ψ_n and Φ_n is purely because of the finite statistics used in the determination of Ψ_n. The procedure used for correcting for detector effects is discussed later in Appendix A.1.4.

A.1.3 Determining the detector resolution

As mentioned before, due to the finite number of particles of the system, the measured flow vector $\overrightarrow{Q_n}$ fluctuates around its true value $\overrightarrow{Q_n}^T$. Assuming Gaussian-like fluctuations, which is true when the multiplicity is large, (central-limit theorem) such dispersion distribution can be expressed as :

$$\frac{dN}{dQ_{x,n}dQ_{y,n}} = \frac{1}{\pi\sigma_n^2}\exp\left(-\frac{\left|\overrightarrow{Q_n} - \overrightarrow{Q_n}^T\right|^2}{\sigma_n^2}\right), \tag{A.10}$$

with equal variance in x and y direction,

$$\sigma_y^2 = \sigma_x^2 \equiv \frac{\sigma_n^2}{2} \tag{A.11}$$

σ_n scales with the measured multiplicity as $\sqrt{N}$.

In radial co-ordinates $\overrightarrow{Q_n}$ is given by $(Q_n, n\Psi_n)$ and $\overrightarrow{Q_n}^T$ is given by $(Q_n^T, n\Phi_n)$. The dispersion equation A.10 written in terms of Q_n and relative angle $n\Delta\Psi_n$ ($= n\Psi_n - n\Phi_n$) between measured and true flow vectors becomes:

$$\frac{dN}{Q_n dQ_n d\left(n\Delta\Psi_n\right)} = \frac{1}{\pi\sigma_n^2} \times \exp\left(-\frac{Q_n^2 + {Q_n^T}^2 - 2Q_n Q_n^T \cos n\Delta\Psi_n}{\sigma_n^2}\right) \quad \text{(A.12)}$$

Integrating out the Q_n in Eq. A.12, gives the expression for the dispersion distribution for the event-plane angle,

$$\frac{dN}{d\Delta n\Psi_n} = \frac{\exp(-\chi_n^2)}{\pi}\left\{1 + z\sqrt{\pi}\left[1 + rf(z)\right]\exp(z^2)\right\} \quad \text{(A.13)}$$

with $\chi_n = Q_n^T/\sigma_n$ and $z = \chi_n^2 \cos n\Delta\Psi_n$.

As Q_n^T is proportional to the flow signal v_n and multiplicity N, while $\sigma_n \propto \sqrt{N}$, this implies $\chi_n \propto \sqrt{N}v_n$. This implies that if the measured multiplicity is larger by factor of 2, χ_n would increase by a factor of $\sqrt{2}$. This is the basis for the two-subevent method for calculating the event-plane resolution.

Event-plane resolution: The general expression for event-plane resolution can be derived directly from Eq. A.13,

$$\langle\cos\Delta n\Psi_n\rangle = \frac{\chi_n\sqrt{\pi}}{2}e^{-\frac{\chi_n^2}{2}}\left[I_0(\frac{\chi_n^2}{2}) + I_1(\frac{\chi_n^2}{2})\right]. \quad \text{(A.14)}$$

Where, the I_n are the modified Bessel functions of the first kind. In order to calculate the resolution, χ_n needs to be determined. This is done by the two-subevent or three-subevent methods.

Two-subevent method

This method involves dividing the detector into two sub-detectors (or subevents) having nearly equal acceptance and to determine the event-plane for each of them. The two event-planes obtained from the two subevents are labelled as Ψ_n^A and Ψ_n^C. Both of these will fluctuate independently about the true event-plane according to Eq. A.13 but with a χ value $\sqrt{2}$ smaller that that of the full detector. This is because χ scales with number of particles as $\sqrt{N}$ and each of the two subevents have half the number of particles than the full detector. The subevent χ is denoted as χ_{sub} :

$$\chi_{sub} = \chi_A = \chi_C = \frac{\chi}{\sqrt{2}} \quad \text{(A.15)}$$

Since the fluctuations $n(\Psi_n^A - \Phi_n)$ and $n(\Psi_n^C - \Phi_n)$ are independent fluctuations, the distribution of the relative angle $\Delta n\Psi_n' = n(\Psi_n^A - \Psi_n^C) = n(\Psi_n^A -$

$\Phi_n) - n(\Psi_n^C - \Phi_n)$ is given by a convolution of Eq .A.13 as:

$$\frac{dN}{d\Delta n\Psi_n'} = \frac{e^{-\chi_{sub}^2}}{2}\left[\frac{2}{\pi}(1+\chi_{sub}^2) + z(I_0(z)+L_0(z)) + \chi_{sub}^2(I_1(z)+L_1(z))\right] \tag{A.16}$$

where $z = \chi_{sub}^2 \cos(\Delta n\Psi_n')$ and L_0 and L_1 are modified Sturve functions. This distribution is normalized between 0 and π. The distribution $n(\Psi_n^A - \Psi_n^C)$ can be experimentally measured and then fitted with Eq. A.16 to obtain χ_{sub}. From which the full detector's χ can be obtained (by multiplying by $\sqrt{2}$) and used in Eq. A.14 to obtain the full detector's resolution.

There is another method of obtaining the sub-detector resolution. Consider the cosine of $n(\Psi_n^A - \Psi_n^C)$:

$$\begin{aligned}\cos\left(n(\Psi_n^A - \Psi_n^C)\right) &= \cos\left(n(\Psi_n^A - \Phi_n) - n(\Psi_n^C - \Phi_n)\right)\\ &= \cos\left(n(\Psi_n^A - \Phi_n)\right)\cos\left(n(\Psi_n^C - \Phi_n)\right)\\ &\quad + \sin\left(n(\Psi_n^A - \Phi_n)\right)\sin\left(n(\Psi_n^C - \Phi_n)\right)\end{aligned} \tag{A.17}$$

Since the individual fluctuations in $(\Psi_n^A - \Phi_n)$ and $(\Psi_n^C - \Phi_n)$ are independent of each other, averaging over many events gives:

$$\begin{aligned}\left\langle\cos\left(n(\Psi_n^A - \Phi_n)\right)\cos\left(n(\Psi_n^C - \Phi_n)\right)\right\rangle &= \left\langle\cos\left(n(\Psi_n^A - \Phi_n)\right)\right\rangle\\ &\quad \times\left\langle\cos\left(n(\Psi_n^C - \Phi_n)\right)\right\rangle\\ \left\langle\sin\left(n(\Psi_n^A - \Phi_n)\right)\sin\left(n(\Psi_n^C - \Phi_n)\right)\right\rangle &= \left\langle\sin\left(n(\Psi_n^A - \Phi_n)\right)\right\rangle\\ &\quad \times\left\langle\sin\left(n(\Psi_n^C - \Phi_n)\right)\right\rangle\end{aligned} \tag{A.18}$$

Since the fluctuations of the observed event-plane about the true event-plane must be symmetric (that is, the probability of $\Psi_n^{A/C} - \Phi_n$ to be $+\Delta\Psi_n$ and $-\Delta\Psi_n$ are the same), when averaged over many events:

$$\left\langle\sin\left(n(\Psi_n^{A/C} - \Phi_n)\right)\right\rangle = 0 \tag{A.19}$$

Thus Eq. A.17 averaged over many events becomes:

$$\begin{aligned}\left\langle\cos\left(n(\Psi_n^A - \Psi_n^C)\right)\right\rangle &= \left\langle\cos\left(n(\Psi_n^A - \Phi_n)\right)\right\rangle\left\langle\cos\left(n(\Psi_n^C - \Phi_n)\right)\right\rangle\\ &= \left\langle\cos\left(n(\Psi_n^{A/C} - \Phi_n)\right)\right\rangle^2\end{aligned} \tag{A.20}$$

The last equality in Eq. A.20 follows from the fact that $\left\langle \cos\left(n(\Psi_n^{A/C} - \Phi_n)\right)\right\rangle$ which are the resolutions of sub-detectors A and C repectively, are equal to each other. Thus the sub detector resolution is obtained as:

$$\left\langle \cos\left(n(\Psi_n^{A/C} - \Phi_n)\right)\right\rangle = \sqrt{\langle \cos\left(n(\Psi_n^{A} - \Psi_n^{C})\right)\rangle} \tag{A.21}$$

The RHS of the above equation is experimentally evaluated and used to obtain the sub-detector resolution. This resolution can be used in Eq. A.14 to obtain the sub-detector χ_{sub}. From which the full detector χ can be obtained as $\sqrt{2}\chi_{sub}$. In principle, both the fit method (Eq. A.16) and the $\langle\cos\rangle$ method (Eq. A.21 followed by Eq. A.14) should give the same value of χ_{sub} (and hence same value of χ). Any difference in between the two values can be used as a systematic error on the event-plane resolution.

Three-subevent method

The three-subevent method does not require knowledge of χ_n. Instead, it directly calculates the resolution of a given detector A by using its correlation with the event planes from two other detectors B and C sitting at different η windows.

$$\begin{aligned}\mathrm{Res}\{n\Psi_n^A\} &= \langle\cos(n(\Psi_n^A - \Phi_n))\rangle \\ &= \sqrt{\frac{\langle\cos\left(n\left(\Psi_n^A - \Psi_n^B\right)\right)\rangle\langle\cos\left(n\left(\Psi_n^A - \Psi_n^C\right)\right)\rangle}{\langle\cos\left(n\left(\Psi_n^B - \Psi_n^C\right)\right)\rangle}}\end{aligned} \tag{A.22}$$

This can be proven by expanding the three cosines as (see Eq. A.17–A.20):

$$\begin{aligned}\langle\cos(n(\Psi_n^A - \Psi_n^B))\rangle &= \langle\cos(n(\Psi_n^A - \Phi_n))\rangle\langle\cos(n(\Psi_n^B - \Phi_n))\rangle \\ \langle\cos(n(\Psi_n^A - \Psi_n^C))\rangle &= \langle\cos(n(\Psi_n^A - \Phi_n))\rangle\langle\cos(n(\Psi_n^C - \Phi_n))\rangle \\ \langle\cos(n(\Psi_n^B - \Psi_n^C))\rangle &= \langle\cos(n(\Psi_n^B - \Phi_n))\rangle\langle\cos(n(\Psi_n^C - \Phi_n))\rangle.\end{aligned} \tag{A.23}$$

Plugging the above into the RHS of Eq. A.22 completes the proof. Once $\mathrm{Res}\{n\Psi_n^A\}$ is known, it can be used to calculate the χ_n using Eq. A.14.

A.1.4 Event plane flattening

Detector effects such as inefficiencies or dead/hot-regions can affect the determination of the event-planes (beyond statistical fluctuations). For example, if the Forward calorimeter has a few towers with higher gains than the rest, then the Q-vectors will get more contribution from these towers, and will have a tendency to align along them. Similarly regions with dead towers will result in the Q-vector getting less contribution from those regions and will be aligned opposite to them. The presence of detector effects can be checked by measuring the $E_{\mathrm{T}}\phi)$ averaged over many events. Since the orientation of the collision is completely random from event to event (in the lab frame), $E_{\mathrm{T}}(\phi)$ averaged over many events should be independent of ϕ.

Figure A.1 shows the 2-D E_{T} map for the two Fcal sub-detectors in ϕ and η, summed over all events in the (0-70)% centrality interval. Clear modulations are seen along the ϕ direction due to detector non-uniformity. This distribution is then projected onto the ϕ axis and expanded as a Fourier series. The left panel of Figure A.2 shows the 1D "acceptance function", and the first six Fourier moments plotted individually around the mean values of the histogram, together with the sum of all terms up to n=6 (dashed line). The phases for each n, are drawn as vertical bars on the same figure. The Fcal acceptance function shows a significant modulation for n=1, 2 and 4.

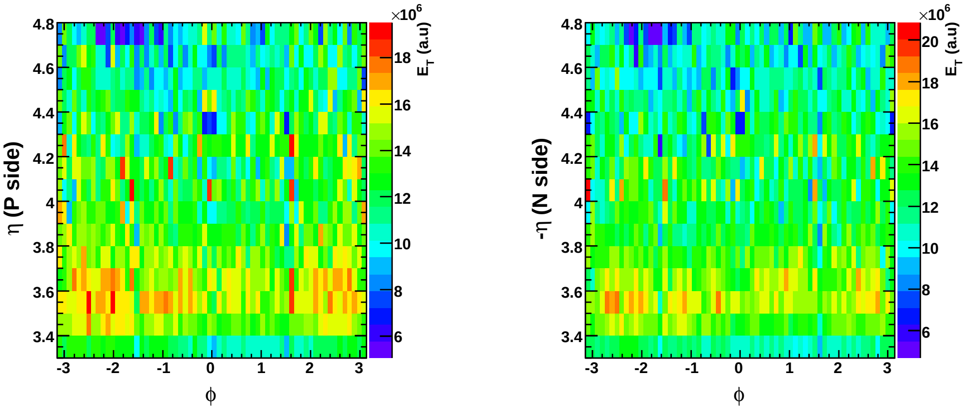

Figure A.1: FCal (layers 1+2) E_T distribution, intergated over (0-70)% centrality for positive η (left) and negative η (right). The first and last η slices centered at $|\eta|$=3.25 and $|\eta|$=4.85 are not used in this analysis and have been excluded from the figures.

These detector modulations affect the determination of the Ψ_n, and need to be accounted for. As the orientation of the collision is completely random in the lab frame, the distribution of the Q-vector and thus the $n\Psi_n{}^3$ angles should be completely flat in ϕ. In order to demonstrate the non-flatness of the raw measured, i.e. uncorrected Ψ_n (denoted as Ψ_n^{Raw}), the distributions of $2\Psi_2^{\mathrm{Raw}}$ and $3\Psi_3^{\mathrm{Raw}}$ obtained from the FCal are plotted for a few centralities in Fig.A.3.

---

[3] The orientation of the n^{th}-order Q-vector is given by $n\Psi_n$

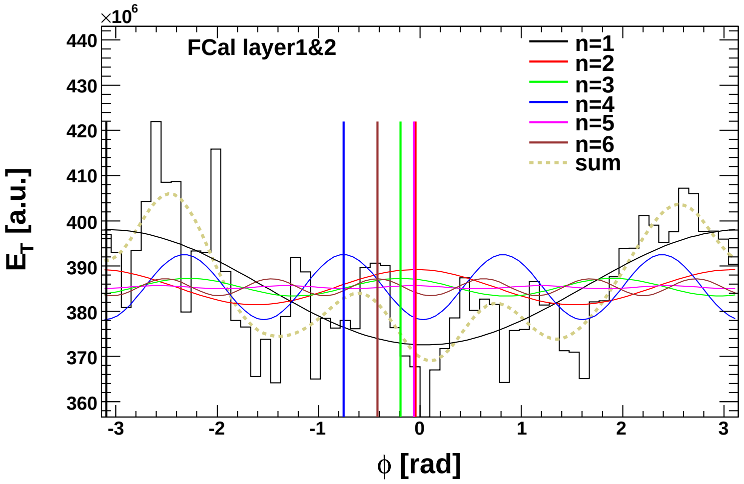

Figure A.2: FCal $E_{\mathrm{T}}(\phi)$ (layers 1+2) distribution integrated over the (0-70)% centrality interval and over η.

Clearly significant non-flatness is seen in these distributions indicating the need to correct the Ψ_n^{Raw}.

Recentering and rescaling of the Q-vector

As mentioned before, the Q-vector distribution does not have any prefered direction. Thus, we must have :

$$\langle Q_{n,x} \rangle = \langle Q_{n,y} \rangle = 0 \tag{A.24}$$

Due to the acceptance effects mentioned above, the raw Q-vectors averaged over many events, have non-zero x and y components. The Q-vector is recentered at (0,0) by subtracting these out. This recentering procedure is done order by order for all Q-vectors. Since the mean values of the raw Q-vectors depend on the centrality, this recentering in done is narrow bins of centrality (1% bins in our case).

$$\begin{aligned} Q_{n,x}^{\mathrm{recentered}} &= Q_{n,x}^{\mathrm{Raw}} - \langle Q_{n,x}^{\mathrm{Raw}} \rangle \\ Q_{n,x}^{\mathrm{recentered}} &= Q_{n,x}^{\mathrm{Raw}} - \langle Q_{n,x}^{\mathrm{Raw}} \rangle \end{aligned} \tag{A.25}$$

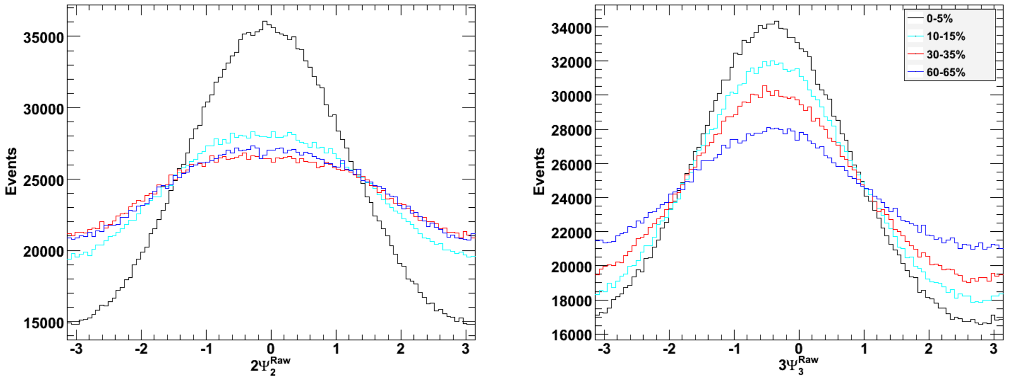

Figure A.3: The event plane distribution for Ψ_2^{Raw} and Ψ_3^{Raw} obatined from the FCal for four different centralities. The error bars should be $\sqrt{\mathrm{N}_{\mathrm{Events}}}$ and are suppressed for clarity.

Flattening of the event plane

The event-planes obtained from the recentered Q-vectors are designated as Ψ_n^{meas}. The distributions for $n\Psi_n^{\mathrm{meas}}$ are almost flat. Any remaining modulations in these distributions are "flattened" by calculating the Fourier coefficients of the $n\Psi_n^{\mathrm{meas}}$ distributions, given by $\langle\cos(kn\Psi_n^{\mathrm{meas}})\rangle$ and $\langle\sin(kn\Psi_n^{\mathrm{meas}})\rangle$ for order k, and then rotating the Ψ_n^{meas} values by small angles $\Delta\Psi_n$ to remove these modulations. The $\Delta\Psi_n$ are given by:

$$\Delta\Psi_n = \sum_{k=1}^{k_{max}} \frac{2}{kn}\left(-\langle\sin(kn\Psi_n^{\mathrm{meas}})\rangle\cos(kn\Psi_n^{\mathrm{meas}}) + \langle\cos(kn\Psi_n^{\mathrm{meas}})\rangle\sin(kn\Psi_n^{\mathrm{meas}})\right) \tag{A.26}$$

Where k_{max}=12 in this analysis. Finally the fully corrected event-plane is obtained as :

$$\Psi_n = \Psi^{\mathrm{meas}} + \Delta\Psi_n \tag{A.27}$$

Figure.A.4 shows the Raw, recentered and flattened event-planes for two different centralities for n=2-6. From the plots it is clear that the recentering take care of most of the detector anisotropies and the flattening only makes minor corrections.

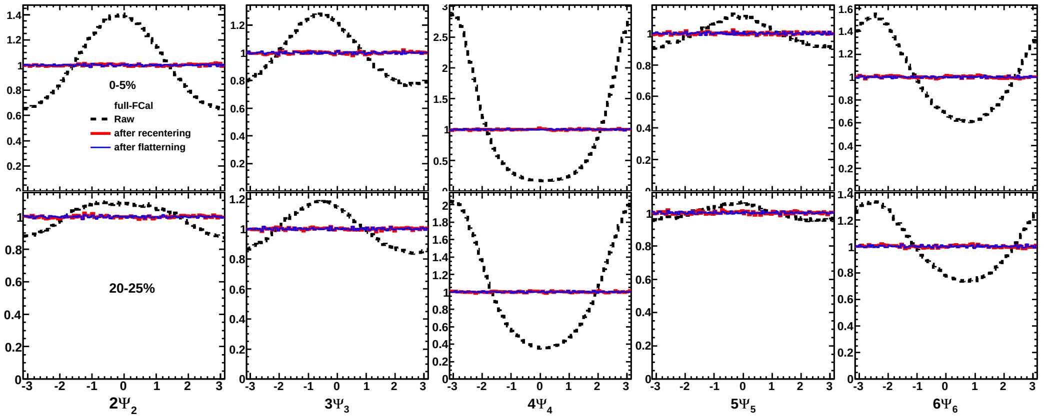

Figure A.4: The Raw, recentered and flattened distributions for Ψ_2–Ψ_6 obtained for full-FCal (layers 1+2).

Meaning of the shifts $\langle Q^{\mathrm{Raw}}_{n,x/y} \rangle$

We now take a detailed look at the shifts $\langle Q^{\mathrm{Raw}}_{n,x/y} \rangle$. First we explain what these $\langle Q^{\mathrm{Raw}}_{n,x/y} \rangle$ mean physically.

The Q-vector in an event for an ideal detector can be written as a function of phi as:

$$Q^{\mathrm{Ideal}}(\phi) = Q_0\left(1 + \sum_{n=1}^{\infty} 2v_n \cos(n\phi - n\Psi_n)\right) \tag{A.28}$$

However, the measured raw energy distribution will be affected by the detector efficiency ϵ, as:

$$Q^{\mathrm{Raw}}(\phi) = Q^{\mathrm{Ideal}}(\phi) \times \epsilon(Q^{\mathrm{Ideal}}(\phi), \phi) \tag{A.29}$$

Where the efficiency is taken to be both a function of the true deposited energy $Q^{\mathrm{Ideal}}(\phi)$ and the angle ϕ. If this assumption is relaxed to make the efficiency only a function of ϕ [4], we get:

$$Q^{\mathrm{Raw}}(\phi) = Q^{\mathrm{Ideal}}(\phi) \times \epsilon(\phi) \tag{A.30}$$

---

[4] Or if the correction is done in narrow centrality bins so that the E_{T} does not change too much from one event to another.

The efficiency function can be expanded in a Fourier series as:

$$\epsilon(\phi) = \epsilon_0 \left(1 + \sum_{n=1}^{\infty} 2\epsilon_n \cos(n\phi - n\Psi_n^{Det})\right) \tag{A.31}$$

Substituting this into the expansion of the Raw Q-vector, gives:

$$\begin{aligned}
Q^{\text{Raw}} &= Q_0\left(1 + \sum_{n'=1}^{\infty} 2v_{n'} \cos(n'\phi - n'\Psi_{n'})\right) \times \epsilon(\phi) \\
&= Q_0\left(1 + \sum_{n'=1}^{\infty} 2v_{n'} \cos(n'\phi - n'\Psi_{n'})\right) \\
&\quad \times \epsilon_0\left(1 + \sum_{n''=1}^{\infty} 2\epsilon_{n''} \cos(n''\phi - n''\Psi_{n''}^{Det})\right) \\
&= \epsilon_0 Q_0\left(1 + \sum_{n'=1}^{\infty} 2v_{n'} \cos(n'\phi - n'\Psi_{n'})\right. \\
&\quad \left. + \sum_{n''=1}^{\infty} 2\epsilon_{n''} \cos(n''\phi - n''\Psi_{n''}^{Det}) + O(\epsilon_{n'} v_{n''})\right)
\end{aligned} \tag{A.32}$$

where, terms of Order $O(\epsilon_{n'} v_{n''})$ have been ignored in the above formula. This gives for $Q_{n,x}^{\text{Raw}}$ and $Q_{n,y}^{\text{Raw}}$:

$$\begin{aligned}
Q_{n,x}^{\text{Raw}} &= \int Q(\phi)\cos(\phi)d\phi = \epsilon_0 Q_0\left(v_n \cos(n\Psi_n) + \epsilon_n \cos(n\Psi_n^{Det})\right) \\
Q_{n,y}^{\text{Raw}} &= \int Q(\phi)\sin(\phi)d\phi = \epsilon_0 Q_0\left(v_n \sin(n\Psi_n) + \epsilon_n \sin(n\Psi_n^{Det})\right)
\end{aligned} \tag{A.33}$$

If the event-plane angles Ψ_n were calculated from the raw Q_n values, we would get :

$$\begin{aligned}
\Psi_n^{\text{Raw}} &= \tan^{-1}\left(\frac{\epsilon_0 Q_0\left(2v_n \sin(n\Psi_n) + 2\epsilon_n \sin(n\Psi_n^{Det})\right)}{\epsilon_0 Q_0\left(2v_n \cos(n\Psi_n) + 2\epsilon_n \cos(n\Psi_n^{Det})\right)}\right) \\
&= \tan^{-1}\left(\frac{v_n \sin(n\Psi_n) + \epsilon_n \sin(n\Psi_n^{Det})}{v_n \cos(n\Psi_n) + \epsilon_n \cos(n\Psi_n^{Det})}\right) \\
&\neq \Psi_n
\end{aligned} \tag{A.34}$$

Now we explain how the recentering corrects this. When averaged over many events, as the event-plane angles (Ψ_n) are completely random, Eq. A.32 becomes:

$$\left\langle Q^{\mathrm{Raw}} \right\rangle \;=\; \epsilon_0 Q_0 \Big(1 + \sum_{n''=1}^{\infty} 2\epsilon_{n''} \cos(n''\phi - n''\Psi_{n''}^{Det}) \Big) \tag{A.35}$$

This gives:

$$\begin{aligned}
\left\langle Q_{n,x}^{\mathrm{Raw}} \right\rangle &= \int \left\langle Q^{\mathrm{Raw}}(\phi) \right\rangle \times \cos(n\phi) d\phi = \epsilon_0 Q_0 \left(\epsilon_n \cos(n\Psi_n^{Det}) \right) \\
\left\langle Q_{n,y}^{\mathrm{Raw}} \right\rangle &= \int \left\langle Q^{\mathrm{Raw}}(\phi) \right\rangle \times \sin(n\phi) d\phi = \epsilon_0 Q_0 \left(\epsilon_n \sin(n\Psi_n^{Det}) \right) \qquad \text{(A.36)}
\end{aligned}$$

Equations.A.35 and A.36 also give the physical meaning of $\left\langle Q_n^{\mathrm{Raw}} \right\rangle$. Up to a normalization constant Q_0(independent of n), $\left\langle Q_n^{\mathrm{Raw}} \right\rangle$ measures the n^{th} harmonic coefficient in the Fourier expansion of the detector efficiency $\epsilon(\phi)$. From one centrality to another, Q_0 will change, but ϵ_0, ϵ_n and Ψ_n^{Det} will remain same. In other words, while the magnitude of $\left\langle Q_n^{\mathrm{Raw}} \right\rangle$ will from one centrality to another, the direction will remain fixed. Further as Q_0 is independent of n, the magnitudes of the different $\left\langle Q_n^{\mathrm{Raw}} \right\rangle$ will scale by the same amount from one centrality to another.

The effects of the recentering on the Q-vectors are given by:

$$\begin{aligned}
Q_{n,x}^{\mathrm{recentered}} = Q_{n,x}^{\mathrm{Raw}} - \left\langle Q_{n,x}^{\mathrm{Raw}} \right\rangle &= \epsilon_0 Q_0 \left(v_n \cos(n\Psi_n) \right) \\
Q_{n,y}^{\mathrm{recentered}} = Q_{n,y}^{\mathrm{Raw}} - \left\langle Q_{n,y}^{\mathrm{Raw}} \right\rangle &= \epsilon_0 Q_0 \left(v_n sin(n\Psi_n) \right) \qquad \text{(A.37)}
\end{aligned}$$

Calculating the Ψ_n from the recentered Q-vectors, gives:

$$\Psi_n^{\mathrm{recentered}} = \tan^{-1}\Big(\frac{Q_{n,y}^{\mathrm{recentered}}}{Q_{n,x}^{\mathrm{recentered}}}\Big) = \tan^{-1}\Big(\frac{\epsilon_0 Q_0 \left(v_n \sin(n\Psi_n) \right)}{\epsilon_0 Q_0 \left(v_n \cos(n\Psi_n) \right)}\Big) = \Psi_n \tag{A.38}$$

Thus the recentered Q-vectors give the correct event-planes.

In Eq. A.32 terms of $O(\epsilon_{n'} v_{n''})$ had been ignored. These terms make the $\Psi_n^{\mathrm{recentered}}$ to be slightly different than the Ψ_n. These terms are accounted for by the flattening procedure (Eq. A.26-A.27).

Shifts $\langle Q_{n,x/y}^{\mathrm{Raw}} \rangle$ for the FCal

In this section a study of the shifts $\langle Q_{n,x/y}^{\mathrm{Raw}} \rangle$ for the FCal are presented. Only one run is analyzed so that run-by-run changes in the detector acceptance (if any) do not affect the observations. Also the results presented here are only for layer-1 of the FCal. The left panel of Fig. A.5, shows the $\langle Q_{n,y}^{\mathrm{Raw}}\rangle$ vs $\langle Q_{n,x}^{\mathrm{Raw}}\rangle$ correlation for n=1-6. Each harmonic is represented by a different color and the different points for a particular harmonic are for different centralities: 20 bins of 5% centrality width with the most central (0-5)% events corresponding to the highest magnitude of $\langle Q_n^{\mathrm{Raw}}\rangle$). The right plot shows similar correlations, but with the Q-vectors rescaled such that the point corresponding to the (0-5)% centrality interval has a magnitude of 1.0.

From these figures, the two scaling relations that were mentioned in the last section can be clearly seen. As the centrality bin changes, the magnitude of the shifts change (as they should), but the direction is extremely stable. The expected scaling in the magnitudes of the Q_n^{Raw} is also seen, which is evident from the right plot. When the most central class has been scaled to have $|Q_n^{\mathrm{Raw}}| = 1.0$, the other centralities have roughly the same magnitude independent of n.

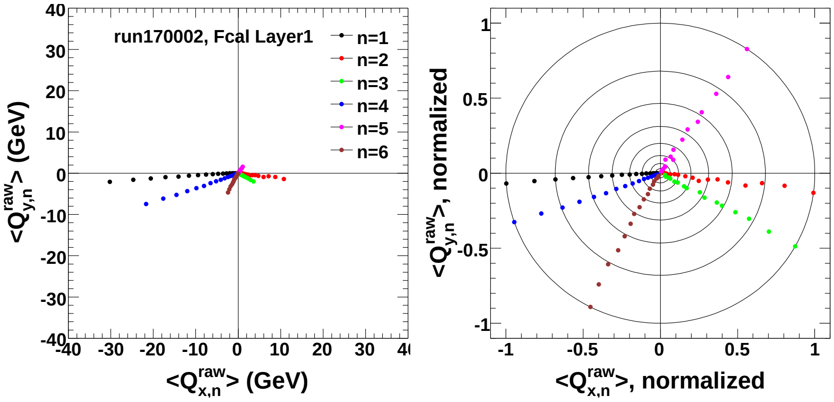

Figure A.5: $\left\langle Q_{n,y}^{\mathrm{Raw}}\right\rangle$ vs $\left\langle Q_{n,x}^{\mathrm{Raw}}\right\rangle$ for n=2-6. Left Plot is unscaled, right plot is scaled such that the most central(0-5%) bin has $|\left\langle Q_n^{\mathrm{Raw}}\right\rangle| = 1.0$.

A.1.5 Resolution from three-subevent method

The three-subevent method method (Eq. 3.12 or Eq. A.22) is also used to calculate the FCal resolution. The main advantages of three-subevent method are :

- It makes no assumptions about the functional form of the dispersion distribution of Ψ_n relative to Φ_n.
- It can be used to directly calculate the resolution of the full-FCal, as opposed to the two-subevent method, which gives the resolution of the

sub-detector ($\mathrm{FCal}_{\mathrm{P(N)}}$), which is then used to obtain the full-FCal resolution.

The three detectors have to be well separated in η in order to minimize the short-range correlations. Also the reference detector (B and C) themselves must have good resolutions, otherwise the resolution for detector A obtained from this method would have large statistical and systematic error.

Detectors used for three-subevent study

The large coverage of the ATLAS Electro-Magnetic Calorimeter (EMCal) system, which includes the Electro-Magnetic Barrel ($|\eta| < 1.5$) and the Electro-Magnetic end-cap ($1.5 < |\eta| < 3.2$) with fine segmentation in η and ϕ, allows for a very flexible choice for the detectors B and C (detector A is either the full-FCal or sub-FCal). The tracking detectors are also used as reference detectors where the Ψ_n are obtained using tracks with p_{T} >0.5 GeV. The naming convention for the reference detectors used in the three-subevent method is listed in Table A.1. All the detectors are symmetric about η=0. The names in Table A.1 refer to the detectors with the positive and negative η segments combined. When only one half of the detector is used, a subscript 'P' or 'N' is added to indicate whether the positive or negative η side is being used, for example $\mathrm{EMB0}_{\mathrm{N}}$ refers to the negative η side of the EMB0 detector. All the detectors listed Table A.1 are calibrated using the recentering-flattening procedure described in Appendix A.1.4.

Three types of three-subevent studies

To suppress the short-range correlations (non-flow correlations), a minimum one unit η separation is required in between any pair of the three detectors. A large set of three-subevent measurements are done. They are categorized into three types. In Type-I analysis, A is chosen to be the full-FCal. Detectors B and C are chosen such that the combination $A + B + C$ is symmetric about $\eta = 0$, one example is EMB0 for B and EME0 for C. The list of Type-I combinations used are given in Table A.2.

These combinations directly give the resolution for the full-FCal (i.e. without calculating the sub-FCal resolution). Fig. A.6 shows the full-FCal resolution for n=2-6 obtained for the different Type-I combinations as a function of centrality. The resolution obtained from the two-subevent method is also shown for comparison. The different combinations have been given small offsets along the x-axis so that they can be clearly seen. Fig. A.7 shows the ratios of the three-subevent resolutions to the two-subevent method results. For n=2, the ratios are systematically below 1.0 in central collisions by up to

Detector	Name	Description	$\|\eta\|$ coverage
1	EMB0	EM Barrel	0-0.5
2	EMB1	EM Barrel	0.5-1.5
3	EMB2	EM Barrel	0-1.5
4	EME0	EM End Cap	1.5-2.1
5	EME1	EM End Cap	1.5-2.7
6	EME2	EM End Cap	1.5-3.2
7	EMB1EME0	EM Barrel + End Cap	0.5-2.1
8	ID0	Inner Detector	0.5-2.0
9	ID1	Inner Detector	0-2.5

Table A.1: Detectors used in the three-subevent method to determine full-FCal and sub-FCal resolutions. If only one side of the detector is used, a subscript 'N' or 'P' is added to indicate whether the negative or the positive η side is being used. For the Inner Detector, only tracks with p_{T} >0.5 GeV are used.

Type-I checks	
Check 1	FCal – EMB0 – EME0
Check 2	FCal – $\mathrm{EMB1_P}$ – $\mathrm{EMB1_N}$
Check 3	FCal – $\mathrm{EMB1EME0_P}$ – $\mathrm{EMB1EME0_N}$
Check 4	FCal – $\mathrm{EME0_P}$ – $\mathrm{EME0_N}$

Table A.2: List of Type-I combinations for obtaining full-FCal resolution via three-subevent method. See Table.A.1 for description of the detectors.

5% and in mid-central collisions by 1%, then spread out for peripheral collisions by about ±5%. For n=3 and 4, a small systematically increasing trend of the ratios towards peripheral collisions is seen, but the change is within ±3% across most of the centrality range. For n=5, the ratio is systematically above one and increases toward more peripheral collisions to about (5-10)%. For n=6, there is a large spread between the ratios with about ±30% variation, and in most cases the ratio is systematically lower than 1, although the statistical uncertainties are also large.

In Type-II analysis, A and B are $\mathrm{FCal_N}$ and $\mathrm{FCal_P}$, and C is chosen from the list of reference detectors. Detector C is required to have a one unit η separation form both $\mathrm{FCal_{P/N}}$ and is placed symmetrically in between them. This combination gives the resolution for $\mathrm{FCal_P}$ from Eq. 3.12 (Eq. A.22). The detectors A and B are thew swapped (i.e. $A = \mathrm{FCal_N}$ and $B = \mathrm{FCal_P}$)

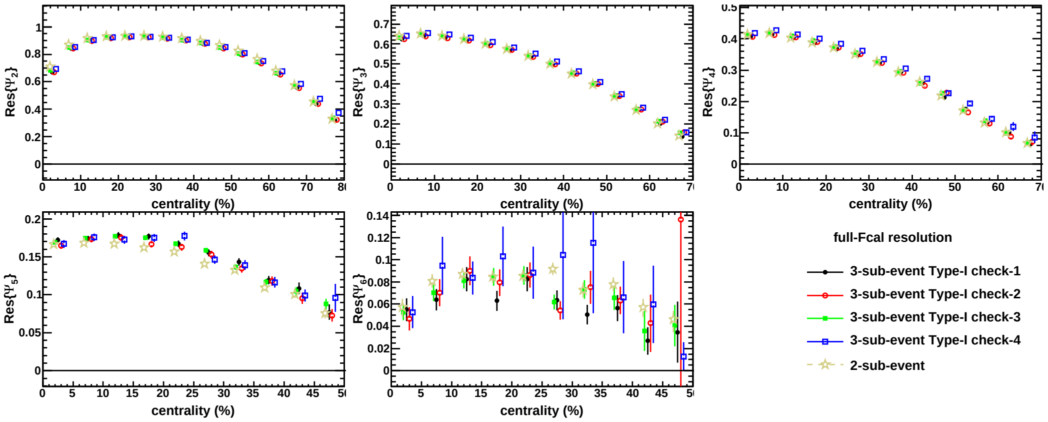

Figure A.6: The resolutions for n=2–6 obtained for the full-FCal from Type-I three-subevent combinations. The full-FCal resolution obtained from the two-subevent method is also shown for comparison. Error bars are statistical errors only. The x-axis covers the centrality range over which the final results are presented and is different for the different n.

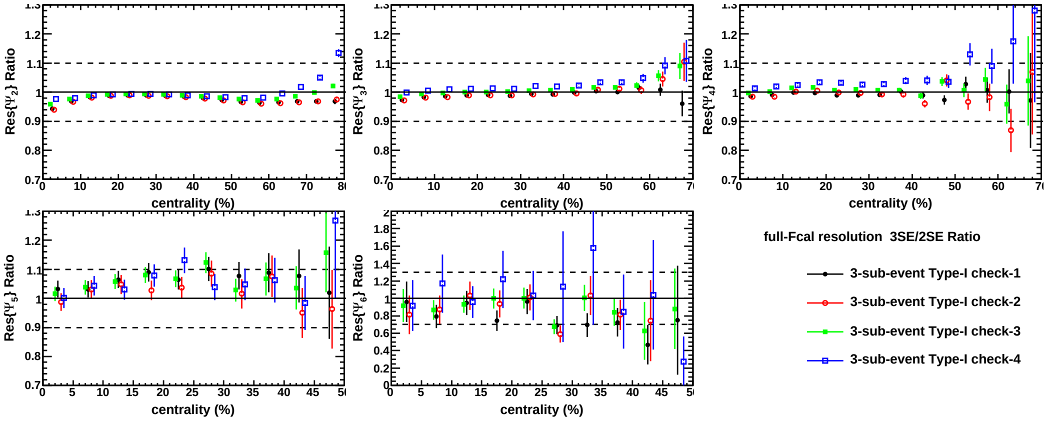

Figure A.7: The ratio of full-FCal resolutions for n=2–6 obtained from Type-I three-subevent combinations to the ones obtained from the two-subevent method. Error bars are statistical errors only. The x-axis covers the centrality range over which the final results are presented and is different for the different n.

while keeping the same C to calculate the resolution for $\mathrm{FCal_N}$. From the resolutions, the χ values for the $\mathrm{FCal_N}$ and $\mathrm{FCal_P}$ are obtained using Eq 3.7 (Eq. A.14), then combined to get the full-FCal χ as $\chi_{\mathrm{full}} = \sqrt{\chi^2_{\mathrm{FCal_N}} + \chi^2_{\mathrm{FCal_P}}}$. Which is again plugged back into Eq 3.7 (Eq. A.14) to obtain the resolution for full-FCal. In total five Type-II checks are performed as listed in Table A.3.

Note that this method also gives the $\mathrm{FCal_P}$ or $\mathrm{FCal_N}$ resolutions as they are calculated at the intermediate step.

Type-II checks	
Check 1	$\mathrm{FCal_N} - \mathrm{EMB0} - \mathrm{FCal_P}$ and $\mathrm{FCal_P} - \mathrm{EMB0} - \mathrm{FCal_N}$
Check 2	$\mathrm{FCal_N} - \mathrm{EMB1} - \mathrm{FCal_P}$ and $\mathrm{FCal_P} - \mathrm{EMB1} - \mathrm{FCal_N}$
Check 3	$\mathrm{FCal_N} - \mathrm{EME1} - \mathrm{FCal_P}$ and $\mathrm{FCal_P} - \mathrm{EME1} - \mathrm{FCal_N}$
Check 4	$\mathrm{FCal_N} - \mathrm{EMB2} - \mathrm{FCal_P}$ and $\mathrm{FCal_P} - \mathrm{EMB2} - \mathrm{FCal_N}$
Check 5	$\mathrm{FCal_N} - \mathrm{EMB1EME0} - \mathrm{FCal_P}$ and $\mathrm{FCal_P} - \mathrm{EMB1EME0} - \mathrm{FCal_N}$

Table A.3: List of Type-II combinations for obtaining sub-FCal resolution via three-subevent method. See Table A.1 for description of the detectors.

Figure A.8 shows the ratio of full-FCal resolutions for n=2-6 obtained from Type-II combinations, to the ones obtained from the two-subevent method as a function of centrality. The same ratios are also shown for sub-FCal resolutions in Fig. A.9. The agreement for full-FCal is quite good for all harmonics and no systematic variations of the ratios with centrality are seen. The only noticeable difference is a ~ 1% downward shift of the ratios for n=3 and 5, and a ~ 2% downward shift of the ratios for n=4. The agreements for the sub-FCal resolutions are even better for all harmonics.

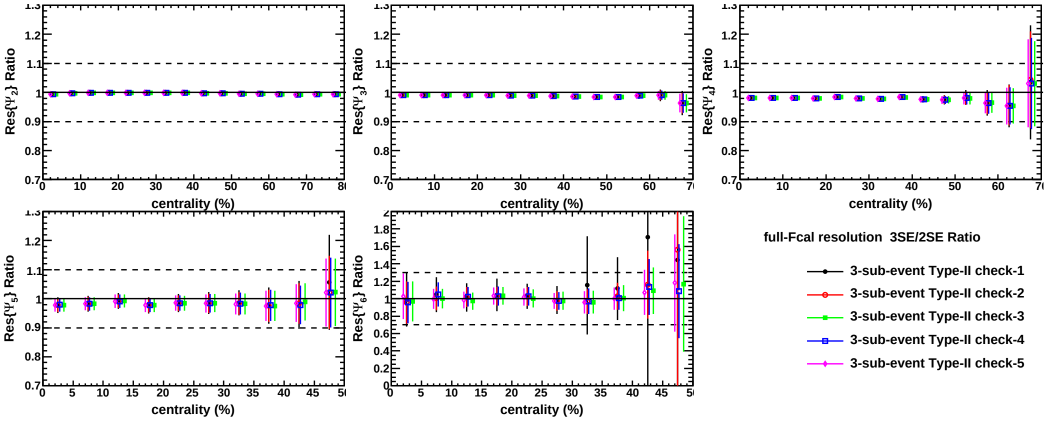

Figure A.8: The ratio of full-FCal resolutions for n=2-6 obtained from Type-II combinations to the ones obtained from the two-subevent method. Error bars are statistical errors.

In Type III analysis, the resolution is calculated for the two sides of FCal in two separate three-subevent studies, and then combined according to the

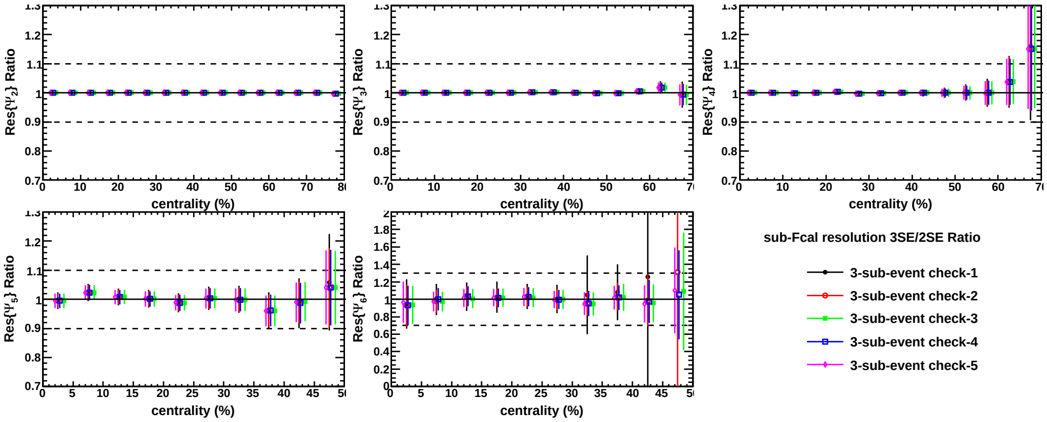

Figure A.9: The ratio of $\mathrm{FCal_P}$ resolutions for n=2-6 obtained from Type-II combinations to the ones obtained from the two-subevent method. Error bars are statistical errors.

standard formulae Eq. 3.7 and Eq. 3.9 that relates the two sub-detector resolutions to the full detector resolution. Detectors B and C are chosen such that one of them is at positive η while the other is at negative η and they have an η separation greater than 1.0 from the first detector ($\mathrm{FCal_P}$ or $\mathrm{FCal_N}$) and from each other. As listed in Table A.4, a total of six Type-III checks are performed for both $\mathrm{FCal_P}$ and $\mathrm{FCal_N}$. Since $\mathrm{FCal_P}$ or $\mathrm{FCal_N}$ resolutions are calculated at the intermediate step, this type also gives the sub-FCal resolutions.

Type-III checks	
Check 1	$\mathrm{FCal_P} - \mathrm{EMB2_P} - \mathrm{EME2_N}$
Check 2	$\mathrm{FCal_P} - \mathrm{EMB1_P} - \mathrm{EME2_N}$
Check 3	$\mathrm{FCal_P} - \mathrm{EMB1EME0_P} - \mathrm{EMB1EME1_N}$
Check 4	$\mathrm{FCal_P} - \mathrm{EMB1EME0_P} - \mathrm{ID0_N}$
Check 5	$\mathrm{FCal_P} - \mathrm{ID1_P} - \mathrm{EMB1EME0_N}$
Check 6	$\mathrm{FCal_P} - \mathrm{ID0_P} - \mathrm{EME_N}$

Table A.4: A list of Type-III combinations where $\mathrm{FCal_P}$ is chosen as the first detector. Similar combinations are used for $\mathrm{FCal_N}$ by swapping P and N for all three detectors. Note that $\mathrm{FCal_P}$ and $\mathrm{FCal_N}$ are not used simultaneously as in Type-II case. See Table A.1 for description of the detectors.

Figure A.10 shows the ratio of Full-FCal resolutions for n=2-6 obtained for FCal from Type-III combinations to the ones obtained from the two-subevent method as a function of centrality. A good agreement is seen with the two-subevent values for n=2 except in peripheral events. For n=3 and 4, the three-subevent values are systematically higher than the two-subevent values but are within $\sim 4\%$. For n=5, the ratio is systematically larger than one by about 10% in mid-central collisions. For n=6, the three-subevent results are systematically lower than those obtained from two-subevent methods by as much as 30% in mid-central collisions. Same ratios for sub-FCal resolutions are shown in Fig. A.11, the systematic trends as function of centrality are quite similar as the full-FCal case. However the deviation for n=2, 3 and 4 are somewhat larger (but remain independent of centrality), reaching about 5% for both n=3 and 4. The level of deviation for n=5 and 6, are however quite similar to that for the full-FCal case.

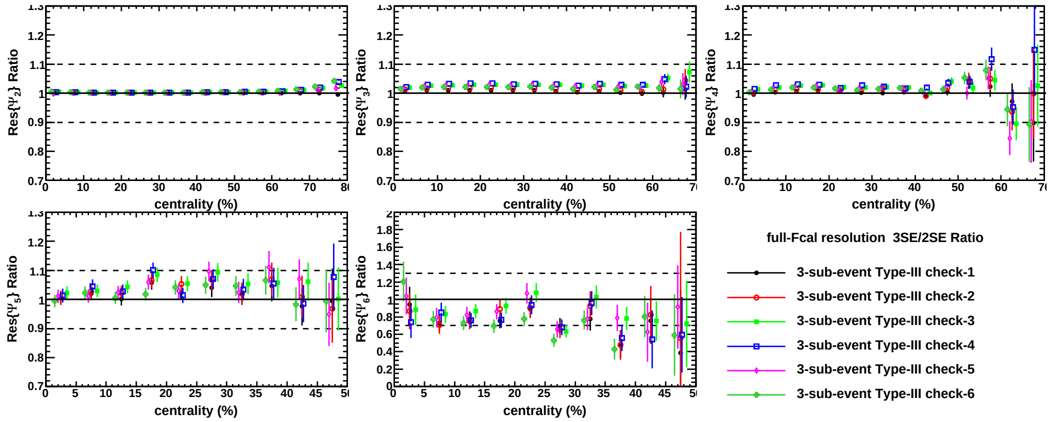

Figure A.10: The ratio of full-FCal resolutions for n=2–6 obtained from Type-III combinations to the ones obtained from the two-subevent method. Error bars are statistical errors.

The resolutions measured from the three-subevent study are used to estimate the systematic errors in the resolutions. They are also used to correct the resolutions for n=5 and 6 obtained from the two-subevent method (see Section 3.2.5).

A.2 Systematic error calculation and cross-checks

A.2.1 Dependence of v_n on running periods

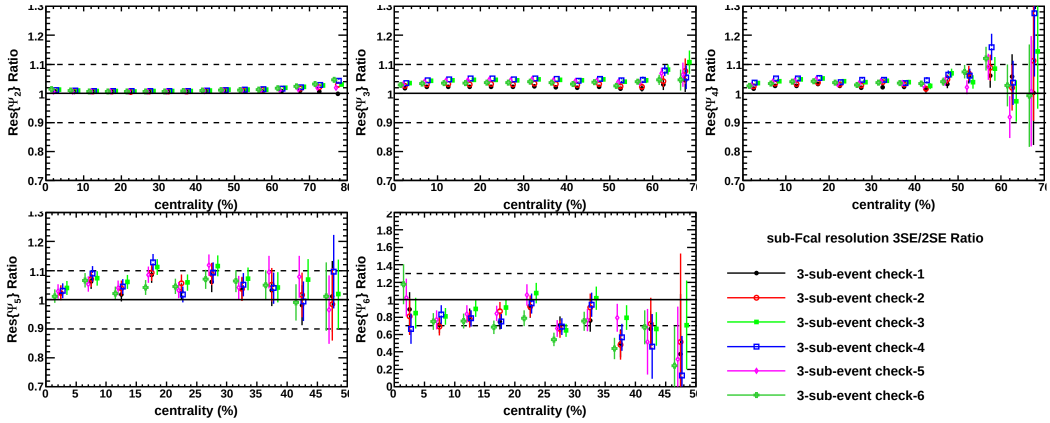

Figure A.11: The ratio of $\mathrm{FCal_P}$ resolutions for n=2–6 obtained from Type-III combinations to the ones obtained from the two-subevent method. Error bars are statistical errors.

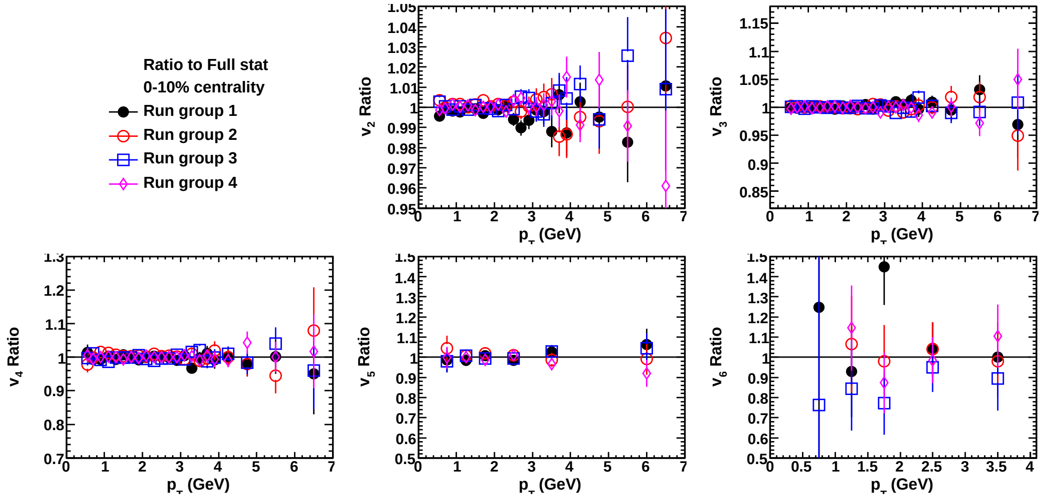

Figure A.12: p_{T} dependence of v_n for four different run groups for (0-10)% centrality.

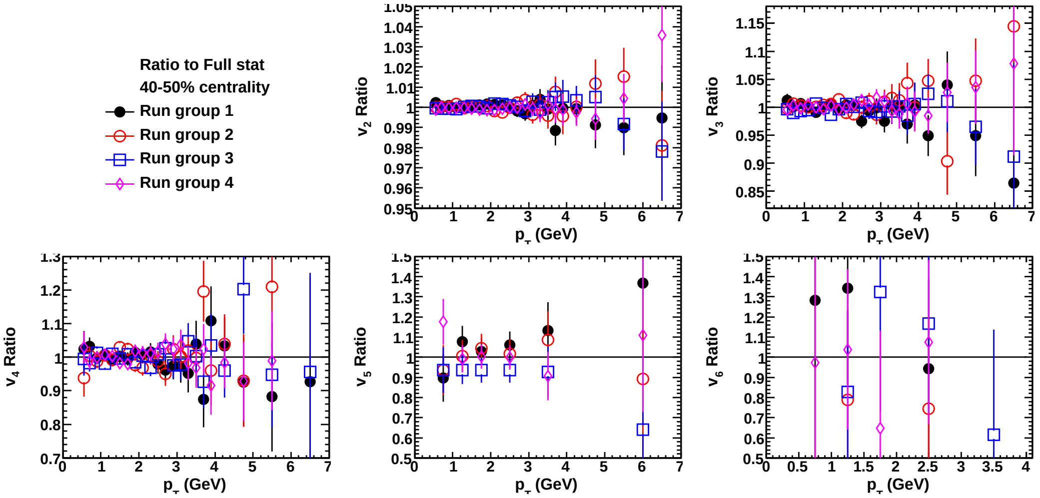

Figure A.13: p_T dependence of v_n for four different run groups for (40-50)% centrality.

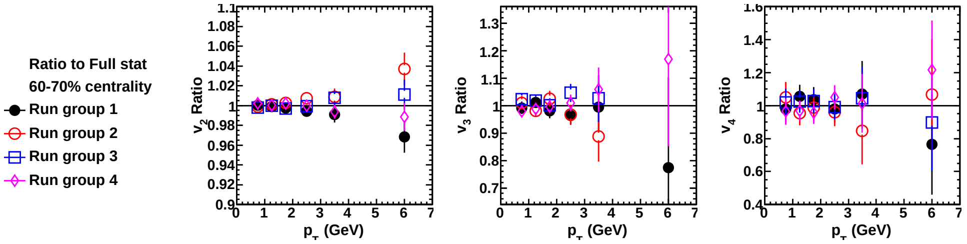

Figure A.14: p_T dependence of v_n for four different run groups for (60-70)% centrality.

A.3 Additional results plots

A.3.1 η dependence

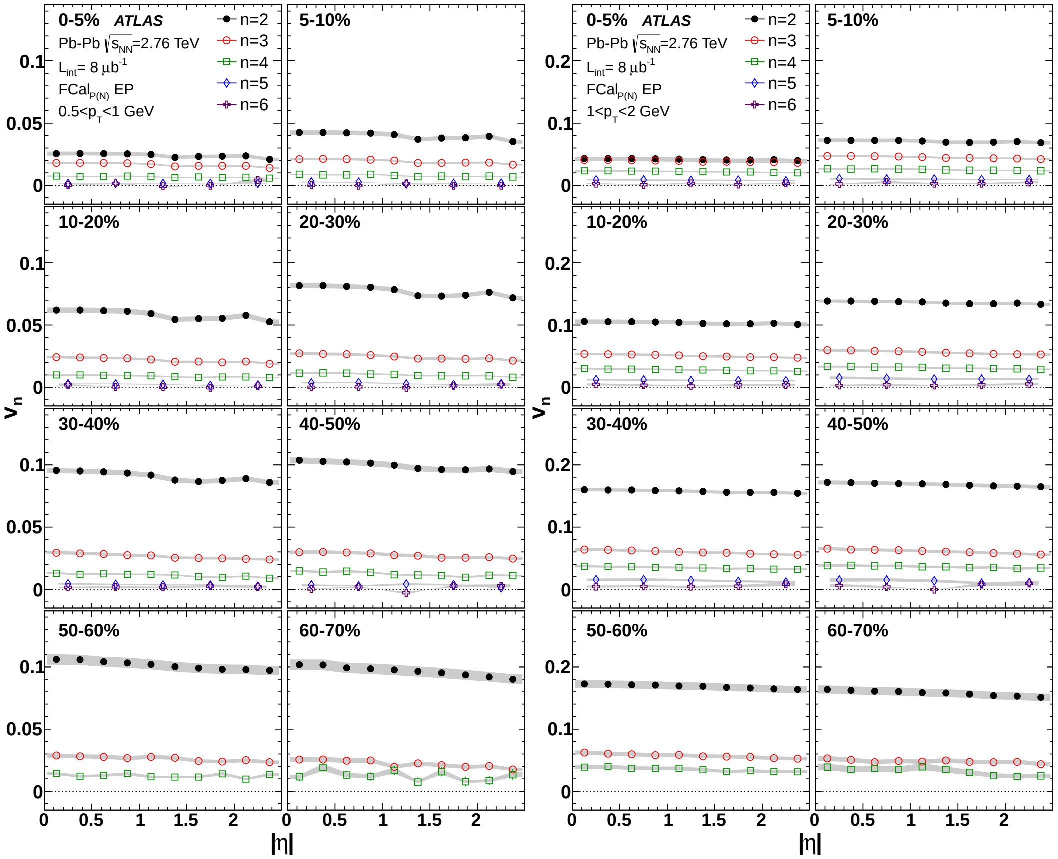

Figure A.15: Left two columns: η dependence of v_n for $p_{\mathrm{T}} \in (0.5, 1.0)$ GeV. Right two columns: η dependence of v_n for $p_{\mathrm{T}} \in (1, 2)$ GeV. Each panel corresponds to a different centrality class. The values are obtained using sub-FCal event-planes.

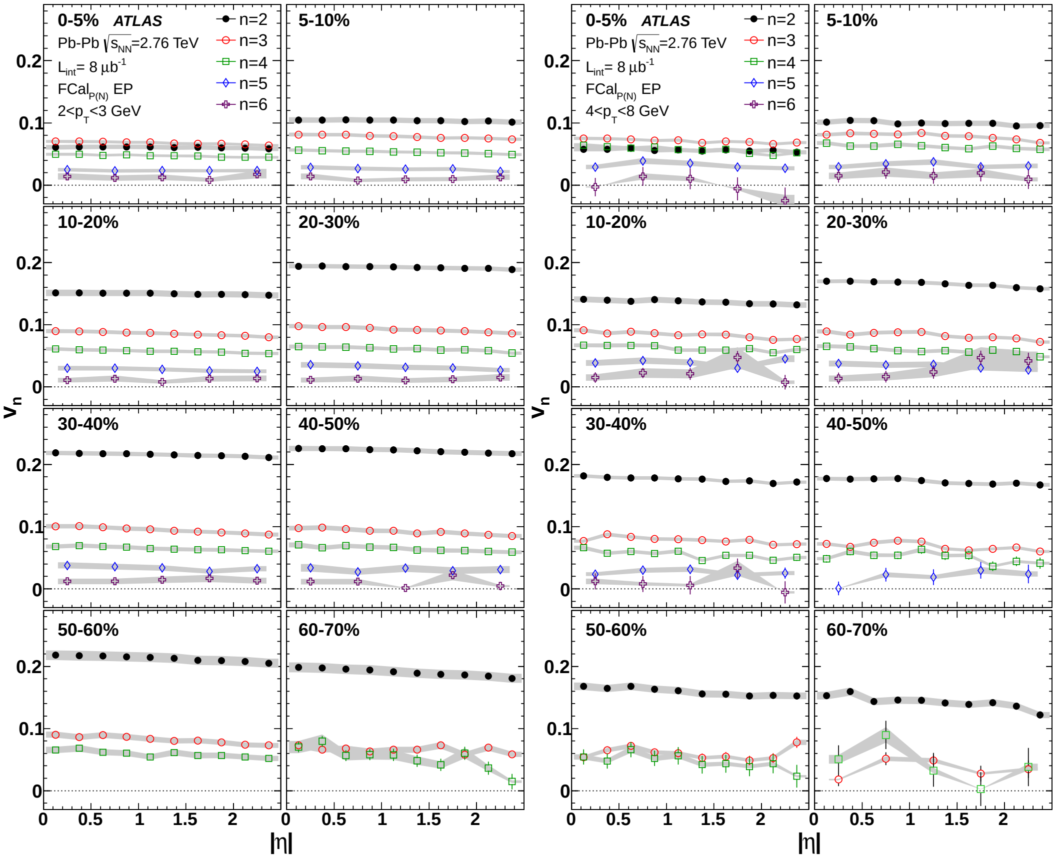

Figure A.16: Left two columns: η dependence of v_n for $p_{\rm T} \in (2, 3)$ GeV. Right two columns: η dependence of v_n for $p_{\rm T} \in (4, 8)$ GeV. Each panel corresponds to a different centrality class. The values are obtained using sub-FCal event-planes.

A.4 Comparison between results for full-FCal and $\mathrm{FCal}_{\mathrm{P(N)}}$

Figure A.17 shows the ratios of $v_n(p_\mathrm{T})$ obtained from $\mathrm{FCal}_{\mathrm{P(N)}}$ to those obtained using full-FCal for various centrality selections. The $\mathrm{FCal}_{\mathrm{P(N)}}$ results are higher than those from full-FCal for v_2 by about 5%, but the difference decreases for mid-central collisions to about 2%. Also, the difference is almost independent of p_T, except for most central 0-5% and peripheral collisions ($> 70\%$). The results for v_3 and v_4 are more consistent across all centralities. The deviation for v_5 and v_6 are much larger, but these measurements have considerable statistical and even larger systematic uncertainties (the systematic uncertainties are not shown for clarity).

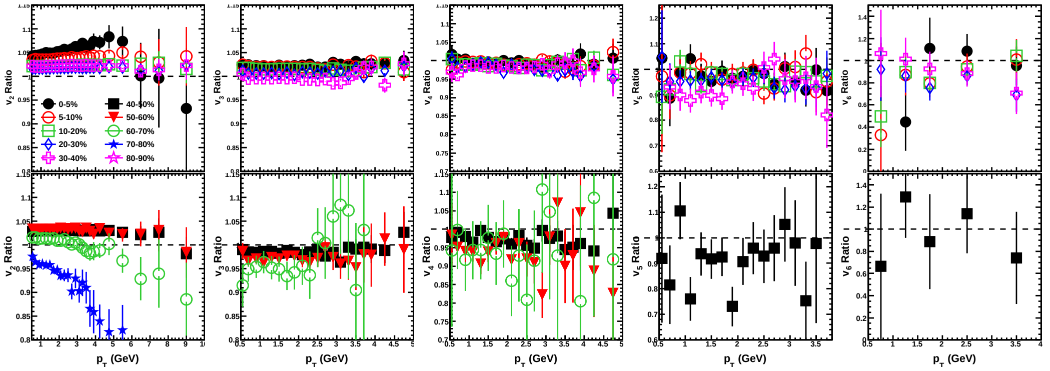

Figure A.17: Ratios of v_n obtained from $\mathrm{FCal}_{\mathrm{P(N)}}$ to those obtained from full-FCal for various centrality selections in (0-40)% for top panels and (40-80)% for the bottom panels. From left to right, they are $v_2 - v_6$.

Figure A.18 shows comparisons for the η dependence between the $\mathrm{FCal}_{\mathrm{P(N)}}$ and full-FCal results for $p_\mathrm{T} \in (1, 2)$ GeV and several centrality selections. The η dependence is stronger for the $\mathrm{FCal}_{\mathrm{P(N)}}$ results. This can be seen more clearly in the ratio plots shown in Fig. A.19. Similar ratio plots for other p_T are shown in Figs. A.20–A.21. For v_2 the change is relatively small in mid-central events but becomes larger in central and peripheral events. For $n > 2$, we see the ratios drops with η by about 10% independent of centrality, again showing that $\mathrm{FCal}_{\mathrm{P(N)}}$ results have stronger η dependence. The full-FCal measurement uses tracks with $\eta \in (-2.5, 2.5)$, while the $\mathrm{FCal}_{\mathrm{P(N)}}$ measurement uses the tracks from the opposite η side, thus the η-gap is larger for the $\mathrm{FCal}_{\mathrm{P(N)}}$ (both on average and at minimum separation) measurements. This results in the bias from short-range correlations to be smaller for the $\mathrm{FCal}_{\mathrm{P(N)}}$ measurements, resulting in a stronger η dependence.

Based on these observations, we conclude that the differences between the full-FCal and $\mathrm{FCal}_{\mathrm{P(N)}}$ are within (1-5)% for η integrated results, the only outlier would be the v_2 in (0-5)% central collisions which shows about 5% difference. The $\mathrm{FCal}_{\mathrm{P(N)}}$ results show stronger η dependence as the η separation between the ID and the sub-FCal is larger, and thus the $\mathrm{FCal}_{\mathrm{P(N)}}$ are less susceptible to short-range correlations.

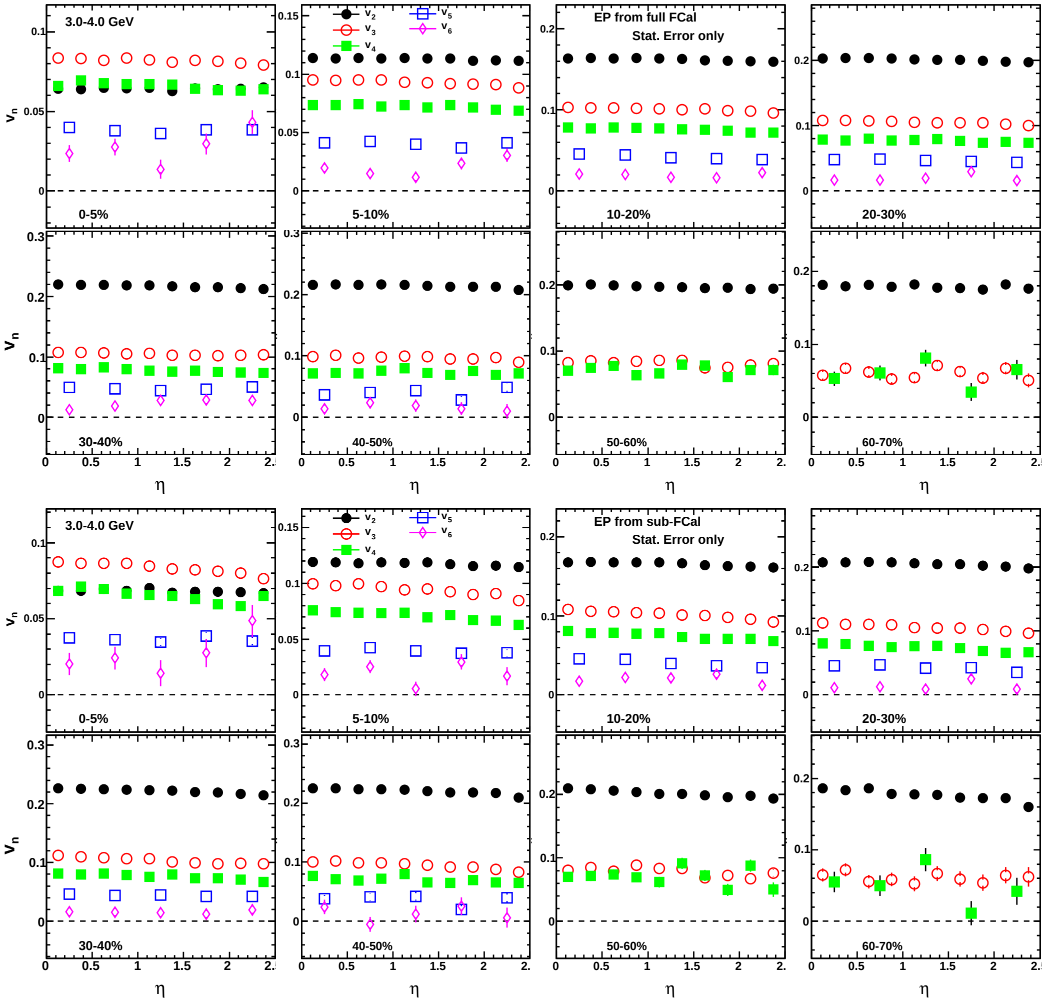

Figure A.18: Top two rows: $v_n(\eta)$ for $p_{\mathrm{T}} \in (1,2)$ GeV from full-FCal. Bottom two rows: $v_n(\eta)$ for $p_{\mathrm{T}} \in (1,2)$ GeV from fill-FCal. Each panel is a different centrality bin.

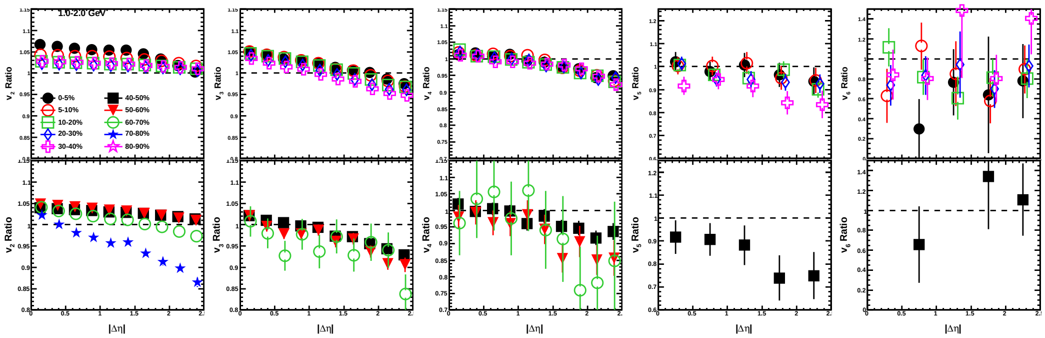

Figure A.19: Ratios of the v_n from FCal$_{P(N)}$ to those obtained from full FCal for 1-2 GeV for various centrality selections. From the left to right they are v_2, v_3, v_4, v_5 and v_6, respectively.

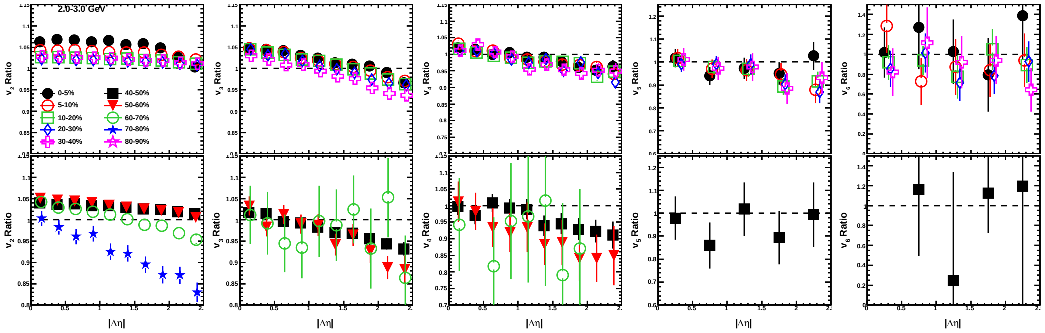

Figure A.20: Same as previous plot but for $p_{\mathrm{T}} \in (2,3)$ GeV.

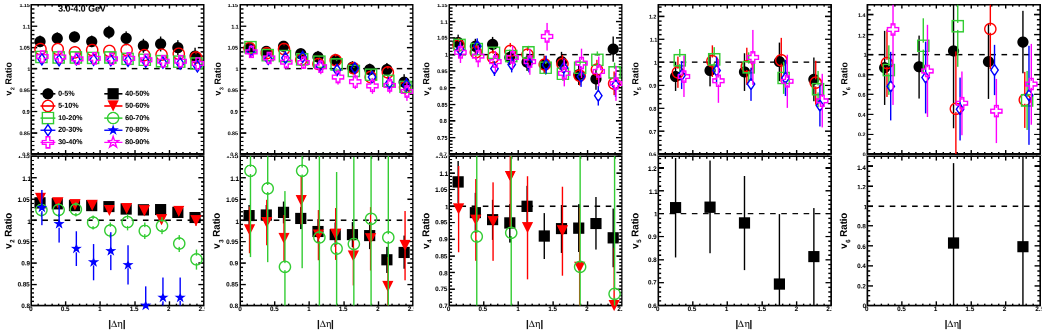

Figure A.21: Same as previous plot but for $p_{\mathrm{T}} \in (3,4)$ GeV.

Appendix B

Two-particle correlations

B.1 Accounting for detector acceptance via event mixing

The two-particle correlation method uses event mixing to remove detector effects. The foreground pairs are considered by taking the trigger and partner from the same event. The measured pair distribution in $\Delta\phi$ averaged over many events is given by:

$$\begin{aligned}
N^{Foreground}_{Measured}(\Delta\phi) &= \frac{1}{N_{events}} \sum_{events} \int \Bigg(N^{ab}(\phi_1 - \phi_2)\epsilon^a(\phi_1)\epsilon^b(\phi_2) \\
&\quad \delta(\phi_1 - \phi_2 - \Delta\phi) \Bigg) d\phi_1 d\phi_2 \\
&= \frac{1}{N_{events}} \sum_{events} N^{ab}(\Delta\phi) \int \epsilon^a(\phi_1)\epsilon^b(\phi_1 - \Delta\phi) d\phi_1 \\
&= \left(\int \epsilon^a(\phi_1)\epsilon^b(\phi_1 - \Delta\phi) d\phi_1 \right) \times \frac{1}{N_{events}} \sum_{events} N^{ab}(\Delta\phi) \\
&= \epsilon^{ab}_{pair}(\Delta\phi) \times \frac{1}{N_{events}} \sum_{events} N^{ab}(\Delta\phi) \\
&= \epsilon^{ab}_{pair}(\Delta\phi) \times N^{Foreground}_{ideal}(\Delta\phi) \qquad \text{(B.1)}
\end{aligned}$$

Where, $\epsilon^a(\phi)$ and $\epsilon^b(\phi)$ are the efficiencies for detecting particles of type a and b (as function of ϕ), $N^{ab}(\Delta\phi)$ is the pair distribution that would be obtained in an ideal detector on an event by event basis. And $N^{Foreground}_{ideal}(\Delta\phi)$ is the ideal pair distribution averaged over many events (which is what we want to obtain). Eq. B.1 shows that the measured pair distribution is the ideal pair distribution function times the pair acceptance function $\epsilon^{ab}_{pair}(\Delta\phi)$. The pair acceptance function is simply the convolution of the individual efficiencies $\epsilon^a(\phi)$ and $\epsilon^b(\phi)$:

$$\epsilon^{ab}_{pair}(\Delta\phi) = \int \epsilon^a(\phi_1)\epsilon^b(\phi_1 - \Delta\phi)d\phi_1 \tag{B.2}$$

If the pair acceptance function $\epsilon^{ab}_{pair}(\Delta\phi)$ can be evaluated then the $N^{Foreground}_{Ideal}(\Delta\phi)$ can be obtained as :

$$N^{Foreground}_{Ideal}(\Delta\phi) = \frac{N^{Foreground}_{Measured}(\Delta\phi)}{\epsilon^{ab}_{pair}(\Delta\phi)} \tag{B.3}$$

The pair acceptance can be reconstructed by the event mixing method. In this method, mixed-event pairs are measured by taking trigger and partner from different events.

$$\begin{aligned} N^{Mixed}_{Measured}(\Delta\phi) = \int \left(\frac{1}{N_{events}}\sum_{events} N^a(\phi_1)\right) \times \left(\frac{1}{N_{events}}\sum_{events} N^b(\phi_2)\right) \\ \times \epsilon^a(\phi_1)\epsilon^b(\phi_2)\delta(\phi_1 - \phi_2 - \Delta\phi)d\phi_1 d\phi_2 \end{aligned} \tag{B.4}$$

Where, $N^a(\phi)$ and $N^b(\phi)$ are the true single particle yields for particles a and b. For the mixed background, the trigger and partner are completely uncorrelated, so the following substitutions can be made:

$$\begin{aligned} \frac{1}{N_{events}}\sum_{events} \Psi^a(\phi_1) &= \langle N^a \rangle \\ \frac{1}{N_{events}}\sum_{events} \Psi^b(\phi_2) &= \langle N^b \rangle \end{aligned} \tag{B.5}$$

Where $\langle N^a \rangle$ and $\langle N^b \rangle$ are the average angular yields of particles of type a and b respectively. The above equation simply means that the true single particle yields have no preferred direction when averaged over many events. Thus the mixed pair distribution becomes:

$$\begin{aligned} N^{Mixed}_{Measured}(\Delta\phi) &= \int \langle N^a\rangle\langle N^b\rangle \epsilon^a(\phi_1)\epsilon^b(\phi_2)\delta(\phi_1-\phi_2-\Delta\phi)d\phi_1 d\phi_2 \\ &= \langle N^a\rangle\langle N^b\rangle \int \epsilon^a(\phi_1)\epsilon^b(\phi_2)\delta(\phi_1-\phi_2-\Delta\phi)d\phi_1 d\phi_2 \\ &= \langle N^a\rangle\langle N^b\rangle \int \epsilon^a(\phi_1)\epsilon^b(\phi_1-\Delta\phi)d\phi_1 \\ &= \langle N^a\rangle\langle N^b\rangle \epsilon^{ab}_{pair}(\Delta\phi) \end{aligned} \tag{B.6}$$

Dividing the measured foreground pairs by the background gives:

$$\begin{aligned} \frac{N^{Foreground}_{Measured}(\Delta\phi)}{N^{Mixed}_{Measured}(\Delta\phi)} &= \frac{N^{Foreground}_{Ideal}(\Delta\phi)\epsilon^{ab}_{pair}(\Delta\phi)}{\langle N^a\rangle\langle N^b\rangle\epsilon^{ab}_{pair}(\Delta\phi)} \\ &= \frac{N^{Foreground}_{Ideal}(\Delta\phi)}{\langle N^a\rangle\langle N^b\rangle} \\ &= C(\Delta\phi) \end{aligned} \tag{B.7}$$

Where $C(\Delta\phi)$ is the correlation function that we wanted to construct.

In this derivation, only the dependence of the pair distributions and pair efficiency on $\Delta\phi$ has been considered. It is very straightforward to extend it to also include $\Delta\eta$ dependence. Eq.B.1 generalizes to :

$$N^{Foreground}_{Measured}(\Delta\phi,\Delta\eta) = \epsilon^{ab}_{pair}(\Delta\phi,\Delta\eta) \times N^{Foreground}_{ideal}(\Delta\phi,\Delta\eta) \tag{B.8}$$

The pair acceptance is given by:

$$\epsilon^{ab}_{pair}(\Delta\phi,\Delta\eta) = \int \epsilon^a(\phi_1,\eta_1)\epsilon^b(\phi_1-\Delta\phi,\eta_1-\Delta\eta)d\phi_1 d\eta_1 \tag{B.9}$$

Similarly the mixed events distribution becomes:

$$N^{Mixed}_{Measured}(\Delta\phi,\Delta\eta) = \langle N^a\rangle\langle N^b\rangle\epsilon^{ab}_{pair}(\Delta\phi,\Delta\eta) \tag{B.10}$$

And finally for the correlation function is obtained as :

$$
\begin{aligned}
C(\Delta\phi,\Delta\eta) &= \frac{N^{Foreground}_{Measured}(\Delta\phi,\Delta\eta)}{N^{Mixed}_{Measured}(\Delta\phi,\Delta\eta)} \\
&= \frac{N^{Foreground}_{Ideal}(\Delta\phi,\Delta\eta)\epsilon^{ab}_{pair}(\Delta\phi,\Delta\eta)}{\langle N^a\rangle\langle N^b\rangle\epsilon^{ab}_{pair}(\Delta\phi,\Delta\eta)} \\
&= \frac{N^{Foreground}_{Ideal}(\Delta\phi\Delta\eta)}{\langle N^a\rangle\langle N^b\rangle} \qquad \text{(B.11)}
\end{aligned}
$$

Note that the formalism derived here is completely general. Not only can it be applied to heavy-ion collisions but also to *p*-*p* collisions as well. Of course, the shape of the correlation function will differ depending on the colliding system, but the trick of dividing by the mixed background in order to account for the pair acceptance will always work.

B.2 Factorization of two-particle correlations in heavy ion collisions

In heavy-ion collisions the yield of particles about can be expanded in a Fourier series as:

$$dN^a/d\phi = N^a_0\left(1 + 2\sum_{n=1}^{\infty} v^a_n \times \cos(n\phi - n\Phi_n)\right) \qquad \text{(B.12)}$$

Where v^a_n are the flow harmonics and Φ_n are the event-planes. The superscript a is used to indicate dependence on other parameters such as particle species, p_T etc. If the dominant effect in the dynamics of the collision is flow, then the two-particle correlation can be reconstructed from the single particle yields:

$$
\begin{aligned}
&C(\Delta\phi) \propto \int \left(1 + 2\sum_{n=1}^{\infty} v_n^a \times \cos(n\phi_1 - n\Phi_n)\right) \\
&\times\left(1 + 2\sum_{m=1}^{\infty} v_m^b \times \cos(m\phi_2 - n\Phi_m)\right)\delta(\phi_1 - \phi_2 - \Delta\phi)d\phi_1 d\phi_2 \\
&= \int \left(1 + 2\sum_{n=1}^{\infty} v_n^a \times \cos(n\phi_1 - n\Phi_n)\right) \\
&\times\left(1 + 2\sum_{m=1}^{\infty} v_m^b \times \cos(m\phi_1 - m\Delta\phi - n\Phi_m)\right)d\phi_1 \\
&= \int \left(1 + 2\sum_{n=1}^{\infty} v_n^a \times \cos(n\phi_1 - n\Phi_n)\right. \\
&\left. +2\sum_{m=1}^{\infty} v_m^b \times \cos(m\phi_1 - m\Delta\phi - m\Phi_m)\right)d\phi_1 \\
&+ \int 4\sum_{n,m=1}^{\infty} v_n^a v_m^b \cos(n\phi_1 - n\Phi_n) \times \cos(m\phi_1 - m\Delta\phi - m\Phi_m)d\phi_1
\end{aligned}
\tag{B.13}
$$

Using $\int \cos(n\phi + \delta)d\phi = 0$, the terms linear in v_n become 0. So the expression for the correlation becomes:

$$
C(\Delta\phi) \sim \int \left(1 + 4\sum_{n,m=1}^{\infty} v_n^a v_m^b \cos(n\phi_1 - n\Phi_n) \times \cos(m\phi_1 - m\Delta\phi - m\Phi_m)\right)d\phi_1
\tag{B.14}
$$

Using $2\cos(A) \times \cos(B) = \cos(A+B) + \cos(A-B)$ this can be written as:

$$\begin{aligned}
C(\Delta\phi) \sim \int \Bigg(& (1 + 2\sum_{n,m=1}^{\infty} v_n^a v_m^b \cos(n\phi_1 - n\Phi_n + m\phi_1 - m\Delta\phi - m\Phi_m) \\
& + 2\sum_{n,m=1}^{\infty} v_n^a v_m^b \cos(n\phi_1 - n\Phi_n - m\phi_1 - m\Delta\phi - m\Phi_m)\Bigg) d\phi_1 \\
= \int \Bigg(& 1 + 2\sum_{n,m=1}^{\infty} v_n^a v_m^b \cos((n+m)\phi_1 - n\Phi_n - m\Phi_m - m\Delta\phi) \\
& + 2\sum_{n,m=1}^{\infty} v_n^a v_m^b \cos((n-m)\phi_1 - n\Phi_n + m\Phi_m - m\Delta\phi)\Bigg) d\phi_1 \qquad \text{(B.15)}
\end{aligned}$$

Again using $\int \cos(k\phi + \delta)d\phi = 0$ for $k \neq 0$, all the cosine terms vanish except the n=m terms. This gives:

$$C(\Delta\phi) \sim \int \left(1 + 2\sum_{n=1}^{\infty} v_n^a v_n^b cos(-n\Delta\phi)\right) d\phi_1 \qquad \text{(B.16)}$$

Since the integrand is independent of ϕ_1, the integration just gives a factor of 2π, which we drop as we are interested in only the angular shape. This gives

$$C(\Delta\phi) \sim 1 + 2\sum_{n=1}^{\infty} v_n^a v_n^b cos(n\Delta\phi) \qquad \text{(B.17)}$$

Thus, the harmonics obtained from the two-particle correlations are simply the product of the corresponding single particle harmonics of the same order:

$$v_n^{correlation} = v_n^a \times v_n^b \qquad \text{(B.18)}$$

However, this scaling relation can be violated due to many reasons. For example due to correlations coming from jets and also from lack of collective behavior in the medium. It is of importance to note that while measuring the single particle distribution (Eq.B.12) required knowledge of the reaction plane, the two-particle correlation (Eq.B.17) can be calculated without determining the reaction plane.

B.3 Systematic errors in 2PC method

B.3.1 Monte Carlo studies

Direct detector simulation of Pb+Pb collisions provide another handle on the systematic uncertainties of the 2PC v_n measurements. For this purpose, a detailed Monte-Carlo study is done using events generated by the event generator HIJING [138]. Since HIJING lacks any physics that can generate flow, a flow-afterburner code is used that implements a v_2 signal by artificially rotating the generated particles by appropriate angles [61]. However, the exact implementation of the rotations also introduces small signals for v_4 and v_6. The final set of particles are run through a full GEANT simulation of the ATLAS detector, and then analyzed.

The analysis procedure is identical to real data analysis with similar cuts on the reconstructed tracks. However, due to limited event statistics, the mixed events are matched within 5 mm in z-vertex, instead of the 1 mm matching used in data analysis (it is not a big effect as discussed in Section B.3.2). Also the analyses are done in large intervals of p_{T}, η and centrality wherever possible to reduce statistical fluctuations.

In order to determine the truth $v_{n,n}(v_n)$, a similar 2PC analysis is done using the generated tracks (i.e. the tracks from the event generator), which are the compared to the reconstructed $v_{n,n}(v_n)$ to determine the systematic errors. Only charged primary[1] tracks are used for the truth analysis.

Figure B.1 shows the $v_{n,n}$ and v_n at generator level integrated over a broad centrality and p_{T} range. As expected from the flow-afterburner only clear even order harmonic flow signals are observed. The odd order flow signals are very small, in particular $v_{3,3}$ and $v_{5,5}$ signal are consistent with zero, there is a very small non-zero signal for $v_{1,1}$ possibly due to artificial momentum imbalances introduced in the rotation procedure of the flow implementation since this procedure does not explicitly enforce momentum conservation.

In Fig.B.2 the truth and reconstructed $v_{2,2}$ as a function of centrality and p_{T} for fixed-p_{T} correlations for $|\Delta\eta| < 5$. The reconstructed values are systematically higher than the truth values by about 1-3% on the $v_{2,2}$ level, and have some centrality and p_{T} dependence. This translates into a 0.5-1.5% difference for v_2. Figure B.3 and B.4 show the same studies done for $v_{4,4}$ and $v_{6,6}$. It is seen that the deviation between truth and reconstructed values are appreciably larger. Overall the $v_{4,4}$ and $v_{6,6}$ signal for correlations at reconstruction level are about 4% and 10% higher than the correlation at truth level, which

---

[1] Primary tracks are the ones produced at the collision vertex as opposed to secondary tracks which can be from decays that are displaced from the primary vertex. In the data the $z0\sin(\theta)$ and $d0$ cuts remove secondary particles.

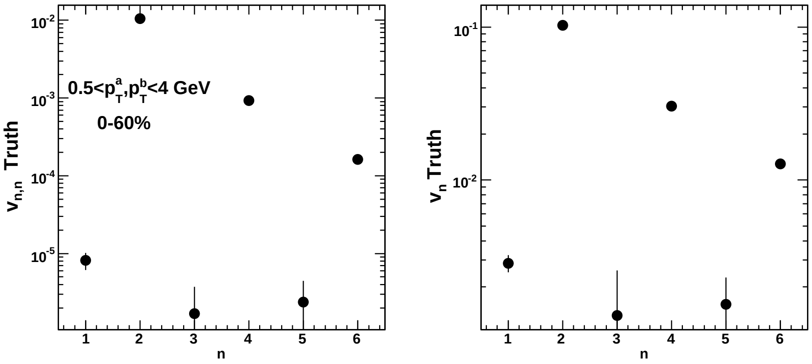

Figure B.1: The $v_{n,n}$ and v_n at generator (truth) level for fixed-p_{T} correlation in $(0.5-4.0)$ GeV, $|\Delta\eta| \in (0,5)$ and $(0-60)\%$ centrality.

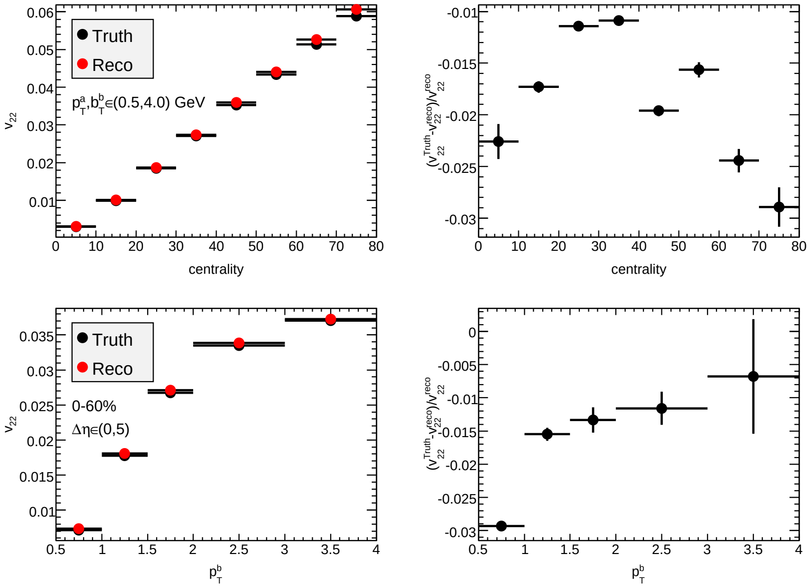

Figure B.2: Left Plots: $v_{2,2}$ values obtained from the correlations as a function of $\Delta\eta$ for truth(black) and reconstructed(red) tracks. Right Plots: The fractional difference between truth $v_{2,2}$ and reconstructed $v_{2,2}$. Top panels shows the centrality dependence while the bottom panel shows the p_{T} dependence. All plots are made for $|\Delta\eta| < 5$.

translate into a 2% and 5% error for v_4 and v_6 respectively.

In summary, it is seen that the reconstructed distribution are systematically higher than the truth for harmonics n=2,4,6, where there is an input signal.

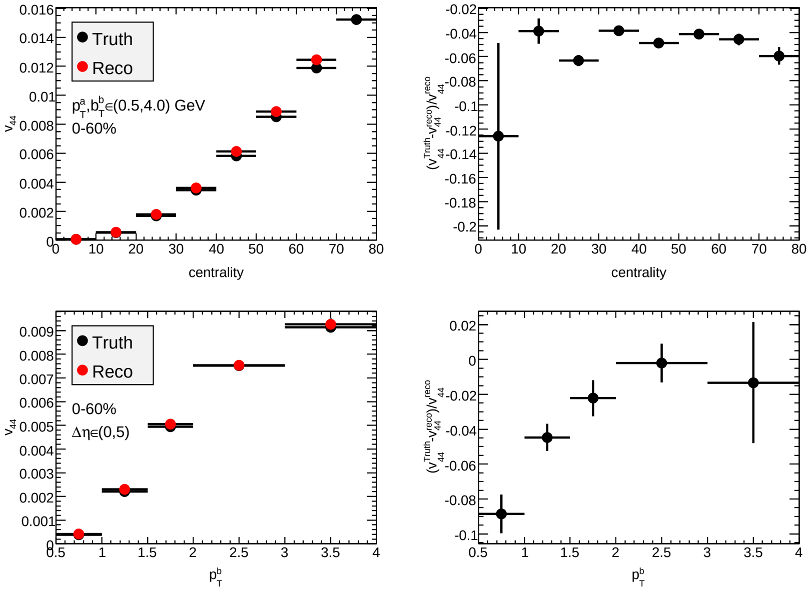

Figure B.3: same as Figure B.2 but for $v_{4,4}$

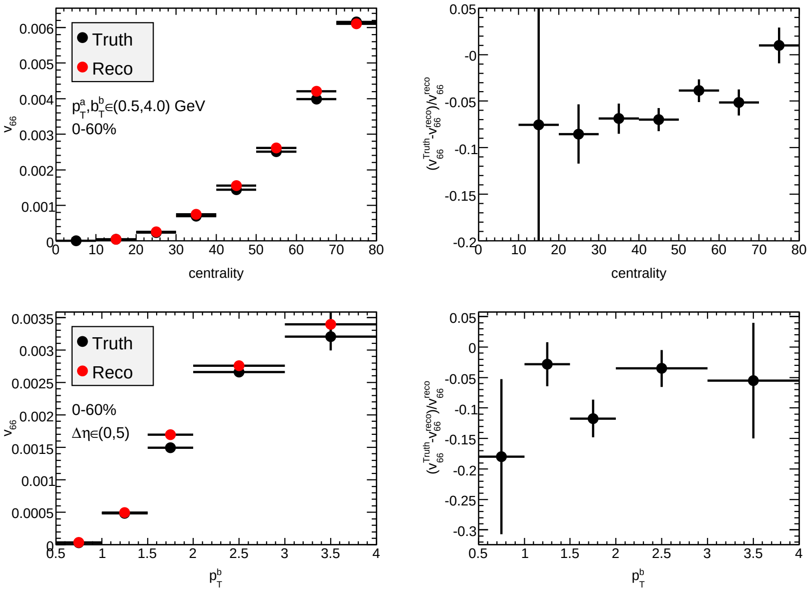

Figure B.4: same as Figure B.2 but for $v_{6,6}$

The fractional deviations from the true flow signal seems to increase with decreasing flow signal ($n = 2 \to 4 \to 6$). With the assumptions that the difference smoothly interpolates as function of n, the systematic error for v_3 is taken to be the average deviation seen for v_2 and v_4, and that for v_5 to be the average deviation seen for v_4 and v_6. The measured v_1 is typically in between v_2 and v_4, however, its error is conservatively quoted as that for v_4. Table B.1 summarizes the systematic deviation between the reconstructed and truth for v_n. They are conservatively quoted to cover the centrality and p_{T} dependent variations.

δv_n (%)					
n=1	n=2	n=3	n=4	n=5	n=6
2%	$< 1.5\%$	1.5%	2%	3.5%	5%

Table B.1: Estimated systematic deviation of v_n constructed from two-particle azimuthal correlation between MC reconstructed and MC truth particles. They are conservatively quoted to cover the centrality and p_{T} dependent variations

B.3.2 Systematic study of event mixing procedure

The 2PC analysis uses the event mixing technique to estimate the pair acceptance. The mixed-events are matched with within 5% in centrality and $1\,mm$ in z-vertex. Each event is typically mixed with 20 other events in order for the mixed-event distribution to have much larger statistics. The two events used for mixing are separated, by $\sim (4k - 80k)$ events between them[2].

Potential detector effects present in same-event pairs that are not accounted for in the mixed events need to be checked. There are three possible sources that can lead to deviation from the true pair acceptance.

1. The two mixed events are typically separated in time, any transient variation in the detector conditions can affect the same-event pairs but not the mixed event-pairs.
2. The effect of finite centrality bin width in the mixing.
3. The effect of finite z-vertex matching in the mixing.

There are also some other effects that are not accounted for by event mixing that are present in same-event pairs. For example in the same-event the

---

[2] Since 5% centrality binning is used for mixing, one in 20 events will have the same centrality bin. Similarly because of $1\,mm$ z-vertex binning, one in 200 events will be in the same z-vertex bin (events with z_{vtx}100 mm are used in the 2PC analysis). Thus two events in the same mixing bin have a typical minimum separation $\sim 20 \times 200 = 4k$ and a maximum separation of $4k \times 20 = 80k$.

presence of the trigger track might affect the ability to reconstruct the associated track, however such effects only affect close pairs, i.e. small $\Delta\eta$–$\Delta\phi$ separation. Since the 2PC analysis involves pairs with $|\Delta\eta| > 2$, these effects are not an issue.

To quantify the variation of pair acceptance, it should first be pointed out that any relative change of the pair acceptance by a small perturbation $h(\Delta\phi)$, adds linearly to the Fourier coefficients:

$$\begin{aligned} h &\propto 1 + 2\sum_n (\epsilon_n \cos(n\Delta\phi)) \\ dN/d\Delta\phi \times h &\propto 1 + 2\sum_n (v_{n,n} + \epsilon_n)\cos(n\Delta\phi) + \sum_{n,m} O(v_{n,n}\epsilon_m) \end{aligned} \quad \text{(B.19)}$$

Thus the influence of a check or a cut can be evaluated by simply studying the Fourier transform of the ratio of the pair acceptances with and without the cut.

Check I : effects of proximity mixing

To check the time dependence of the pair acceptance, a special mixing procedure is run in which two mixed-event pools are kept. The first pool uses events that are separated from each other by less than m events in between. The second "delayed" pool uses events that are within $[m, 2m]$ from each other (see Fig. B.5). This is done for $m = 10k$, $20k$ and $40k$ and the variation of the pair acceptance is studied by taking the ratio of the mixed pair distribution constructed from the two pools. The results are showed in Fig. B.6 for $2 < |\Delta\eta| < 5$. It is seen that the disagreement is less than (1-2)$\times 10^{-6}$ for n=6, but slightly larger for n=1 and 2. The difference seems to grow a little for higher p_{T}.

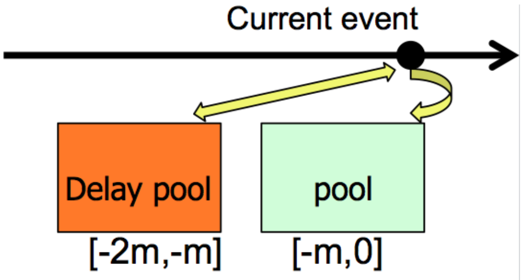

Figure B.5: The idea of a delayed pool used for event mixing.

Figure B.7 shows the same study but for $|\Delta\eta| < 0.1$. It is seen that the systematic deviations are about factor of two larger. While for an intermediate

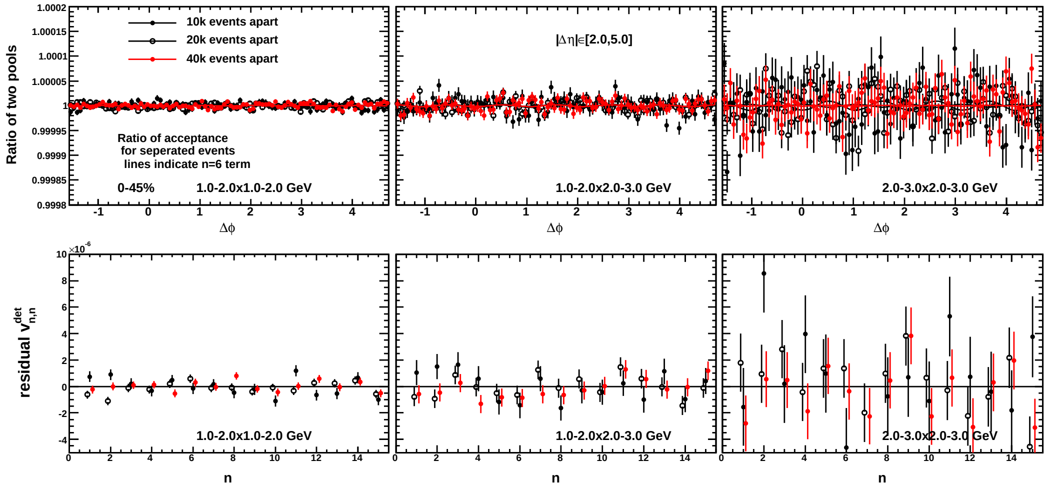

Figure B.6: The variation of pair acceptance for $|\Delta\eta| \in (2, 5)$ (top panels) and corresponding residual $v_{n,n}$ (bottom panels) for three correlations: (1-2)×(1-2) GeV (left), (2-3)×(1-2) GeV (middle) and (2-3×(2-3) GeV (right). This is done for $2 < |\Delta\eta| < 5$. The curves is the upper panels indicate the residual fake $v_{6,6}$ contribution. The (0-45)% centrality interval is used to increase the pair statistics.

$\Delta\eta$ slice, for example $0.5 < \Delta\eta| < 1.0$, shown in Fig. B.8, the deviation is in between. Table B.2 summarizes the systematic errors estimated from this study.

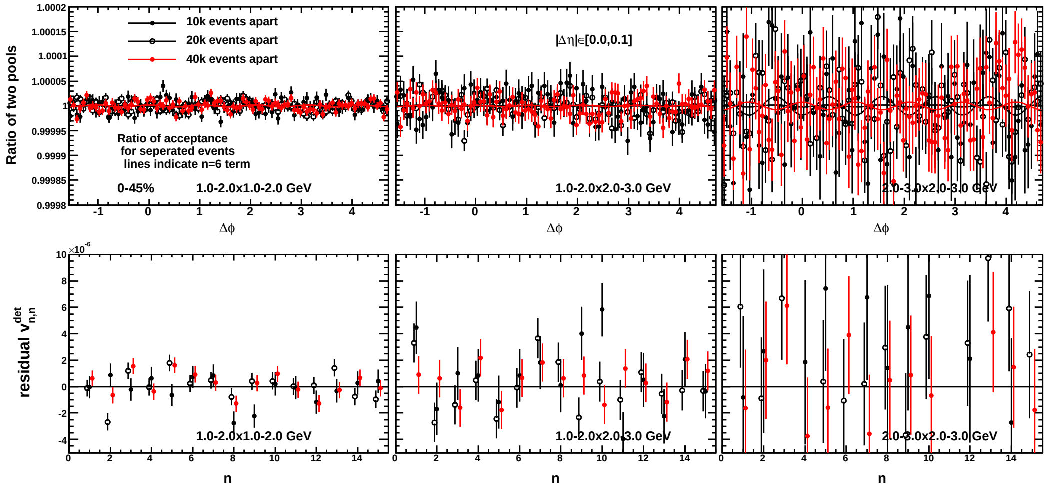

Figure B.7: Same as previous plot but for $|\Delta\eta| < 0.1$.

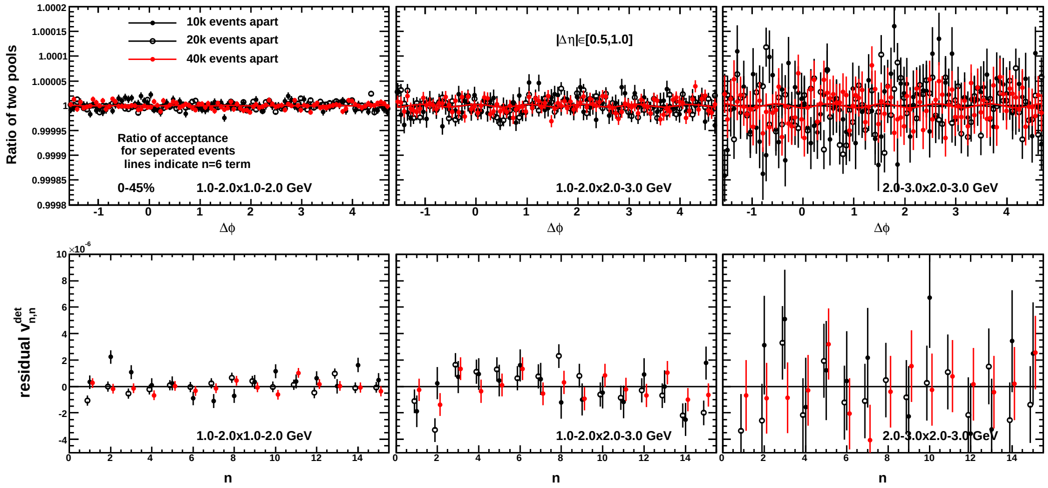

Figure B.8: Same as previous plot but for $0.5 < |\Delta\eta| < 1.0$.

	residual $v_{n,n}$ $(\times 10^{-6})$		
p_T selections	$2 < \|\Delta\eta\| < 5$	0.1 $\|\Delta\eta\|$ slice	0.5 $\|\Delta\eta\|$ slice
$p_T^a, p_T^b < 2$ GeV	1	2.5	2
$p_T^a, p_T^b > 2$ GeV	2.5	5.5	4
$p_T^a > 2$ GeV, $p_T^b <2$ GeV	1.8	4	3

Table B.2: Residual time dependent variation of the $v_{n,n}$ for various p_T selections and $\Delta\eta$ bin widths.

Check II : effects of centrality matching

Centrality matching is necessary only if the pair acceptance has a centrality dependence. Since fairly narrow centrality bins are used in the event mixing (matched within 5%), the centrality dependence, if any, can have only a small effect. To estimate this residual dependence, the mixed-event pair-distributions are constructed for three different centrality matchings: 2.5%, 5% and 10%. The 2.5% and 5% centrality matched pair distributions are then divided by the 10% matched pair distribution. The Fourier transformation of this ratio gives the variation of the $v_{n,n}$ when changing the centrality matching from 2.5% to 10%, and is used to estimated the systematic uncertainties associated with centrality matching. The results for three representative $|\Delta\eta|$ bins are shown in Figures B.9-B.11. For the $2 < |\Delta\eta| < 5$ slice, the variation is less than 10^{-6} for $p_T < 2$ GeV, but increases to about 2×10^{-6} for (2-3) GeV. The variation is also appreciably larger for narrow $\Delta\eta$ bins. The errors from this check are conservatively quoted to be independent of n, they are listed in

Table B.3

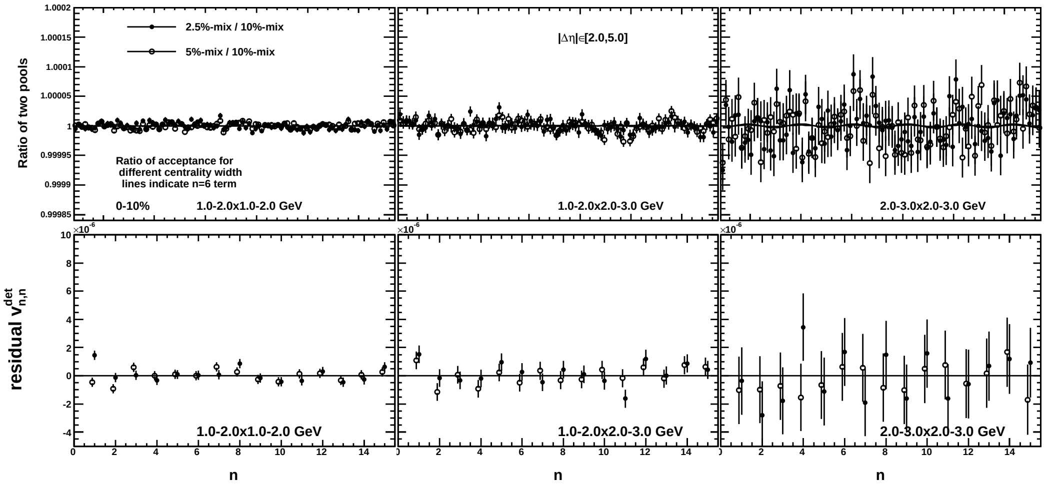

Figure B.9: The variation of the pair acceptance (top panels) and corresponding residual $v_{n,n}$ (bottom panels) of 2.5% and 5% centrality mixing relative to 10% centrality mixing for three correlations: (1-2)×(1-2) GeV (left),(2-3)×(1-2) GeV (middle) and (2-3)×(2-3) GeV (right). This is done for $2 < |\Delta\eta| < 5$. The curves on the top panels indicate the residual fake $v_{6,6}$ contribution. The (0-10)% centrality range is used.

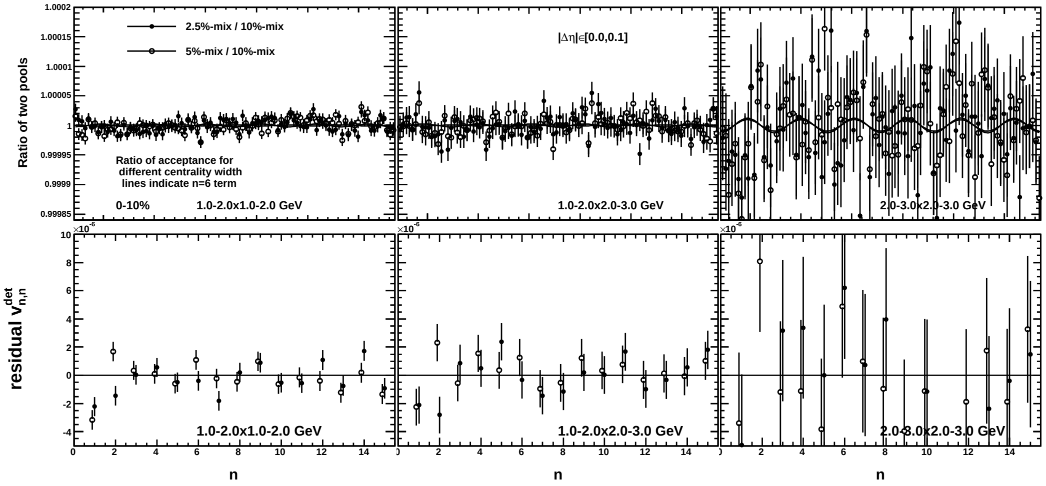

Figure B.10: Same as previous plot but for $|\Delta\eta| < 0.1$.

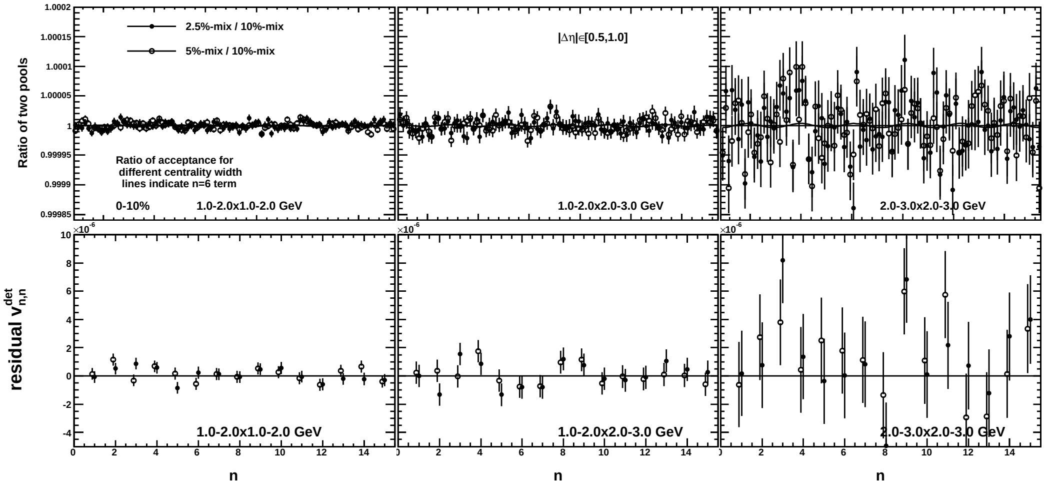

Figure B.11: Same as previous plot but for $0.5 < |\Delta\eta| < 1.0$.

	residual $v_{n,n}$ ($\times10^{-6}$)		
p_{T} selections	$2 < \lvert\Delta\eta\rvert < 5$	0.1 $\lvert\Delta\eta\rvert$ slice	0.5 $\lvert\Delta\eta\rvert$ slice
$p_{\mathrm{T}}^{a}, p_{\mathrm{T}}^{b} < 2$ GeV	1	3	1.5
$p_{\mathrm{T}}^{a}, p_{\mathrm{T}}^{b} > 2$ GeV	2	3	2
$p_{\mathrm{T}}^{a} > 2$ GeV, p_{T}^{b} <2 GeV	1.25	3	3

Table B.3: Residual centrality dependent variation of the $v_{n,n}$ for various p_{T} selection and $\Delta\eta$ bin width

Check III : effects of z-vertex matching

The holes/inefficiencies in the detector are present at different values of η depending on the position of the z-vertex. A finite z-vertex binning used for the mixed events can thus have an impact on the accuracy with which the mixed-events reproduce the pair acceptance. The 2PC analysis uses a narrow binning of 1 mm to match the mixed events. To quantitatively evaluate the residual effect of z-vertex binning, the mixed-event pair distribution are evaluated for several different z-vertex binning sizes ranging from 25 mm to 1 mm. The ratio of the different pair distributions is then taken to that for the 1 mm binning. The Fourier transform of these ratios is used to determine the residual effects of z-vertex matching on $v_{n,n}$. A wide centrality range of (0-45)% is used to maximize the pair statistics. Figures B.12- B.14 show the results for three different $\Delta\eta$ ranges. To guide the eye, $\pm 2 \times 10^{-6}$ bands are plotted on all the $v_{n,n}$ vs n plots (bottom panels). A significant dependence on the z-binning is noticed, especially for the $|\Delta\eta| \in (0, 0.1)$ bin (Fig. B.13). However, the changes from 5 mm to 1 mm binning are relatively small. The differences tend to increase a little for the higher p_{T} bin combinations, and also seem to have small but significant systematic variation with n. In particular, the deviation for n=2 is larger than for other harmonic terms. However, since the $v_{2,2}$ signal is fairly large, this error, when converted into relative error, becomes very small (typically less than 1%). Hence is much smaller than the other sources of systematic errors. The errors from z-vertex matching are conservatively assigned independent of n to cover the variation between 5 mm mixing and 1 mm mixing for n>2. They are listed in Table B.4.

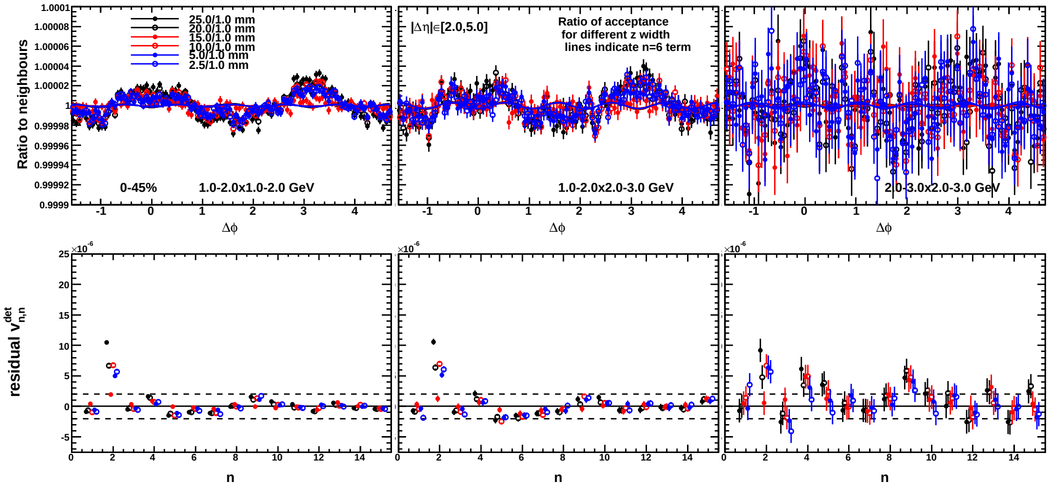

Figure B.12: The variation of pair acceptance (top panels) and corresponding residual $v_{n,n}$ (bottom panels) for various z-vertex binning relative to 1 mm binning for three correlations: (1-2)×(1-2) GeV (left), (2-3)×(1-2) GeV (middle) and (2-3)×(2-3) GeV (right). This is done for $2 < |\Delta\eta| < 5$. The curves on the top panels indicate the residual fake $v_{6,6}$ contribution. Dashed lines on the bottom panels indicate $\pm 2 \times 10^{-6}$ band. The (0-45)% centrality interval is used to increase the pair statistics.

Summary of the uncertainty

The final systematic errors from residual detector systematic estimated by the above three checks are included in Table B.5. They are obtained as the quadrature sum of all three sources. Note that these are absolute errors. The errors for the v_n are obtained by propagation of these errors when calculating the v_n via fixed-p_{T} (Eq. 4.7) or mixed-p_{T} (Eq. 4.9) correlations.

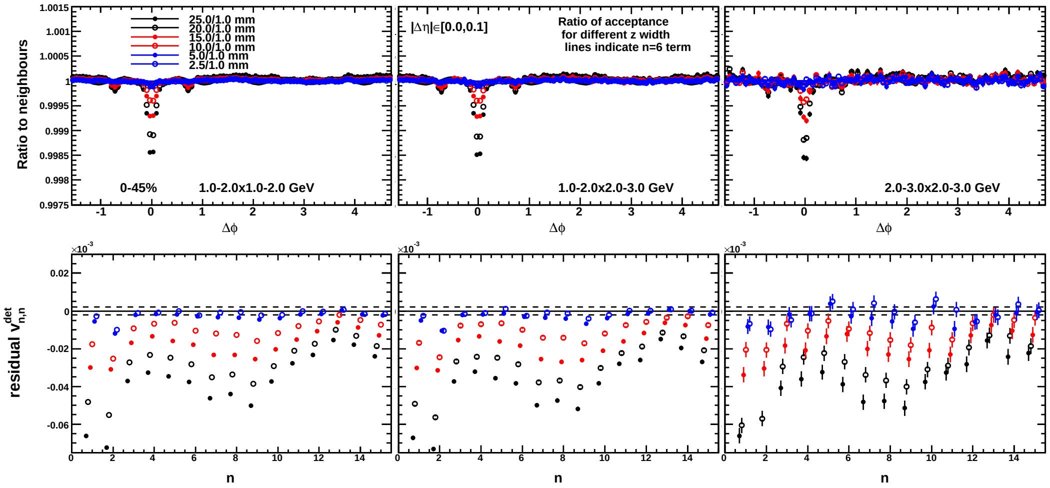

Figure B.13: Same as previous plot, except for $|\Delta\eta| \in (0.0, 0.1)$.

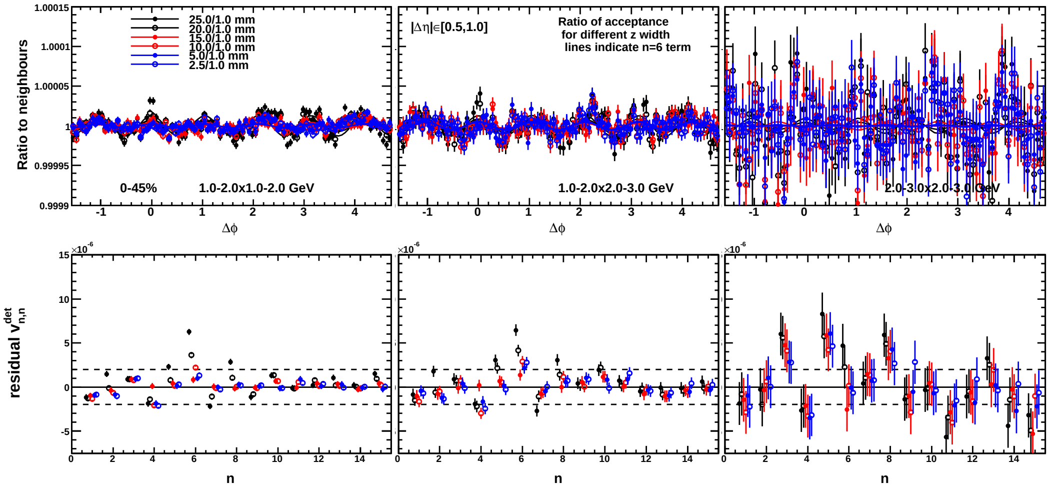

Figure B.14: Same as previous plot, except for $|\Delta\eta| \in (0.5, 1.0)$.

	residual $v_{n,n}$ $(\times10^{-6})$		
p_{T} selections	$2 < \|\Delta\eta\| < 5$	0.1 $\|\Delta\eta\|$ slice	0.5 $\|\Delta\eta\|$ slice
$p_{\mathrm{T}}^{a}, p_{\mathrm{T}}^{b} < 2$ GeV	2	4	3
$p_{\mathrm{T}}^{a}, p_{\mathrm{T}}^{b} > 2$ GeV	5	6	4
$p_{\mathrm{T}}^{a} > 2$ GeV, $p_{\mathrm{T}}^{b} <2$ GeV	3	7	5

Table B.4: Residual z-vertex binning dependent variation of the $v_{n,n}$ for various p_{T} and $\Delta\eta$ bins.

	residual $v_{n,n}$ ($\times 10^{-6}$)		
p_{T} selections	$2 < \|\Delta\eta\| < 5$	0.1 $\|\Delta\eta\|$ slice	0.5 $\|\Delta\eta\|$ slice
$p_{\mathrm{T}}^{a}, p_{\mathrm{T}}^{b} < 2$ GeV	2.5	5.0	3.2
$p_{\mathrm{T}}^{a}, p_{\mathrm{T}}^{b} > 2$ GeV	6	8.7	6
$p_{\mathrm{T}}^{a} > 2$ GeV, $p_{\mathrm{T}}^{b} <2$ GeV	3.7	8.6	6.6

Table B.5: The systematic errors for $v_{1,1} - v_{6,6}$ estimated for effects not cancelled out by event mixing. These are calculated as the quadrature sum of values in Tables B.2-B.4.

B.4 Additional plots for $v_{1,1}$ and v_1

Figure B.15-B.16 show the fit result with default set up for other centrality selections used for v_1 analysis.

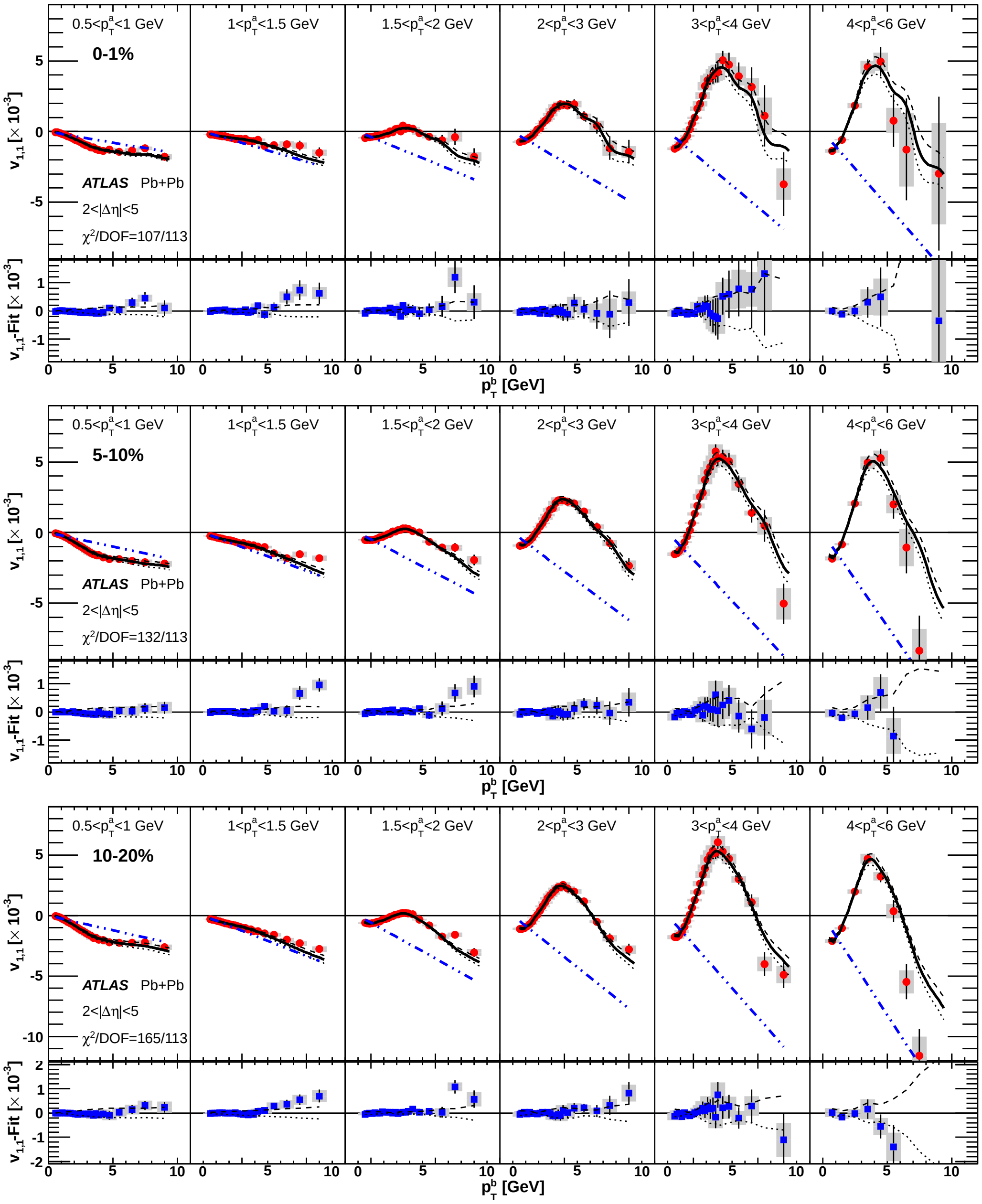

Figure B.15: Same as Fig. 4.18 but for (0-1)%, (5-10)%, and (10-20)% centrality intervals

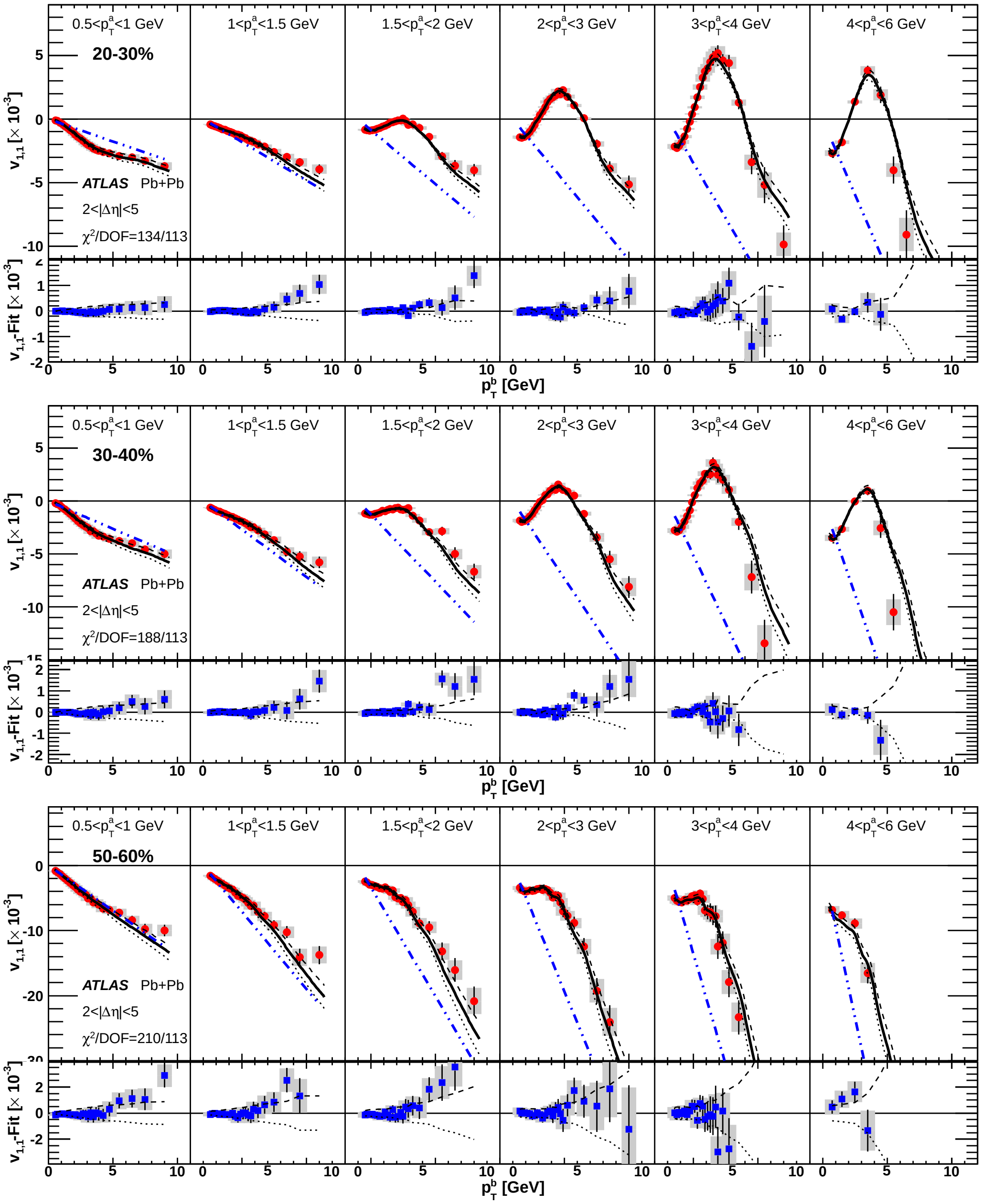

Figure B.16: Same as Fig. 4.18 but for (20-30)%, (30-40)%, and (50-60)% centrality intervals.

Appendix C

Event by Event v_n measurements

C.1 Response functions

Figure C.1 shows the difference of the x-component of the per-particle flow vector for the two symmetric half-IDs for n=2 in four centrality ranges. Also shown are fits to a Gaussian function. The lower panels show the ratio of the distribution to the fit. The fits work well up to 50% centrality. However significant deviations are observed in the tails of the distributions for more peripheral collisions. The same behaviour is seen for higher order harmonics as illustrated by Figure C.2.

Since the distributions in Figs. C.1-C.2 represent the difference between two independent estimates of v_n, sampled M times from the same underlying azimuthal distribution, where the M is the multiplicity, the resulting distributions should instead be described by the student's T-distribution. To check whether this is the case, the distributions are fit with both a T-distribution and a Gaussian function for the (65-70)% centrality interval as shown in the left panel of Fig. C.3. The T-distribution describes the measured distribution quite well. The degrees of freedom extracted from the fit is about 50, this can be compared with the event multiplicity in half ID which is about 80. The right panel of Fig. C.3 also shows the distribution obtained with an η gap of 2 units between the subevents. The non-Gaussian tail is seen here as well, and is again well described by the T-distribution. This implies that the tail has nothing to do with non-flow effects, instead it is statistical in origin. This is checked in a simple toy MC simulation where tracks are generated according to the experimental multiplicity. This is shown in Fig. C.4, where the flow-vector difference between two sub-subevents are plotted for n=2. A non-Gaussian

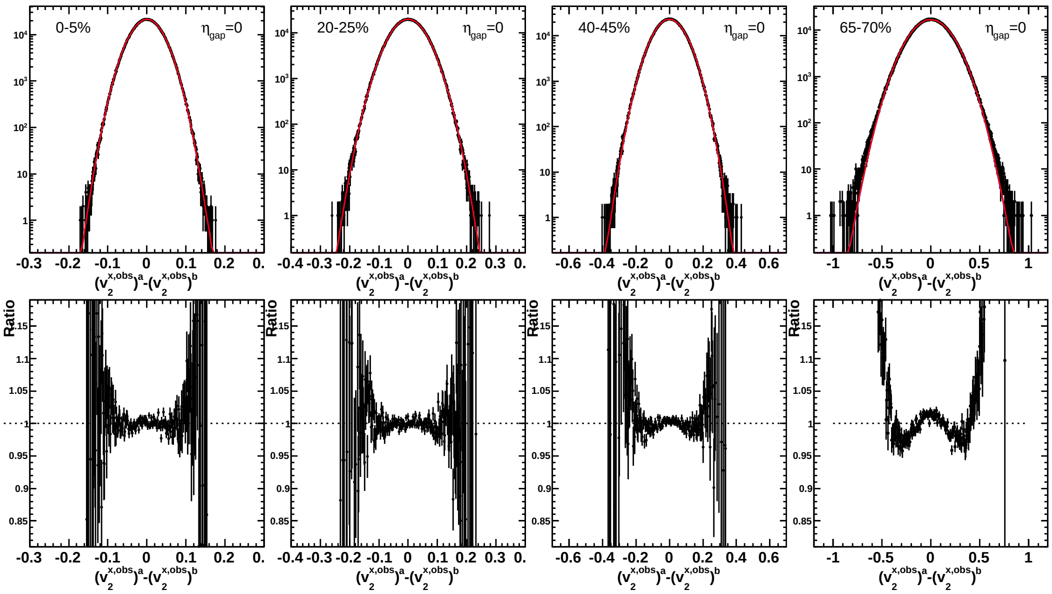

Figure C.1: Top panels: The difference between the x-components of the per-particle flow vector measured in the two symmetric half-IDs without an η gap, for n=2 in four centrality intervals. The red lines indicate a fit to a Gaussian function. Lower panels: The ratio of the distribution to the fit.

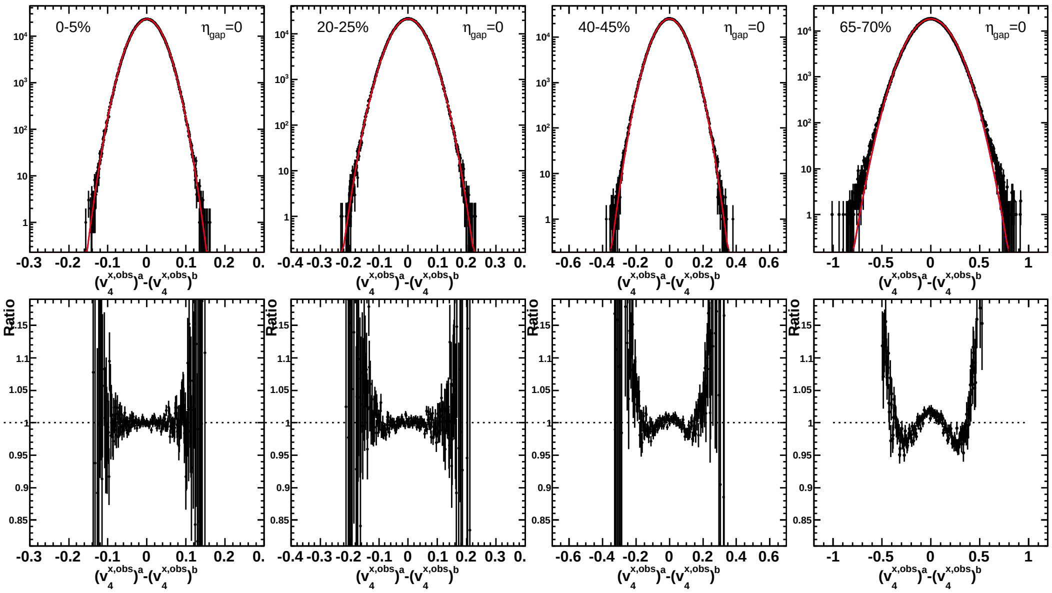

Figure C.2: Same as previous plot but for n=4.

tail indeed shows up.

Figures C.5-C.7 summarize the basic properties of the difference of per-

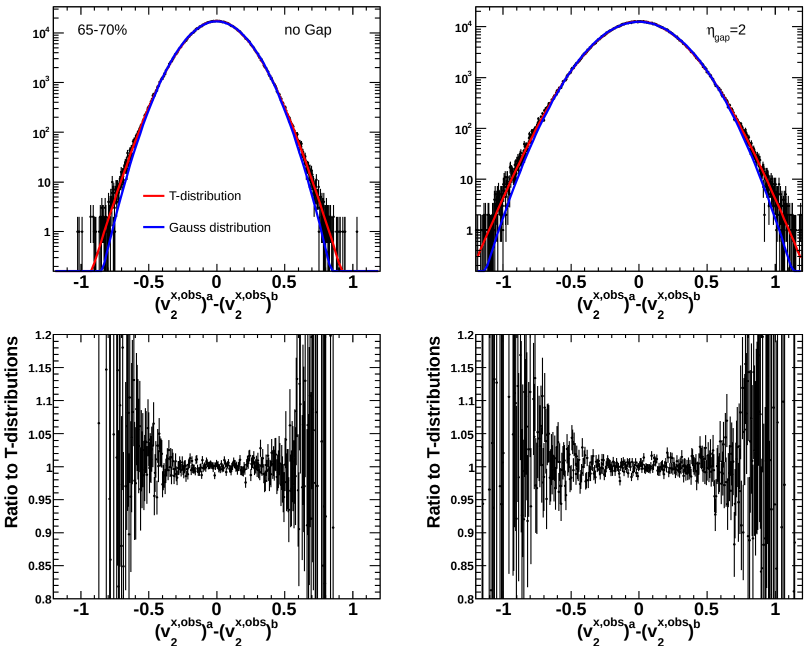

Figure C.3: The difference between the x-component of the per-particle flow vector measured in the two symmetric half-IDs without a η gap (top left) and with η gap of 2 units (top right) for $n = 2$ in the (65-70)% centrality interval. Fits to a Gaussian function (blue) and a to student's T-distribution (red) are also shown. The bottom panels show the ratio of data to the student's T-distributions.

particle flow vector between the two symmetric half-IDs (such as those shown in Fig. C.1), which are the starting points for obtaining the response functions used in the unfolding. The centrality bins 1-13 correspond to 5% steps for the (0-70)% centrality range, while the bins 14-19 corresponds to 1% steps for the (0-5)% centrality range. These figures show that the Gaussian description works well until the (50-55)% centrality where the χ^2/NDF is less than 1.5 but deviates strongly for more peripheral collisions (top left panels). The mean (top right panels) of the distributions are less than 1% of the width of the distributions. The width in x and y directions are very similar to each other (bottom left panels). The differences between the widths in the two directions, as shown by their ratios (bottom right panels) are less than 1% for n=2, about 1% for n=3, and less than 2-3% for n=4. These small differences indicate that the residual detector effects are minimal.

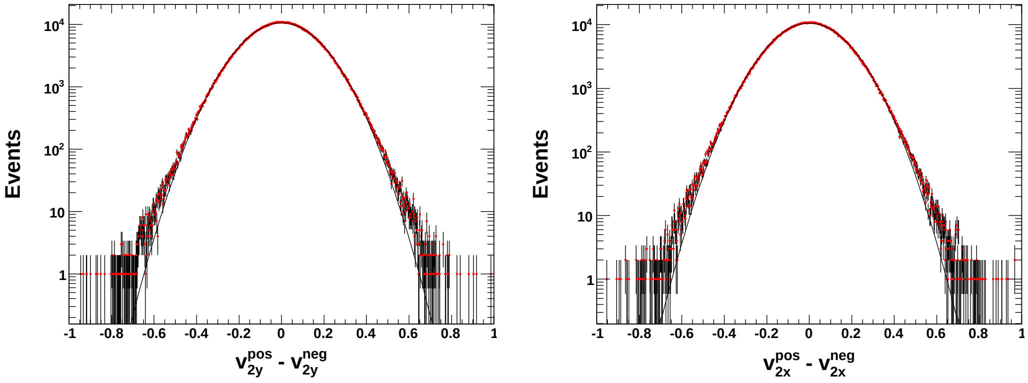

Figure C.4: The difference between the x-components (left panel) and y-components (right panel) of the per-particle flow vector calculated in two subevents for n=2, generated in a simple toy MC. The multiplicity for the toy MC is sampled from the multiplicity distribution measured in the (65-70)% centrality bin. The lines are a fit to a Gaussian function, clearly showing the presence of a non-Gaussian tail.

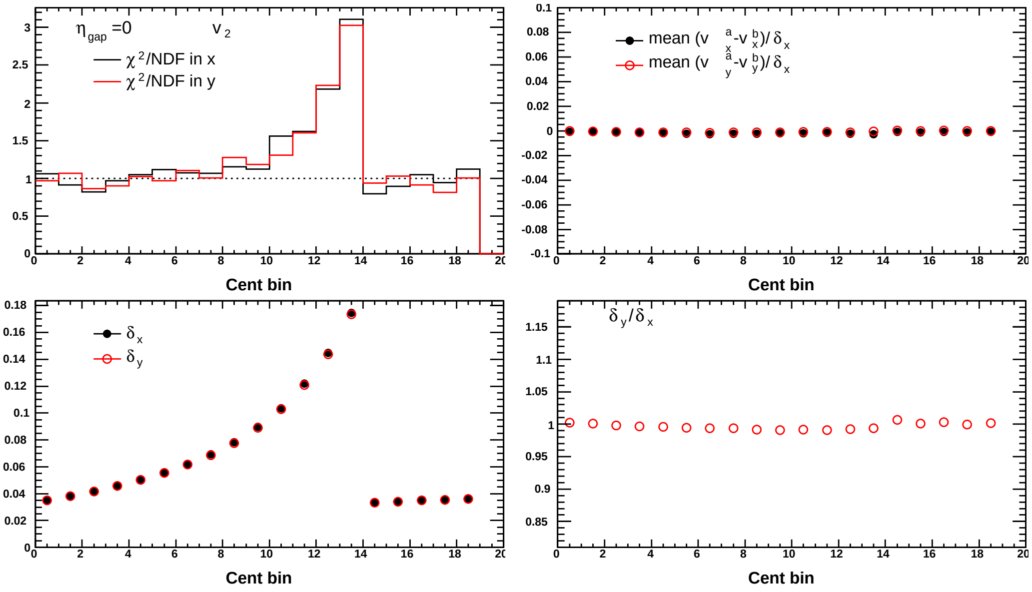

Figure C.5: As a function of centrality, the quality of the fit of Gaussian to the x and y components (top left), the mean of x and y components (top right), the width of the x and y components (bottom left), and the ratio of the widths (bottom right). Plots are for n=2.

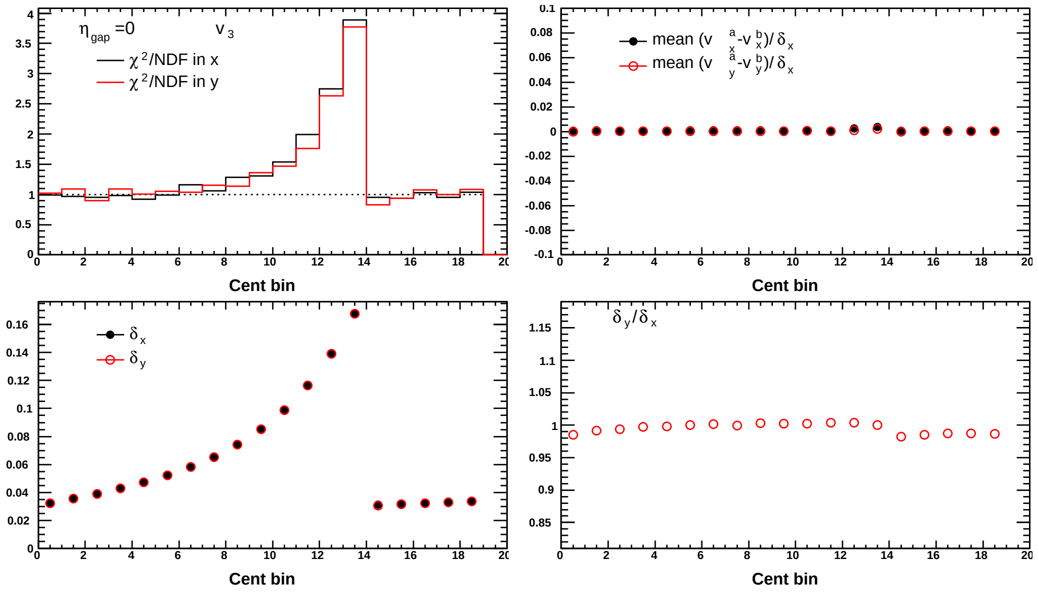

Figure C.6: Same as previous plot but for n=3.

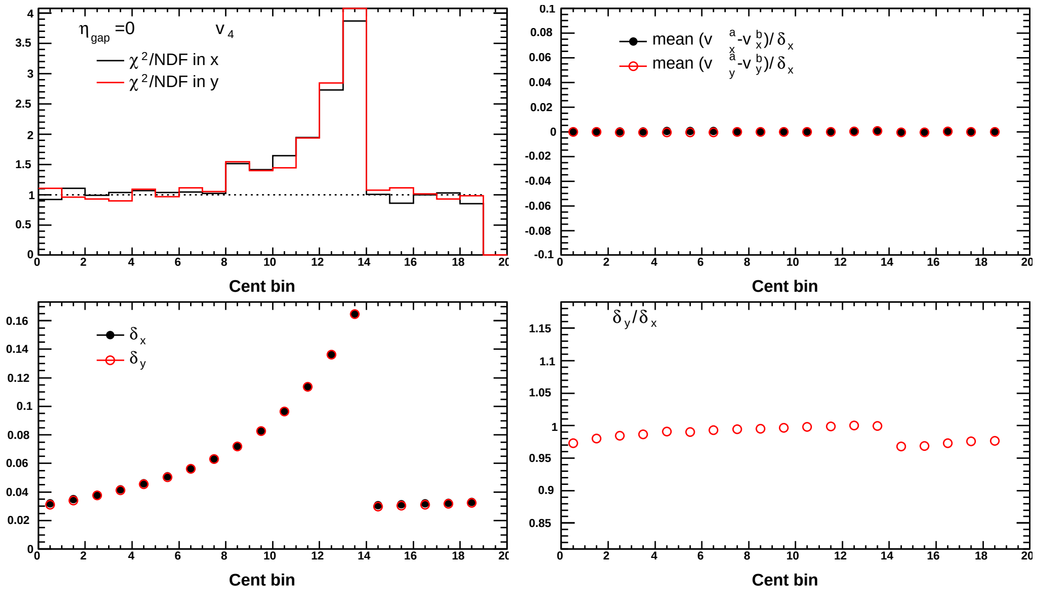

Figure C.7: Same as previous plot but for n=4.

Appendix D

Event-plane correlations

D.1 Resolution correction

Here the EP resolution correction formula (Eq. 6.10) is proven for two-plane correlations. The generalization to three-plane correlations is straightforward. The measured raw correlations can be expressed as:

$$\begin{aligned}
\cos(k(\Psi_n - \Psi_m)) &= \cos(k(\Psi_n - \Phi_n) - k(\Psi_m - \Phi_m) + k(\Phi_n - \Phi_m) \\
&= \cos(k(\Phi_n - \Phi_m)) \cos(k(\Psi_n - \Phi_n)) \cos(k(\Psi_m - \Phi_m)) \\
&\quad + \cos(k(\Phi_n - \Phi_m)) \sin(k(\Psi_n - \Phi_n)) \sin(k(\Psi_m - \Phi_m)) \\
&\quad - \sin(k(\Phi_n - \Phi_m)) \sin(k(\Psi_n - \Phi_n)) \cos(k(\Psi_m - \Phi_m)) \\
&\quad - \sin(k(\Phi_n - \Phi_m)) \cos(k(\Psi_n - \Phi_n)) \sin(k(\Psi_m - \Phi_m))
\end{aligned} \tag{D.1}$$

Where, as per the usual notation Φ_n and Φ_m are the true event-plans and Ψ_n and Ψ_m are the measured event-planes.

Averaging over a large number of events, the sine terms in Eq. D.1 become zero. This is true because the fluctuations of Ψ_n about Φ_n are statistical and thus have an equal probability to be positive and negative. Assuming that the average of product of terms in Eq. D.1 can be replaced by the product of their averages (or that the fluctuations of Ψ_m and Ψ_n about their truth values are uncorrelated, this will be justified later), one obtains:

$$\begin{aligned}
\langle \cos(k(\Psi_n - \Psi_m)) \rangle &= \langle \cos(k(\Phi_n - \Phi_m) \rangle \langle \cos(k(\Psi_n - \Phi_n) \rangle \langle \cos(k(\Psi_m - \Phi_m)) \rangle \\
&= \langle \cos(k(\Phi_n - \Phi_m)) \rangle \mathrm{Res}\{k\Psi_n\} \mathrm{Res}\{k\Psi_m\}
\end{aligned} \tag{D.2}$$

Where, $\mathrm{Res}\{k\Psi_n\}) = \langle\cos(k(\Psi_n - \Phi_n))\rangle$ and $\mathrm{Res}\{k\Psi_m\} = \langle\cos(k(\Psi_m - \Phi_m))\rangle$[1]. This gives:

$$\begin{aligned}\langle\cos(k(\Phi_n - \Phi_m))\rangle &= \langle\cos(k(\Psi_n - \Psi_m))\rangle/(\mathrm{Res}\{k\Psi_n\}\mathrm{Res}\{k\Psi_m\}) \\ &= \langle\cos(k(\Psi_n - \Psi_m))\rangle/\mathrm{Res}\{k(\Psi_n - \Psi_m\} \qquad \text{(D.3)}\end{aligned}$$

Where

$$\mathrm{Res}\{k(\Psi_n - \Psi_m)\} = \mathrm{Res}\{k\Psi_n\}\mathrm{Res}\{k\Psi_m\} \qquad \text{(D.4)}$$

Note that the net resolution is the product of two single-plane resolutions and can become very small and thus have large uncertainties. Similarly for the three-plane correlations, the resolutions are product of three individual single-plane resolutions. The resolutions are the main constraining factors that determine which two and three-plane correlations are measurable.

In order to ensure that the assumptions listed in the above derivation are correct, it has to be ensured that the same particles are not used in the determination of Ψ_n and Ψ_m, otherwise the fluctuations of Ψ_m and Ψ_n about their truth values might be correlated. Thus while calculating $\cos(N(\Psi_n - \Psi_m)$, the Ψ_n and Ψ_m must be measured is different parts of the detector. Similarly, for the three-plane correlations, the three event-plane angles must be measured in three separate parts of the detector..

D.2 Two-plane correlation analysis

D.2.1 Resolution determination

2SE results

Figure D.1 shows the relative angle distribution $dN/d\left(n\left(\Psi_n^{\mathrm{N}} - \Psi_n^{\mathrm{P}}\right)\right)$ between the positive η and negative η ECalFCal. From these distributions the resolution factors are calculated as:

$$\mathrm{Res}\{k\Psi_n^P\} = \mathrm{Res}\{k\Psi_n^N\} = \sqrt{\langle\cos k\left(\Psi_n^N - \Psi_n^P\right)\rangle} \qquad \text{(D.5)}$$

The red and blue histograms are foreground and background distributions, respectively. The background distributions are calculated from mixed-events, i.e. by combining the Ψ_n^N from one event with Ψ_n^P from another event with similar centrality (matched within 5%) and z-vertex (matched within 3 cm). Both the foreground and mixed-event distributions are normalized to unity.

---

[1] Note that for k=n, $\mathrm{Res}(k\Psi_n)$ is simply the event-plane resolution for the n^{th} harmonic used in the EP method.

The mixed-event distributions serve as estimations of the detector effects, while the foreground distribution contains both detector effects and physics. To cancel these non-physical structures, the correlation functions are obtained by dividing the foreground by the mixed-event distributions[2]:

$$C(n(\Psi_n^N - \Psi_n^P)) = \frac{S(n(\Psi_n^N - \Psi_n^P))}{B(n(\Psi_n^N - \Psi_n^P))} \tag{D.6}$$

The resolution factors are then calculated from these correlations functions. This procedure is almost identical to that used to obtain the raw correlation signal in Section 6.2.1, except here the correlations are between the event-planes of the "same order".

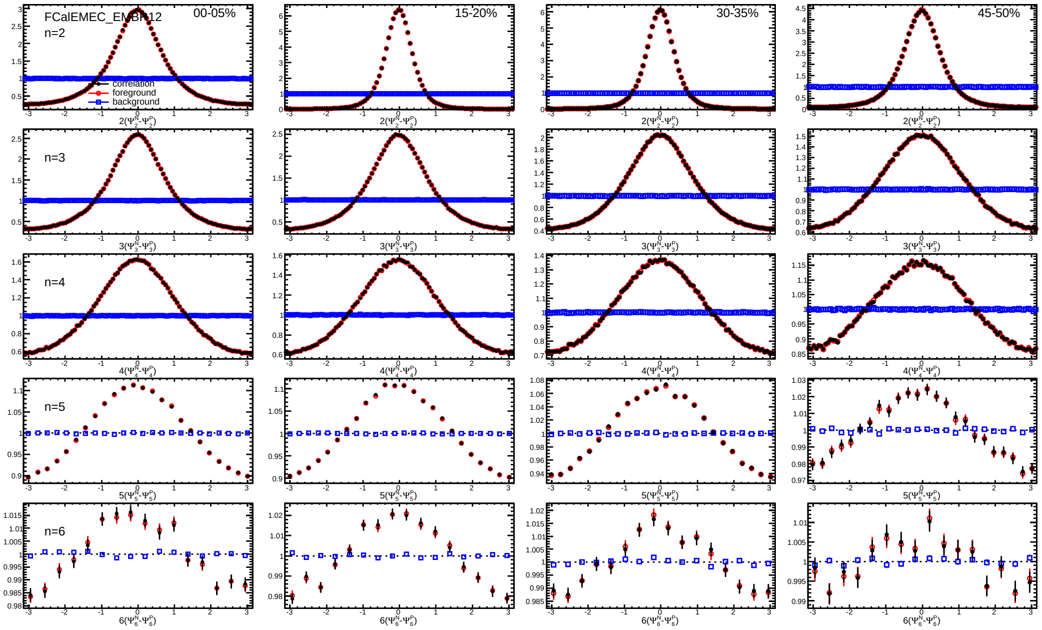

Figure D.1: The 2SE correlation functions $C(n(\Psi_n^N - \Psi_n^P))$ for event-plane at same order. Top to bottom rows corresponds to n=2-6, and columns correspond to different centrality intervals.

The left panels in Fig. D.2 show the centrality dependence of the cosine average, $\left\langle \cos jn\left(\Psi_n^N - \Psi_n^P\right)\right\rangle$, calculated from the 2SE correlation. The square root of the cosine average gives the subevent resolution (Eq. D.5). The right

---

[2] This method of event mixing was not implemented in the EP v_n analysis where the resolution for the sub-FCal was directly obtained from the foreground distribution of $\Psi_n^P - \Psi_n^N$. Here that method by is improved by using event mixing to further cancel out detector effects.

panels of Fig. D.2 show the values of $\left\langle \sin jn\left(\Psi_n^N - \Psi_n^P\right)\right\rangle$ relative to the cosine component which are an estimate of the systematic effects. The magnitude of the sine terms correlates with the cosines and has a negative sign. The origin of these non-zero sine terms can be understood as the result of a simple rotation of Ψ angle in the P-side relative to the Ψ angle in the N-side. Such a rotation can arise from energy mis-calibration, dead areas or low efficiency areas in the calorimeters and leads to a relative shift δ between the Ψ_n measured in the two sides. The measured cosine and sine terms are modified due to this shift as:

$$\begin{aligned}
\left\langle \cos jn\left(\Psi_n^{\rm N} - \Psi_n^{\rm P} + \delta\right)\right\rangle &\approx \left\langle \cos jn\left(\Psi_n^{\rm N} - \Psi_n^{\rm P}\right)\right\rangle \cos jn\delta \\
\left\langle \sin jn\left(\Psi_n^{\rm N} - \Psi_n^{\rm P} + \delta\right)\right\rangle &\approx \left\langle \cos jn\left(\Psi_n^{\rm N} - \Psi_n^{\rm P}\right)\right\rangle \sin jn\delta \\
\frac{\left\langle \sin jn\left(\Psi_n^{\rm N} - \Psi_n^{\rm P} + \delta\right)\right\rangle}{\left\langle \cos jn\left(\Psi_n^{\rm N} - \Psi_n^{\rm P} + \delta\right)\right\rangle} &\approx \tan jn\delta \approx jn\delta
\end{aligned} \tag{D.7}$$

If the sine term is purely related to a global rotation of one-side relative to the other side, then the ratio should be independent of centrality and proportional to j and n. From Fig. D.2 it is seen that this is indeed the case, with $\delta \sim$ 0.01 radians or half a degree. Note that a pure rotation is not removed by dividing by the mixed-event distribution. This is because a rotation of a uniform distribution still yields a uniform distribution, and hence the rotation only manifests itself if the amplitude of the correlation is non-zero. The event-mixing technique accounts only for non-physical correlations that lead to non-uniform distributions in $n\left(\Psi_n^{\rm N} - \Psi_n^{\rm P}\right)$.

In this analysis, the value of the $\langle\sin\rangle$ terms in the 2SE correlation is used as an estimation of systematic errors, which is reduced by half for the actual resolution calculation (due to taking the square root from subevent correlation to resolution Eq. D.5). Note that this is an overestimation of the actual influence on the measurement: the fractional change in the cosine term in Eq. D.7 due to a rotation δ is:

$$1 - \cos jn\delta \approx (jn\delta)^2/2 \approx \tan^2 jn\delta/2 \tag{D.8}$$

which is a very small number. Even for jn=12, the fractional change is only about $0.12^2/2 = 0.5\%$ in the resolution value. Nevertheless, the magnitude of the sine term is quoted as the absolute error (or the magnitude of $\langle\sin\rangle/\langle\cos\rangle$ term as the relative error).

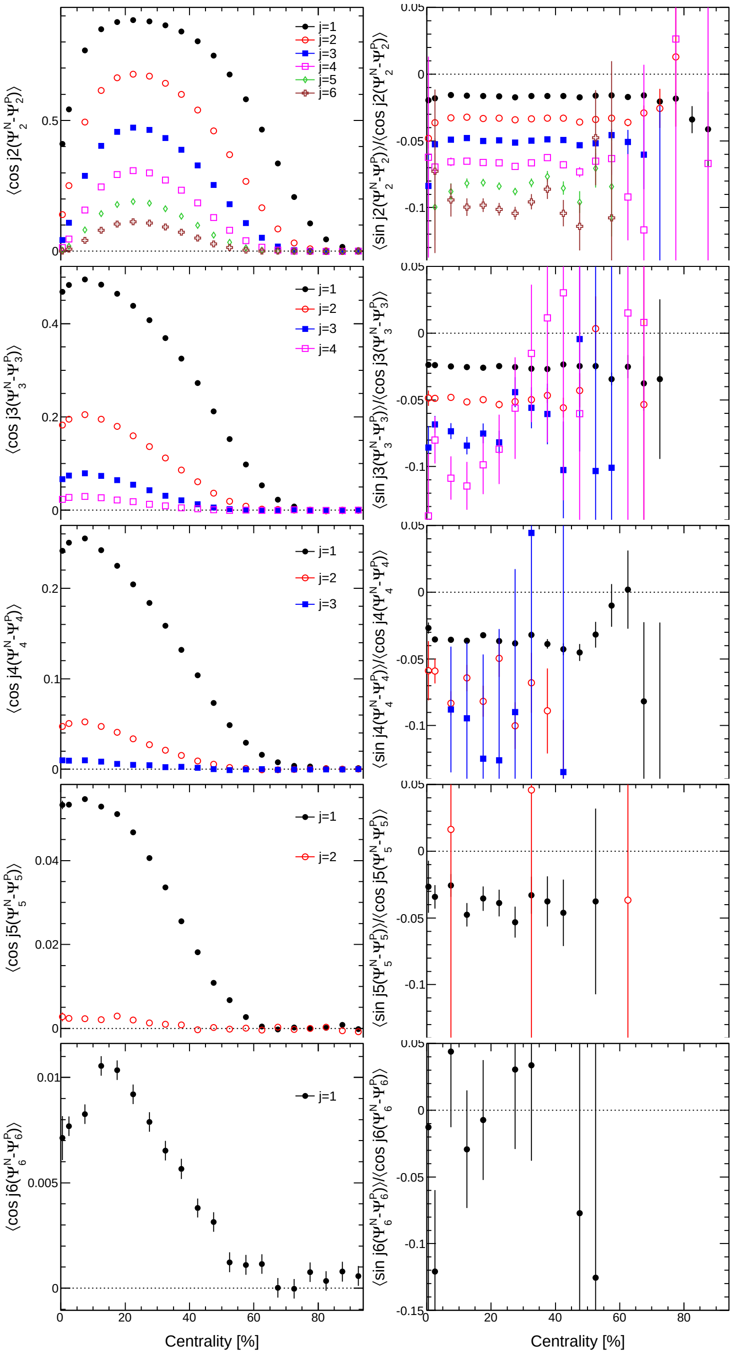

Figure D.2: Centrality dependence of $\left\langle \cos jn\left(\Psi_n^N - \Psi_n^P\right)\right\rangle$ values (left panels) and $\left\langle \sin jn\left(\Psi_n^N - \Psi_n^P\right)\right\rangle / \left\langle \cos jn\left(\Psi_n^N - \Psi_n^P\right)\right\rangle$ values (right panels). Each row corresponds to the order of the event-plane (n=2–6 from top to bottom). The different symbols in each panel corresponds to different values of j.

3SE results

The systematic uncertainties of the resolution correction are evaluated using the three-subevent method:

$$\mathrm{Res}\{k\Psi_n^{\mathrm{A}}\} = \sqrt{\frac{\langle \cos k\left(\Psi_n^{\mathrm{A}} - \Psi_n^{\mathrm{B}}\right)\rangle \langle \cos k\left(\Psi_n^{\mathrm{A}} - \Psi_n^{\mathrm{C}}\right)\rangle}{\langle \cos k\left(\Psi_n^{\mathrm{B}} - \Psi_n^{\mathrm{C}}\right)\rangle}} \tag{D.9}$$

with reference detectors taken from different η ranges. It should be emphasized that all the cosines in Eq. D.9 are calculated from the correlation function defined in Eq. D.6. The checks can be roughly divided into two types. In Type-I analysis, the resolutions are calculated separately for $\mathrm{ECalFCal_P}$ and $\mathrm{ECalFCal_N}$ in two separate 3SE studies with the reference detectors B and C chosen to be EM-barrel and FCal from the opposite η side. These two detectors have an η separation greater than 1.0 from the $\mathrm{ECalFCal_{P(N)}}$ and from each other.

In the Type-II analysis, A and B are chosen as $\mathrm{ECalFCal_N}$ and $\mathrm{ECalFCal_P}$ respectively, and C as the $\eta \in (-.5, .5)$ part of the EM-barrel. This detector is denoted as EMBR0, it is situated symmetrically between $\mathrm{ECalFCal_N}$ and $\mathrm{ECalFCal_P}$. This allows the calculation of the resolution for $\mathrm{ECalFCal_P}$ via Eq. D.9. Then the A and B are swapped detectors while keeping EMBR0 as C to calculate the resolution for $\mathrm{ECalFCal_N}$. The Type-II checks are similar to the 2SE method, as one can see from the following equation:

$$\mathrm{Res}\{\Psi_n^{\mathrm{Det_P}}\} = \sqrt{\frac{\left\langle \cos\left(n\left(\Psi_n^{\mathrm{Det_P}} - \Psi_n^{B}\right)\right)\right\rangle \left\langle \cos\left(n\left(\Psi_n^{\mathrm{Det_P}} - \Psi_n^{\mathrm{Det_N}}\right)\right)\right\rangle}{\left\langle \cos\left(n\left(\Psi_n^{\mathrm{Det_N}} - \Psi_n^{B}\right)\right)\right\rangle}} \tag{D.10}$$

$$\mathrm{Res}\{\Psi_n^{\mathrm{Det_N}}\} = \sqrt{\frac{\left\langle \cos\left(n\left(\Psi_n^{\mathrm{Det_N}} - \Psi_n^{B}\right)\right)\right\rangle \left\langle \cos\left(n\left(\Psi_n^{\mathrm{Det_P}} - \Psi_n^{\mathrm{Det_N}}\right)\right)\right\rangle}{\left\langle \cos\left(n\left(\Psi_n^{\mathrm{Det_P}} - \Psi_n^{B}\right)\right)\right\rangle}} \tag{D.11}$$

with $\cos\left(n\left(\Psi_n^{\mathrm{Det_N}} - \Psi_n^{B}\right)\right)$ and $\cos\left(n\left(\Psi_n^{\mathrm{Det_P}} - \Psi_n^{B}\right)\right)$ cancelling each other if the resolution are the same for $\mathrm{ECalFCal_N}$ and $\mathrm{ECalFCal_P}$, and the end results would be identical to the two-subevent formula Eq. D.5. However the main advantage here is that there is no need to make the assumption that the $\mathrm{ECalFCal_N}$ and $\mathrm{ECalFCal_P}$ have the same resolution. The list of 2SE checks are summarized in Table D.1.

The resolutions found by Type-I and Type-II 3SE combinations are next compared to the resolutions obtained by the 2SE method. Figure D.3 shows, as a function of centrality, the ratio of the resolutions (i.e. Type-I/2SE and

Type-I checks	Type-II checks
$\mathrm{Det_P} - \mathrm{EMBR_N} - \mathrm{FCAL_N}$	$\mathrm{Det_P} - \mathrm{EMBR0} - \mathrm{Det_N}$
$\mathrm{Det_N} - \mathrm{EMBR_P} - \mathrm{FCAL_P}$	$\mathrm{Det_N} - \mathrm{EMBR0} - \mathrm{Det_P}$

Table D.1: List of 3SE combinations for ECalFCal resolution calculation.

Type-II/2SE) for the 2^{nd}-order event-plane (i.e. n=2) and for various values of j (in $\mathrm{Res}\{2j\Psi_2\}$). Type-I results show an almost centrality independent deviation from the 2SE values, which increases almost linearly with increasing j values, while the Type-II results are consistent with no deviation from the 2SE results, except for very peripheral collisions. Note that the “mirror-image” behavior of the two sets of points in the right-hand plots (Type-II/2SE) follows from the defining formulae Eq. D.10 and Eq. D.11 and the choice of detectors used. These comparisons are repeated for n=3–6 in Figs. D.4-D.7, respectively. Similar systematic deviations are observed with only slight centrality dependence.

Table D.2 summarizes the systematic uncertainties for the ECalFCal. They include contributions of the non-vanishing sine terms from the 2SE correlation, as well as the deviations of the 3SE results. The systematic uncertainties from the two sources are quoted as centrality independent (conservatively) and then added in quadrature.

Error for $\mathrm{Res}\{jn\Psi_n\}$					
n	2	3	4	5	6
3SE comparison [%]	$1.4j$	$3.9j$	$3.3j$	$5.5j$	$18j$
sine component [%]	$1.0j$	$1.7j$	$2.0j$	$2.5j$	$5\ j$
total [%]	$1.7j$	$4.3j$	$3.9j$	$6.0j$	$19j$

Table D.2: Summary of systematic uncertainties for individual $\mathrm{Res}\{jn\Psi_n\}$ from 2SE/3SE comparison (Figs. D.4-D.7), and sine component of the 2SE correlations (Fig. D.2). Note that the uncertainties of $\mathrm{Res}\{jn\Psi_n\}$ are found to be proportional to values of j.

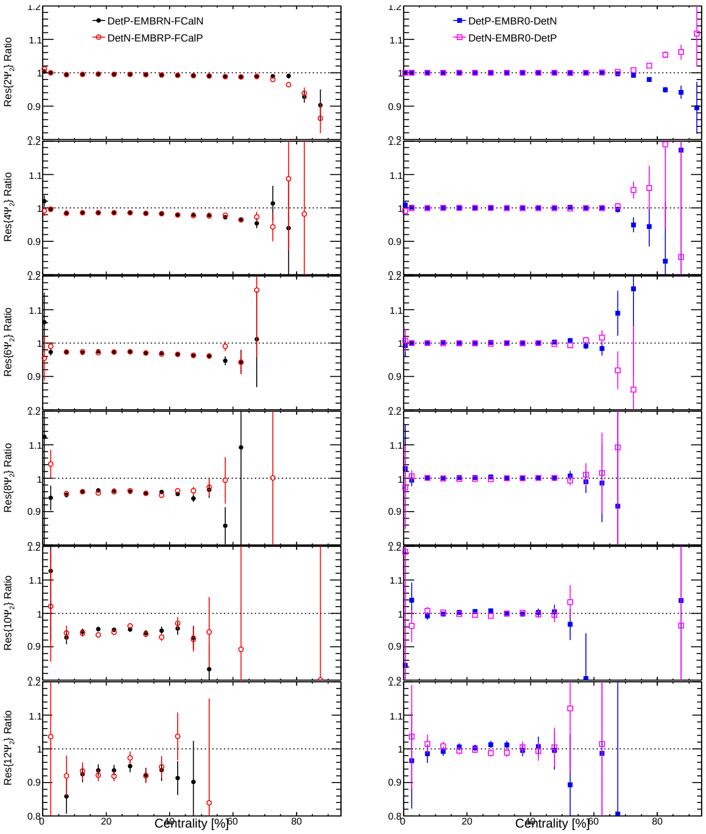

Figure D.3: The centrality dependence of the ratios of 3SE results to 2SE results for Type-I (left panels) and Type-II (right panels) checks for 2^{nd}-order event-plane. Each row is for different j as in Res$\{2j\Psi_2\}$.

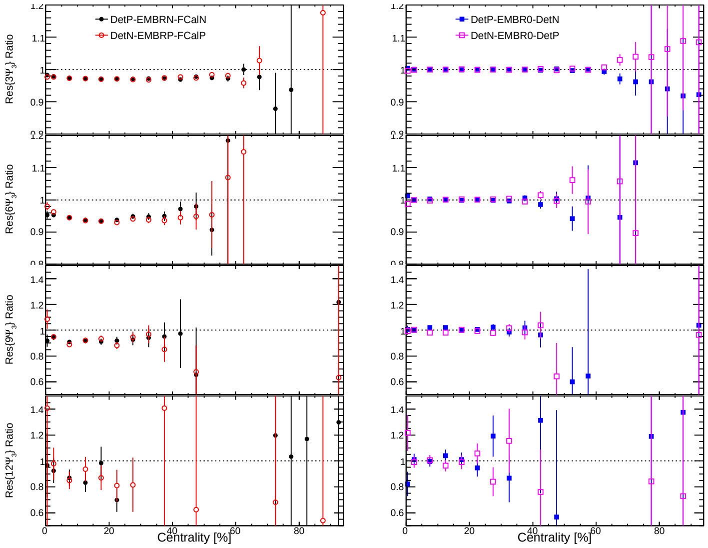

Figure D.4: The centrality dependence of the ratios of 3SE results to 2SE results for Type-I (left panels) and Type-II (right panels) checks for 3^{rd}-order event-plane. Each row is for different j as in $\text{Res}\{3j\Psi_3\}$.

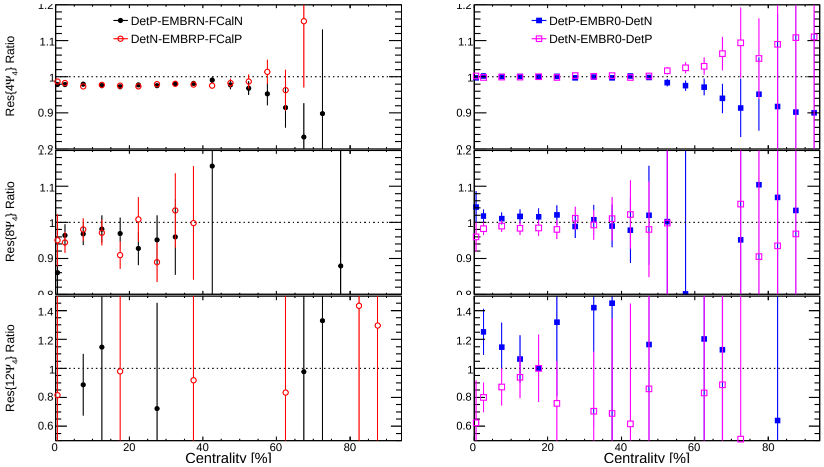

Figure D.5: The centrality dependence of the ratios of 3SE results to 2SE results for Type-I (left panels) and Type-II (right panels) checks for 4^{th}-order event-plane. Each row corresponds to different values of j as in $\text{Res}\{4j\Psi_4\}$.

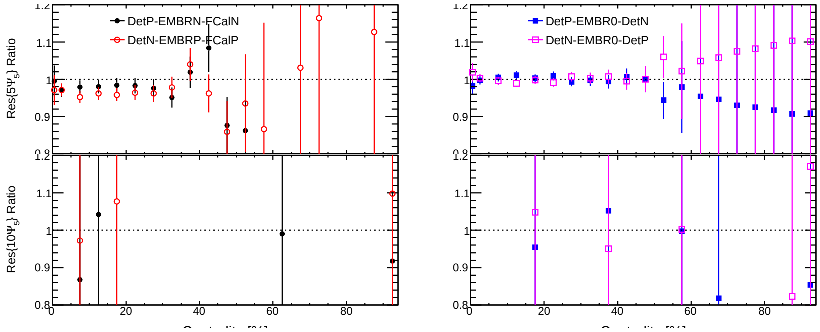

Figure D.6: The centrality dependence of the ratios of 3SE results to 2SE results for Type-I (left panels) and Type-II (right panels) checks for 5th-order event-plane. Each row corresponds to different values of j as in $\mathrm{Res}\{5j\Psi_5\}$.

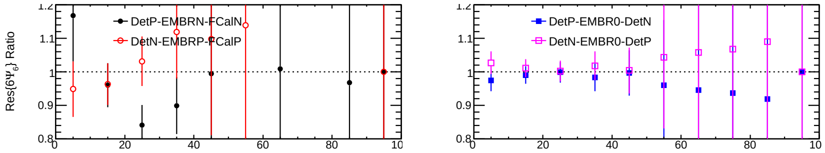

Figure D.7: The centrality dependence of the ratios of 3SE results to 2SE results for Type-I (left panel) and Type-II (right panel) checks for 6th-order event-plane $\mathrm{Res}\{6\Psi_6\}$.